Holger Gottschlag

Small Animal Positron Emission Tomography with Multi-Wire Proportional Counters

— 2010 —

Experimentelle Physik

Small Animal Positron Emission Tomography with Multi-Wire Proportional Counters

Inauguraldissertation
zur Erlangung des Doktorgrades
der Naturwissenschaften im Fachbereich Physik
der Mathematisch-Naturwissenschaftlichen Fakultät
der Westfälischen Wilhelms-Universität Münster

vorgelegt von
Holger Gottschlag
aus Ibbenbüren

— 2010 —

Dekan:	Prof. Dr. J. P. Wessels
Erster Gutachter:	Prof. Dr. J. P. Wessels
Zweiter Gutachter:	PD Dr. K. Reygers

Tag der Disputation:	16.07.2010
Tag der Promotion:	16.07.2010

Contents

1. Introduction

Positron Emission Tomography (PET) is a medical imaging technique used to visualise metabolic processes within the body. The distribution and kinetics of a tracer molecule can be investigated. This tracer molecule acts as a marker for molecular targets and receptors. Being conjuncted with a positron emitting nuclide, its decay radiation is observed. PET examinations can help to identify some of life's biggest threats like cancer, cardiac insufficiency and plaques in cardiac vessels that may lead to myocardial infarction.

By expanding PET techniques to small animals like mice or rats, they can help to improve research on preclinical questions dealing with the evolution of the serious diseases mentioned and their treatment. Because a PET examination, unlike alternative invasive methods like dissection, is not fatal for the animal, results are much more meaningful and the animal can be imaged more than once and therefore long term studies can be performed.

In the design of a small animal PET scanner one has to take the size of the animal and the resulting special requirements for spatial resolution and photon detection efficiency into account. A mouse heart is about 10 times smaller than a human heart and beats 10 times faster. Modern human PET scanners reach a spatial resolution of the order of 4 mm. Improving small animal PET devices to proportionate resolutions is not possible due to physical limitations. Nevertheless, it is intended to reach this limit which is slightly below 1 mm for ^{18}F based tracer molecules.

Another important performance parameter of PET imaging devices is sensitivity. Sensitivity is the capacity of a scanner to detect annihilation photons. Its value is given by the number of measured counts per radioactive decay. As the amount of radioactivity that can be safely injected is limited, the sensitivity should be as high as possible.

To build such a dedicated PET device, different approaches have been employed. Most of them concentrate on traditional scintillation crystal detector concepts which are widely used in clinical PET. They provide spatial resolution of the order of the size of the used crystals and sufficient energy resolution to reject Compton-scattering induced image blurring. As a drawback, these devices have a relative small field-of-view which limits the system's sensitivity. In addition the spatial resolution degrades with increasing distance of the object to the centre of the system.

Alternative PET scanner designs based on multi-wire proportional counters (MWPCs) have been proposed since the 1970s and suffer a niche existence since then. The reason for that is the lack of energy resolution and a more complex design which needs trained

personnel that can deal with high voltage calibration and gas supply service. Nevertheless this approach provides unparalleled spatial resolution and a large field-of-view without off-centre resolution degradation. Another big advantage is the lower price of such a system in comparison to crystal based scanners.
The University Hospital of Münster operates two quadHIDAC small animal PET scanners based on MWPC detectors that are coupled to complex electron converters. With these machines spatial resolutions close to the physical limits have been measured and sufficient system sensitivity is obtained. Unfortunately, the service and support with spare parts for the detector has become a problem as the manufacturer discontinued his activities including support and maintenance of the quadHIDAC.
Because of the advantages of MWPC-based PET scanners, the development of an optimised detector concept is anticipated. The optimisation is meant not only in terms of sensitivity and resolution improvement but also in the simplification of production processes and the use of fast modern electronics.
This thesis will propose a design of an optimised, easy to build MWPC-based small animal PET scanner. In the development process tools and knowledge from detector and electronic developments in high-energy physics experiments could be transferred. In particular the Institut für Kernphysik in Münster is involved in the ALICE TRD project [ALI01] at CERN as well as in TRD developments for the CBM experiment [CBM05] at FAIR, GSI.
In addition, the quadHIDACs converter design is revisited and possible improvements based on simulation results are presented. It is shown how simulations can help to deal with the absence of energy resolution by calculating scatter distributions of test sources. These results can be used as input values for reconstruction algorithms and build the foundation of quantitative PET with the quadHIDAC as a representative of multi-wire proportional chamber based small animal PET scanners.

2. Medical Imaging Techniques

In the history of medicine multiple approaches of non- or minimal-invasive visual diagnosis of internal diseases and malformations have been made. Some of these use ionising radiation, others do not. Some are appropriate for bone structures and hard tissue, others are made for examination of soft tissues. Even other modern imaging techniques are appropriate for the visualisation of the metabolism of certain drugs or nutrients. This allows to discriminate prevalent morphological and functional techniques where the borders between the two blur with ongoing research:
In order to assess the overall condition of a patient, it is often useful to combine functional and morphological techniques. Covering multiple imaging techniques in just one device,

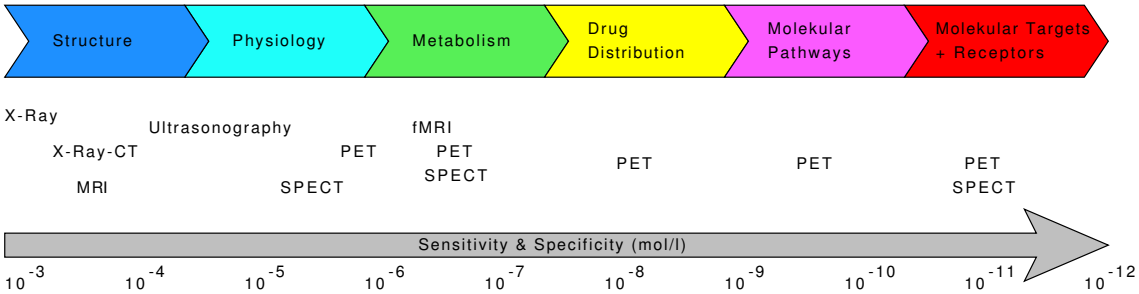

Figure 2.1: The spectrum of medical imaging techniques ordered by their ability to image decreasing concentrations of specific molecules inspired by [Jon96].

combinations like PET/CT, PET/MRI and also PET/US (explained in the following sections) represent the current state of the art. The improvement in sensitivity is one of the biggest challenges for all imaging modalities, as it is directly related to the amount of tracer activity and radiation dose that has to be injected. Figure 2.1 shows the needed sensitivity for different examinations and appropriate imaging techniques. In the following sections a short overview of the most important and widely used imaging techniques is given.

2.1 Morphological Imaging Techniques

2.1.1 X-Ray Imaging

X-Radiation are electromagnetic waves within an energy range of roughly 120 eV to 250 keV. It is produced in cathode tubes originally invented by J. Hittorf and W. Crookes. W. C. Röntgen accidentally discovered X-rays in 1895, when working with a cathode tube. As he surrendered a patent on his discovery, the X-ray technology rapidly spread in medicine as well as in industry. In an X-ray tube electrons are liberated thermally from a cathode and then accelerated towards an anode made of some material with a high proton number (mostly tungsten or molybdenum). Here they produce on the one hand continuum Bremsstrahlung radiation and on the other hand a characteristic radiation depending on the anode material. This characteristic radiation is induced by transitions of higher shell electrons of the anode materials atoms into lower shells (called K-, L- and M-shells).
In medical imaging, X-rays are used to detect abnormities in human tissue. Depending on the material and density of the tissue, the X-rays will be attenuated due to the photoelectric effect and Compton scattering. Therefore, the energy (and also the radiation exposure) needs to be adapted to the tissue under investigation: soft tissue needs lower energies resulting in larger biological effects due to radiation than for example the examination of bone structures.
An X-ray detector is used to measure this radiation attenuation inside the examined tissue. In the most simple case, the detector is just a photographic plate which is blackened depending on the intensity of the incoming radiation. Today, also X-ray image intensifiers are available, which provide live images of the patient, often used for angiography and for online control during operations. For a more detailed description of X-ray techniques see e.g. [JAN01].

2.1.2 X-Ray Computed Tomography (CT)

As an improvement of X-ray imaging, X-ray computed tomography reaches back to the early 1970's. Based on the work of A. M. Cormack it was G. Houndsfield who produced the first CT-prototypes. For their developments both have been awarded the Nobel price for medicine in 1979.
In computed tomography the X-ray attenuation of an object is measured from different angles. Using a Radon transformation, which was described by J. Radon in 1917, the lost volume information of the measured single projections can be recovered. With the help of computers, tomographic images and also 3D visualisations of the back-projected volume-information can be calculated. That makes CT a very precise and powerful morphological imaging technique. The number of CT examinations in the United States grew by a factor

of 5 since 1990. However, a drawback of the method is that the applied radiation dose in most examinations, especially in abdominal CT, is not negligible. Doses of up to 20 mSv are applied during a single examination, which is about ten times the dose that an average person is exposed to per year. In the USA the percentage of cancers that may be attributable to the radiation of CT studies was estimated to be 1.5 to 2% [B$^+$07b]. Thus in order to avoid unnecessary radiation exposure one has to check individually, if a CT scan is inevitable or if it can be replaced by a more expensive MRI or less precise ultrasonography examination. For a detailed description of modern X-ray CT physics see [Buz08].

2.1.3 Ultrasonography (US)

Medical ultrasonography goes back to an invention by P. Langevin, who took profit of the discovery of the piezoelectric effect by P. and J. Curie in 1880. He used ultrasound waves created by a quartz-crystal to seek for enemy submarines during World War I. In the year 1937 K. Dussik was the first physician, who used US to image an ventricle of the brain. US is the most frequently used imaging technique in today's medicine.
In contrast to X-ray imaging, sonography is often used for imaging of soft tissue, especially viscera. The acoustic waves applied to the patient are reflected and absorbed by the tissue. Reflected waves are detected by the device so that an image can be calculated. Sonography devices use frequencies from 1 to 40 MHz depending on the kind of the examination. Lower frequencies provide less spatial resolution, but allow imaging of deeper areas in the patients body. The injection of recently developed special contrast agents (so called micro bubbles) improves image contrast and has the ability to advance US to functional imaging. Drugs constained in these micro bubbles can be applied very precisely in the patient. US-waves are then used to let the bubbles burst and release the drug [TP04]. The use of acoustic waves is an advantage in terms of radiation exposure as US has almost[1] no negative influence on the patient. It is cheap, fast and readily available. As a drawback, US images are not always easy to interpret, so that the efficiency of the method depends to some degree on the skill of the physician. For more information on the physics of US see e.g. [Kan02].

2.1.4 Magnetic Resonance Imaging (MRI)

MRI can create images of soft tissues without using ionising radiation. Hence it is less harmful to the patient then a comparable CT examination. Even after 20 years of expe-

[1] In prenatal US secondary sound wave emission in the uterus that is hearable for the child can occur, reaching noise levels up to 100 dB. Evidences for neuronal effects of prolonged US could not be confirmed yet [RD06].

rience with electromagnetic fields produced by an MRI device no evidence for harmful behaviour to the human body has been observed. Due to the high magnetic fields applied in an MRI scanner, patients should neither have a cardiac pacemaker nor wear anything ferromagnetic inside the examination room. Despite the danger of accelerated objects, any metal will lead to distortions during the measurement.
Magnetic Resonance Imaging is dedicated to the inspection of soft tissue and blood vessels. Using contrast agents, MRI can replace invasive angiographic examinations. Especially the larger blood vessels can be visualised in great detail.
To understand the basics of MR imaging, one has to deal with the nuclear properties of matter. MRI is based on the observation of nuclear magnetic resonances which were first measured by I. Rabi in 1938. In the following years F. Bloch and E. Purcell worked independently of each other on magnetic resonance measurements. Both were rewarded with the Nobel prize in 1952 for their work on nuclear magnetic precision measurements. It took until 1972, when P. Lauterbur and P. Mansfield presented the first MRI images of the human body. They shared the Nobel prize for medicine of 2003 for their discoveries concerning MRI.
Atoms with uneven numbers of nucleons have a non-vanishing total spin and thus a magnetic momentum. So does the hydrogen atom (^{1}H), which appears in large quantities in nearly all parts of the human body. Other important atoms are nitrogen (^{14}N), phosphor (^{31}P), sodium (^{23}Na) and flour (^{19}F). Using a high static magnetic field (in human MRI scanners typically $1-3$ Tesla) it is possible to partially align the spins of the observed nuclei parallel or anti-parallel to the static magnetic field lines. Depending on the strength of the magnetic field and the temperature, parallelly aligned nuclei are energetically preferred compared to anti-parallel ones:

$$\frac{\text{parallel}}{\text{anti-parallel}} = e^{-dE/k_BT},$$

with the energy difference between parallel and anti-parallel states $dE \approx 10^{-8}\,\text{eV}$ (depending on the applied magnetic field) and the Boltzmann constant $k_B \approx 8,6173 \cdot 10^{-5}\,\text{eV/K}$. Only the fully parallelly aligned nuclei will create a measurable signal later on. Because of the intrinsic angular momentum a spin precession with the Larmor-frequency $\omega_L = \gamma \cdot |B|$ around the magnetic field lines occurs. Here $\gamma = \frac{\vec{\mu}}{\vec{s}}$ is the gyromagnetic ratio of the particles magnetic moment $\vec{\mu}$ and its spin $\vec{s}$. The precession angle can now be synchronised and increased up to 180 degrees with respect to the field lines by short radio wave pulses at frequencies matching the Larmor-frequency of the observed nuclei. After a short time span, typically of the order of seconds, called the spin-grid relaxation time (T1), the precession angle falls back to its initial state. T1 is defined as the time in which the longitudinal magnetisation is re-established at 67% of the initial

magnetisation. The energy is emitted as high frequency electromagnetic waves which can be measured using a suitable antenna. The contrast of T1 images can be changed by altering the repetition time, which is the time between two excitations. The time T1 strongly depends on the density of the observed tissue. Tissue with higher density has a shorter relaxation time. Therefore, T1-measurements are appropriate to differentiate between certain types of tissue like fat or water.
The spin-spin relaxation time (T2) describes the time needed to dephase the transverse magnetisation due to spin-spin interactions. T2 is defined as the time in which the transverse magnetisation falls down to 37%. By modifying the echo time, which is the time between excitation and signal readout, the contrast of T2 images can be adjusted. While in T1 pictures water appears dark, in T2 it appears pale. Hence, T2 images can be used to detect pathologic changes in tissue which are known to attract more water than normal tissue.
In order to obtain spatial information from the measured signals, a additional gradient fields are needed. It is orders of magnitude smaller than the longitudinal static magnetic field, but it alters the Larmor frequency of the observed atoms in the way that excitation occurs only in a small area. By tuning the excitation frequency it is possible to choose a certain slice along the longitudinal axis for visualisation.
For further information on the MRI technology see e.g. [Kol07] or [W$^+$06].

2.2 Functional Imaging Techniques

2.2.1 Functional Magnetic Resonance Imaging (fMRI)

Advancements of the MRI technology allow to visualise brain activities. It is for example possible to identify connections between certain brain areas and body functions. Modern fMRI does not need any kind of contrast agent and is therefore fully non-invasive. The so called BOLD (blood oxygen level-dependent imaging) imaging technique visualises the blood flow in the brain using different magnetic properties of oxygenated and deoxygenated haemoglobin. Active brain areas show an increased oxygen metabolism inducing an increase of the local blood flow in these areas. The high blood flow then leads to an oxygen outflow, which is higher than the oxygen usage of the brain. Therefore, the veins contain more diamagnetic oxyhaemaglobin than paramagnetic deoxyhaemaglobin. The magnetic field is less distorted than elsewhere in the brain. These field inhomogenities will accelerate the T2 (see section 2.1.4) relaxation times. These are called T2*. Measuring this MR gradient echo signal, one can reconstruct the areas of increased brain activity. Further details can be found in [Kol07] and [W$^+$06].

2.2.2 Doppler Ultrasonography (US)

The Doppler US technique is an improvement to the conventional US technique. It uses the frequency shift of ultrasound waves reflected by moving target material. Doppler US is used to visualise the speed of blood flow and pressure in blood vessels. It can detect blood clots and defective valves of veins and also of the heart. Because it is non-invasive and does not produce ionising radiation, it is a riskless angiographic method. For some examinations contrast agents can be used to improve the image quality. For further information on Doppler US see e.g. [Kan02].

2.2.3 Single Photon Emission Computed Tomography (SPECT)

As an advancement of the 2D equivalent technique called gamma scintigraphy, SPECT can provide 3D data of functional processes in the body. Thus SPECT is in direct competition with Positron Emission Tomography (PET) (see section 3). While PET detects positron emitting radiotracers, SPECT uses gamma emitters (e.g. ^{99m}Tc with an photon energy of 143 keV), bound to proper tracer molecules. Whereas the positron range limits the spatial resolution in PET, this is not a problem in SPECT. Also, due to the much simpler electronics, SPECT is a less expensive technique than PET. In addition, the tracer molecules used for SPECT can be produced without expensive accelerator methods using so-called generators. As a drawback SPECT devices cannot reach comparable sensitivity levels to PET, which however suffers from lower spatial resolution.
One of the first relevant publications dealing with SPECT techniques was written by David E. Kuhl and Roy Q. Edwards [KE63] in 1963. They used data taken from emission measurements with a scintillator based pinhole gamma camera developed by Hal Anger [Ang58, Ang64] in 1953 to produce the first tomographs.
A SPECT camera typically consists of a gamma detector with a collimator lense in front of it. The whole camera is moved around the patients body, such that photons heading into all directions are measured and the needed data for tomographic images is acquired. The collimator consists of some material with a high atomic number, mostly lead or tungsten. In order to ensure that only photons originating from perpendicular angles hit the detector, the collimator has to be thick enough to shield all other angles and its structure has to be as finely segmented as possible to minimise the minimum angle of separation. Often drilled pinhole designs are used for this purpose. Inevitably the collimator leads to a high reduction of sensitivity compared to PET detectors. With SPECT a spatial resolution of about 7 mm can be achieved with clinical cameras. Small animal versions can reach resolutions up to 1.5 mm [J$^+$94]. For more information on SPECT and SPECT devices see [WA04].

3. Positron Emission Tomography

Positron Emission Tomography (PET) is the most sensitive of all functional medical imaging techniques. It allows to visualise for example metabolic processes of the body or the neuroreceptor activity of the brain. It images local activities of metabolism-specific molecules that contain a positron emitter. These cannot be distinguished by the organism and are treated like normal unlabelled molecules. A few minutes after injection of this so-called tracer, it will enrich in areas of high metabolic activity. The emitted positrons will thermalise and bind to local electrons forming positronium. The positronium will then annihilate after a short half life ($t \approx 10^{-10}\,\mathrm{s}$) mostly into two photons at an angle of nearly 180°. Figure 3.1 shows a schematic sketch of such an annihilation process.

These photons will then interact with a position sensitive detector placed around the

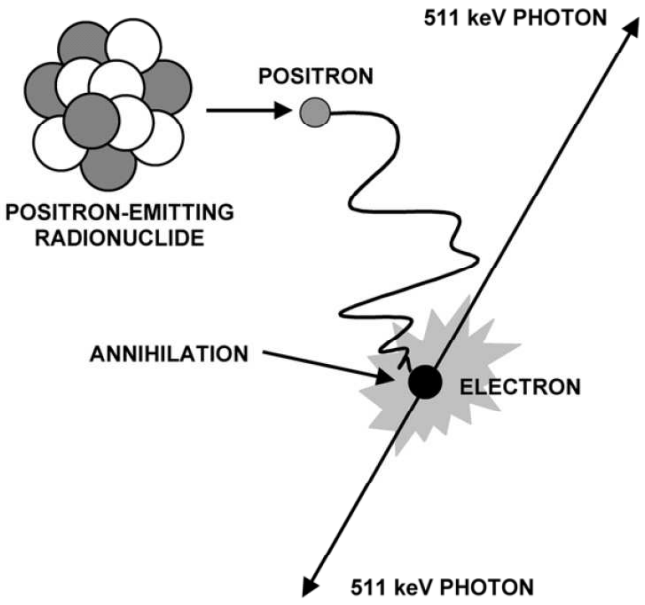

Figure 3.1: Basic sketch of the annihilation process in PET [Phe06]. After the decay positron loses nearly all of its energy due to multiple scattering it will combine with a local electron and form a positronium state which subsequently decays, predominantly into two photons.

patient. Subsequent reconstruction software will usually connect the hit-points in the detector to lines called lines-of-response (LORs). Having many LORs the original image can be reconstructed using proper algorithms.

Isotope	Production Methods	Half-Life	Mean e^+ Energy (keV)	Max. e^+ Energy (keV)	e^+ Range in Water (mm)	
					Max.	Mean
^{11}C	Cyclotron: ^{14}N(p,α)	20.38 min	386	960	4.1	1.1
^{13}N	Cyclotron: ^{16}O(p,α)	9.96 min	492	1198	5.1	1.5
^{15}O	Cyclotron: ^{14}N(d,n) or ^{15}N(p,n)	2.03 min	735	1732	7.3	2.5
^{18}F	Cyclotron: ^{18}O(p,n) or ^{20}Ne(d,α)	109.7 min	250	634	2.4	0.6
^{68}Ga	Generator	68 min	830	1899	8.2	2.9
^{82}Rb	Generator	1.27 min / 6.3 h	1479 / 360	1535 / 722	14.1	5.9

Table 3.1: Commonly used radio isotopes in PET. Cyclotron reactions are taken from [IAE09], half-lifes and energies from [Nat09b] and ranges in water from [B$^+$05].

As Positron Emission Tomography has been explained in numerous publications and books, the following sections are not meant to provide a complete description of all aspects of PET. The focus will be set on the most important points with respect to later chapters, and in addition some points neglected in most literature will be mentioned.

3.1 Tracers in PET

A tracer is a specific molecule that has been labeled with a radioactive atom. The labeled molecule should behave just like its unlabeled counter part with respect to metabolism. The idea to use radioactive isotopes as a marker for the uptake of the corresponding stable isotope is not new. The first publications reach back to 1923, when G. de Hevesy measured the distribution of radioactive lead (^{212}Pb) in horse-beans [Hev23]. Since then, tracers have been further developed to highly specific probes, made for the visualisation of biochemical processes on the basis of molecular interactions between tracer and target cells. They are appropriate detection systems for quantitative, non-invasive measurements used for diagnosis and therapy of a manifold of diseases. In order to keep the radiation exposure for the patient as low as possible, positron emitters with short half lifes are used as markers. Table 3.1 lists some commonly used radionuclides in PET. In order to produce these radionuclides a generator or a cyclotron is needed, depending on the nuclide to be produced. In a generator the target nuclide is produced by the decay of a more stable radioactive mother nuclide. ^{68}Ga is produced by ^{68}Ge via an electron capture process with a half life of 271 days. ^{82}Rb is produced by the electron capture of ^{82}Sr, which has a half life of 25.5 days.
The cyclotron reactions for other relevant nuclides can be found in Table 3.1. Depending on the half-life of the isotopes, the injection of the radio-pharmaceutics needs to be done directly after the production. As the half-life of ^{15}O is only 2 minutes, the patient is connected directly to the cyclotron via a few tubes and intermediate stages only. Especially

^{18}F has become very popular, mostly because of its adequate life time and its chemical properties (it can easily replace an OH-group), that allows to label molecules with a production loss of about 50 %. From 1 GBq of ^{18}F activity coming out of the cyclotron, 500 MBq is left after the radiochemistry process of which 370 MBq can be given to the patient. It takes about 50 minutes from the cyclotron to the patient.
The most deployed tracer molecule today is ^{18}F-Flourodeoxyglucose (FDG) which is used to visualise the glucose uptakes in cardiologic and oncologic questions. Figure 3.2 displays the chair conformation of the FDG molecule. Not only glucose can be la-

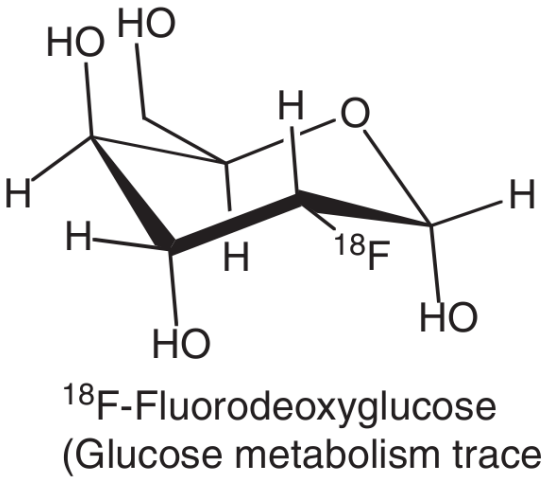

Figure 3.2: The ^{18}F-Flourodeoxyglucose (FDG) molecule [WA04]. In comparison to the unlabeled glucose molecule, an OH-group has been replaced by the radioactive ^{18}F.

beled with ^{18}F, but also other molecules like 3,4-dihydroxy-6-18F-fluoro-L-phenylalanine (^{18}FDOPA) used as a neurotransmitter tracer in brain imaging, ^{18}F-Chlorine for studies of e.g. prostate cancer or ^{18}F-fluoroestradiol (FES) for the examination of breast cancer, to mention just a few of them, are commonly used in clinics today.

3.2 Physics of Positron Emission Tomography

3.2.1 PET Basics

The radioactive component of a tracer molecule in the target area will undergo a β^+-decay where a proton in the nucleus is converted into a neutron. On the microscopic level, the

weak force converts an u-quark into a d-quark followed by the emission of a positron and a neutrino mediated by the exchange of the virtual W^+-Boson:

$$p \rightarrow n + e^+ + \nu_e \tag{3.1}$$

Figure 3.3 shows a Feynman graph of the positron decay. Here the W^+ Boson is an mediator of the weak interaction. It is produced by $u + \overline{d} \rightarrow W^+$ and has a mass of $80.398\,\mathrm{GeV/c^2}$. In comparison the mass of the proton and neutron is just $m_n = 939.565\,\mathrm{MeV/c^2}$ and $m_p = 938.272\,\mathrm{MeV}/c^2$. During the beta-decay the energy for the W-boson has to be taken from the vacuum for a short period of time, following the Heisenberg uncertainty principle $\Delta E \cdot \Delta t \geq \frac{\hbar}{2}$. This causes the short range of the weak interaction.

The energies of the emitted positrons follow their specific spectra depending on the

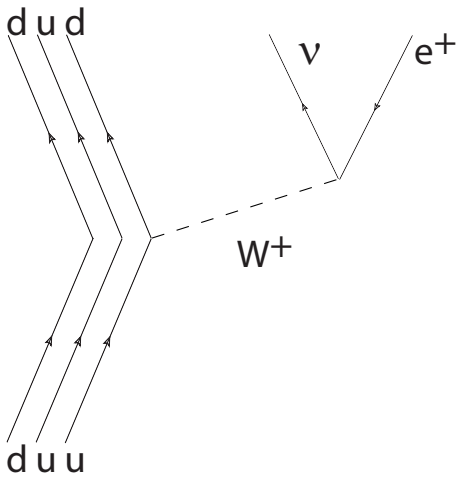

Figure 3.3: Feynman graph of the β^+ decay. A virtual W^+-boson mediates the conversion of a u-quark into a d-quark. It decays then into a positron and a neutrino. The other two quarks of the hadron do not participate in the reaction.

mother nuclide [C+83]. Some of these spectra, as for example the one of the common nuclide ^{18}F can also be described analytically. Details will be shown in section 5.3.3. After a range of the order of 0.4 mm root mean square (for ^{18}F) depending on the tracer used (see Figure 7.4 for ^{18}F and [Der79], [LH99] or Table 3.1 for other positron emitters) the positron can combine itself with a local electron and form a positronium state. For this formation process one has to take two theories into account [Tao76]. The first one,

presented by Aadne Ore in 1949 is known as the Ore-Gap theory. Here, the formation of positronium during a collision of an electron with an molecule

$$e^+ + M \rightarrow Ps + M^+ \tag{3.2}$$

is most likely, when

$$I_M > E > I_M - I_p \tag{3.3}$$

where I_M is the ionization potential of the medium, I_p is the ionization potential of the positronium and E is the energy of the original positron. The cross section for positronium formation is almost zero if $E > I_M$ (it scales with $\ln(E)/E$ at high energies [Loh86]). In this case the positron will more likely undergo inelastic scattering. On the other hand the reaction will not take place, if $E < I_M - I_p$. These considerations lead directly to a maximum positronium formation probability of

$$P_{\max} = \frac{I_p}{I_M} \tag{3.4}$$

which gives an indication of the positron range in different materials.
Considering the successful formation process the energy of the resulting positronium would then be

$$E_p = E - I_M + I_p. \tag{3.5}$$

As a result of the mass difference between molecule and ejectile it is assumed here that the kinetic energy is carried by the positron before and the positronium after the collision. A drawback of the Ore-theory is that it can be applied only for gaseous media. The widely accepted model is therefore the spur model by O. E. Mogensen from 1974 [Mog74] and its enhancements in the following years. It considers the competitive electron-ion reactions on the trace of the traveling positron in dense media. Therefore this model is applicable also to fluids and solids. Interactions of positronium in dense matter lead to conversion of ortho-Ps (spin 0) to para-Ps (spin 1) and also reduces its half-life. Figure 3.4 shows the rough idea behind this model.

The energy levels of Positronium are very similar to hydrogen and can be calculated as

$$E_n^{\text{pos}} = -\alpha^2 mc^2 \frac{1}{4n^2} \quad (\alpha \approx \frac{1}{137}; n = 1, 2, 3, \ldots) \tag{3.6}$$

with a ground state binding energy of $E_{\text{binding}} = -6.8\,\text{eV}$ which is half of the hydrogen binding energy. Positronium is a hydrogen like state with the only difference that the electron and positron are equidistant with respect to the centre of mass.

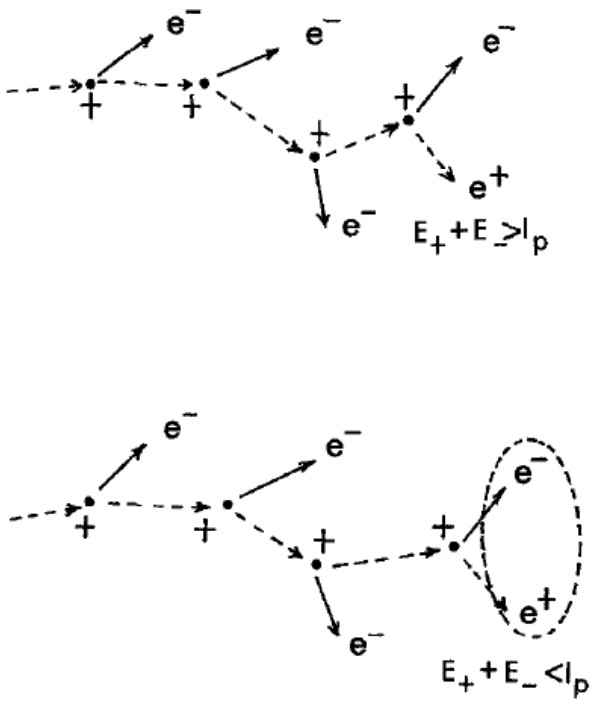

Figure 3.4: Sketch of the spur model [Tao76]. In the upper case the total energy of electron and positron is higher than the coulombic attractive potential of the Ps, so that no Ps is formed. The lower case shows the successful generation of Ps.

Positronium can exist in two flavours, depending on the spin orientation of its components. The singlet is called orthopositronium with the base vector

$$|s=0,s_z=0\rangle = \frac{1}{\sqrt{2}}(e^-_\uparrow e^+_\downarrow - e^-_\downarrow e^+_\uparrow) \tag{3.7}$$

and the triplet state is called parapositronium

$$|s=1,s_z=1\rangle = e^+_\uparrow e^-_\uparrow \tag{3.8}$$

$$|s=1,s_z=0\rangle = \frac{1}{\sqrt{2}}(e^-_\uparrow e^+_\downarrow + e^-_\downarrow e^+_\uparrow) \tag{3.9}$$

$$|s=1,s_z=-1\rangle = e^-_\downarrow e^+_\downarrow. \tag{3.10}$$

The arrows indicate the z-components of the spins. Due to spin conservation orthopositronium decays to an even number of photons, dominantly two with 511 keV center of mass energy each, and a half-life of $t_{\frac{1}{2}} \approx 1.25 \cdot 10^{-10}$ s.
Parapositroniom with parallel spin configuration (s=1) emits mostly three (or higher un-

even numbers) of photons following spin conservation. The possibility of just one photon being emitted by the parapositronium is excluded by spin-, energy-momentum- and also charge conjugation parity preservation

$$(-1)^{l+s} = (-1)^n \tag{3.11}$$

where n is the number of photons. Since positron and electron can only annihilate when their wave functions overlap it is most likely with $l = 0$, that means only S-states are (practically) possible. So the triplet state $^3S_1$ will annihilate into at least three photons. Figure 3.5 shows the Feynman graph of the ortho-Ps and para-Ps decay. The branching

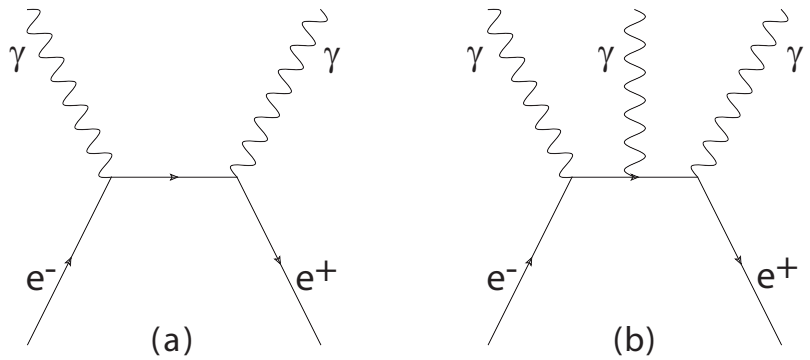

Figure 3.5: Feynman graphs of possible positronium decays. Subfigure (a) shows the lowest order decay of singlet state called Orthopositronium into an even number (here: two) of photons. (b) shows the triplet state called parapositronium and its decay into an uneven number (here: three) of photons.

ratio of two- and three- photon decays is [M$^+$88]

$$\frac{\sigma_{2\gamma}}{\sigma_{3\gamma}} = 372.$$

In contradiction, it was measured [V$^+$00] that in nearly 97.5 % of all cases the singlet case will occur, resulting in the emission of two collinear photons. Since the according publication was not-peer-reviewed, uncertainties may be possible. It was proposed that the detection of three and more photonic decays can be suppressed by applying energy cuts (see Figure 3.6). Nevertheless, for all practical purposes three photon and higher order decays can be neglected.

A typical kinetic energy of 10 eV for the positronium at the time of decay leads to a Doppler broadening of about 2.5 keV for photons emitted parallel and anti-parallel to the momentum direction of the positronium [M$^+$88]. This kinetic energy also leads to a Gaussian variation of the two photon annihilation angle of $\phi = 0.54^\circ$ FWHM [S$^+$06] re-

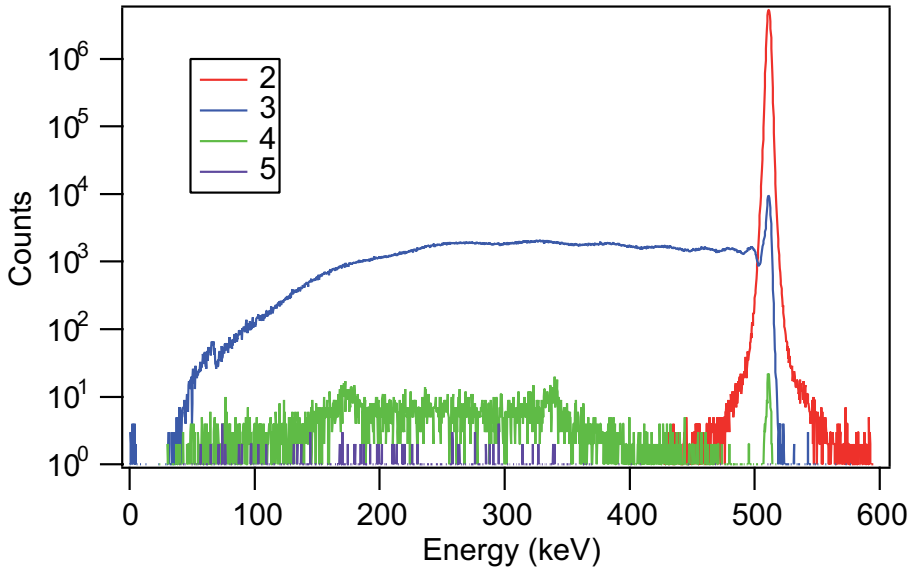

Figure 3.6: Energy spectra of Ps annihilation photons measured in Gammasphere by the Weak Interactions Group at the University of California [V$^+$00]. The number of annihilation photons has been identified by application of data cuts.

sulting in a mean angle of $\Psi = 179.46°$. For the position blurring this leads to a Gaussian distributed uncertainty with a FWHM of

$$\Delta_{NC} = \tan\frac{\phi}{2} \cdot \frac{D}{2} \approx 0.00236 \cdot D \tag{3.12}$$

with D being the diameter of the PET scanner.
The annihilation photons can now be measured directly through a photoelectric effect in the detector or they can undergo scattering in either the tissue or the detector beforehand. Figure 3.7 shows the effect of scattered and random events on the detected lines-of-response (LORs).

3.2.2 True Events

An coincidence event is called a *true event*, if both of the annihilation photons are measured in a single detector element without having undergone scattering before reaching the detector. Neglecting non-collinearity the LOR of a true event will intersect the positronium annihilation point. The detection process is the result of a single photoelectric effect

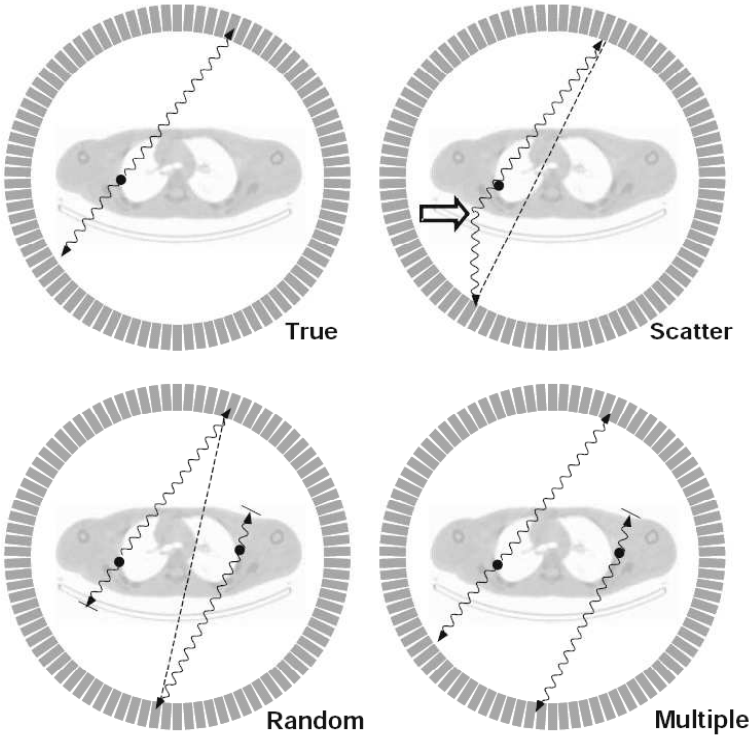

Figure 3.7: Sketch of possible PET event cases [B+05]. An event is called *true*, if both photons are detected directly. In a *scattered* event one or both of the photons underwent Compton- or Rayleigh scattering before being detected. *Randoms* are mostly generated due to two subsequent decays from which one photon of both decays is detected. In a *multiple* event more than two photons are detected. Because the scanner can not decide which is the right combination, such events are normally rejected during the data acquisition.

of the arriving photon in the detector material. Here, typically an inner shell electron is ejected with the kinetic energy

$$E_{\mathrm{kin,e^-}} = E_\gamma - E_b \tag{3.13}$$

where E_b is the binding energy of ejected K-shell electron and $E_\gamma = 511\,\mathrm{keV}$ the energy of the arriving annihilation photon. The cross section for the photoelectric effect cannot be described analytically for all Z and energies, but is

$$\sigma_{\mathrm{PE}} \propto \frac{Z^n}{E_\gamma^{\frac{7}{2}}} \tag{3.14}$$

where n varies between 4 and 5 depending on the photon energy. For $E_\gamma = 511\,\text{keV}$ it is $n \approx 4.4$ [Eva55]. The top-left illustration in Figure 3.7 shows a line-of-response of a true coincidence.

3.2.3 Scattered Events

In addition to the non-collinearity effects and the positron range, object- and detector scattering will blur the detector answer. A sketch of scattered events is shown in the top-right of Figure 3.7. Compton scattering describes the interaction between a photon and an electron from the outer shell of an atom. The result of this interaction is a change of direction of the incoming photon and the ejection of the electron. Neglecting the binding energy of the loosely bound electron, the energy of the photon after undergoing Compton scattering can be written as

$$E_\gamma' = \frac{E_\gamma}{1 + \frac{E_\gamma}{m_0 c^2}(1 - \cos\Theta_c)} \tag{3.15}$$

where Θ_c is the angular difference of the photon momentum direction before and after the Compton scattering. In order to limit scattered events, PET detectors use the photon energy to select these events. A common cut value is $\sim 350\,\text{keV}$, which means that scattering angles larger than $\approx 60^\circ$ are suppressed. Figure 3.8 shows the energy dependence of the photons scattering angle and its cross section.
The differential cross section of Compton scattering incidents is described by the Klein-Nishima formula [Kno89]

$$\frac{d\sigma}{d\Omega} = Z r_0^2 \left(\frac{1}{1+\alpha(1-\cos\Theta)}\right)^2 \left(\frac{1+\cos^2\Theta}{2}\right) \left(1 + \frac{\alpha^2(1-\cos\Theta)^2)}{(1+\cos^2\Theta)[1+\alpha(1-\cos\Theta)]}\right) \tag{3.16}$$

where $\alpha = h\nu/m_0c^2 = 1$ for 511 keV annihilation photons and $r_0 \approx 2.818 \cdot 10^{-15}\,\text{m}$ is the classical electron radius. Often neglected is the coherent scattering of photons known as Rayleigh scattering. Photons scatter here without any energy loss at an atom as a whole, where all electrons of the atom participate in a coherent way. The scattering angle is obtained by the Rayleigh formula $(1+\cos^2\Theta)\sin\Theta$ and the squared Hubbell's form factor $FF^2(q)$ [HØ79], which adds the dependence on the initial photon energy, as

$$\Phi(E,\Theta) = \left(1+\cos^2\Theta\right) \times FF^2(q) \tag{3.17}$$

where $q = 2E\sin\left(\frac{\Theta}{2}\right)$ is the momentum transfer [Cul95, WMU04]. For low initial photon energies the form factors are isotropic, while at high energies they are forward peaked.

Material	Cross Section [$\frac{cm^2}{g}$] for 511 keV Photons			PE (%)	PE^2 (%)
	Photoelectric Effect	Compton scattering	Rayleigh scattering		
Water	$1.78 \cdot 10^{-5}$	$9.58 \cdot 10^{-2}$	$2.15 \cdot 10^{-4}$	(0.02)	(0.0003)
Lead	$7.84 \cdot 10^{-2}$	$6.68 \cdot 10^{-2}$	$1.10 \cdot 10^{-2}$	50.2	25.2
Gold	$7.02 \cdot 10^{-2}$	$6.77 \cdot 10^{-2}$	$1.03 \cdot 10^{-2}$	47.4	22.4
BGO	$5.56 \cdot 10^{-2}$	$7.14 \cdot 10^{-2}$	$8.0 \cdot 10^{-3}$	41.2	17.0
LSO	$3.79 \cdot 10^{-2}$	$7.28 \cdot 10^{-2}$	$6.59 \cdot 10^{-3}$	32.3	10.4

Table 3.2: Cross sections for 511 keV photons transversing materials appearing in PET imaging taken from the NIST XCOM database [Nat09a]. Bismuth germanate (BGO) and Cerium-doped lutetium oxyorthosilicate (LSO) are common used scintillator materials in commercial PET scanners. $PE = 100 \cdot \sigma_{PE}/(\sigma_{PE} + \sigma_{CS} + \sigma_{RS})$ is the ratio between non-scattered and scattered events. PE^2 is the true coincidence efficiency.

Table 3.2 shows cross sections for the photoelectric effect, the Compton effect and Rayleigh scattering of common detector and tissue materials transversed by the annihilation photons. Due to the $Z^{4.4}$-dependence of the photoelectric effect described in Section 3.2.2, the fraction of true coincidences can be increased by using high-Z materials like lead, gold or tungsten.

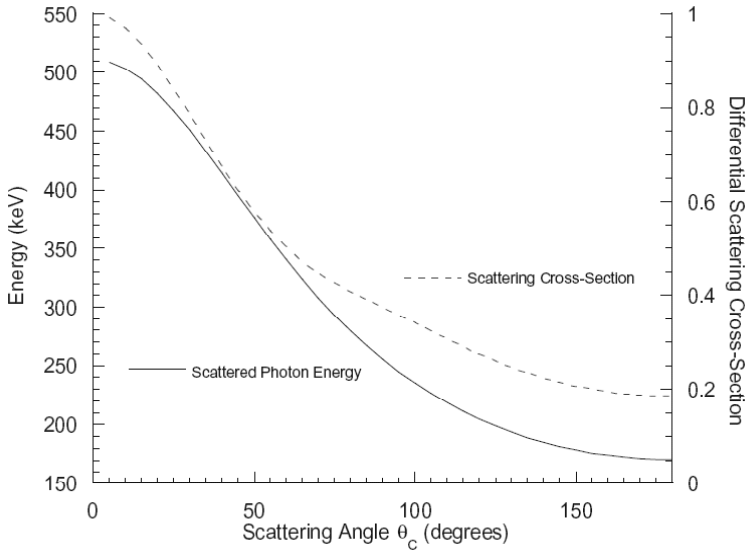

Figure 3.8: Angular propability distribution and photon energy after Compton-scattering of 511 keV photons [B+05].

3.2.4 Random Events

Randoms are caused by high tracer activities and long coincidence time windows of the PET scanner. If two consecutive positron decays occur within the coincidence time window and produce two photons each, from which one of each decay photon is detected, the resulting event is called a random event as shown in Figure 3.7.
The average rate of randoms per detector pair a,b can be calculated as

$$< C_{R,a,b} >= 2 \cdot \Delta t_c \cdot s_a \cdot s_b \tag{3.18}$$

where Δt_c is the timing resolution, $2 \cdot \Delta t_c$ the coincidence time window and s_a,s_b are the rates of the singles on detectors a,b. For the special case of a MWPC based PET scanner with 4 detectors as the quadHIDAC or the MSPET device, the average rate of randoms is

$$< C_R >= 2 \cdot 2 \cdot \Delta t_c \cdot \left(\frac{s}{4}\right)^2 = 2 \cdot \Delta t_c \cdot s^2 \cdot \frac{1}{8} \tag{3.19}$$

where the factor $\frac{s}{4}$ considers that only coincidence events on opposite detectors are allowed and s is the total number of singles measured. The factor two accounts for the two pairs of opposite detector blocks. The equation holds for similar singles rates on opposite detectors. In addition the inverse singles rate has to be small against the coincidence time window. For the spatial distribution of random events different approaches will be proposed later in this thesis (see Section 7.1.7).

3.2.5 Multiple Events

The bottom-right picture in Figure 3.7 displays a multiple event. Multiple events imply the detection of more than two events within the coincidence time window of the PET scanner. This can be due to a high activity-to-coincidence-time-window fraction or less likely due to a three photon decay of the positronium. In any of these cases the scanner cannot decide if and when which pair of hit-points originates from the same decay. Hence, multiple events are usually rejected by the detector electronic.

3.2.6 Parallax effect

The maximum spatial resolution for thick detector elements without depth-of-interaction capability is achieved in the center of the scanner's field-of-view (FOV). If the source is moved off-center, the probability that either more than one or not the nearest detector to the corresponding LOR will be hit. The point-spread-function (PSF), which is the response of the detector to a point-like source, would therefore be broadened and degrades

the spatial resolution in the direction of movement. Depending on the scanner's size and the detector elements used, this effect can reduce the resolution by a factor of 1.5 during a movement of 280 mm [Sie07]. Figure 3.9 illustrates this so-called parallax effect. It can

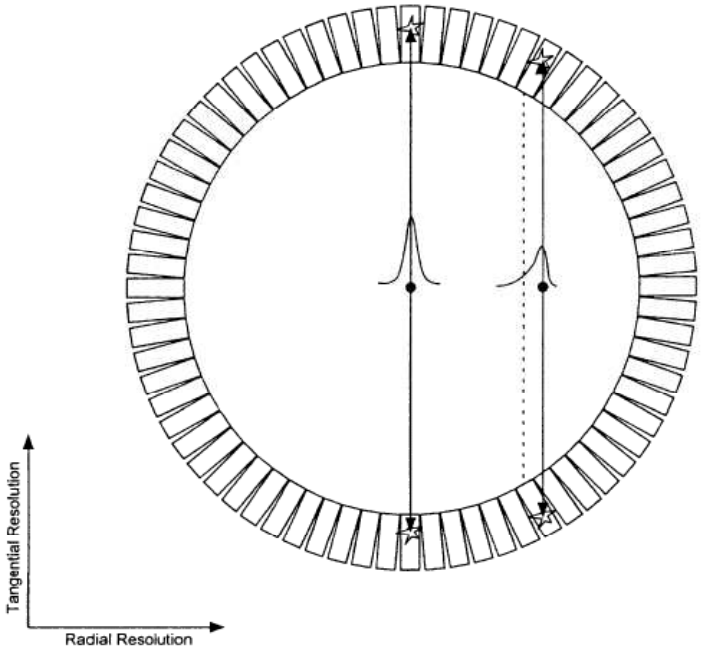

Figure 3.9: Illustration of the parallax effect [Phe06]. The point spread function of an off-center source is broadened due to a penetration of multiple detector elements. This effect is especially observed in ring scanners.

be approximated by the expression

$$\Delta_{pa} = \alpha \frac{r}{\sqrt{r^2 + R^2}} \tag{3.20}$$

which is sensitive to the distance r from the centre, the scanner's ring radius R and a factor α, which depends on the thickness and type of the used scintillator material. For 30 mm thick BGO or LSO crystals, α is assumed to be 12.5 mm [DGB07].

3.2.7 Sensitivity and Noise-Equivalent-Count-Rate

The sensitivity S of a PET device is defined as rate of true coincidences measured per second for a given source activity A:

$$S = \frac{C_t}{A}. \tag{3.21}$$

The sensitivity is a measure for the ability of the tomograph to detect photons. As the source strength is attenuated by the source volume material itself, one has to measure the sensitivity at different source volume diameters in order to extrapolate to a source volume with no attenuation.
An additional problem is to discriminate true and scattered events, especially in cameras without intrinsic energy resolution. Hence, often the random corrected number of total coincidences, consisting of true C_t and detector scattered coincidences C_s is used to define the absolute sensitivity S_{abs} of the system as

$$S_{\text{abs}} = \frac{C_t + C_s}{A}. \tag{3.22}$$

However, the sensitivity of a device cannot directly be used as a measure for image quality. Noise caused by scattered and also randoms events will deteriorate the image contrast. Therefore, the noise-equivalent count rate (NECR) is used to describe the system's imaging performance as

$$NECR = \frac{C_t^2}{C_t + C_s + \alpha k C_r} \tag{3.23}$$

where $1 < k < 2$ depends on the method used for the estimation of randoms. In case of a delayed coincidence time window, k is assumed to be 2 due to the additional statistical noise measured in the time frame. In case of a noiseless randoms calculation, as introduced in Formula (3.18), it is $k = 1$ [WA04]. The factor α considers the fraction of the transverse field-of-view (FOV) occupied by the object [WB04]. This implies a flat approximation of the randoms distribution over the whole FOV. Therefore, it can easily be seen that neither sensitivity nor NECR of different devices can be compared in a straightforward manner. Different energy resolutions and cuts applied for scatter rejection as well as different randoms estimation methods have to be taken into account.

3.2.8 Summary

By looking at the physics of PET one can see that there are different effects limiting the spatial resolution of the PET camera. Here, the range of the positron within the object

examined depending on the energy spectra of the nuclide used, and the non-collinearity of the annihilation photons has to be pointed out. The system's image quality is reduced by scatters, randoms and the parallax effect in case scanners without depth-of-interaction information are used.

3.3 A Short History of (Small Animal) PET

The first approaches to positron emission tomography date back to 1950, when the group of G. Brownell at the Massachusetts General Hospital placed two sodium iodide detectors opposite to each other in order to image brain tumours by measuring the annihilation radiation of positrons. The results were published in 1951 [Swe51], when also Wrenn, Good and Handler published their studies on a similar topic [W$^+$51]. Figure 3.10 shows a picture of the device by Brownell et. al. and the measurement results of a 2D brain scan. Since then it took nearly 20 years until reconstruction methods based on the work of J.

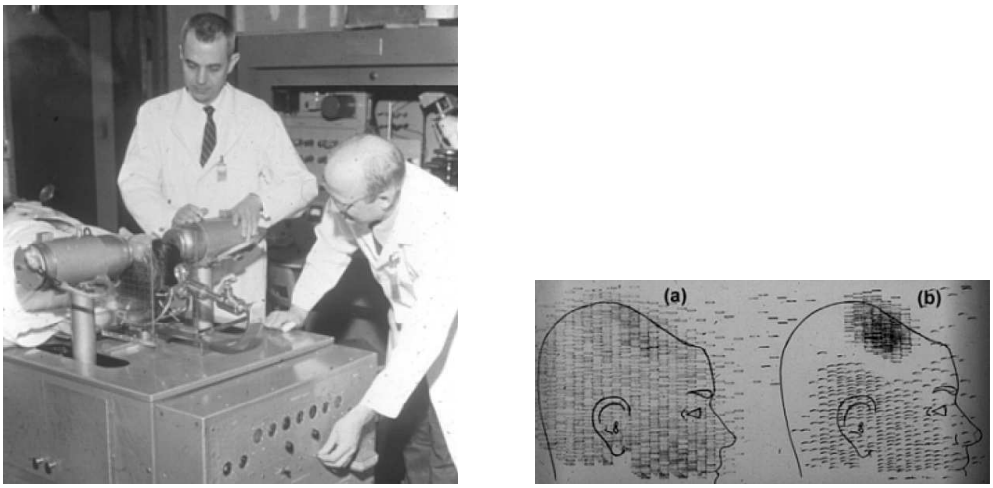

(a) (b)

Figure 3.10: In the right picture the first clinical PET camera in 1953 with Drs. Brownell (left) and Aronow is shown. In the left picture the results of the PET scan are presented, showing a coincidence scan (a) and an unbalanced scan (b). The unbalanced scan records asymmetries of single rates in both detectors, which lets one determine the existence of a tumour and as well identify the brain side in which it is located [Bro99].

Radon [Rad17] allowed to produce more detailed tomographic images. Enormous developments have increased the sensitivity by a factor of 10^3 and spatial resolution by a factor of 10. It was not only the development of new scintillator materials and photo-multipliers but also the developments of electronics, computers and reconstruction algorithms which have let PET become a standard technology for larger hospitals and medical centres. In

parallel to the device development, also radio-tracers have become a lot more specific so that manifold diseases can be examined today. Since the early 1990's not only clinical applications but also preclinical research is done using PET and preclinical PET devices dedicated to small animals are available. Due to the increasing demand of PET also in clinical examinations, research and clinic soon became more and more competing for measuring time so that special devices for preclinical medicine were developed. This did not only improve the availability but also the adaption to special questions in research. Especially in terms of spatial resolution and sensitivity these dedicated devices have to meet demands close to the physical limits. Today various groups are developing small animal PET scanners using different technologies to adapt their devices to these applications. Some of these are presented in Section 3.5.

3.4 Small Animal PET

PET in animals as a non-invasive in-vivo imaging technique is a very promising alternative to classical in-vitro methods like tissue dissection or auto-radiography. The biggest advantage of these methods is that using PET the animal can be studied more than once. Therefore, each animal can act as its own control object, which permits more accurate results compared to the measurements of variances of control groups involving different animals.
Directly connected to this point is the high cost-efficiency, resulting from a lower number of animals needed for a study. These costs imply gene typing, genetic manipulation, breading and special treatments.
Having the same examination methods for humans and animals available is very beneficial, because results are easy to compare and therefore more significant than using classical in-vitro methods. There is a growing interest in small animal PET in various biological and pharmaceutical industries.
The main problems of small animal PET studies are the limited availability of scanners, the high infrastructural needs for some special tracers and the limited resolution and sensitivity of today's small animal PET devices.
Most notably mice and rats are very interesting to study, because they are genetically and also physiologically similar to humans. This holds for mice even more than for rats. 80 % of their genes match with humans. In addition, there are tools at hand for genetic manipulation of these species, so that certain defects or modifications can be extensively investigated. Rats have the advantage that their inner organs are quite large in comparison to mice. Hence, it is easier to operate on them and also easier to interpret the reconstructed PET images. As a drawback rats are more expensive and there are also less genotyped rat models than mouse models available. Since mice are more similar to humans, rats are

used in fewer studies (mostly neuroscience) in small animal PET today.
In order to compare human PET studies with small animal studies, the small animal scanner needs to provide spatial resolution at the physical limit and a sensitivity, which is as large as possible. A 30 g mouse is about 2000 times lighter than a human being. With a spatial resolution of about 10 mm ($\approx$ 1 ml in volume) in a human PET scanner, the small animal complement needs to reach < 1 mm (respectively $< 1\,\mu$l in volume). In terms of sensitivity at levels of $0.3-0.6\%$ in one reconstruction plane (2D) and $2-4\%$ considering all LORs (3D) an improvement by a factor of 1000 is clearly not possible. The workaround here would be to increase the dose of radioactivity induced in the animals. However, that is only possible in certain limits, because a too large dose would change the biological behaviour of the studied animal. Also the tracer concentration in the blood is subject to restrictions. One cannot inject more than 0.25 ml of volume safely into a mouse. However, the limits can be slightly increased using tracers (like FDG) which are naturally present in high concentrations in the studied organism. As a result of these considerations, not more than $100\,\mu$Ci[1] of radioactivity can be given to a mouse. Another system specific limit is the count rate performance and the dead time behaviour of the scanner, which will increase random coincidences.

3.5 PET Scanners

3.5.1 Basic Requirements for (Clinical) PET Scanners

Clinical PET scanners for humans generally consist of multiple rings of scintillation detectors. Because of the large ring diameter of about 900 mm which gives a patient port of about 700 mm, the non-collinearity of the annihilation photons is a major issue for the achievable spatial resolution. Following formula 3.12 non-collinearity leads to a uncertainty of $\Delta_{\mathrm{NC}} = 2.16$ mm. Adding a mean positron range of $\Delta_{\mathrm{PR}} = 0.6$ mm [B$^+$05] for ^{18}F and following formula (3.24), the theoretically possible spatial resolution neglecting detector and reconstruction effects will be in the order of $\Delta_{\mathrm{th.}} = 2.24$ mm. The resolution of a PET scanner can be obtained by a mathematical convolution of occuring errors. Derenzo et. al. [DMHB93] have proposed an empirical approximation for the calculation of the reconstructed image resolution in the following way:

$$\Delta_{\mathrm{tot.}} = a \cdot \sqrt{(\frac{d}{2})^2 + b^2 + \Delta_{\mathrm{nc}}^2 + \Delta_{\mathrm{pr}}^2 + \Delta_{\mathrm{pa}}^2}. \tag{3.24}$$

Here a is a factor which considers the reconstruction uncertainties ($1 \leq a \leq 1.3$), d is the size of the basic detector elements (usually: crystal size) and b is an additional factor deal-

[1] $1\,\mathrm{Ci} = 3.7 \cdot 10^{10}\,\mathrm{Bq}$

ing with contributions from detector identification accuracy worsened by e.g. crosstalk of adjacent detectors. The contributions Δ_{nc}, Δ_{pr} and Δ_{pa} account for annihilation photon non-collinearity, positron range and the parallax error described by Equation (3.20). Especially the optimization of factors d and b is subject of many developments. The main problem here is that the crystals have to be as small as possible. However, due to the limited stopping power of the scintillation materials there is a lower limit to the size of the crystals below which signals are induce in more than one crystal. To reduce this problem, one uses materials with high stopping power and low Compton scatter affinity like bismuth germanate (BGO). Another challenge is the dimension of the photo-detector. Regular photomultiplier tubes (PMTs) have a diameter of at least 10 mm. In the simplest case light guides are used, which will attenuate the light signal. Another often used method is to use one PMT to read out multiple scintillation crystals. The position is then reconstructed via a light sharing encoding. Modern systems use squared PMTs and scintillation crystals which are segmented by slits of different depth. R. Lecomte has presented a nice overview of different light sharing approaches in [Lec09].
Despite the spatial resolution also the sensitivity and as a measure of the signal-to-noise ratio the noise-equivalent count rate (see Formula (3.23)) has to be optimized. High sensitivity means necessitates acquisition times, faster measurements and therefore a more economic usage of the (quite expensive) scanner. Thus, less radiation dose exposure for the patient can be achieved. In order to improve the sensitivity the easiest (but most-expensive) way is to increase the scanners field-of-view (FOV) by reducing dead angles and increasing the number of detector rings. Also the diameter of the ring should be as small as possible. The limit here is the size of the patient. Dedicated scanners like the Siemens HRRT[2] brain scanner (see table 3.3) make use of these effects and gain high sensitivity and spatial resolution. On the other hand one should be aware that additional detector rings will lead to additional scatters and randoms blurring.
More recent developments use time-of-flight (TOF) information to improve the signal-to-noise ratio and therefore the effective sensitivity. The time difference of both annihilation photons detections is used to identify not only a line-of-response but also an area on this line of response where the decay has happened most likely. A gain in signal-to-noise ratio can be expected, when the localisation of the decay on the LOR is smaller than the Object size. For the localisation one can write

$$\Delta x = \frac{1}{2} \cdot c \cdot \Delta t_{\mathrm{TOF}} \tag{3.25}$$

[2] **H**igh **R**esolution **R**esearch **T**omograph

where $c = 30\,\frac{\text{cm}}{\text{ns}}$ is the speed of light and Δt_{TOF} is the difference of the measured detector arrival times of the two photons. The gain in signal-to-noise ratio is then [Bud83]

$$\frac{\text{SNR}_{\text{TOF}}}{\text{SNR}_{\text{non-TOF}}} = \sqrt{\frac{D_{\text{object}}}{\Delta x}}. \tag{3.26}$$

The most challenging part here is the synchronicity and the time resolution of the detector elements. Scanners with LSO and LYSO scintillators reach a timing resolution of $\sim 600\,\text{ps}$ FWHM [K$^+$08, M$^+$06], which results to $\Delta x = 9\,\text{cm}$ following formula (3.25) and a gain in SNR of 2.1 following formula (3.26) and assuming a patient size of 40 cm in diameter. The timing resolution might even be improved to $\Delta t_{\text{TOF}} \sim 300\,\text{ps}$ [K$^+$04] by using lanthanum bromide ($LaBr_3$:Ce) scintillators leading to a SNR gain of nearly 3. While these improvements seem promising for whole-body human PET scanners, dedicated systems or small animal systems would require a timing resolution of at least $\Delta t_{\text{TOF}} = 100\,\text{ps}$ to improve in SNR.

Systematic problems like scatters, randoms and also parallax effects (see chapter 3.2) occuring especially off-center have to be kept as small as possible. Scatters can be neglected using detectors with high energy resolution and large cross section for the photo electric effect. Here BGO would be the material of choice concerning the PE cross-section. With an energy resolution of only 3% at 662 keV $LaBr_3$:Ce on the other hand offers the best energy resolution but suffers from a doubled attenuation length compared with BGO, LYSO or LSO. Therefore, thicker crystals are needed, which will, however, increase the parallax effect even more. To correct for that, the depth of interaction in the crystals has to be measurable. To overcome this task different approaches have been proposed. Siemens uses broadenings in point spread functions, depending on the DOI of the photon, in their HD-PET technique [PKMC06, Sie07]. Because of this high resolution photo-detectors are needed. Other approaches use sandwiched constructions consisting of different scintillation materials with different response times [S$^+$99].

Multimodality is a very prominent feature of commercial PET scanners. Actually so prominent that there is no standalone whole body human PET scanner available on the market but only PET/CT combinations. Here the X-ray CT device is mounted in front of the PET scanner acting as an independent device. In a PET/CT scan, the PET and the CT measurement have to be performed following each other, but controlled by the same data acquisition unit. Using geometric transformations, the reconstructed CT image can be superimposed onto the PET image. Using PET/CT not only the diagnose precision is enhanced, but also the PET attenuation correction for quantification can be done much faster using CT. While traditional attenuation correction with ^{137}Cs gamma emitters ($E_\gamma = 622\,\text{keV}$) or ^{68}Ga/^{68}Ge positron emitters takes about 20 minutes, a CT scan ($E_\gamma \approx 80\,\text{keV}$) can be done within a minute, which is much more cost efficient, because

the patient throughput is higher. Because of the energy-dependence of the attenuation, the CT attenuation has to be adapted using proper conversion algorithms [K$^+$98].

	Ring Diameter (mm)	Scintillator	Crystal Size (mm^3)	Transaxial Spatial Resolution (mm)	Sensitivity@center (cps[1]/MBq)
Philips Gemini GLX [Phi09, B$^+$07a]	885	GSO	$4 \times 6 \times 30$	5.3	7700
Philips Gemini TF [Phi09, S$^+$07]	903	LYSO	$4 \times 4 \times 22$	4.7	7000
GE Advance NXi [B$^+$03]	927	BGO	$4 \times 8 \times 30$	4.8	n.a.
GE Discovery STE [T$^+$07]	886	BGO	$4.7 \times 6.3 \times 30$	4.9	8800
Siemens HR+ [B$^+$03, H$^+$04]	824	BGO	$4 \times 4.4 \times 30$	5.1	6650
Siemens Accel [B$^+$03, H$^+$04]	824	LSO	$6.4 \times 6.4 \times 25$	5.7	6362
Siemens TruePoint HI-REZ [E$^+$08, B$^+$07a, Sie07, PKMC06]	824	LSO	$4 \times 4 \times 20$ (HI-REZ)	4.2 (HD-PET:2.1)	8100
Siemens HRRT [dJ$^+$07, vV$^+$08]	312	LSO/LYSO	$2.1 \times 2.1 \times 10$ double layer	2.3	29000

[1] cps: counts per second

Table 3.3: Overview of some of today's commercial human PET scanner properties. The Philips Gemini TF uses time-of-flight information. The used LYSO crystals allow a timing resolution of the order of 600 ps FWHM [K$^+$08, M$^+$06]. Siemens HD-PET uses depth of interaction information reconstructed from point spread function width [PKMC06]. The Siemens HRRT mentioned here is a dedicated brain scanner.

Table 3.3 lists some prominent modern PET scanners. A older but more complete list of modern PET scanners can be found in the review article of J.Humm et. al. [HRG03]. As in all comparisons of PET scanners it has to be clarified that not all of the results are based on the same measurement methods and technological substructures. Even though the National Electric Manufactures Association (NEMA) has proposed the NU 2 – 2001 standard for "Performance Measurements of Positron Emission Tomographs" [NEM01], it cannot be applied to all scanners in the same manner. Especially for scanners with small FOVs like brain, breast or small animal PET scanners some prescribed measurements need sources that are larger than the FOV. Also differences in energy cuts are not considered. A supplementary summary of modern detector technology can be found in [Lec09].

3.5.2 Small Animal PET Scanners

Small animal PET scanners cannot be considered as smaller versions of whole-body human scanners. The demands for such devices in terms of sensitivity and spatial resolution are totally different. Dealing with a scale factor of 1 : 10 not only a very high resolution,

	Man	Scale	Mouse
Heart Size	$5-10\,\mathrm{cm}$	10 : 1	$5-10\,\mathrm{mm}$
Myocardium	$1\,\mathrm{cm}$	10 : 1	$1\,\mathrm{mm}$
Heart Rate	70/min	1 : 10	700/min

Table 3.4: Comparison of scales in mice and men. Difficulties in adapting clinical PET devices to small animal versions become obvious.

but also good sensitivity and a high NECR is needed in order to image the small amounts of radioactivity in a mouse that are at $\sim 37\,\mathrm{MBq}$ about ten times less than the typical human dose. Because of the high detection efficiency and good energy resolution at feasible costs, scintillation crystal-based PET cameras constitute the bulk of all commercial available instruments.
In addition, there are plenty of detector developments based on almost every type of particle detector currently being pursued. The most promising are the semiconductor based MEDIPIX detectors and Avalanche Photo Diodes (APDs), which provide sub-millimetre resolution and a one-one coupling of detector and readout channel. This would lead to $b = 0$ in Formula (3.24) and therefore improves spatial resolution.
In the following sections a selection of small animal PET scanners is presented. It is not intended to summarise the best devices, but to demonstrate the diversity of concepts, no matter wheather they are already commercially available or still under development. A special focus is set on MWPC related projects.

The RatCAP project

The RatCAP project was initializsed by a group at Brookhaven National Laboratory (BNL) in Upton, USA. As an offspring of high energy physics experiments, RatCAP is a non-commercial research project. The special feature of RatCAP is that it is mounted directly on the head of a rat like a helmet. Therefore, the non-collinearity blurring is minimized in this pure brain scanner concept. The scanner itself consists of 12 detector blocks comprising 4×8 LSO crystals of the size $2 \times 2 \times 5\,\mathrm{mm}^3$ read out by an array of avalanche photo diodes (APDs). The preliminary spatial resolution has been measured as $1.28\,\mathrm{mm}$ using a $< 1\,\mathrm{mm}$ ^{22}Na point source [VWS$^+$04]. As a drawback of the design, the helmet itself is very heavy ($150\,\mathrm{g}$) in comparison to the weight of a rat ($\sim 300\,\mathrm{g}$). So studies are necessary that prove that the helmet won't affect the animals natural behaviour. In order to inure the rat to the weight, a sleeve which will later carry the detector is mounted to the skull of the rat soon after birth. Because of the weight this device cannot be used to image a mouse brain.

The ClearPET project

Another scintillation crystal based PET scanner was proposed by the Crystal Clear Collaboration. Its design is based on dual layer LSO/LuYAP crystals [Z$^+$05]. The used crystals are $2 \times 2 \times 8\,\mathrm{mm}^3$ in size and are read out by a PMT with an active area of $18.1 \times 18.1\,\mathrm{mm}^2$. So 64 crystals are read out with just one PMT. The detector ring has a inner diameter of 120 mm. The axial length is 110 mm. The mean spatial resolution measured with a 1 mm ^{18}F point source has been measured as 1.48 mm. The sensitivity for an energy window of $350 - 650\,\mathrm{keV}$ is 4.2 % and the NECR saturates at 250 kcps for an activity of 55 MBq. The timing resolution of 2 ns FWHM allows for efficient suppression of randoms.

Resistive Plate Chambers

Resistive Plate Chambers are cost efficient, easy to build, and provide timing resolution down to 50 ps. They consist of high voltage parallel electrode plates with small gas filled gaps in between. The plates are made of some high volume resistivity material of $10^7 - 10^{12}\,\Omega$cm. A traversing charged particle ionizes molecules in the small gas gaps. At high gas gains above 10^8 the so called streamer mode sets in, where photons created in the avalanche will extend the gas multiplication so that a plasma channel between the opposite plates developes. The high resistivity of the plates keeps the plasma channel locally confined, so that their position can be read out (most commonly through intersected cathode strips). The affected area will not be able to detect further particles until it is recharged again (this can take up to $\sim 1\,\mathrm{s}$). So the resistivity of the plates will on the one hand help to keep the discharge locally restricted, on the other hand it will limit the rate capability of the detector to some kHz/cm^2. A more detailed investigation of RPC detectors can be found in [RLV03].
The RPC-PET device developed by A. Blanco et. al. [BCC$^+$06] consists of 17 electrode plates and 16 gas gaps of 0.3 mm thickness. It reaches a very high spatial resolution of 0.52 mm FWHM using point like ^{22}Na sources. The timing resolution was measured as $< 300\,\mathrm{ps}$ allowing a coincidence timing window of $\sim 1\,\mathrm{ns}$. As the system is still under development, the material of the electrodes, which will have to act as converters has not been optimised yet. Also the readout of RPCs has shown to be very challenging as the high voltage discharges make it hard to get clear signals without channel cross talk and a passable noise level. The missing energy resolution as in most gaseous detectors may be another drawback of this detector concept.

Straw Tube Approach

An interesting and MWPC-related approach has been pursued by Proportional Technologies, Houston, USA [LMA01]. Their detector is composed of close packages of straw tubes. The 2 mm thick tubes are surrounded by 25 μm lead foils sandwiched between two thin Mylar® foils. The inner foil is copper plated to provide conductivity for charge collection. Using a 10 μm anode wire, a longitudinal resolution of 1 mm for a single tube could be achieved using a 4 GS/s scope readout. In a 20-tube stack the longitudinal resolution with 20 μm wire is measured as 1.7 mm. A sensitivity of 2.7 % is achieved with two 20-straw arrays placed 50 cm apart. The timing resolution is 8.8 ns FWHM [SML$^+$02].

Other Detector Techniques

Besides the mentioned PET detectors there are various other ideas for medical imaging detecting devices. For example the use of liquid xenon has been explored [CLS$^+$02] since the 1970s. Liquid xenon can be used as a detection medium in MWPCs or also be read out via photo-multipliers. The scintillation characteristics of liquid xenon are comparable to NaI(Tl) detectors. Since it can be used as a detection medium in MWPCs, the produced electrons can be extracted locally and thus offer good spatial resolution. As a drawback, the xenon has to be cooled down to $\sim -100\,^\circ$C to keep it in its liquid state. It has also been found that the created charge signals in such a detector will be small and need special low noise amplification. Electron attachment processes caused by small concentrations of electronegative components will reduce the measurable signal pulse heights even more. In order to avoid this, a high purity of xenon is needed.
Gas electron multipliers (GEMs) [Sau97] are thin, copper plated insulating sheets etched with a dense matrix of holes (usually 70 μm in diameter and 140 μm separated from each other). They can be used in different configurations for electron multiplication in gaseous detectors. The challenge for its application in PET is the implementation of a proper photon-electron converter. A lead sheet for example can be placed not closer than 2 mm away from the GEM foil which would degrade the position resolution to the same order. GEMs can be read out using a pad matrix similar as in MWPCs or semiconductor detectors like for example the Medipix chip [BDR$^+$07, BCH$^+$07] or even an optical CCD chip [TBA$^+$02]. In the field of gas avalanche radiation detectors with medical imaging potential also the MICROMEGAS [CDGR02], the MicroCAT [SBJ$^+$98] and the Micro-groove [BBB$^+$99] concepts should be mentioned.

3.5.3 MWPC-based PET Scanners

The RAL Concept

The Mark I Rutherford Laboratory positron camera is not really a small animal PET device, but perhaps the first device based on MWPCs dedicated to positron imaging. It was developed in the 1980s by a group around J.E. Bateman at the Rutherford Appleton Laboratory in Chilton, England [Bat80, BCS+84]. The design of the proposed system consists of an MWPC with a combined cathode/converter. The converter here is made of lead or lead alloy with a pattern of rectangular cells formed by spark-erosion. The pattern shall increase the efficiency of the converter by increasing the surface area. The detector reached a spatial resolution of 6 mm and an efficiency of 6 % [MOB+89]. A similar approach using simple flat converters has been investigated by R.A. Reynolds in 1975 [RSO75].

The High Density Avalanche Chamber Concept

The high density avalanche chamber (HIDAC) consists of a multi-wire chamber detector sandwiched between two solid photon-to-electron converters. A scheme of such a detector is shown in Figure 3.11. The converter consists of alternating layers of solid conductive sheets and insulation, perforated with holes. Electrons produced in the material can escape into a hole. With a high voltage applied between the solid sheets, the electron will be accelerated along the field lines towards the MWPC. On its way it will undergo further avalanche multiplication. In the MWPC the electron cloud will drift towards the anode wire plane, where it is extracted. The moving electrons and ions will induce charge on the cathode tracks. Using charge division techniques the position of the electron avalanche can be reconstructed.

The first ideas for a hybrid detector for ionising radiation have been proposed in 1974 by Lim et. al. [LCK+75] at Lawrence Berkley Laboratory and in parallel but independently from each other by Jeavons et. al. [JCS75] at CERN. Lim used a 4 layer lead honeycomb structured converter, reaching a resolution of $6-7$ mm. Later on they experimented with lead glass converters and hexagonal detector configurations [DGLL+82]. Jeavons always relied on drilled holes. He started with a 1 mm copper/0.1 mm Mylar composition with 2 mm diameter holes in it. After the potential for positron imaging was proposed, the first in vitro images of a heart were shown by Jeavons in 1979 [Jea79]. The development of the CERN prototype, especially in the early years of the detector has been subject of many publications [CJSS73, JCS75, JFL+76, JC76, JTF+78, Man78, Jea79, JKL+80, PHJ+75, TCM+83, JHH+83, TFJ+87, Tow88, J+99] and patent descriptions [Jea95, Jea02]. The latest version quadHIDAC, which is installed at the University Hospital of Münster, is

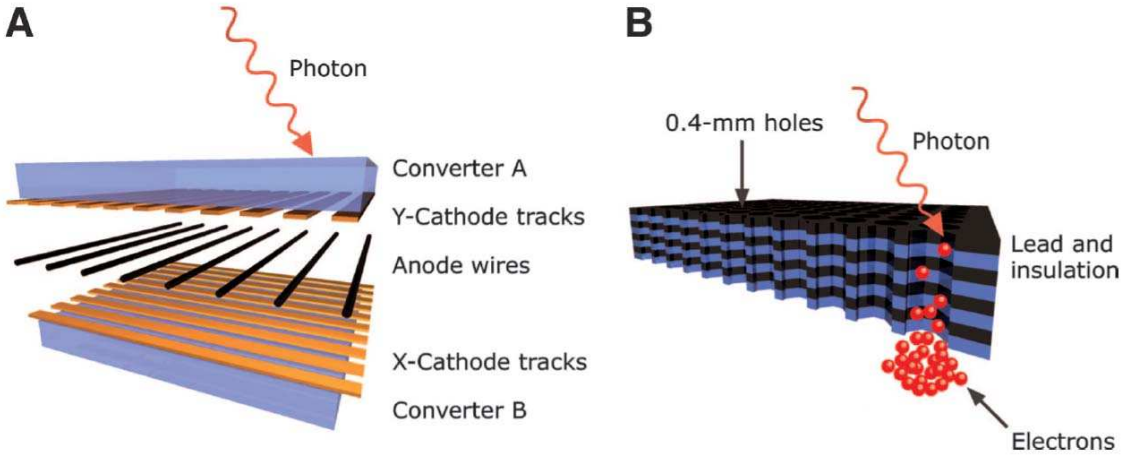

Figure 3.11: Schematic drawing of a HIDAC detector (A) and the photon converter principle (B) [S+05]. The detector consists of a MWPC sandwiched by two photon-to-electron converters. Each converter consists of interleaving layers of lead and insulation drilled with a dense matrix of small holes. An incoming 511 keV photon is converted into an electron via a photoelectric- or a Compton process in the converter material. When it reaches one of the holes, it is accelerated by an electrical field towards the MWPC. On its way through the holes avalanche multiplication will occur.

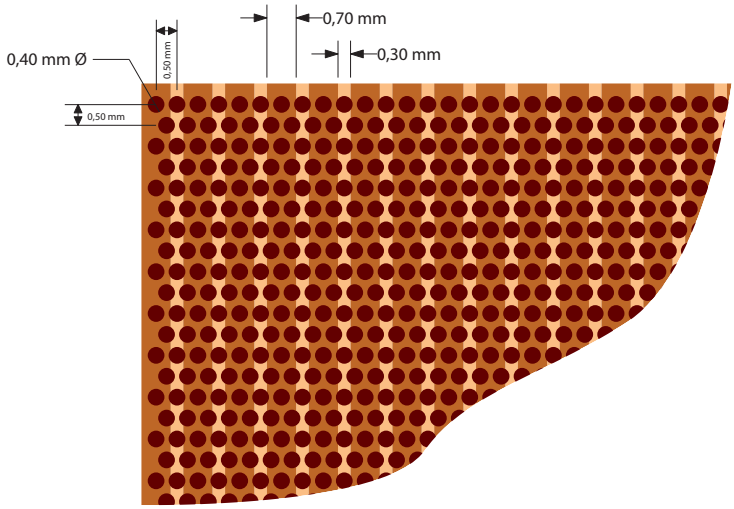

Figure 3.12: Sketch of the quadHIDAC's pad-plane and hole matrix geometry. The plane was digitized with a scanner in order to obtain the exact dimensions. (Drawing by N. Heine.)

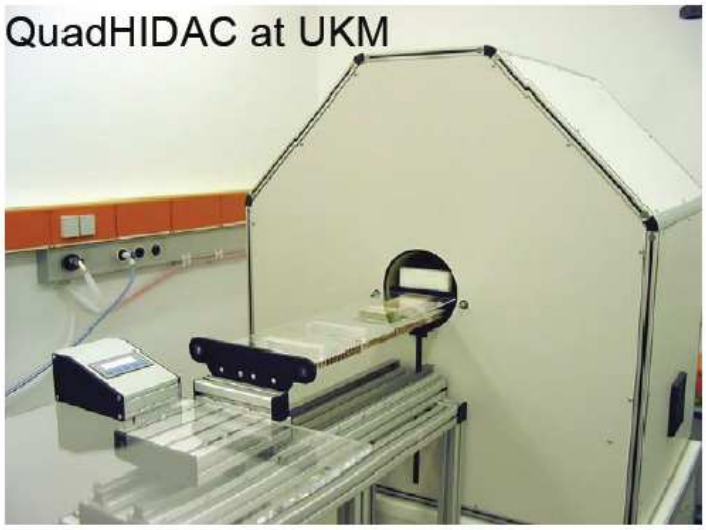

(a)

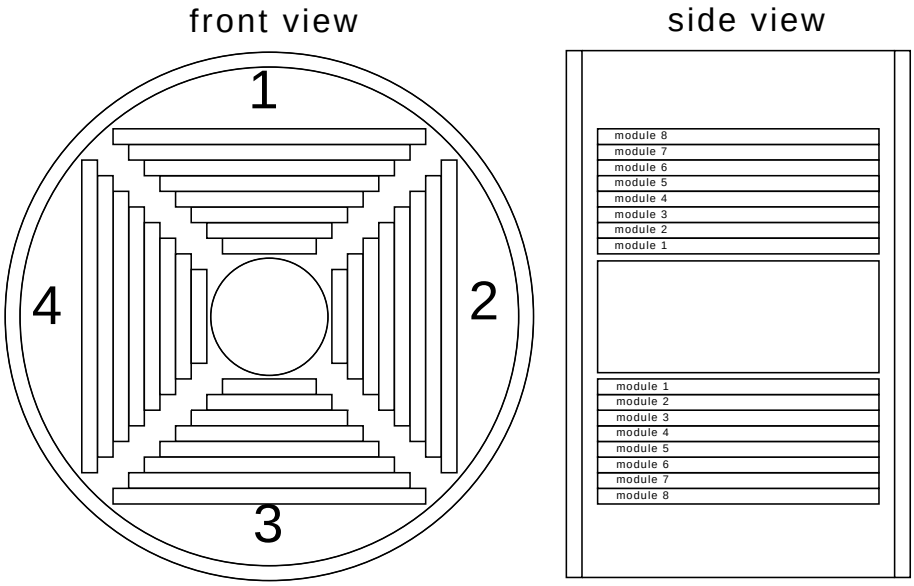

(b)

Figure 3.13: The quadHIDAC small animal PET scanner (a) and its detector module configuration (b). 8 modules comprise a detector block. 4 detector blocks enclose the gantry.

comprised of four detector blocks each containing 8 detector modules shown in Figure 3.13. The drilled holes are now 0.5 mm appart and 0.4 mm in diameter. Figure 3.12 shows a drawing of a disassembled pad plane. The chambers are read out with pads of 0.7 mm width, which are grouped in blocks of 12 pads to reduce the number of read-out channels. The grouping and readout scheme is shown in Figure 3.14. A drawback of this

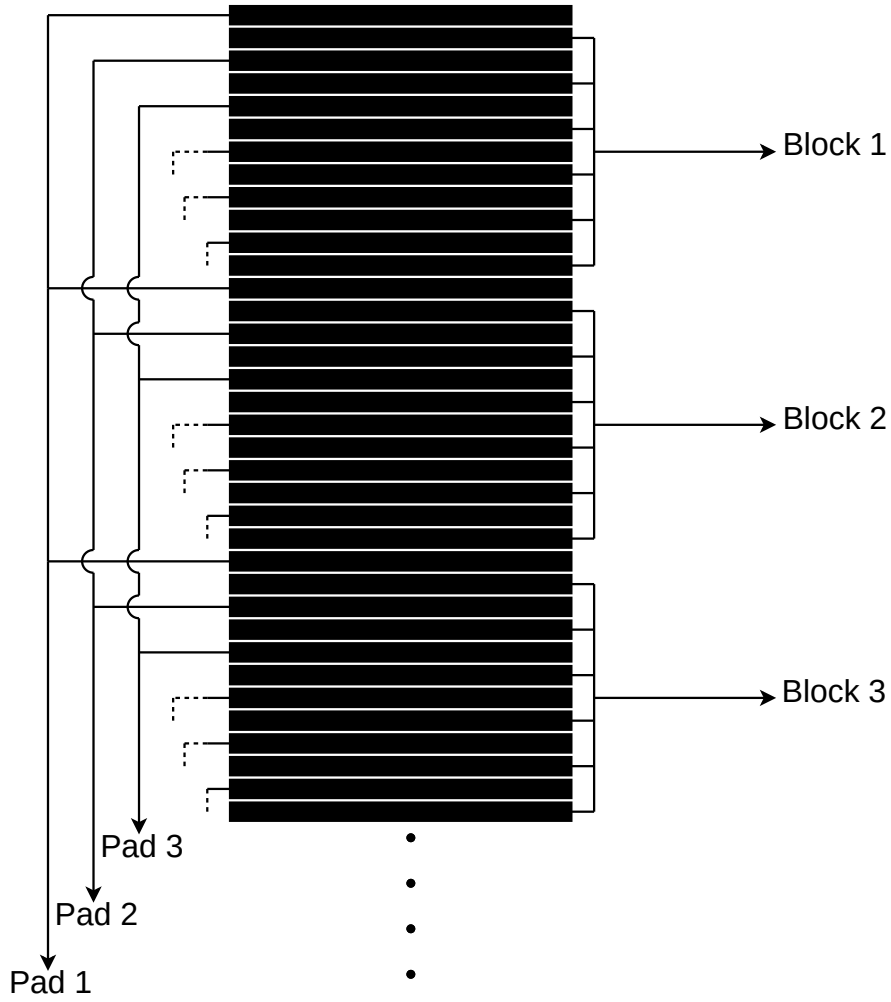

Figure 3.14: The drawing shows the idea of the quadHIDAC pad grouping scheme. The pads are arranged in blocks of 12. The block number and the pad number within the blocks are read out seperatly. The combination of both will give the exact position information.

grouping is a possible large position error in case of channel crosstalk or noise. Table 3.5 summarizes detailed technical specifications of the latest quadHIDAC design. The values are taken from publications [S$^+$05], private communications [Jea05], and measurements performed on defective modules. Note that the specifications differ slightly from the ones

Number of Detector Blocks	4
Number of Modules per Block	8
Rotation Speed	6 s for 180°
Size of Module 1	$135 \times 280\,\mathrm{mm}^2$
Size of Module 2	$155 \times 280\,\mathrm{mm}^2$
Size of Module 3	$173 \times 280\,\mathrm{mm}^2$
Size of Module 4	$195 \times 280\,\mathrm{mm}^2$
Size of Module 5	$213 \times 280\,\mathrm{mm}^2$
Size of Module 6	$231 \times 280\,\mathrm{mm}^2$
Size of Module 7	$251 \times 280\,\mathrm{mm}^2$
Size of Module 8	$271 \times 280\,\mathrm{mm}^2$
Field-Of-View	max. $179.5 \times 179.5 \times 280\,\mathrm{mm}^3$
Gantry Port	Cylindrical, 165 mm in Diameter
Wire Material	Gold-Plated Tungsten
Wire Diameter	20 μm
Wire Separation	1.5 mm
Anode-to-Cathode Distance	3 mm
Typical Anode Potential	$2000 - 2200\,\mathrm{V}$
Filling Gas	Ar Bubbled Through Liquid DIME (C_6H_14O)
Number of Converters per Module	2
Number of Lead Layers per Module	16
Hole Diameter	0.4 mm
Hole Separation	0.5 mm
Lead Thickness	60 μm
Insulation Thickness	140 μm
Entrance Window	200 μm Insulation + 50 μm Lead without Holes
Typical Converter Potential Difference	$3000 - 3300\,\mathrm{V}$
Pad Width	0.7 mm
Gap Between Pads	0.3 mm
Coincidence Window	40 ns
Dead Time After Single Hit	160 ns
Dead Time After Coincidence	400 ns
Readout Speed	320 MB/s via a 128−Bit Bus
Output Format	List-Mode Stream, Coincidences Only

Table 3.5: Specification of the quadHIDAC small animal scanner in its latest version as installed at the University Hospital of Münster.

given in the latest publication of A. Jeavons [J+99]. The 32-module quadHIDAC reaches an average spatial resolution of 1.07 mm and a sensitivity of 13.7 cps/kBq in the centre of the FOV. The count rate saturates at 370 kcps with 19 MBq activity [S+05]. Besides the development efforts of the groups of C.B. Lim and A. Jeavons, two other groups have dealt with the HIDAC principle: one located in Dresden at FZ Rossendorf and another one in Kingston, Canada at the Queens University. P. Manfrass et. al. tried to explore the electrical limits of the converter concept [MEF+88]. B.T.A. McKee et. al. developed the Q-PET detector, a camera for small volumes, reaching a spatial resolution below 3 mm [MDH+88, MDH94].

3.5.4 Other Dedicated Scanners

In addition to the presented PET and small animal PET cameras, there are also other dedicated cameras for special clinical and preclinical purposes available and/or under development. Especially, the diagnosis of breast cancer could be significantly improved by the use of PET techniques. Due to similar dimensions, most of these breast imaging approaches are based on small animal PET developments. For example the RatCAP group is considering a breast scanner version of their scanner by slightly adapting its dimensions. There are also ideas for a straw tube brain scanner [ASM+08] based on the same ideas as the small animal version presented above. Also ideas to perform breast scans with HIDAC techniques have been made [OWEJ06]. The problem here is, as in all MWPC based detectors the dead areas in edges of the construction needed for gas tightness and stability. In addition, the electric field and thus the gain of MWPCs is not homogeneous at the edges of a chamber. Therefore, the most important areas of the breast - near the body - cannot be imaged. Therefore, MWPCs are unlikely to ever play a relevant role in breast imaging.

3.5.5 Future Prospects

The future of small animal PET is promising for different detector technologies. The most important thing for each approach is to concentrate on its strength. If the task is to construct a commercial allround PET device with a large FOV and good resolution and sensitivity, presumably the crystal based cameras are in advantage, mainly because of their development advance gained in 30 years of clinical PET developments. On the other hand, most of all APD based cameras will find their way, even if they still suffer from a very small field-of-view. Dedicated applications like ex-vivo heart studies should already be realisable using today's state of the art APDs.
MWPCs will have to focus on their high resolution and very large FOV without suffering from parallax effects. Also the straw-tube and other niche techniques might profit from their inherent properties to compensate missing energy resolution and low sensitivity. In conclusion, the choice of scanner will strongly depend on its application.
For all further developments the capability of multi-modality will be essential. As in clinical PET also in small animal studies combinations with X-ray CT, MRI and ultrasound will be a key feature of future devices. As developments of combined devices are very expensive and stand alone devices of different modalities are already available, in a first step a manual approach is most reasonable, where PET and the second modality are applied consecutively to the same frame of reference. Special bed-constructions are under investigation to fulfil the demands [Sch08].

3.6 Reconstruction Algorithms

In order to obtain images from coincidence data measured by the detector, dedicated reconstruction algorithms are needed. The easiest way to compare simple phantom measurements with simulations is to use parallel projections. In order to do that, the 3D coordinates of the hit-positions in the detectors have to be transformed into a quadruple of two angles and two points:

$$f(x_1,y_1,z_1,x_2,y_2,z_2) \rightarrow p(\phi,\theta,y,z) \tag{3.27}$$

In order to keep the memory consumption within reasonable limits, (ϕ,θ,y,z) need to be binned. In the later shown measurements and simulations 64 ϕ angles and 15 θ angles have been used. The y,z-binning varies between 0.05 mm and 1 mm depending on the needed precision. The binned data points are then integrated over all angles and z-coordinates so that they can be visualised in a two dimensional histogram:

$$\text{Paraproj}(y) = \int_\phi \int_\theta \int_z p(\phi,\theta,y,z)\,d\phi\,d\theta\,dz. \tag{3.28}$$

Figure 3.15 shows an example projection of one single angle. Parallel projections are

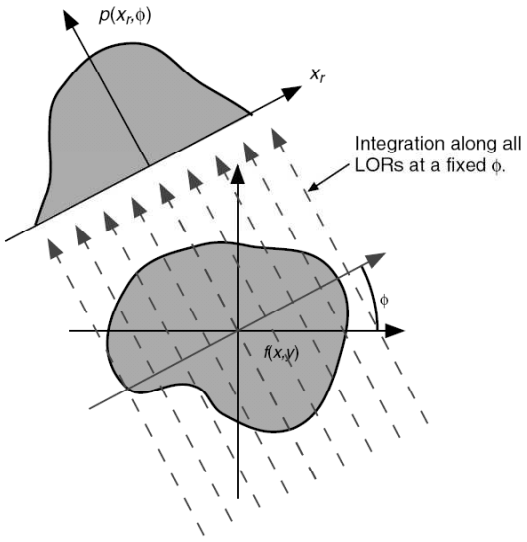

Figure 3.15: 2D Projection obtained by integration of all LORs of a certain angle [WA04]. Doing this for all ϕ,θ and z values and summing over all single projections one attains the 3D parallel projection of the object.

well suited to quantitatively visualise detector response functions of simple objects. But

since they do not return an image, they are not sufficient for the analysis of preclinical and clinical questions and complex structures. Hence, additional image reconstruction methods are needed.
The most common one is here the Radon transformation based filtered back-projection, which is the standard model in X-ray CT. Details about this method can be found in [NW01]. Even though they can also be used in PET, as a drawback they do not take the statistical nature of the data into account. Therefore, modern PET devices use iterative algorithms. Figure 3.16 shows the basic idea of such iterative algorithms. One begins

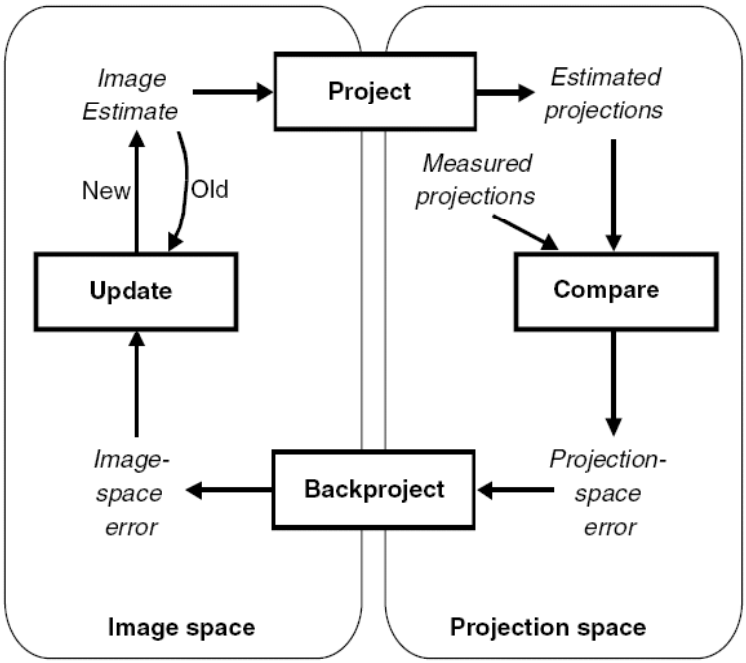

Figure 3.16: Flowchart of a generic iterative reconstruction algorithm [WA04].

with an estimate of the complex image, which can be assumed to be for instance a simple cylinder. In the next step, projections of this image estimate are performed and compared with the measured projections. In contrast to the parallel projections explained above, the measured projections here are not binned. The difference of the estimate and the measure is back-projected to the image space and then used to improve the image estimate. With the new estimate the algorithm will start its next iteration.
Mathematically as a representative of these algorithms, the expectation maximization (EM) algorithm can be written as

$$f^{k+1} = f^k A^T \frac{g}{Af^k} \frac{1}{A^T \mathbb{1}}, \quad k = 0, 1, \ldots \tag{3.29}$$

where $f : \mathbb{R}^N \rightarrow \mathbb{R}^+$ is the density function describing the tracer distribution within the object. A is a matrix containing a_{ij}-values which are equivalent with the intersection length of a LOR i with a voxel j in the image space. A applied to the images tracer density distribution f will result in the projection space equivalent g of f. $\frac{1}{A^T\mathbb{1}}$ is called the sensitivity matrix and needs to be applied in order to correct for geometrical effects of the scanner.
Since the standard EM converges only slowly, the input data is splitted into subsets which are then computed separately, following a divide and conquer approach. This common used method is called the ordered-subset-expectation-maximization algorithm (OSEM).
For details on iterative reconstruction algorithms see reference [VSK85] and for the OSEM algorithm reference [HL94].

3.6.1 Future Prospects

Reconstruction algorithms still have enormous potential for further improvement of image quality in PET. Siemens has shown this very impressivly by modeling the forward projection matrix between image space and projection space very precisely through a series of measurements of point sources at different positions of the FOV. This technique is known as HD-PET [PKMC06].
Another futur aspect will be the implementation of quantitative algorithms. Therefore the fraction of trues, randoms, and scatters has to be known as well as possible in every voxel of the image space. For crystal based PET scanners this can be done by point source measurements with proper energy cuts, in quite the same manner as Siemens has shown. For PET scanners without energy resolution simulations can be used to obtain these quantities.
In PET images of living organisms, movements of the heart and the lung blur the images. Motion corrections using electrocardiography (ECG) signals for cardiac gating and cameras that register the respiratory movement of a white patch attached to the patients abdomen have been done for humans [DBL$^+$07] but are not clinical standard yet. A similar method is under development for small animals using laser beams instead of cameras. Another approach is to correct for motion blurring using the list-mode stream of the PET scanner and some assumptions on the activity distribution under movement [BDS$^+$09].

4. Conceptional Ideas for the Design of a Novel Small Animal PET Detector Based on MWPCs

In the previous section the basic advantages and disadvantages of different PET scanner designs have been discussed.
The 32−module quadHIDAC camera, installed in Münster, has proven its outstanding performance in terms of spatial resolution and cost efficiency. The characteristic feature of the quadHIDAC is its efficient photon-to-electron converter introduced in Section 3.5.3. A disadvantage of this device is the complex converter design which is quite difficult to manufacture as it needs drilling of very small holes into multiple sandwiched layers of lead. More than 200000 holes have to be drilled into each converter, which takes about a full week of time [Jea05]. The drilling produces a lead film covering the holes, consequently the holes have to be cleaned using adequate acids. In addition to the challenging assembly, the detectors have turned out to be very fault-prone. Little irregularities at the edges of the holes cannot be impeded during the manufacturing process, so that repeated sparks between the lead layers inside the converter are observed. In the course of time, these sparks will erode the material and create conductive channels between layers of different voltage potentials, which in the end will destroy the detector module.
On the user side the major problem of the quadHIDAC is its missing energy resolution and its poor timing resolution, resulting from drift time differences of electrons produced in the extended converter and the inhomogeneous electric field in the converters. The result is an increased rate of randoms. An ideal, less error prone converter for an MWPC based PET detector would most likely not have holes and has to be easy and fast to build. The use, or at least the intensive machining, of toxic components like lead should be avoided using either alternative materials or prefabricated elements. The spatial resolution and the sensitivity should nevertheless be kept on a level comparable to the quadHIDAC detector.
Following these ideas the detector concept of the Münster PET device, in the following called MSPET, can be drafted in a straightforward manner. To keep the detector sensitivity on a level comparable with the quadHIDAC, a similar quantity of converter material has to be used. The abdication of a complex HIDAC-like drilled converter leads to an increase in the number of detector modules in order to achieve the same conversion probability. A first estimate for the number of modules per detector block needed for a similar sensitivity would be $n = 64$, in order to achieve comparable efficiency to a system with 8 HIDAC modules with two converters and 16 layers of lead of which 50 % are holes. It is assumed,

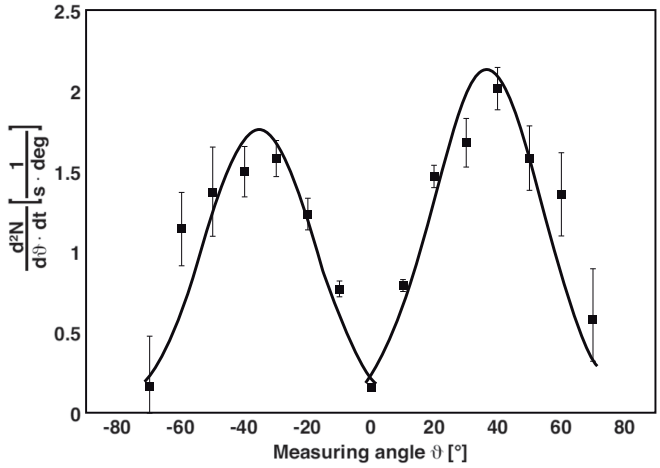

Figure 4.1: Measured angular distribution of electrons leaving a 80 μm lead foil irradiated with a ^{137}Cs source emitting 663 keV photons and 1176 keV electrons [HÖ7]. The leading signs are chosen arbitrarily. Although the mean value of the fitted gaussian shown here is $\alpha = 36.0°$, the data points are compatible with a mean value of slightly above $\alpha = 40°$. As a cross check, comparable Geant4 simulations have been made and will be presented in Figure 6.15.

that two flat foil converters are mounted in one module and both will provide equivalent conversion rates. The challenge in such a detector is the large number of readout channels needed. With roughly 120 channels per module a total number of approximately $30,000$ channels would be needed for the whole PET device. This is challenging, but not impossible to achieve with the use of modern integrated electronics. The number of channels can also be reduced by appropriate channel grouping schemes. Although grouping of channels is unattractive because it entails a loss of information. Therefore, it is always prefered to read out every single channel in order to retain raw data access to all available information from the pads.

The spatial resolution of the new scanner is then limited by the angle of the electrons liberated in the converter and entering the gaseous volume of the detector. As shown in Figure 4.1, first measurements by H. Hünteler [HÖ7] indicated an average angle of $\alpha \approx 40°$. Thus, for sub-millimetre resolution, the chamber should not be thicker than 2 mm in total. The typical electron drift time in such a module will be inherently faster than that of the HIDAC and will thereby reduce the randoms rate through the use of a shorter coincidence-time window.

The optimum converter thickness and material has to be investigated and optimized using proper detector simulations.

As no multi-wire proportional counter with such extreme dimensions has ever been build before, the project is also an attempt to test the limits of this detector concept.

5. Monte Carlo Simulations

Nuclear physics is often faced with very complex problems. Since analytic calculations here become difficult, time consuming and unpractical very quickly, Monte Carlo simulations [MU49] can help to keep things managable. The Monte Carlo method was introduced in 1949 by N. Metropolis and S. Ulam who were inspired by the city of Monte Carlo, Monaco with its famous casinos when searching for a name.
Monte Carlo algorithms use random numbers in order to generate input values for a deterministic model. The model returns a unique result for every input number. When sampling the random numbers on sensible probability distributions depending on the model of the simulation and doing lots of iterations, the results approach the exact analytical solutions. Depending on the complexity of the model and the demands on the precision of the results, the necessary number of iterations and computation time may become very large. Therefore, the usage of computer clusters and distributed systems is essential to generate a reasonable amount of data.

5.1 Geant4

Geant4[1] [A+03] is a toolkit for Monte Carlo simulations of particles traversing matter. It was originally designed for high energy experiments at CERN[2] by the RD44 project who came up with the first production release in 1998. The Fortran-based predecessor Geant3 dates back to 1974. As a result of developments of a joint project with the ESA[3] since 1999 there are low energy extensions [A+99] available. These provide cross section tables reaching down to at least 250 eV, depending on the process, and make Geant4 suitable for PET simulations.
Along with these developments, there are also some sophisticated dedicated tools available for PET: For example the Geant4-based GATE [S+03] or the independently developed PET-EGS [C+99] (based on EGS4 [N+85]), SIMSET [SIM09] and PETSIM [T+92]. Since these codes are dedicated to cylindrical, crystal-based PET only, the quadHIDAC PET code was developed from scratch on the basis of the generic Geant4 toolkit version 9.0. Most of the simulations have been performed on a cluster of 136 Opteron

[1] Geant stands for **Ge**ometry **an**d **t**racking

[2] European Organization for Nuclear Research, formerly known as **C**onseil **E**uropén pour la **R**echerche **N**ucléaire

[3] **E**uropean **S**pace **A**gency

processors at the Institut für Kernphysik in Münster. 250 million positron decays could be tracked within 26 hours using 50 processors.

5.2 Concept of Geant4

In Geant4 one can discriminate classes which are called before a simulation run is started and those needed for the run itself. Initialisation classes define the experimental setup and the tools, materials, and physics processes that are to be simulated. The basic structure of Geant4 can be understood as a state machine as shown in Figure 5.1. In the pre-

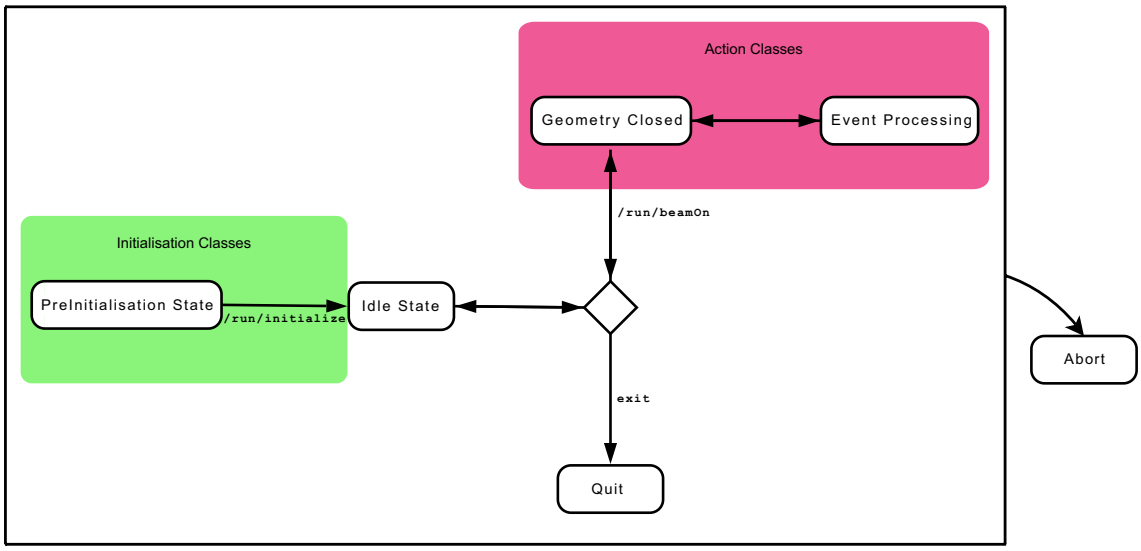

Figure 5.1: Basic structure of Geant4.

initialisation state geometries, materials, particles and physics can be defined. The pre-initialisation state is closed by the command `/run/initialize`. Everything defined by the initialisation classes is now set and the idle state is called. In the idle state a simulation run can be started by the command `/run/beamOn`, which closes the geometry and starts the event processing state, hence the action classes. The run can be terminated normally to the quit state or to the abort state indicating an error.

5.2.1 Initialisation Classes

- **Detector Construction**
  In the detector construction class all volumes, geometries, and materials of the system setup have to be defined. It has to be ensured, that no volume overlaps with

other volumes. Volumes are placed inside other, so called mother volumes. The highest order volume is called world volume. Volumes and materials can be defined recursively. Basic volume geometries like cylinders, spheres and so on are provided by Geant4 classes. When defining a geometry, one has to start with the definition of a solid. A solid is a basic geometry like for example a box of certain dimensions. In the next step a material can be assigned to the solid which makes it a logical volume. Instances of the logical volume can now be placed in some mother volume which makes it a physical volume.

- **Physics List**
  The physics list class defines all the physics processes needed for the simulation task. In addition all particles to be generated have to be defined. Geant4 provides basic classes for the most relevant physics processes and also definitions for elementary particles. Unwanted processes or particles can be switched off. The particle data is implemented using the NIST[4] data [Nat09a]. As Geant4 is originally dedicated to the simulation of high energy experiments, the low energy cross section tables for physics processes are less precise. Therefore, external groups have implemented more detailed physics lists even for low energy applications [A$^+$99] currently reaching down to $10-250\,\mathrm{eV}$ depending on the process. Some of these working groups have been affiliated with the Geant4 Collaboration so that the low energy packages are certified. There are two basic low energy packages available: One based on the Livermore Library [PCC$^+$91, CHK97, PCS97] and one based on Penelope[5] [SFVS01]. Both packages provide comparable descriptions of the relevant processes [AGI$^+$05]. The differences between both packages are marginal, with regard to the implemented application. The most prominent drawback of both models is the missing accuracy of multiple scattering processes in thin foils. Therefore, the standard Geant4 implementation has to be used here, adding a small inaccuracy to the simulation results. Another important value to define in the physics list is the production cut. In general, all particles generated in the simulation are tracked until they have reached the minimum energy listed in the physics tables. This energy cut therefore defines the minimum kinetic energy of a particle at the time of its production.

[4] **N**ational **I**nstitute of **S**tandards and **T**echnology
[5] **PEN**etration and **E**nergy **LO**ss of **P**ositrons and **E**lectrons

5.2.2 Action Classes

- **Primary Generator Action**
  The primary generator class creates primary beam particles and defines their energy and direction.

- **Run Action**
  A run in Geant4 is, analogous to real experiments, a set of events which share the same framework conditions. No changes on the geometry or physics lists can be made while a run is in progress.
  The run action class can be viewed as the global control structure of the simulation just below the main class level. It can advise the detector construction class to build and return the geometry. The construction of the physics list is assigned and finally it lets the event action methods produce and process events.

- **Event Action**
  All primary particles are pushed onto a stack at the beginning of an event. One particle after another is then popped from the stack and sent to the tracking manager for further processing. The event manager also receives produced secondary particles and processes them in the same manner until the stack is empty.

- **Stacking Action**
  Primary events which are not yet processed by the event action class wait on a stack to be picked up.

- **Tracking Action**
  A track in Geant4 carries information of a particle at the current time. The current track is deleted, when the particle decays, has lost all its kinetic energy or leaves the world volume. It is in the responsibility of the user to store needed track information in so-called trajectory objects for access at later times.
  Tracks of particles received from the event action classes are processed by the tracking manager. Tracks are calculated using the stepping action classes. Secondary particles are returned to the event manager for further processing.

- **Stepping Action**
  A step is the smallest unit of particle movement in Geant4. Coming from a `PreStepPoint` the stepping action class calculates the position of the `PostStepPoint`. It considers the particle energy, direction and cross section table for its calculations. A step is completed when the next physics process occurs, or the volume boundary is reached (which is handled as a process itself, called transportation).

5.3 quadHIDAC Simulation Code

For a better understanding of the behavior of the quadHIDAC small animal PET scanner, extensive simulations have been performed. The design of the quadHIDAC, as described in [J$^+$99, Jea95, Jea02] and [S$^+$05] has therefore been implemented. Furthermore, to compare the simulation results with measurements, some standard phantom sources, including line-, mouse-, rat- and point sources, have been implemented.

5.3.1 Detector Construction

The quadHIDAC small animal PET scanner was already introduced in Section 3.5.3. Based on publications, patent discriptions and measurements performed on defective HIDAC modules the dimension parameters for the hole distances and material thicknesses were obtained and can be found in Table 3.5.
Based on these values a corresponding simulation setup has been implemented. Figure 5.2 shows a visualisation of a $5 \times 5 \times 12.9\,\mathrm{mm}^3$ piece of a simulated detector module. The image has been rendered with the DAWN visualisation toolkit [TK97]. One can see the outer insulation, the outer lead foil and the stack of 16 alternating lead and insulation layers drilled with holes. The thickness of a simulated module is 12.9 mm, which is 0.3 mm less than a real one. The difference is most likely the result of unknown contributions of glue between the parts of the modules. Log file headers of quadHIDAC measurements report a distance of 14 mm between two neighbouring modules. The first module begins at $X = 89.2\,\mathrm{mm}$ away from the centre of the FOV. Since the modules in the simulation have been stacked together without any gaps in between, the sizes have been adapted to the quadHIDAC's angular coverage and not to the real dimensions. The size differences are noted in Table 5.1. In sum a simulated detector bank is 8.8 mm shorter than a real one. Figure 5.3 shows the complete simulation setup including a hit distribution map of a point source simulation. To keep the simulation on a manageable level, only two opposite detector banks have been implemented. Nevertheless it is possible to simulate a virtual four module quadHIDAC by switching coordinates of the source volume position and the detector reference system. The simulation results can be merged later to get the full quadHIDAC simulation. Especially for source volumes positioned off-centre this method is recommended. Altogether the setup contains two blocks of eight detector modules comprising over 200 million basic elements, most of them with holes in it.
Of course all relevant dimensions and materials can easily be changed in order to test or optimize these with respect to different questions.

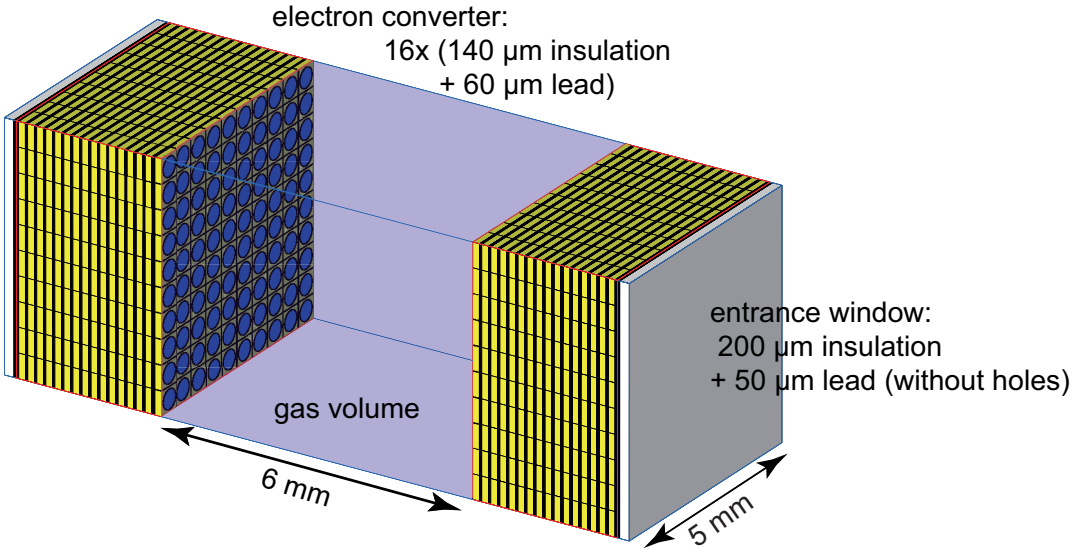

Figure 5.2: $5 \times 5 \times 12.9\,\mathrm{mm}^3$ piece of a simulated detector module. One can see the two converters and the gaseous volume in between. The converters consist of 16 layers of alternating lead and insulation. The entrance window is made of a gas tight insulation foil followed by a solid lead sheat without holes in it.

Module Number	Real quadHIDAC Module Size [mm^2]	Module Size in the Simulation [mm^2]	Space Angle α [°]	Space Angle β [°]
1	135×280	135×280	74.23	114.99
2	155×280	153×276.5	73.81	107.21
3	173×280	169×273.5	72.86	100.13
4	195×280	189×271.5	73.24	93.72
5	213×280	205×269.5	72.52	87.91
6	231×280	221×268	71.92	82.66
7	251×280	239×267	71.85	77.9
8	271×280	257×266	71.8	73.58

Table 5.1: The modules of the quadHIDAC have been adapted to the angular coverage of the real quadHIDAC. The sizes of the individual modules therefore differ from the real dimensions. α is the angular opening in the X-Y plane and β the opening in the X-Z plane.

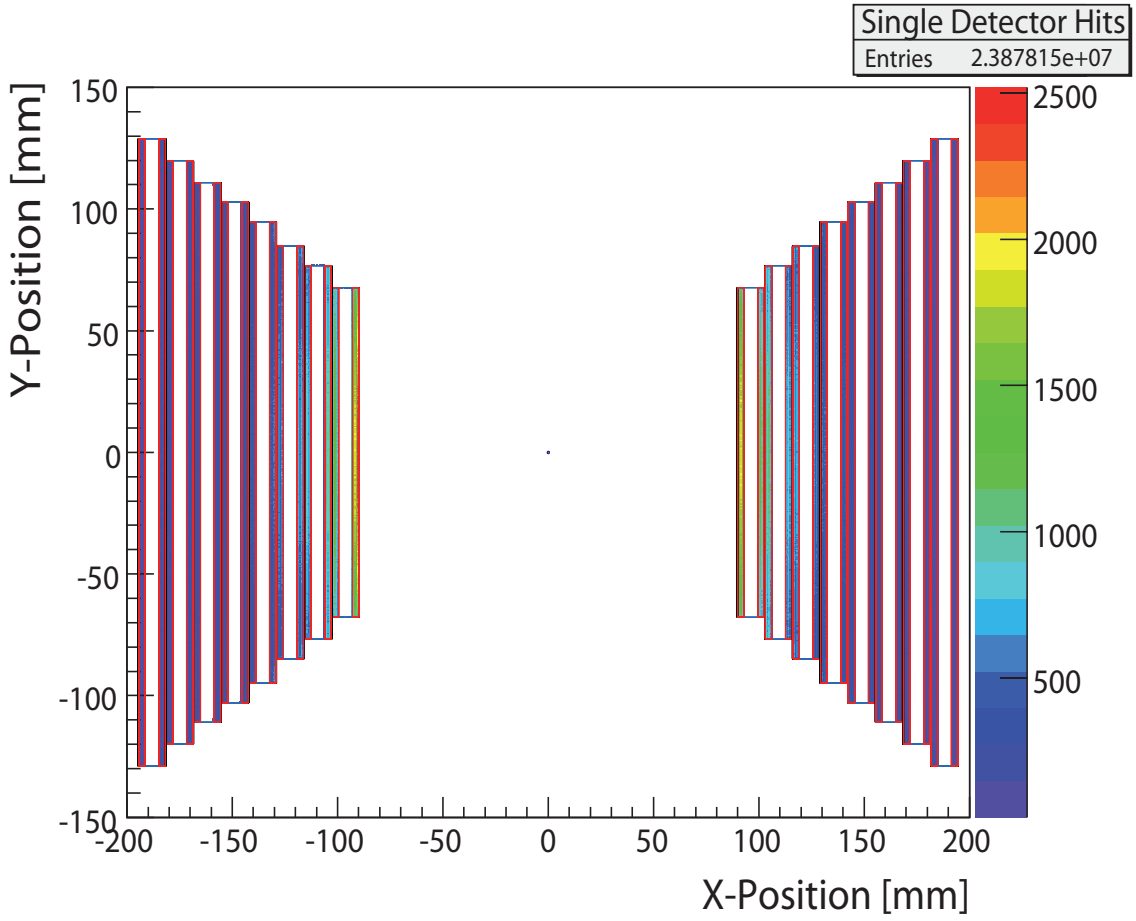

Figure 5.3: Geometry of the HIDAC detector as implemented in the simulation code. In this illustration a wire grid sketch of the geometry setup made with DAWN was superimposed with a simulated detector hit map produced by an 1 mm point source filled with ^{18}F in water.

5.3.2 Physics

Geant4 allows switching physics processes needed for the simulation on and off. For the presented PET simulations, all relevant particles and processes have been switched on, namely:

- The photon, with the processes photoelectric effect, Compton scattering, Rayleigh scattering and gamma conversion.
- The electron, undergoing multiple scattering, ionisation and bremsstrahlung.
- The positron, influenced by multiple scattering, ionisation, bremsstrahlung and annihilation,
- and with minor influence the μ^+ and the μ^-, that can be used for cosmics tests, with the processes multiple scattering, ionisation, bremsstrahlung and pair production.

For all processes but multiple scattering the low energy package based on the Livermore library is used [A+99]. The low energy processes are implemented down to energies of at least 250 eV. Below this value, the particles are removed from the simulation. The above mentioned processes can occur at rest, along a step or post a step. Processes at rest would be for example particle decay or annihilation. Bremsstrahlung and ionisation occur along a step and a decay in flight or during hard scattering. As multiple scattering has not been implemented for the low energy range yet, the standard Geant4 multiple scattering package, which is accurate above ≈ 1 keV is used. The lack of precision directly influences the positron annihilation process. As energies smaller than 10 eV would be needed to describe annihilation photon non-collinearity, the angle between both emitted photons is always exactly 180°. Hence resolution loss caused by non-collinear photons cannot be studied using Geant4 version 9.0.

5.3.3 Primary Generator and Source Volumes

The most frequently used small animal PET tracer molecule at the University Hospital of Münster is ^{18}F-Flourodeoxyglucose (FDG). Even most of the test and calibration measurements have been done with FDG. Since the beta spectrum of ^{18}F can be described quite exactly, positrons sampled on this spectrum are used as particle source for all simulations presented here.

The Beta Spectrum of ^{18}F

The kinetic energy of the primary positrons in the simulation has to be sampled using the energy spectrum of the positron decay of the ^{18}F nuclide. ^{18}F has a mean half life of

109 min and decays, according to Formula (3.1), to ^{18}O with a maximum positron energy of 635 keV:

$$^{18}F \longrightarrow ^{18}O + e^{+} + \nu + Q \tag{5.1}$$

In general a transition of such a decay can be described by the Fermi theory as follows [MK94]:

$$N(p)dp = \frac{2\pi}{\hbar}|\langle f|\hat{H}|i\rangle|^2 \frac{dn}{dW_e} \tag{5.2}$$

$N(p)\mathrm{d}p$ is here the probability per unit time for an electron to be emitted with a momentum between p and $p+\mathrm{d}p$. The matrix element $\langle f|\hat{H}|i\rangle$ contains the Hamilton operator of the weak force. It has been shown experimentally that this operator shows only a very slight energy dependence for most beta spectra. The shape of the spectra is formed mainly by the term $\frac{dn}{dW_e}$ which describes the density of the final states per energy. Following Fermi theory the density of final states per energy interval can now be written in more detail as:

$$\frac{dn}{dW_e} \approx P_e W_e \cdot (W_0 - W_e)^2 \cdot F(Z,W) \cdot C_n \tag{5.3}$$

$$= (W_e^2 - 1)^{\frac{1}{2}} W_e \cdot (W_0 - W_e)^2 \cdot F(Z,W_e) \cdot C_n \tag{5.4}$$

with

$$W_0 = \frac{E_{kin}^{max} + m_0}{m_0} \tag{5.5}$$

and $E_{kin}^{max} = 635\,\mathrm{keV}$, $m_0 = 511\,\mathrm{keV}$ for a positron escaping from the ^{18}F nuclide. $n = 0$ indicates an allowed decay [Sch66]. Because of the negligible energy dependence, the matrix element C_0 can be approximated by a constant.
$F(Z,W)$ is called the Fermi function. It describes the Coulomb interaction between the emitted particle and the daughter nucleus resulting in a slight shift of β^+-spectra towards higher energies and of β^--spectra towards lower energies. The Fermi function F can now be written as

$$F = F_0 L_0 \tag{5.6}$$

where F_0 is the result of the Dirac equation with a point charge nucleus, evaluated at its charge radius. It can be approximated as [Hol92]:

$$F_0 \approx \frac{2\pi y}{1 - e^{-2\pi y}}, \tag{5.7}$$

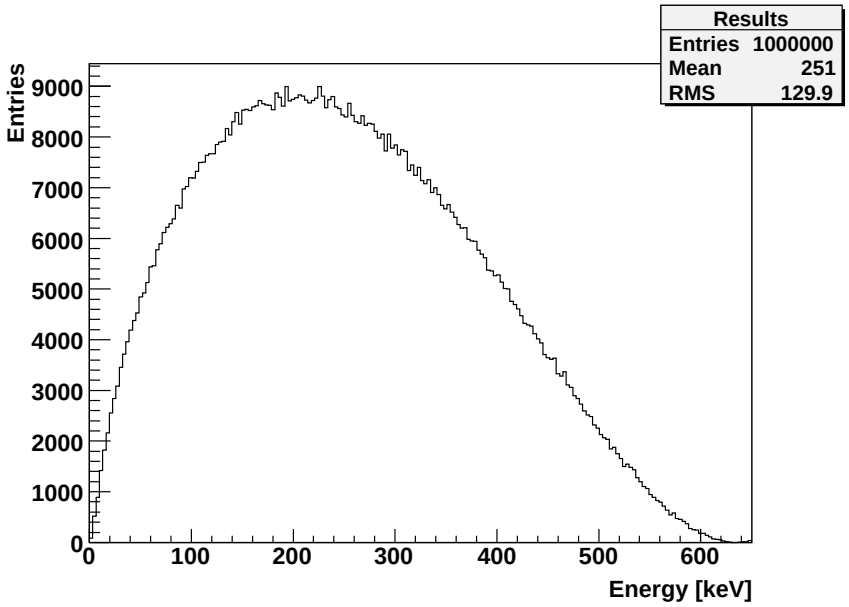

Figure 5.4: Positron energy spectrum of ^{18}F as it is used in all presented simulations.

$$y = \frac{\alpha Z W_e}{P_e} = \alpha Z \frac{W_e}{(W_e^2 - 1)^{\frac{1}{2}}},$$

with Z being the charge number of the daughter nucleus ($Z > 0$ for β^+-decays and $Z < 0$ for β^--decays). L_0 is a correction factor for the finite charge distribution in the nucleus. It can be written as [Hol92]:

$$L_0 \approx \frac{1}{2}(1+\gamma_1), \quad \gamma_1 = \sqrt{(1-\alpha^2 Z^2)}, \quad \alpha \approx \frac{1}{137}. \tag{5.8}$$

For our application, random numbers are sampled on this spectrum using the ROOT [BR$^+$97] random number generator. The system time in seconds is used as initial seed for the random number generator. Since the time information is also part of the output filenames, two data files obtained with the same seed in the same directory cannot exist. This is important if more than one instance of the same program is executed sharing the same data space, e.g. on a computer cluster or a multi-core CPU. Figure 5.4 shows the sampled spectrum which is used in the presented simulations. With a mean energy of 251 keV it is in good agreement with the canonical values [C$^+$83].

Simulated Source Volumes

It is easily possible to implement nearly every source volume geometry based on simple shapes like e.g. boxes, spheres, cylinders or cones. In order to compare the simulations

presented in this thesis with appropriate measurements, the following standard PET phantoms have been implemented:

- **Point-like Source** A point-like source is a water sphere with a small diameter. Primary positrons are distributed uniformly over the volume of the sphere using random numbers. The coordinates are calculated as follows:

$$x = R \cdot \sin\Theta \cdot \cos\Phi \tag{5.9}$$
$$y = R \cdot \sin\Theta \cdot \sin\Phi \tag{5.10}$$
$$z = R \cdot \cos\Theta \tag{5.11}$$

  with $R = r \cdot s_1^{\frac{1}{3}}$, $\Theta = \arccos(1-2s_2)$ and $\Phi = 2\pi s_3$, where s_1, s_2 and s_3 are random values in the range $0 \ldots 1$ and r is the radius of the sphere. The random numbers are generated again using the ROOT[BR+97] random number generator. The point source can be compared to a small ^{18}F-water drained spherical sponge used in quadHIDAC test measurements [Sch08]. Diameters between 0 mm and 3.2 mm have been used for different simulations.

- **Line Source** The simulated line source consists of a cylindrical water volume with a length of 80 mm and a diameter of 1 mm. It is surrounded by a glass pipe of 100 mm length and 3 mm diameter which is intended to stop the positrons. The positrons are distributed uniformly in the water volume:

$$x = R \cdot \cos\Phi \tag{5.12}$$
$$y = R \cdot \sin\Phi \tag{5.13}$$
$$z = \frac{L}{2} \cdot (2 \cdot s_3 - 1) \tag{5.14}$$

  with $R = r \cdot \sqrt{s_1}$, $\Phi = 2\pi s_2$, where s_1, s_2 and s_3 are random values in the range $0 \ldots 1$ and r is the radius of the cylinder. L is the length of the cylinder.

- **Mouse Phantom** In addition to the thin line source, thicker cylinders have been simulated. Usually these cylinders are used as mouse phantoms. They consist of a cylindrical water volume with a length of 76 mm and a diameter of 41 mm. It is surrounded by a 1 mm thick pipe made of polyethylene, which has a length of 150 mm and stops nearly all positrons.

- **Rat Phantom** The rat phantom is quite similar to the mouse phantom except for its dimensions. The water volume here has a diameter of 59 mm and a length of

100 mm. The surrounding polyethylene pipe has a thickness of 1 mm and a length of 150 mm.

5.3.4 Stepping Algorithm and Output Data Format

The stepping algorithm performs the computation of the detectors response of every single particle traversing through the defined geometry. It returns information on

- the event number,
- hit-position coordinates,
- layer number,
- converter number,
- energy of liberated electrons entering the gaseous parts of the detector,
- the energy of the mother-particle,
- the particles creation process,
- the mother particle's creation process,
- the vertex coordinates,
- and original annihilation photon directions.

The output is written to a file containing a ROOT tree [BR+97] format.

Determination of Vertex Properties

In a first step the code looks for a photon track created in an annihilation process by a primary positron. The vertex coordinates of the annihilaton and the photons directions are retained for a possible entry in the ROOT tree later on.

Identification of Scattered Events

Information on production- or interaction-processes and step positions are available only during the computation of that step. This implies that, if one wants to know whether a scatter process has occurred somewhere on a particle track, one has to store this information at the time, the process occurs. Possible scattering processes are here are the Rayleigh and the Compton process. The information on Rayleigh scattering is written

into an array, created and initialised by the `EventAction` class. The lowest step number containing a Rayleigh scattering process is stored for every track. In the same manner Compton scattering processes are stored. The Compton array contains the spatial coordinates of the scattering process, the energy of the photon before the scattering and the step number of the step at whose endpoint the Compton effect occurs. Also the parent track ID number and a scatter flag, indicating weather the particle has been scattered during current or previous steps is stored. The parent ID number `parentID` $= 0$ indicates, that the mother particle is created by the primary generator while photons emitted in the positron annihilation process are assigned `parentID`$= 1$.

Generation of Detector Hits

One major drawback in the current version of Geant4 is its inability to simulate avalanche propagation of electrons in electric fields and thus generating proper detector responses of gaseous detectors.
Hence, in the developed simulation code a hit is obtained, when an electron crosses the geometrical border from any volume into one of the gaseous parts of the detector. These are, in case of the HIDAC design, the holes of the converter and the wire chamber itself. The coordinate of the hit is then the vertex point of the electron. This is most likely somewhere in the converter but can be generally anywhere but in the gaseous parts of the detector. Therefore, every electron entering the gas volume is assumed to produce a measurable signal, while direct conversion of photons in the gas volume is ignored.
If such an electron is identified, the scatter arrays described in the previous Subsection are browsed at the parentID position for the information on the creation process and energy of the mother particle. The particle type of the mother particle is obtained from browsing the stored trajectory object containing the tracks history. Then the event number, the particles vertex position, the kinetic energy of the electron and the detector number of the hit is obtained. The whole event information is then filled into the ROOT tree and the next event can be processed.

Filtering of Coincidences

The presented detector simulation returns a ROOT tree containing information on single hits. In order to filter for coincidence events, these single trees need to be processed. Therefore, a small piece of code looks for single events sharing the same event number, which therefore originate from the same primary particle. Further coincidences are accepted only, if they occur on opposite detector blocks. If, in rare cases, more than two events share the same event number, the electrons with the largest kinetic energy are combined.

Modules	Size in the Simulation [mm^2]
$1-5$	135×280
$6-10$	154.25×278.65
$11-15$	171.53×277.6
$16-20$	192.79×276.81
$21-25$	210.07×276.14
$26-30$	227.36×275.61
$31-35$	246.63×275.16
$36-50$	265.95×274.75

Table 5.2: The modules of the MSPET camera have been adapted to the angular coverage of the quadHIDAC camera denoted in Table 5.1. Events exceeding this dimensions are rejected by the `Stepping Action` class.

5.4 MSPET Simulation Code

The simulation code for the MSPET device itself is similar to that of the quadHIDAC. Apart from the different detector geometry, only the stepping algorithm had to be adapted to the new geometry. The geometry setup is shown in Figure 5.5. A MSPET MWPC module consists of a 2 mm thin gas filled volume which is placed in between two cathode planes. The cathodes base plate is made of 0.5 mm thick FR4, a glass-fibre/epoxy compound material. A thin 35 μm copper layer covers the surface of the FR4 on both sides. The following thin lead, tungsten or gold sheet acts as a photon-to-electron converter. As in the HIDAC simulations there are two detector blocks implemented. Each block contains 50 detector modules. To allow for some flexibility in the choice of detector block dimensions, all modules are initialized with the same size which is $280 \times 280\,\mathrm{mm}^2$, the maximum size simulated here.

The MSPET modules can be cut to the HIDACs space angle coverage by ignoring particles that are detected outside of it during a simulation run in the stepping algorithm, or afterwards during the data analysis. For better comparison to the quadHIDAC detector, the field-of-view is choosen identically. In order to use feasible values, 8 blocks of same sized MSPET detector modules have been used for the presented simulations. Table 5.2 states the module sizes used for the simulations in this thesis.

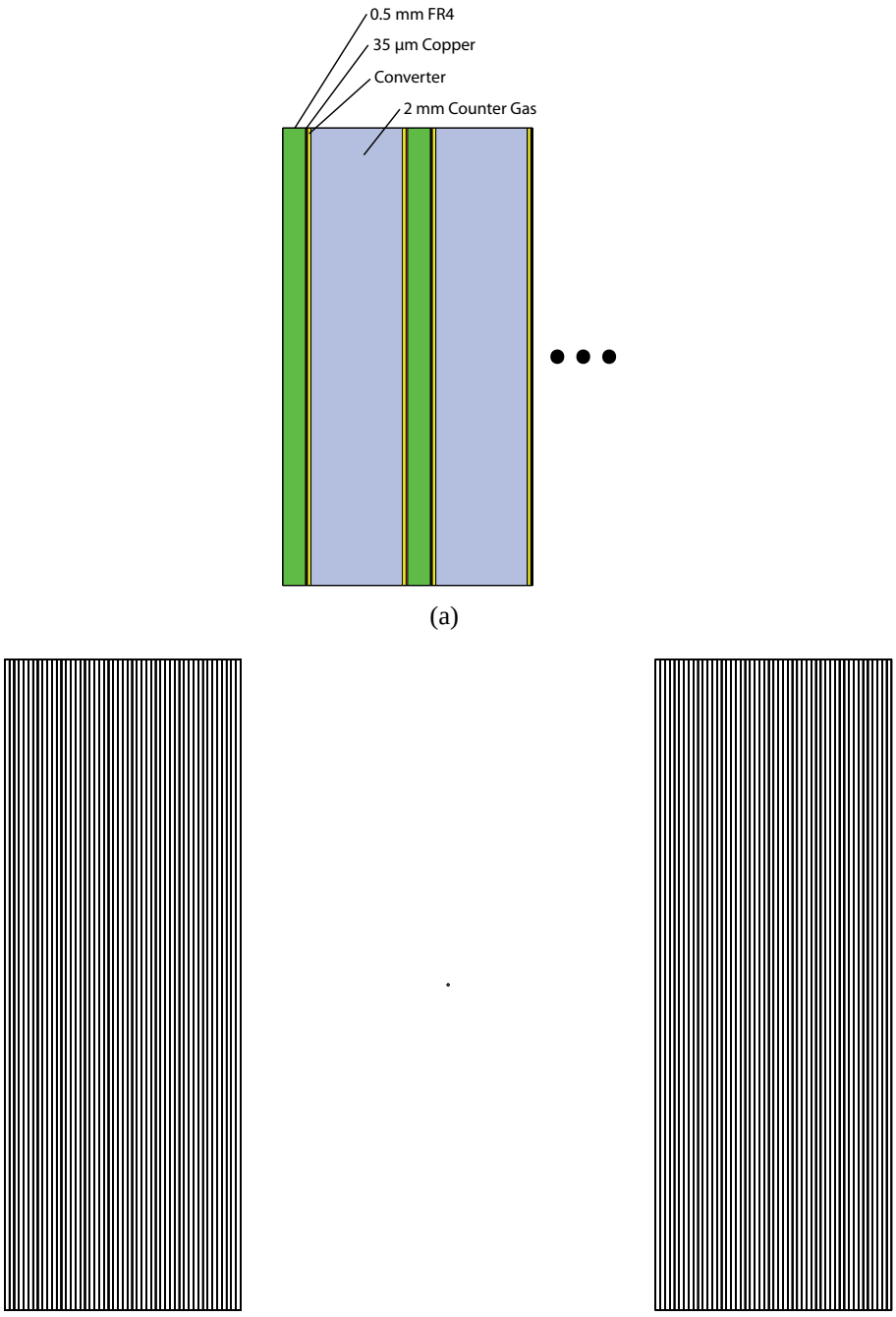

Figure 5.5: (a) shows a close up view of two stacked MSPET detector modules. A 2 mm thick MWPC is sandwiched inbetween 0.5 mm FR4 sheets plated with 35 μm copper and equipped with a thin photoconverter made of either lead, gold or tungsten. 50 layers of these detectors form a full detector module as shown in (b).

6. Construction of a Multi-Wire Proportional Counter for Small Animal PET

To fulfil the demands of a modern small animal PET device, the intended performance specifications have to be considered already during its design. In terms of sensitivity and spatial resolution the new Münster PET device (MSPET) should be comparable with other modern small animal PET scanners. Here above all the quadHIDAC has to be mentioned as the only commercial, wire chamber based, small animal PET scanner. The advantages of MWPCs, which are most of all the large FOV and the good spatial resolution, have to be exploited as well as possible.
The detector should be easy to build, without the demand for expensive special devices. Therefore, something similar to the drilled converter of the quadHIDAC cannot be an option, even if it provides high sensitivity.
To prepare the construction and validate dimensions and specifications of the new wire chambers and converters, simulations and test measurements have been performed.

6.1 Multi-Wire Proportional Counters (MWPCs)

Multi-wire proportional counters (MWPCs) were introduced in 1968 by the group of G. Charpak at CERN [C$^+$68]. He was awarded with the Nobel price in 1992 for his invention. At first glance MWPCs can be seen as an advancement of cylindrical proportional counters. By experimental efforts he proved the common belief wrong, that, due to capacitive coupling of the wires, it would be impossible to extend proportional counters into a second dimension.
Charpak mounted a set of closely spaced anode wires between two cathode plates and applied a constant high voltage to these wires. Each wire acted as an independent proportional counter. Figure 6.1 shows such a MWPC setup. MWPCs were the first devices providing position information for large amounts of particles that could be read out electronically. Allowing fast automatic data processing, they were a great improvement compared to commonly used cloud or bubble chambers.

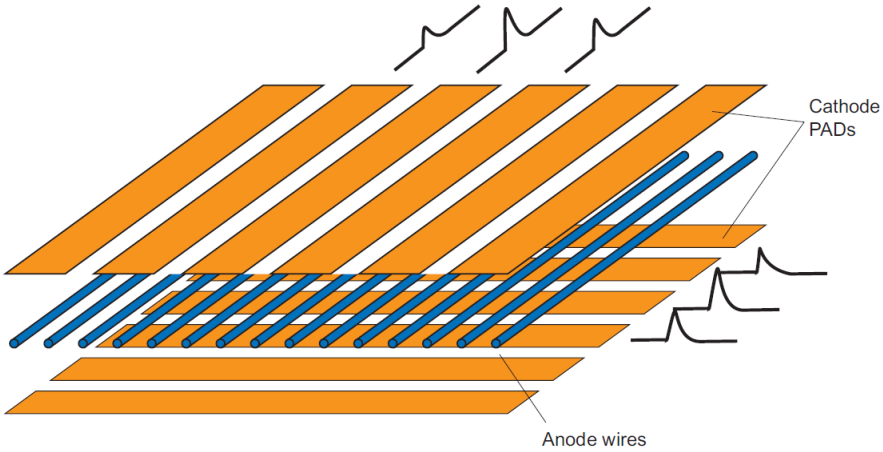

Figure 6.1: Schematic setup of a MWPC with pad readout [Sau77].

6.1.1 Principle of Operation

As MWPCs are derived from proportional counters, their principle of operation is comparable. A particle transversing the gas detector will ionise the gas volume along its path and create electrons. These electrons will start to drift towards the anode wires according to the radial electric field

$$E(r) = \frac{1}{\ln(\frac{b}{a})} \cdot \frac{V}{r} \tag{6.1}$$

of this wire at a distance r. Here a is the anode wires radius, b the distance between anode wire and cathode and V the voltage applied to the wire. As Equation (6.1) describes an ideal radial field of a proportional counter, for MWPCs it holds only for areas close to the wire. An approximation of the electric field in an two dimensional MWPC was given by [Ers72] as

$$E(x,y) = \frac{\pi V_0}{(\pi b - s\ln(\frac{2\pi a}{s}))} \cdot \frac{\sqrt{1+\tan^2(\frac{\pi x}{s})\tanh^2(\frac{\pi y}{s})}}{\sqrt{\tan^2(\frac{\pi x}{s})+\tanh^2(\frac{\pi y}{s})}} \tag{6.2}$$

where s indicates the wire separation, a the wire radius and b the anode-cathode gap. Depending on the chamber size, gas and electric field strength, the electrons drift with $T^e_{\text{drift}} \approx 20\,\text{ns/mm}$, following Figure 6.2, towards the wire.

At distances of only a few wire radii to the anode, the electric field becomes very large ($E \approx 10^6\,\text{V/m}$ at $r = 300\,\mu\text{m}$).

The accelerated electron will ionise gas molecules and thus create additional electrons,

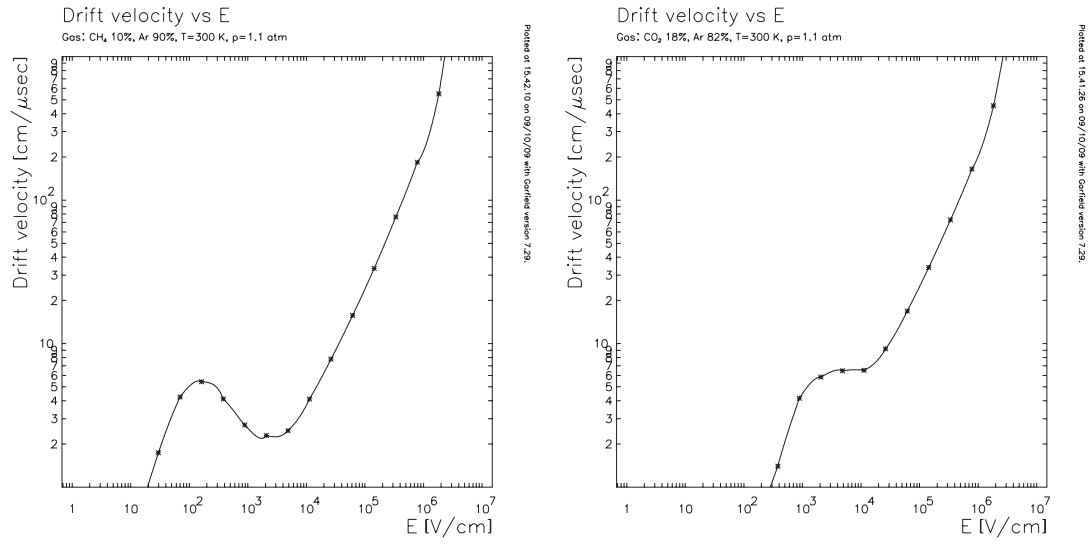

(a) (b)

Figure 6.2: Simulated drift velocity of electrons in (a) P-10 gas and (b) an Ar-CO_2 $(82-18)$ mixture. A chamber with 1 mm anode-cathode- and 1.5 mm wire separation has been used.

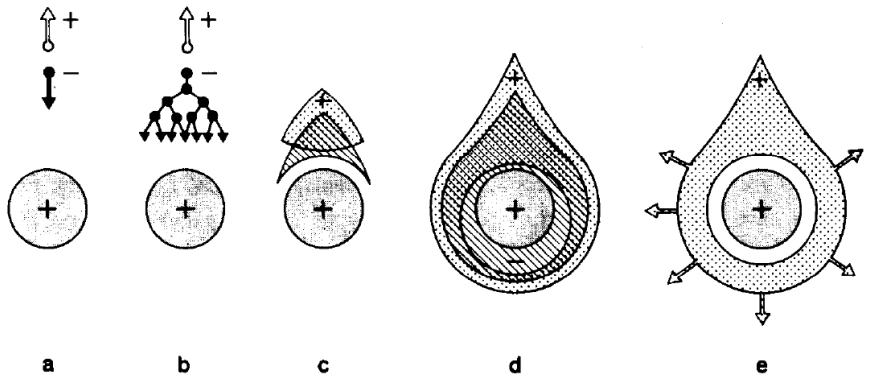

Figure 6.3: Avalanche development close to an anode wire [Sau77]. In the increasing field electrons are multiplied and a drop-like avalanche develops around the wire. The negative electron cloud is extracted by the wire within a few nanoseconds, while the ions start to drift towards the cathode pads.

which form a drop-like avalanche towards the anode wire. A sketch of the avalanche development is presented in Figure 6.3.

For n electrons on a path dr there are

$$dn = n \cdot \alpha \cdot dr$$

electrons created. α is here the first Townsend coefficient (unit: ion pairs/cm). By integration of this formula one can calculate the total number of electrons on a path r as

$$n = n_0 \cdot e^{\alpha r},$$

where the multiplication factor, called gas gain, is

$$M = \frac{n}{n_0} = e^{\alpha r}. \tag{6.3}$$

As for non-uniform electric fields α is a function of the distance to the anode wire, one has to integrate α from the anode radius r_1 to the critical radius r_2, beyond which no gas multiplication occurs:

$$M = exp\left(\int_{r1}^{r2} \alpha(r)dr\right). \tag{6.4}$$

While the calculated results for M can get very large, the experimental breakdown limit, known as the Raether limit is reached at $M \approx 10^8$ or $\alpha r \approx 20$. Here, the detector shows a transition to the so-called Geiger-Müller mode shown in Figure 6.4, where the electron avalanche develops along the full wire or even spreads to neighbouring wires, so that the position information is lost.

For the calculation of $\alpha(r)$ different analytical ansatzes have been published. A review of the methods is given by Kowalski [Kow85] and Aoyama [Aoy84]. All of these ansatzes have in common that they deal with radial electric fields. As for MWPCs this would be only a first approximation, the gas gain has been simulated using the software package Garfield that will be introduced in Section 6.2.

6.1.2 Signal Generation and Readout

Electron multiplication will occur at distances of a few wire radii around the anode wire. The avalanche electrons will be extracted directly and the remaining ions will variate the field of the wire locally, generating a very short electrostatically induced pulse with a duration of the order of 10 ns. The major contribution to the signals measured in the MWPCs is the movement of the ions, that will start to drift towards the cathode as already indicated in Figure 6.3. The ion drift from the wire to the cathode plate will take $T_{\text{drift}}^{\text{ion}} \approx 10\,\mu$s in a MSPET detector.

Using a segmented cathode as shown in Figure 6.1, one can measure induced signals in these segments, called pads, depending on their distance to the avalanche. Since the ion drift and the following de-charging of the pads limit the count rate performance of the detector, a differentiation circuit can be used to separate the electron- from the ion-

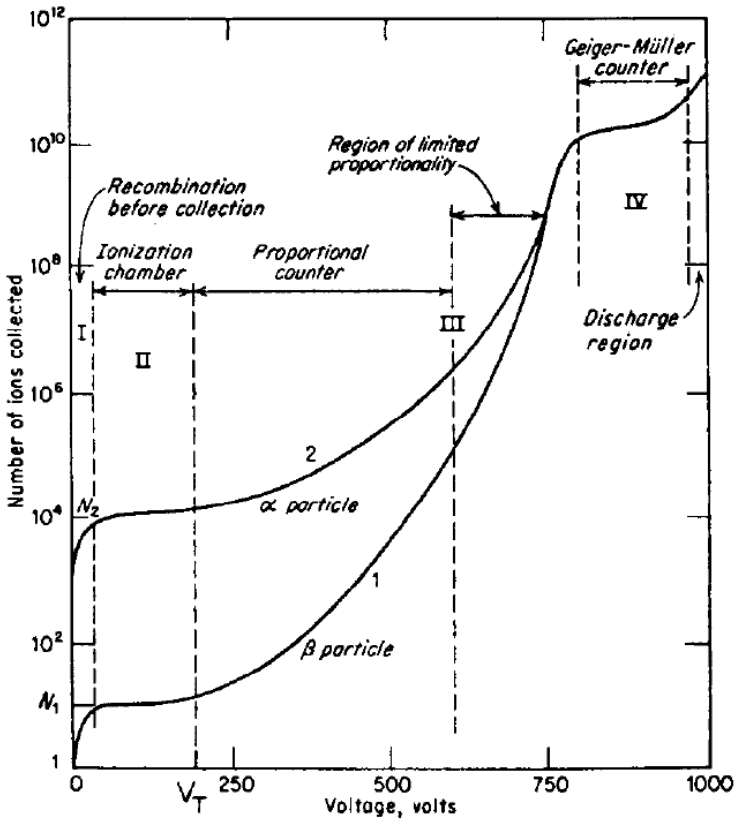

Figure 6.4: Gain-voltage characteristics for a proportional counter [Sau77].

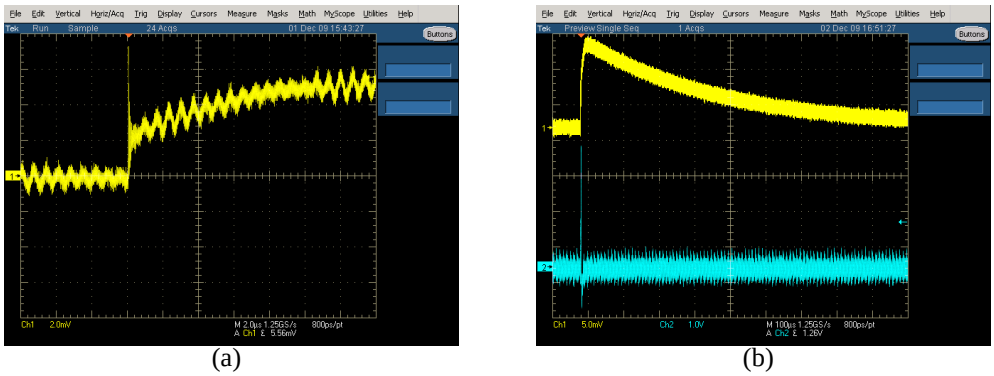

(a) (b)

Figure 6.5: Panel (a) shows a typical pad signal in an MSPET detector module (scale: 2 μs per division). The ion cloud around the wire creates a 10 ns short electrostatic induced pulse on the wire just before the ions start to drift towards the cathode planes. The blue line in (b) displays the output of a differential amplifier (scale: 100 μs per division). The long ion- and RC-decharge tail is here suppressed while the short ion cloud pulse remains.

contribution. A sample pulse and its differentiation, using the electronics described in Section 6.5.2, can be seen in Figure 6.5. Crosstalk between adjacent pads and wires can not be avoided and will lead to slightly increased noise or oscillation. The cathode charge distribution can be obtained semi-empirically by the expression of E. Gatti et. al. [Gat79] discussed by E. Mathieson [Mat88]:

$$\Gamma(\lambda) = 2K_1 \frac{1-\tanh^2 K_2\lambda}{1+K_3\tanh^2 K_2\lambda} \tag{6.5}$$

where $\lambda = x/h$ is the distance of the strip to the avalanche position with h being the anode-cathode separation. K_1 and K_2 depend on K_3 which itself depends on the wire's diameter, separation and the anode-cathode distance:

$$K_1 = \frac{K_2\sqrt{K_3}}{4\tan^{-1}\sqrt{K_3}} \tag{6.6}$$

$$K_2 = \frac{\pi}{2}\left(1-\frac{\sqrt{K_3}}{2}\right). \tag{6.7}$$

Figure 6.6 shows the charge distribution for an MSPET chamber with a wire separation of 1.5 mm, an anode-cathode separation of 1 mm and a wire diameter of 20 μm. The corresponding values for K_3 in parallel and perpendicular direction to the wire have been approximated with the K_3-dependency plots shown in [Mat88] as $K_3^{\parallel} = 0.56$ and $K_3^{\perp} = 0.74$. One can define the pad response function by integrating this charge distribution over the width w of the pad:

$$P(\lambda) = \int_{\lambda-\frac{w}{2}}^{\lambda+\frac{w}{2}} \Gamma(\lambda')d\lambda'. \tag{6.8}$$

A formulation based on K_1, K_2 and K_3 is given by W. Blum, W. Riegler and L. Rolandi [WB08] as

$$P(\lambda) = \frac{2K_1}{K_2\sqrt{K_3}}\left(\arctan\left(\sqrt{K_3}\tanh K_2(\lambda+\frac{w}{2})\right) - \arctan\left(\sqrt{K_3}\tanh K_2(\lambda-\frac{w}{2})\right)\right). \tag{6.9}$$

This function indicates the fraction of the charges induced in the pad as a function of the distance of the avalanche position to the centre of the pad. It is noted that w is here used in units of h. The appropriate pad response function for the MSPET detector with pad width of $w = 3$ mm is shown in Figure 6.7. Assuming a good agreement with a Gaussian, the pad response function can be expressed as [WB93]

$$P(x) = \frac{Q_i}{Q_{i-1}+Q_i+Q_{i+1}} = A\cdot e^{-\frac{y^2}{2\sigma^2}}. \tag{6.10}$$

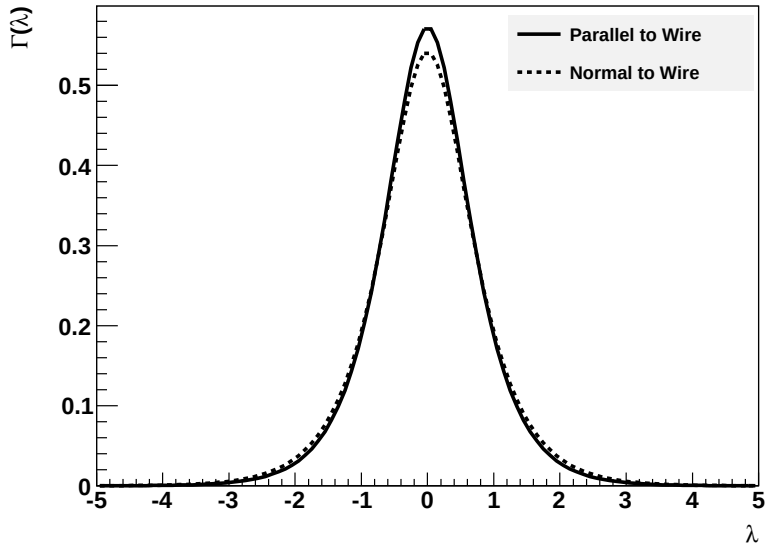

Figure 6.6: Cathode charge distribution for an MSPET chamber parallel and perpendicular to the wire direction with $\lambda = x/h$ and $h = 1\,\text{mm}$.

The charge fraction induced on three adjacent pads can be written as

$$\frac{Q_{i-1}}{Q_{i-1}+Q_i+Q_{i+1}} = A \cdot e^{-\frac{(x+W)^2}{2\sigma^2}} \tag{6.11}$$

$$\frac{Q_i}{Q_{i-1}+Q_i+Q_{i+1}} = A \cdot e^{-\frac{x^2}{2\sigma^2}} \tag{6.12}$$

$$\frac{Q_{i+1}}{Q_{i-1}+Q_i+Q_{i+1}} = A \cdot e^{-\frac{(x-W)^2}{2\sigma^2}}. \tag{6.13}$$

one can now use the relations

$$\frac{Q_i}{Q_{i-1}} = e^{\frac{2xW+W^2}{2\sigma^2}} \tag{6.14}$$

and

$$\frac{Q_{i+1}}{Q_i} = e^{\frac{2xW-W^2}{2\sigma^2}} \tag{6.15}$$

in order to define a weighted function that describes the distance x from the avalanche to the centre of the pad with the highest entry as:

$$x = \frac{1}{a_1+a_2}\left[a_1\left(\frac{W}{2}+\frac{\sigma^2}{W}\ln\left(\frac{Q_i}{Q_{i-1}}\right)\right)+a_2\left(\frac{W}{2}+\frac{\sigma^2}{W}\ln\left(\frac{Q_{i+1}}{Q_i}\right)\right)\right]. \tag{6.16}$$

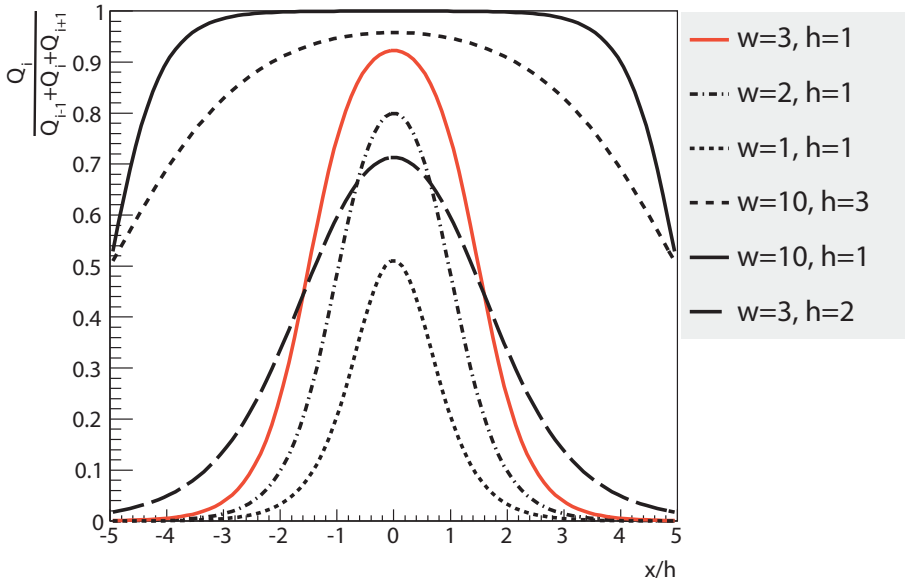

(a)

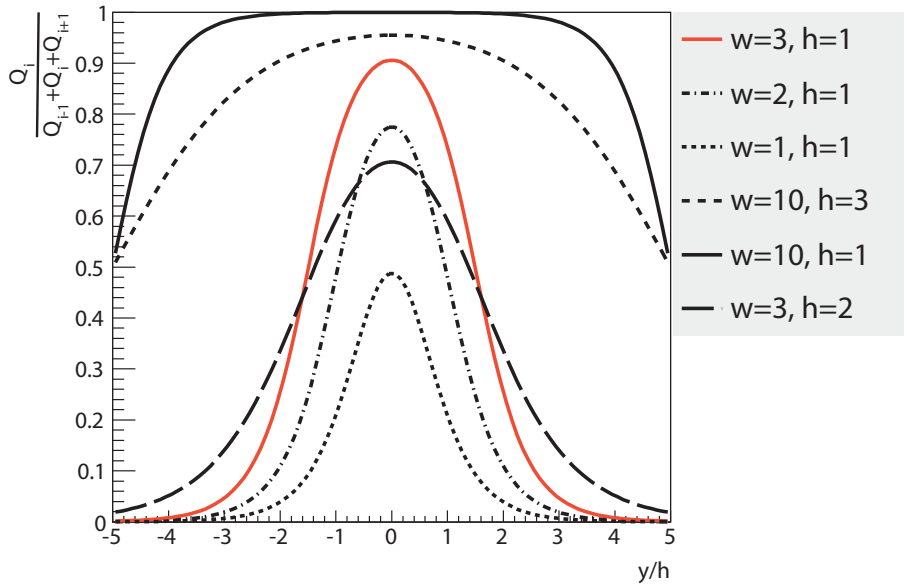

(b)

Figure 6.7: Calculated pad response function for different detector geometries. The wire separation is $s = 1.5\,\text{mm}$ in all cases except for $h = 3$ where it is $s = 2\,\text{mm}$ (these dimensions represent the very first dedicated PET wire chamber prototype build in Münster [HÖ7]). The current MSPET design is highlighted in red. Due to different values for K_3 one has to discriminate the direction with respect to the wire. So (a) shows the PRF in wire direction and (b) for the normal direction respectively. Differences are minor.

Here $a_1 = Q_{i-1}^2$ and $a_2 = Q_{i+1}^2$ are weighting factors which depend on the measured charge on the three single pads. Using this formula, the position resolution can be increased to about $1-2\,\%$ of the pad width. As will be shown later, it is not always easy to define a unique σ in measured data. Hence, to be independent from σ one can also use the ratios

$$\frac{Q_{i+1}}{Q_{i-1}} = e^{\frac{2xW}{\sigma^2}} \tag{6.17}$$

$$\text{and} \qquad \frac{Q_i^2}{Q_{i-1}Q_{i+1}} = e^{\frac{W^2}{\sigma^2}} \tag{6.18}$$

in order to obtain

$$x = \frac{W}{2} \frac{\ln\left(\frac{Q_{i+1}}{Q_{i-1}}\right)}{\ln\left(\frac{Q_i^2}{Q_{i+1}Q_{i-1}}\right)} \tag{6.19}$$

which does not contain any weighting factors. As a result, the position resolution here is expected to be worse than using (6.16), especially when having entries above the noise level on less than three adjacent pads.

6.2 Gas Gain Simulations

When developing a wire chamber, one always has to keep the interplay with the solid detector parts and the gaseous parts in mind. As the detector properties depend on the geometry and gas, tools are needed that account for both. The Garfield software was developed by R. Veenhof at CERN [Vee08]. It can simulate electric fields for user-defined detector geometries and allows to calculate detector properties (e.g. drift velocity, wire sag, electromagnetic and gravitational forces and others). It can also simulate pathways of charged particles in the calculated fields and particle multiplications. In order to do that, Garfield needs to know the gas properties. Therefore it can import files, generated by the programs Magboltz [Bia99] and Heed [Smi05]. While Magboltz computes electron transport properties in arbitrary gas-mixtures, Heed calculates the ionisation of the defined gas molecules by traversing particles. Figure 6.8 shows the gas gain simulation of an MSPET wire chamber. In these simulations a single electron is placed at twelve different equidistant positions at a radius of $400\,\mu$m around the wire. Since this is outside of the avalanche area, the full gain at a given wire can be obtained. Garfield then lets each of these electrons drift towards the wire and calculates the avalanche generation and the resulting secondary electrons. The mean value of secondary electrons generated by each of the twelve primaries is the resulting gas gain. This averaging is necessary due to the

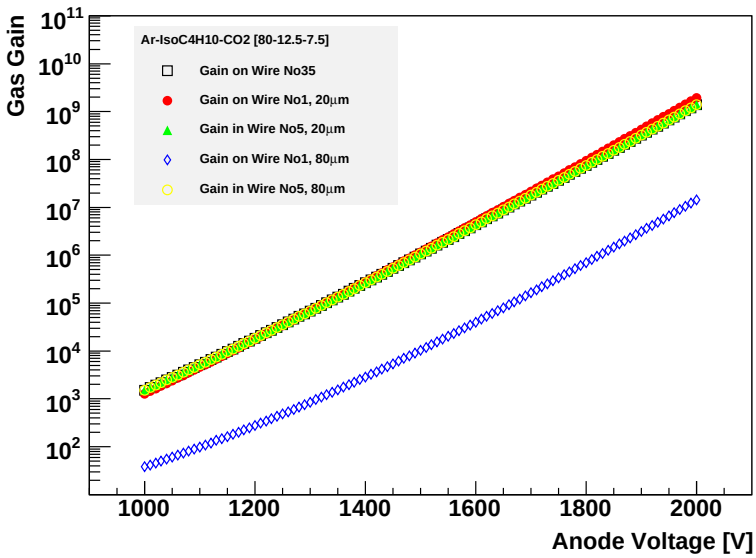

Figure 6.8: Garfield simulation of the gas gain on different wires in an MSPET detector module with an anode-cathode distance of 1 mm. The detector has a total of 74 wires. The gain and thus the electric field is homogeneous over the whole chamber. To avoid electric interactions with the detector walls and an enhanced wire sag, the first and the last wire are replaced with thicker ones to reduce the local electrical field.

different electric field configurations around the wire, caused by the adjacent wires and the cathode planes.
A reasonable gain for an operation in proportional mode of the order of $M = 10^4 - 10^6$ is reached at about $V_0 = 1400\,\mathrm{V}$ for an Argon-CO_2-isobutane $(80 - 12.5 - 7.5)$ gas mixture and a wire diameter of $20\,\mu\mathrm{m}$. The Raether limit is expected to be reached at $V_0 \approx 1800\,\mathrm{V}$. In good approximation, the electric field is homogeneous over the whole chamber, as the gain on different wires is constant. To reduce electrostatic inhomogeneities at the edges of the detector, the first wire is replaced by a thicker one. As can be seen in Figure 6.8, this reduces the obtained gas gain locally.

6.2.1 Specification of the Wire Gap and Diameter

According to F. Sauli [Sau77], the wire-to-wire distance of a MWPC should be normally three or four times smaller than the gap between pad- and wire-plane. Furthermore, he noticed that wire separations of less than 2 mm will in practice be hard to operate, especially for larger surfaces. Nevertheless P.A. Souder [SSD73] had shown previously that the wire gap can be reduced down to 0.5 mm if other relevant parameters like the wire diameter are reduced as well. He used a wire diameter of $5\,\mu\mathrm{m}$ and a gap of 2 mm between anode and cathode planes.
As the foreseen MSPET design has a wire-to-pad distance of just 1 mm, this would imply a very small sub-millimetre wire spacing and a wire diameter of below $2.5\,\mu\mathrm{m}$. Since this is neither practical to construct nor to build, some variations to the literature values had to be made:
The wire diameter is specified as $20\,\mu\mathrm{m}$ because this is the thinnest wire that can be streched, glued and soldered with reasonable effort.
For the specification of a practical wire gap, another Garfield simulation has been made. The gas gain as a measure of the electric field is plotted versus different wire gaps. An anode potential of 1400 V and an Ar-CO_2-isobutane $(80 - 7.5 - 12.5)$ gas mixture has been used. The results are shown in Figure 6.9. One can see that the gain rises with increasing wire separation. This means that adjacent wires become more and more independent of each other until there is no overlap of electric fields at all. As the largest separation with reasonable field properties of the wire plane a value of $s = 1.5\,\mathrm{mm}$ has been chosen for the wire separation.

6.2.2 Gain Variations due to Wire Sag

Due to repulsive electromagnetic forces between adjacent wires, sagging can be observed. In addition, especially in very large wire chambers, gravitational forces and, for chambers

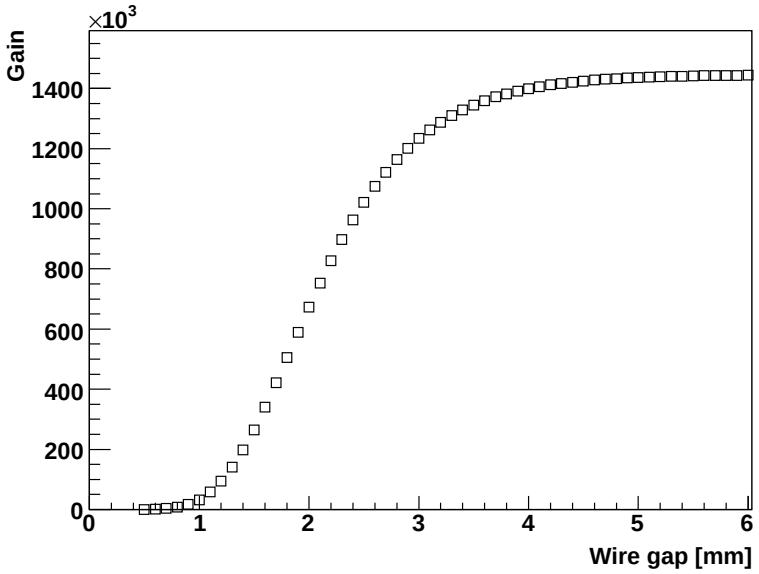

Figure 6.9: Simulation of the gas gain of a central wire under variation of the wire gap. With increasing gap the wires become more and more independent from each other. The gas used here is Ar-CO_2-Isobutane $(80-7.5-12.5)$.The electrostatic potential is 1400 V.

with multiple heterogeneous wire grids, wire frame deformation will cause wire sag. In the small MSPET wire chambers this is not an issue and can be neglected. As wire sag means a shift of the wire position into a certain direction, it will disturb the homogeneity of the electro-magnetic field. Therefore, it is important to control the extent of this sag and the resulting gain variations. Gravitational and electromagnetic forces and the resulting wire sag has again been calculated with Garfield. Figure 6.10 shows the results as a function of the applied anode voltage in x- and y- direction. It can be seen that a slight wire sag can be observed only in x-direction and only on the first wire, where the forces in the wire-grid do not compensate. It is also shown that the use of a thicker first wire further reduces the displacement of that wire down to negligible two wire diameters. The gain variation due to such a displacement is negligible as will be shown in the following section.

6.2.3 Gain Variations due to Wire Displacement

During the assembly of wire chambers it is important to work as precisely as possible. Most of all, an accurate wire gap regularity is an important factor. Variations influence the electric field and therefore the gain of the chamber. In addition, high local electric fields

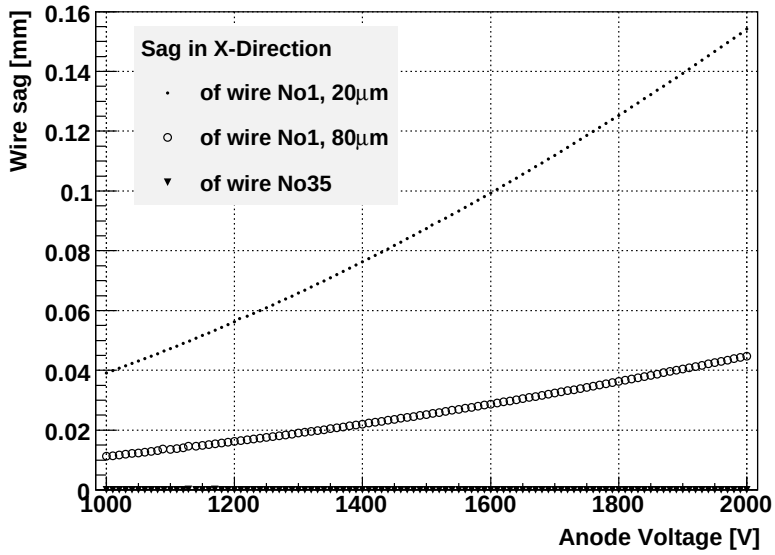

(a)

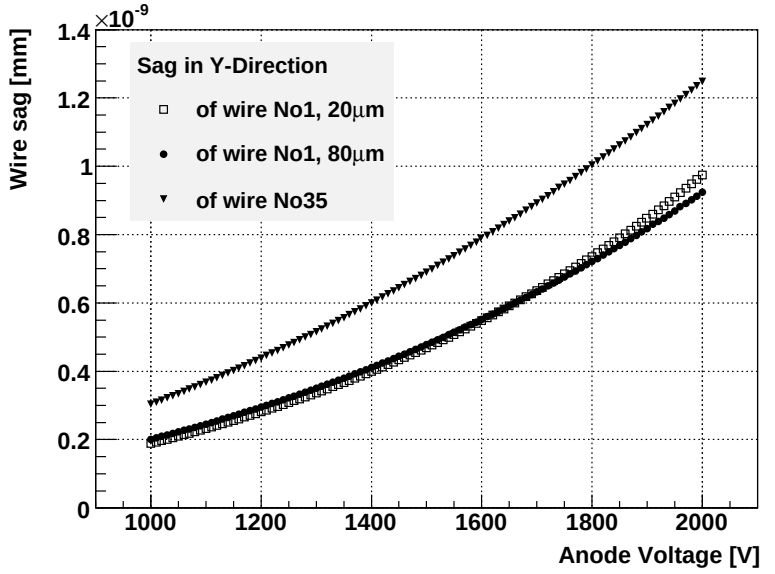

(b)

Figure 6.10: Wire sag in (a) wire-plane and (b) perpendicular direction due to electro-magnetic and gravitational forces. Due to the small dimension of the studied wire chamber the gravitational force has nearly no influence on the sag. Electromagnetic sag can be observed mainly on the first wire (labelled No1 in the Figure) and only in wire-plane(X)-direction. It can be reduced by the replacement of the first wire with a thicker one. Wire No35 indicates a central wire.

increase the potential of gas break-through and sparking which will limit the performance of the whole detector. Nevertheless, the wire placement accuracy is subject to mechanical restrictions. For example, as the whole wire grid is glued on top of the wire frame, there is an offset of one wire radius towards the upper cathode plane. In order to identify critical configurations and to set reasonable limits for wire gap variations, simulations have been performed. Figures 6.11 and 6.12 show the calculated gain variations on a wire shifted in plane direction and on its neighbouring wires. Figure 6.13 shows the influence of a single wire shifted 100 μm towards the pad planes. The influence of the displaced grid can be observed in Figure 6.14. In conclusion, one can bear slight variations in wire gaps up to the order of a few wire diameters. In particular a shift perpendicular to the wire grid direction seems to have minor influence on the gas gain and thus the chambers performance. The effect of an overall 10 μm displacement of the whole grid towards the pad plane has practically no influence on the detector performances.

6.3 Detector Design and Production

6.3.1 Design of the MSPET Chamber

The MSPET chamber in its latest version consists of two milled FR4 frames sandwiched between two combined pad plane/converters. One of the frames carries the wire grid while the other one ensures a constant distance to the pad plane.
The limiting element for the achievable position resolution is the converter itself. Since the conversion processes of annihilation photons to measurable electrons follows the angular distribution shown in Figure 4.1, the exact information of the incoming photon direction is lost. As a cross check for these measurement results, a Geant4 simulation has been performed to determine the angular distribution of the liberated electrons. Figure 6.15 shows the results of this simulation. The exit angle is plotted for a 50 μm lead converter and also for a converter equipped with a 30 μm layer of gold. In both cases the mean exit angle is compatible with 45°. Therefore, it is induced that for every millimetre the electron moves beyond the flat converter, it will be deflected 1 mm from its creation point. In order to reach the planned spatial resolution of the order of 1 mm the distance between converter and wire grid has to be not more than 1 mm.
According to this, both wire- and spacer frames are milled out of 1 mm thick FR4 sheets that are plated with copper. The construction drawings of wire and spacer frame are shown in Fig. A.2 and A.3 of the appendix. While the copper plating on the spacer frame is etched off completely, on the wire frame a copper pattern for the high voltage feeding of the wire grid is kept. The film for this pattern is shown in Figure A.6 of the appendix.
In order to allow for sufficient gas flow, with a diameter of 2 mm the thickest gas pipes

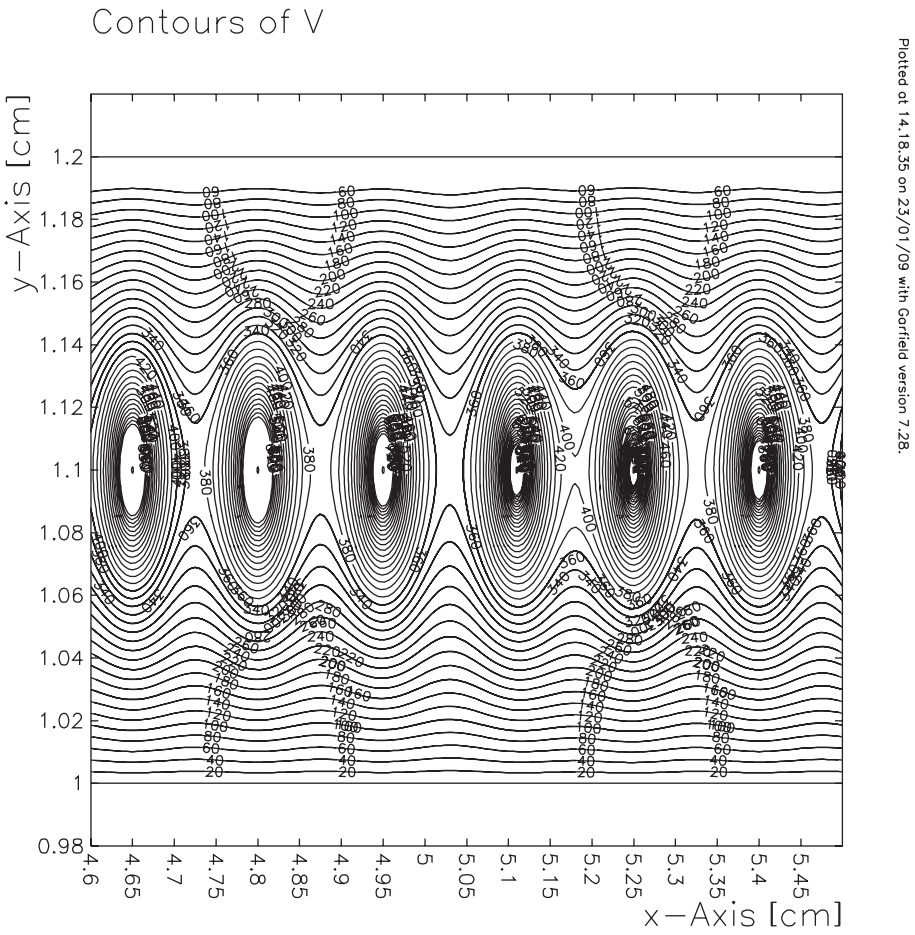

(a)

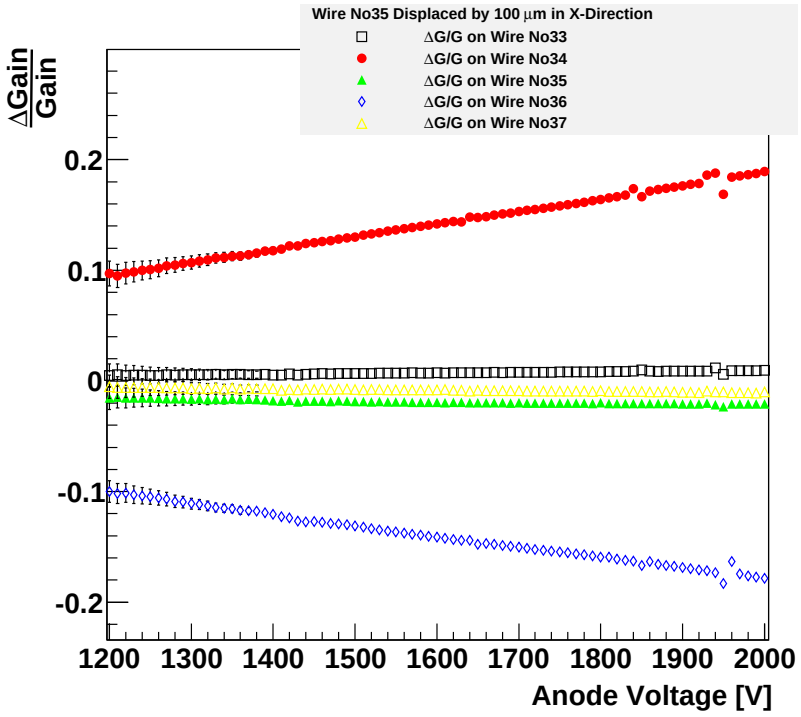

(b)

Figure 6.11: Distortions of the electric field (a) and resulting gain variations (b) due to a shift of wire number 35 by 100 μm in X-direction towards wire number 36.

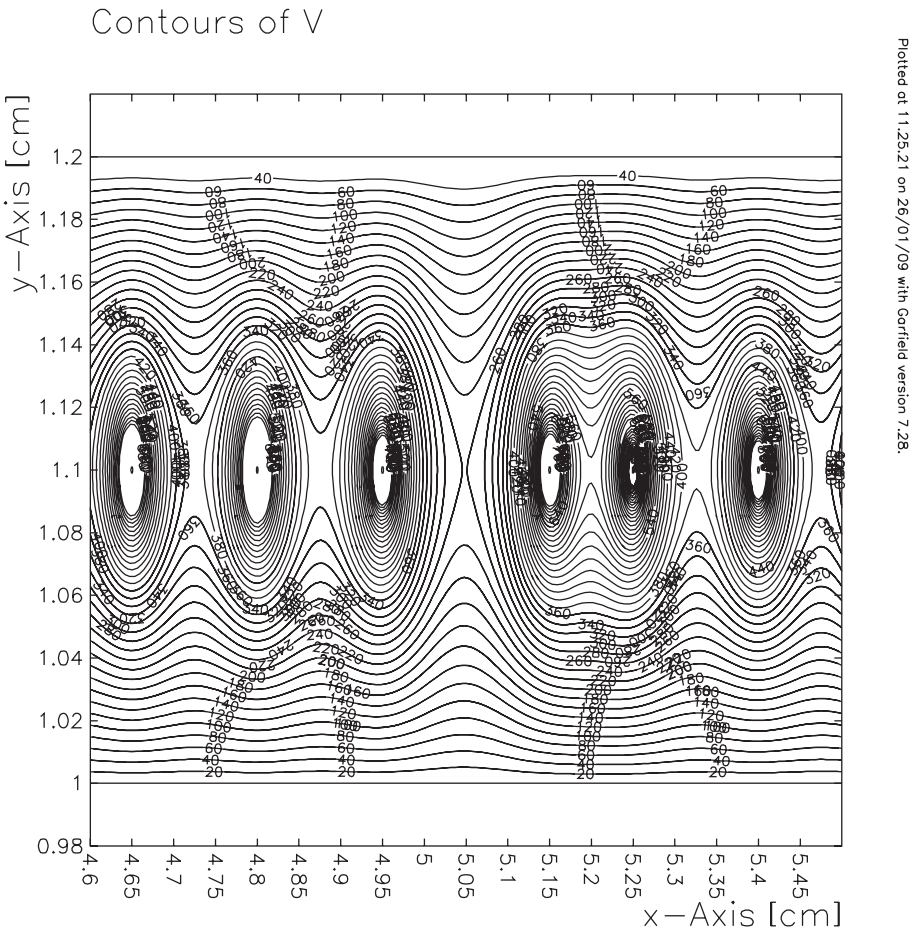

(a)

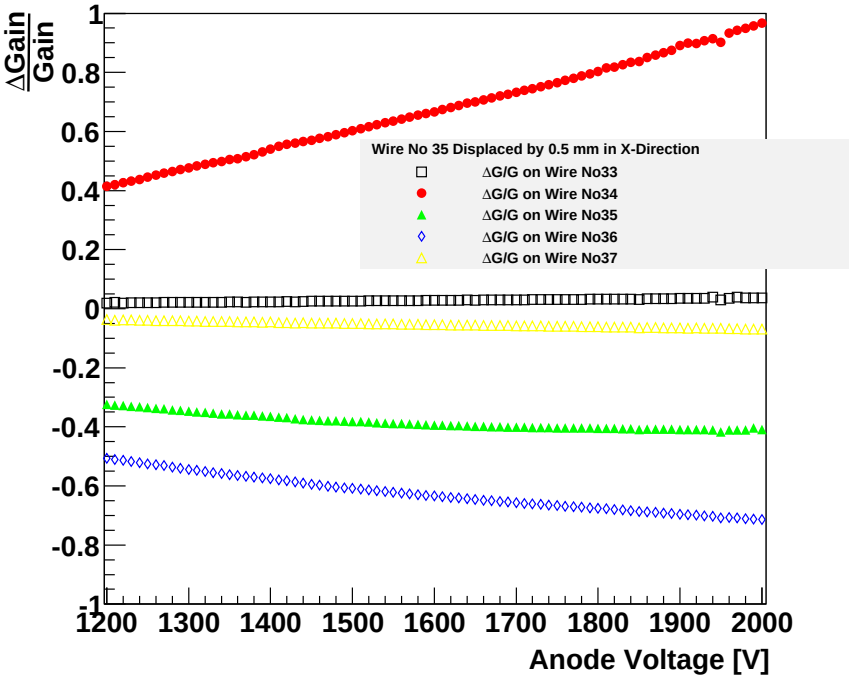

(b)

Figure 6.12: Distortions of the electric field (a) and resulting gain variations (b) due to a shift of wire number 35 by 500 μm in X-direction towards wire number 36.

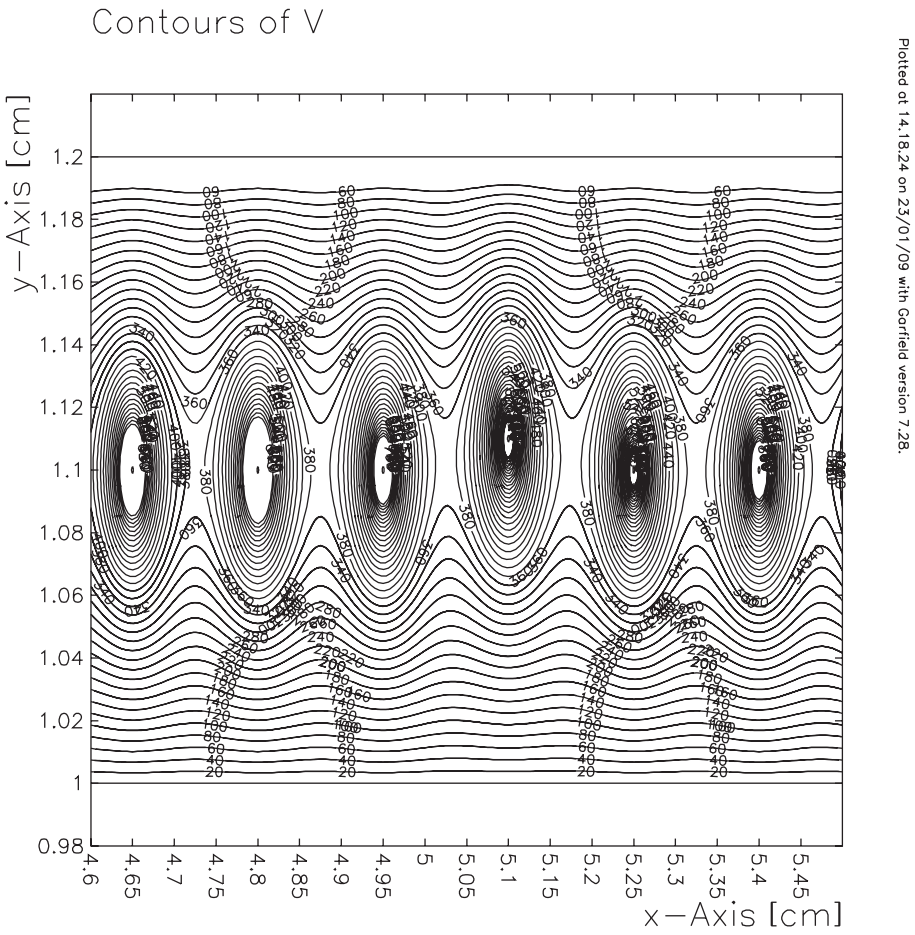

(a)

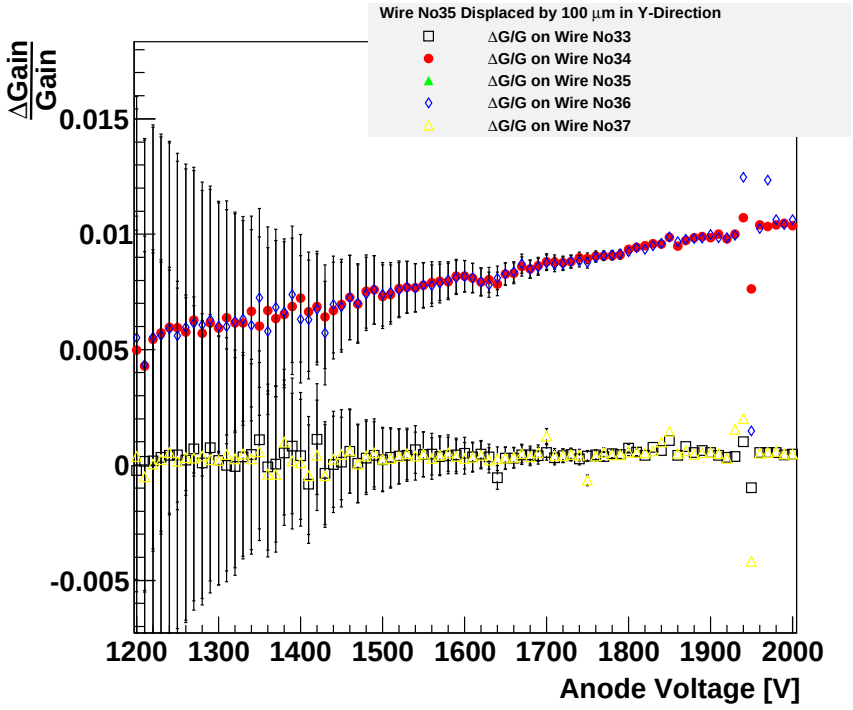

(b)

Figure 6.13: Distortions of the electric field (a) and resulting gain variations (b) due to a shift of wire number 35 by 100 μm in Y-direction.

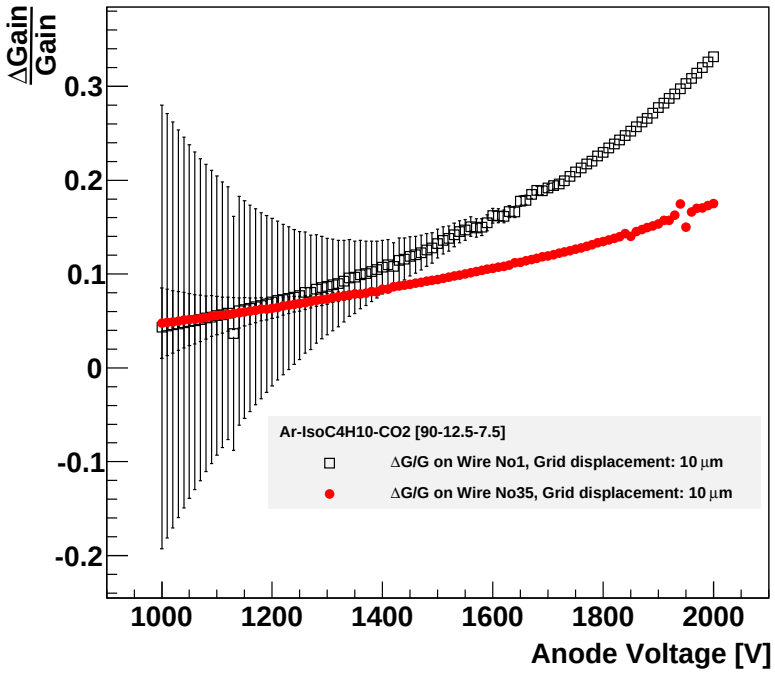

Figure 6.14: Effect of an overall 10 μm displacement of the whole wire grid has only minor influence on the gas gain performance of the MWPC.

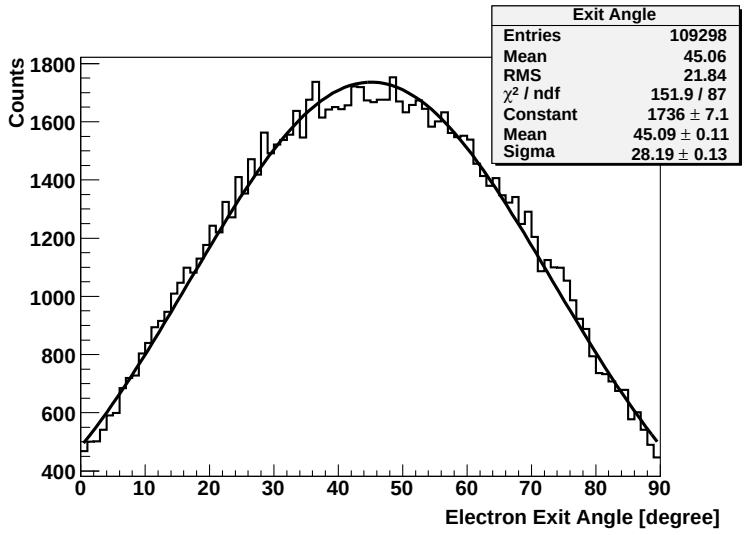

(a)

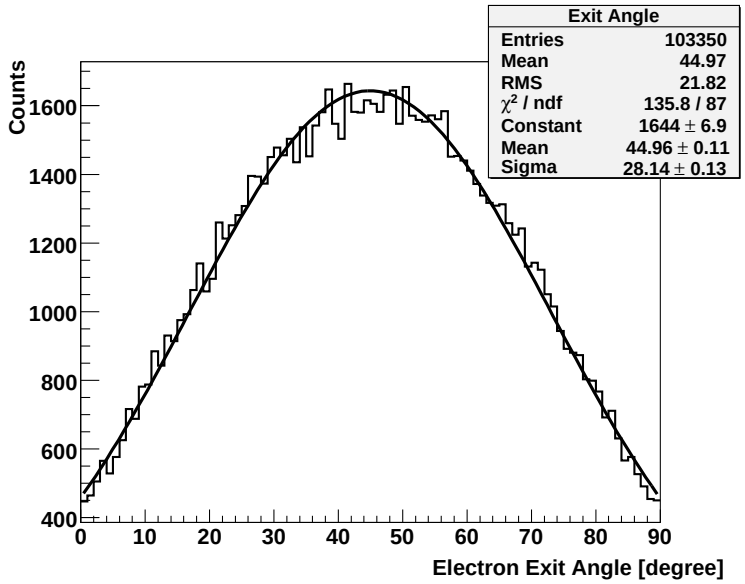

(b)

Figure 6.15: Simulation of the angle of the electrons leaving the converter. Panel (a) shows the results for a stack of 50 detectors with 50μm lead converters. Panel (b) shows the same setup for 30μm gold converters.

that are possible are used. To install these in the thin frames, half holes have been drilled into the wire frame and the spacer frame on both sides, acting as gas inlet and outlet. To reduce the gas stream pressure, the half holes end up in a triangular shaped cut-out. To ensure the stability of the frame this cut-out is only on one of the two stacked frames. The counterpart has a rectangular cut-out into which the gas coming from the triangle cut-out escapes and finally reaches the MWPC. A close-up illustration of the gas channel is shown in Figures A.2 and A.3.

To keep the absorption loss in the active volume of the detector small, the pad planes are made of 0.5 mm thin FR4 sheets. Especially when stacking multiple chambers, a thin entrance window is essential for good detection efficiency and low radiation losses. FR4 was implemented in the simulations as a compound material containing 47.2 % epoxy (C_2H_2) and 52.8 % quartz (SiO_2). The radiation length of a material is defined as the distance over which a high energy electron's energy drops to $1/e$ of its initial value due to bremsstrahlung. Alternatively it is $7/9$ of the mean free path length of a high energy photon undergoing pair production. It can be approximated following [Tsa74] as

$$X_0 = \frac{716.4 \cdot A}{Z(Z+1)\ln(\frac{287}{\sqrt{Z}})}[\frac{\mathrm{g}}{\mathrm{cm}^2}]. \tag{6.20}$$

The weighted radiation length of FR4 is thus $X_0 = 39.67\,\frac{\mathrm{g}}{\mathrm{cm}^2}$ or $X_0[mm] = 213.3\,\mathrm{mm}$ taking the FR4 density to be $1.86\,\frac{\mathrm{g}}{\mathrm{cm}^3}$. Thus for a single layer of FR4 with a thickness of 0.5 mm the attenuation for a stack of 50 modules is

$$\left(\frac{X}{X_0}\right)_{n=1} = 0.234\,\% \quad \text{and} \qquad \left(\frac{X}{X_0}\right)_{n=50} = 11.7\,\%,$$

respectively. For verification of these considerations a Geant4 simulation has been performed. Figure 6.16 displays the result of a simulation of two stacks of 50 MSPET detectors each with different FR4 thicknesses. The results have been normalised to the efficiency obtained with a converter with an infinitesimally small thickness of 0.0001 mm. A coincidence count rate loss of approximately 20 % is observed using 0.5 mm thick FR4 pad carrier material.

The chamber has outer dimensions of $200 \times 200\,\mathrm{mm}^2$. The MWPC gas volume measures $100 \times 100 \times 2\,\mathrm{mm}^3$. To avoid problems resulting from interactions of the electric field of the wires with the edges of the FR4 frame, the wire plane does not cover the whole chamber, but a fiducial area of $88.5 \times 88.5\,\mathrm{mm}^2$.

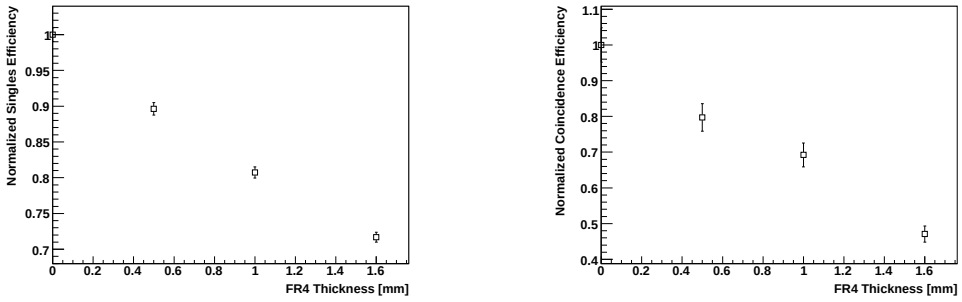

(a) (b)

Figure 6.16: Results of an MSPET count rate simulation using Geant4 showing the efficiency loss for different thicknesses of FR4 as carrier material for the pad plane. The results have been normalised to the efficiency obtained with a converter with an infinitesimally small thickness of 0.0001 mm. For each data point 100000 positrons have been simulated.

6.3.2 Combined Pad-Plane/Converter Design

For the small animal PET detector a position resolution slightly below 1 mm is desirable. To reach this value, the dimension of the pads has to be chosen accordingly. Two pad-planes are arranged perpendicular to each other on both sides of the wire frame. The pads themselves have to fulfil two conflicting demands: sub-millimetre resolution as well as a small number of readout channels. In addition, a simple design is favoured to keep electronics and reconstruction modalities simple.
The easiest approach is to use rectangular pads, since in this case the readout and position reconstruction follows simple mathematics. As a first ansatz a uniform continuous distribution can be used to describe electron events on rectangular pads. The probability density function of an electron to hit a pad of width w at a position x is given by

$$p(x) = \begin{cases} 0 & x < 0 \\ \frac{1}{w} & 0 \leq x \leq w \\ 0 & x > w \quad . \end{cases} \tag{6.21}$$

The expected value for a random position distributed uniformly on this pad is then

$$E(p) = \frac{1}{w}\int_0^w x dx \tag{6.22}$$

$$= \frac{w}{2}. \tag{6.23}$$

The variance is defined as

$$\begin{aligned} V(p) &= E(p^2) - (E(p))^2 && (6.24)\\ &= \frac{1}{w}\int_0^w x^2 dx - \left(\frac{w}{2}\right)^2 && (6.25)\\ &= \frac{1}{3}w^2 - \frac{w^2}{4} && (6.26)\\ &= \frac{w^2}{12}, && (6.27) \end{aligned}$$

resulting in a standard deviation of

$$\sigma = \sqrt{V(p)} = \frac{w}{\sqrt{12}}. \quad (6.28)$$

These considerations have led to a simple strip design with 30 pads, each 3 mm wide with a gap of 0.1 mm. With such pads, a position accuracy of $\frac{3\,\mathrm{mm}}{\sqrt{12}} = 0.866\,\mathrm{mm}$ can be reached without any additional knowledge but the pad number with the largest charge deposit.
As already described in Section 6.1.2 the resolution can be further improved to a few percent of the pad width exploiting the known pad response function. Figure 6.7 shows the pad response function amongst others for the final MSPET geometry with $w = 3\,\mathrm{mm}$ and $h = 1\,\mathrm{mm}$. The signal here is expected to be distributed on two to three pads, which is advantageous for the position reconstruction, that accounts for three pad events (Eq. (6.16)). Following Figure 6.7 smaller pads of 2 mm width could further improve the charge distribution, but go hand in hand with an increased number of read out channels, which has to be avoided, especially bearing in mind that the predicted resolution with 3 mm pads is already sufficient for the foreseen application.
Not only the width of the pads, but also the material needs careful consideration as it acts as photon-to-electron converter for the annihilation radiation of the positrons. Since the dominant conversion processes, the photoelectric- and the Compton effect show a strong Z-dependence (see Eq. (3.14) and (3.16)), materials like tungsten ($Z = 74$), gold ($Z = 79$) or lead ($Z = 82$) are favoured. The idea is to use a standard etched copper pad structure onto which one of the mentioned materials is applied. Since tungsten is very hard to treat and also quite expensive, it turned out to be rather inappropriate. Nevertheless it has an even surface and can be purchased in thin plates. Lead has the benefit, that it is comparably cheap and has also the highest atomic number of the three. Using a lead alloy with small fractions of antimony in it, the lead will become less soft and also loose its tendency to oxidise. The disadvantage is its toxicity and the challenging machining. Gold on the other hand is non-toxic and can be electroplated.
The thickness of the converter now has to be sufficiently large to create a reasonable num-

ber of electrons, but also thin enough to let these electrons escape into the MWPC, where they can be detected. In order to optimise the converter thickness for gold and lead, a Geant4 simulation has been performed. Four stacks containing 50 MSPET detectors each have been irradiated with a ^{18}F point source (diameter: 1 mm). The detection efficiencies for single hits and coincidences have been analysed and are shown in Figure 6.17. The results indicate an optimal thickness of about 40 μm for lead and about 30 μm for gold. The use of a converter on both sides of the MWPC will increase the coincidence efficiency by just 20 % in case of a gold converter and 40 % in case of a lead converter. But using such a double converter will also increase the demands on the homogeneity of the converter-thickness $\Delta_{\text{thick.}} < 10\,\mu$m as the efficiency drops quickly to values even below that for a single sided converter. These considerations in addition to the doubled material costs suggest the use of a single sided converter.
The realisation of the demands that have been obtained by the simulation have shown to be challenging. Especially electroplating of lead has shown to be difficult, because the surface grows quite craggy, since this technique is usually used to metallise thin coatings (<5 μm) and small areas. In Germany, only a single company could be found that is able to electroplate lead[1], which is not a standard request. Attempts to electroplate lead at the Institut für Kernphysik failed quickly because of uncontrolled growth of the lead and missing adhesion on the copper surface. After these experiences, the only reasonable way to obtain a clean lead surface on the pads could be to use pre-machined lead sheets that are glued onto the pad planes and cut according to the pad width afterwards.
Gold on the other hand is not toxic and in principle easy to handle. Electroplating is also possible but loses accuracy with increasing coating thickness. The costs should not be neglected as well when using gold. Nevertheless one pad-plane was electroplated with gold[2]. Unfortunately the thickness of this plating varies between 30 μm and 120 μm, measured at different positions on the same pad plane, which is far outside of the tolerances (see Figure 6.17).

Number of Detector Modules per Stack

In the previous section the expected detection efficiency performance was discussed. For a competitive design, it was proposed to install 50 MSPET modules in each stack. Geant4 simulations have been evaluated in order to study the influence of the number of modules on the single photon detection efficiency. Figure 6.18 shows the results of these efforts. To reach half of the efficiency of a 50 module device only 17 detectors are necessary. Therefore one has to find a trade off between the efficiency needs and production costs.

[1] The company OTR Oberflächentechnik GmbH, Rathenow, Germany was able to provide electroplating of lead.

[2] The electroplating of gold was done by the company Drollinger GmbH, Birkenfeld, Germany.

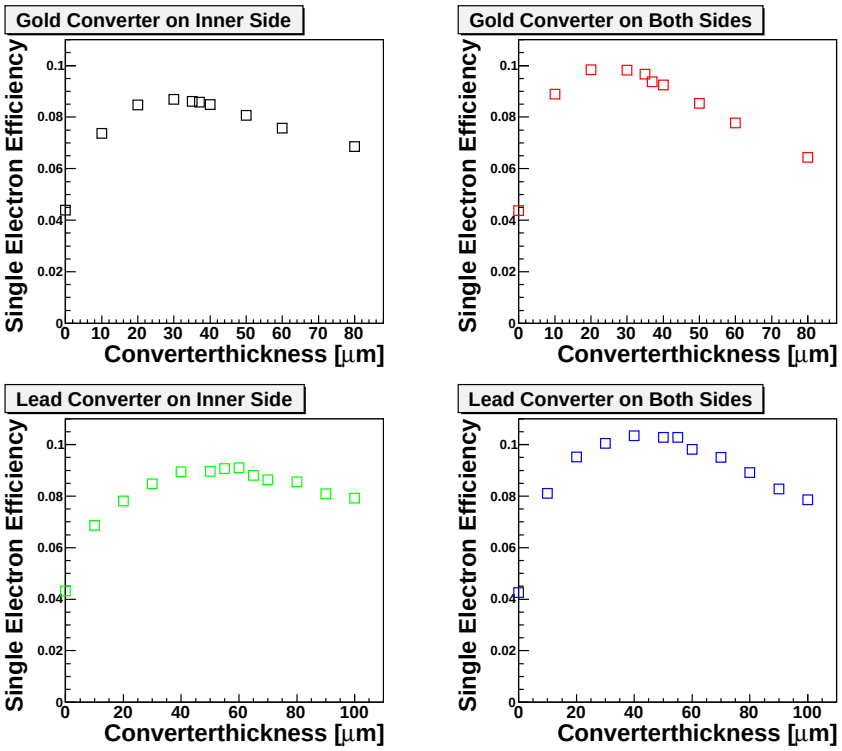

(a)

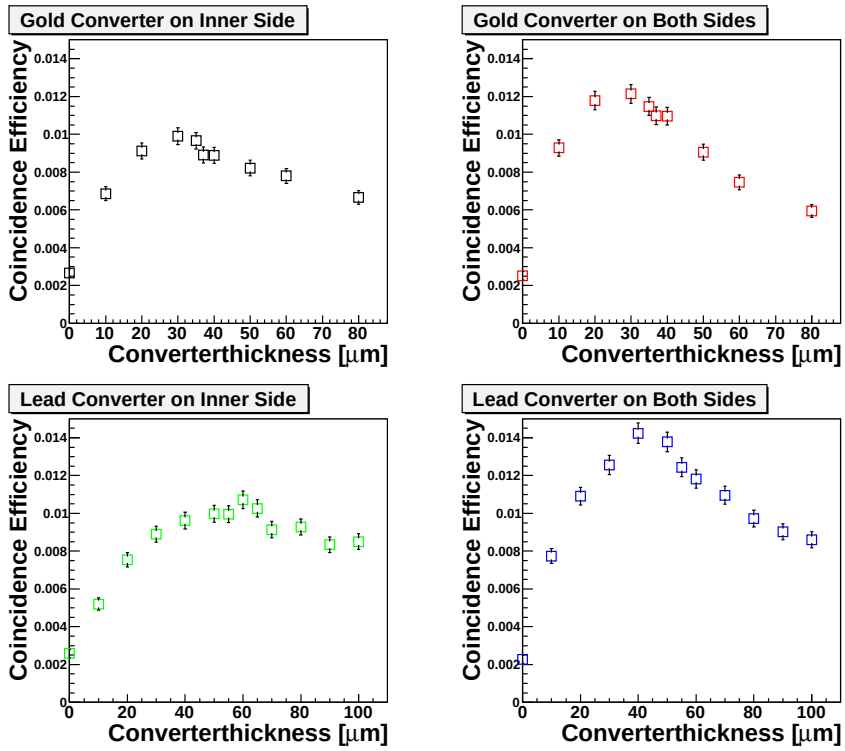

(b)

Figure 6.17: Simulated singles (a) and coincidence (b) efficiencies for different converter foil thicknesses for lead and gold. Four detector modules with 50 layers each have been simulated. The layers have been adapted to the angular coverage of the quadHIDAC by combining five layers to a block and changing the sizes of these blocks with respect to the angular coverage. Each layer is equipped with the supportive 0.5 mm FR4 plates. For each data point 100000 positrons have been simulated.

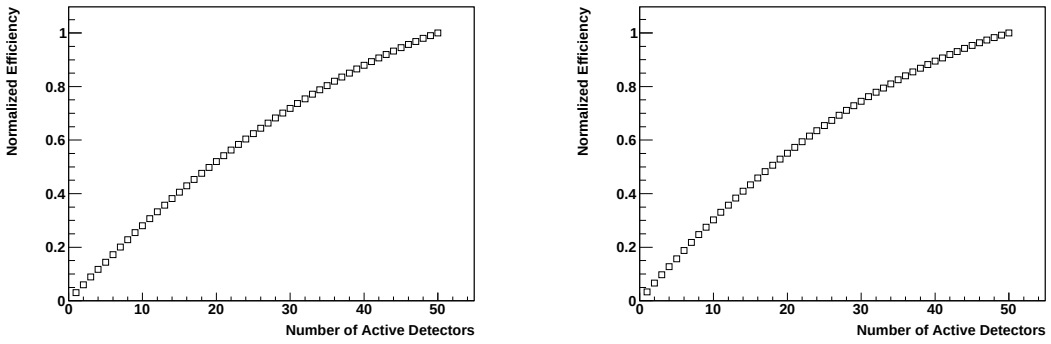

(a) (b)

Figure 6.18: Normalised photon detection efficiency as a function of the number of detector modules per stack. Subfigure (a) displays the results of a Geant4 simulation for a single sided 30 μm gold converter. Subfigure (b) the appropriate results for a 40 μm lead converter attached on both sides of the MWPC.

Looking at the slope of the curve and the results of scatter fraction simulations, shown in Figure 7.27, 30 – 50 modules per stack seems to be reasonable.

Rejected Construction approaches

Prior to the final version of the MSPET chamber several alternative approaches have shown to be problematic or not practicable.

- Thin 25 μm kapton foil metallized with thin copper, pads etched followed by converter sheet of tungsten or lead. Problem: stretching and glueing of kapton foil to chamber frame. A bagging of the foil is observed. Also the metallization of the foils is very tricky, especially when aiming for a homogeneous plating. Etching of pad structures in the thin metal layer quickly provokes cracks and irregular structures that result in a large rejection quantity.

- Sealing of the chamber with Teflon tape: uncontrollable gas leakage, Teflon tape hard to handle

- Electroplating pads with lead or lead alloy: Hard to find a company in Germany that can do it. Lead grows quite uncontrollable on the pads resulting in a very rough surface and interconnected pads.

6.3.3 Wire Grid Winding

As already discussed in Section 6.2.3, the electric field and therefore the gas gain depends strongly on the position of the wires. Hence, to avoid gain fluctuations, the wires have to be placed as equidistant as possible. Furthermore the tension of each wire should be strong enough to withstand mechanical and electrostatic forces leading to wire sag. As the used gold plated tungsten wires have a diameter of only $20\,\mu$m, each wire has to be handled with special care. The tensile strength of these wires is reached at a force of $0.8\,$N. To fulfil the demands, the winding machine shown in Figure 6.19 has been constructed. An overview sketch is also given in Figure A.8 of the appendix. It consists

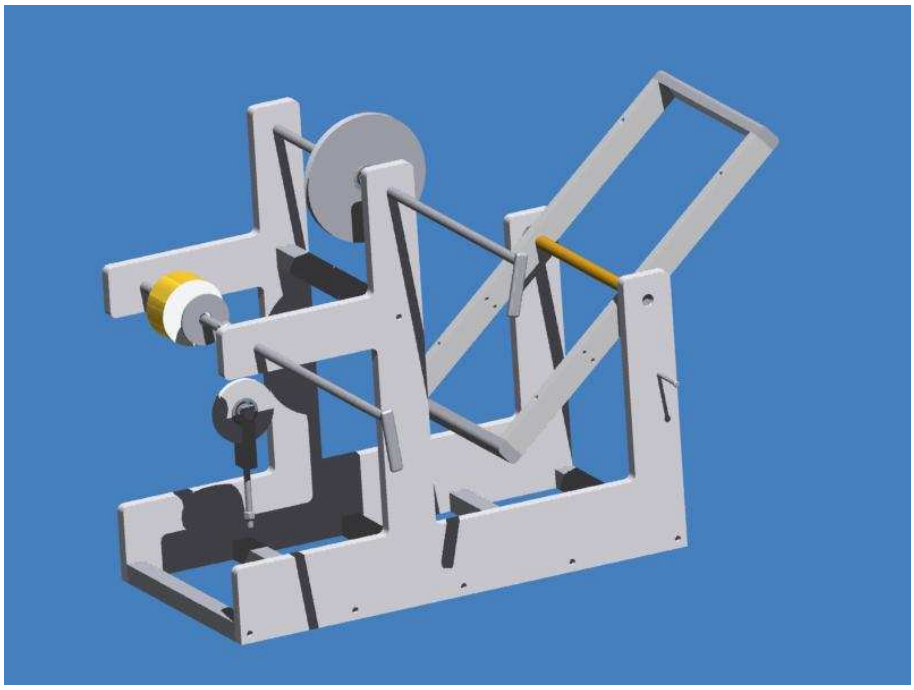

Figure 6.19: A sketch of the wire winding machine build for the MSPET device.

of two threaded rods, one carrying the wire coil and the other one acting as positioning unit using a mounted deflexion pulley. The lose end of the wire is now glued onto the bifid winding frame. In between the two threaded rods a $119.4\,$g load hangs at a second deflexion pulls in the wire putting it to a tension of $0.5\,$N after friction losses.
The wire grid can now be machined by letting the weight down as far as possible by unrolling the wire coil and then pulling it up again by turning the wire frame carefully. The deflexion pulley has to be moved when the wire is on the short side of the winding frame so that the displacement is not transmitted onto the wire grid. After winding and glueing the wires to the winding frame, the first and the last wire of a grid is replaced by

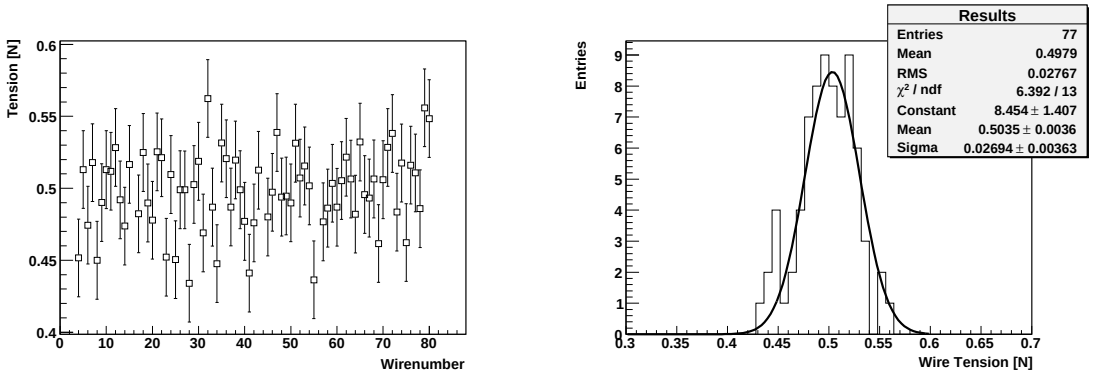

(a) (b)

Figure 6.20: Wire tension measured on a winding frame before attaching the wires to the detector frame. The tension measurement accuracy of the wire test device was determined as $\delta T = \pm 0.027\,\mathrm{N}$ [Got05].

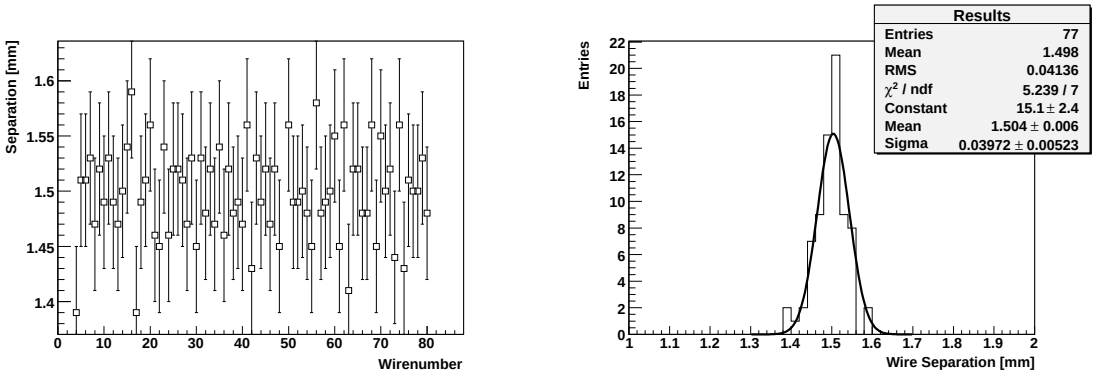

(a) (b)

Figure 6.21: Wire separation measured on a winding frame before attaching the wires to the detector frame. The position measurement accuracy of the wire test device was determined as $\delta x = \pm 0.060\,\mathrm{mm}$ [Got05].

hand with a 80 μm thick copper-beryllium wire. For this the double frame is separated first, so that one gets two wire grids. The old first and last gold wire of the grid is marked with a pen and then cut out with a scalpel. Then the a weight of approximately 120 g is knotted at each end of the new copper wire. It is then placed on the marked spots and aligned between the neighbouring wires manually. Afterwards the new wire is fixed with some epoxy glue in the frame.
After the glue has cured, the tension and separation of the wires are controlled using the wire test device developed in [Got05]. The result of such a measurement is presented in Figures 6.20 and 6.21. With $\sigma_T = 0.027$ N for the tension and $\sigma_x = 40\,\mu$m for the wire gaps it could be shown that the constructed winding machine is well suited for our purposes.
After the quality control, the wire grid has to be transfered onto the FR4 wire frame of the detector. Therefore, the foreseen positions of the first and the last wire are marked on the FR4 surface with a scratching tool. Then the winding frame is placed carefully onto the wire frame, so that the thick copper wires match with the scored marks. To prevent the winding frame to slip, it is weighted by narrow metal plates so that it is still possible to access the glueing areas on the wire frame. The glue (we use here the Araldite AW 106 binder with the Araldite Hardener HV 953 U) is applied with a special gun that has a thin duct, so that the liquid glue is dispensed with a controlled flow. After the glue has cured the wires are soldered and the excess wires still attached to the winding frame can be cut off.

Assembly of the Detector Modules

The assembly of the detector modules has to be done carefully. Especially dust and pollution inside the gas volume and on the wires has to be avoided as much as possible to reduce chamber conditioning times and high voltage breakthrough spots. The surface of the pad planes are polished with very finespun steel-wool and cleaned with acetone afterwards. The wires are cleaned from dust particles using canned air. As the sealing of the chamber is done with epoxy resin glue, the adherent surfaces have to be roughened with sandpaper. As an option to reduce conditioning times of the chambers, all components can be cleaned in an ultra-sonic bath.
After preparing the detector parts as described, in a first step, the wire frame and the distance frame are glued together (we used here the same glue that was used for the wire grids). Glue is applied onto only one of the two frames, preferable on the spacer frame, because here wires cannot be damaged accidentally. It is important that the layer of glue is as thin as possible. Also the glue streak has to be closed, so that gas tightness is assured. The areas around the gas inlet and outlets have to be treated with special care to prevent the gas channels from intrusion by glue. 2 mm metal bolts are inserted to keep

the in- and outlet open. Dowel pins in both corners of the two frames keep them aligned when pressing them together. In order to obtain a uniform pressure on the frames when hardening, a metal plate which is weighted by approximately 3 kg is placed on top of the frames.
After the glue is cured, the pad planes have to be glued to both sides of the wire planes in the same way. Afterwards a simple underpressure test is done to check for gas leaks. A water column is drawn up in a clear hose attached to the gas inlet using a syringe connected to the gas outlet of the chamber. The column should not fall within some hours provided the air pressure stays constant.

6.4 Gas Mixtures for the MSPET Device

6.4.1 Basics about Proportional Counter Gases

The detection of particles in MWPCs is based on the ionisation of gas molecules. To keep the number of energy dissipation modes as small as possible, mono-atomic noble gases are used as the main component of counter gases. Frequently used noble gases are argon or xenon. Xenon is far more expensive than argon, but offers twice as many ionisation encounters per unit length as argon [Par98]. During the avalanche generation close to the wire, not only electrons are produced, but also photons. Depending on their wavelength these photons are able to ionise further gas molecules outside of the avalanchs extend. Therefore the avalanche will be amplified so that the counter may break down. In detail, this will occur, when [WB08]:

$$n_{ph} q > 1. \tag{6.29}$$

That means that the number of photons n_{ph} produced in the avalanche multiplied with the probability q that a photon ionises the gas outside the avalanche area has to be smaller than 1. To avoid a break down, small amounts of so-called quench gases are added to the main component of the gas. Quench gases are long-chained organic molecules with many degrees of freedom. The photon's energy will therefore most likely excite one of these degrees of freedom rather than ionise the molecule and thus avoid the unwanted process. The choice of a proper quencher is essential, since it has to be sensitive to the wavelength of the UV-photons created in the primary gas and the surface material of the detector itself. Therefore the gain and also the breakdown voltage changes under variation of the quencher. Figure 6.22 represents a Garfield gas gain simulation for different gas compositions. More details on wire chamber gases can be found in [Sau77], [Zar89] and [Va'92].

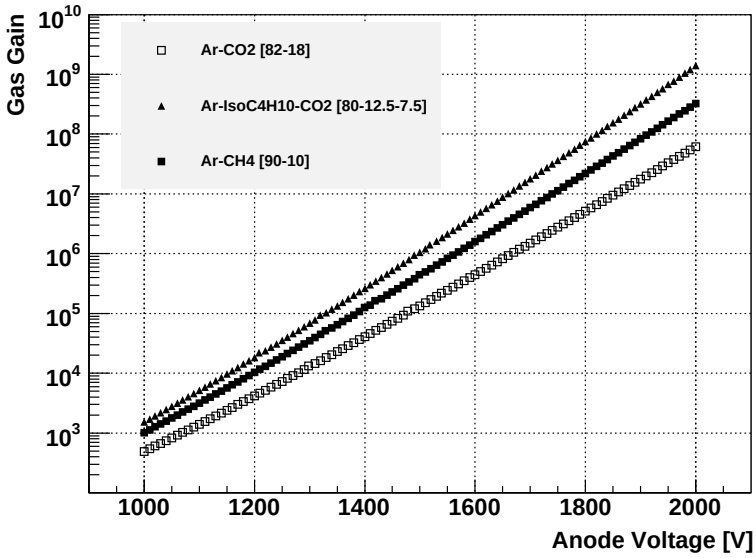

Figure 6.22: Garfield simulation of the gas gain under variation of the gas mixture. The chosen geometry is the proposed MSPET design with a wire separation of 1.5 mm and an anode-cathode gap of 1 mm.

6.4.2 The Penning Effect

Gain measurements and simulations are not easy to compare. In gas mixtures with amounts of gases with a lower ionisation potential than the excitation energies of the principal gas, the gas properties are affected by the so called Penning effect. Also for Ar-isoC$_4$H$_{10}$-CO$_2$ and Ar-CO$_2$ this can be observed. The argon D-states have a mean excitation energy of 14.0 eV which is above the ionisation potentials of isobutane (10.67 eV) and CO$_2$ (13.773 eV). Also the argon S- and P-levels mean excitation energies are with 11.55 eV and 13 eV above the ionisation energy of C$_4$H$_{10}$ so that the following processes can occur:

$$Ar^* + CO_2 \rightarrow Ar + CO_2^+ + e^-, \tag{6.30}$$

$$Ar^* + isoC_4H_{10} \rightarrow Ar + isoC_4H_{10}^+ + e^-. \tag{6.31}$$

Especially for argon based gases with isobutane additions strong Penning effects and therefore an increased gas multiplication factor has to be expected. As a side effect, this increases the energy resolution by decreasing the relative fluctuation in the number of electrons created by the incident radiation, which can liberate more ions per energy unit in a Penning gas. Since the energy transfer rate is not known, it has to be tuned to adequately measured data. The Penning transfer fraction is unique for each gas mixture

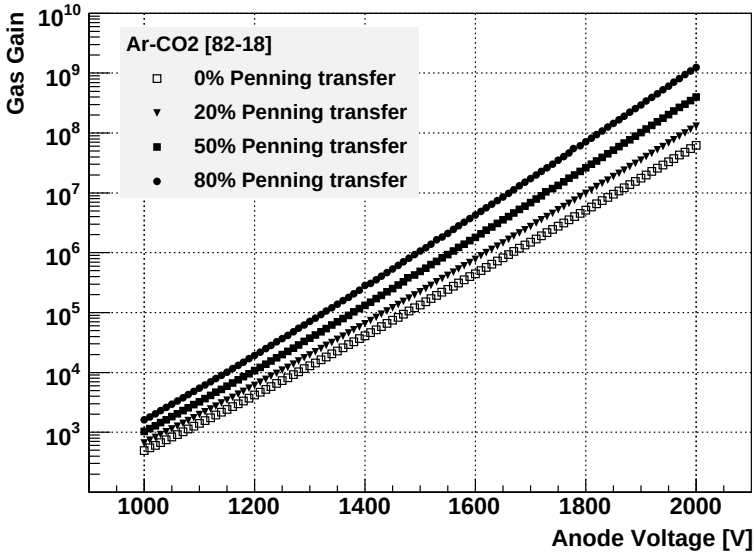

(a)

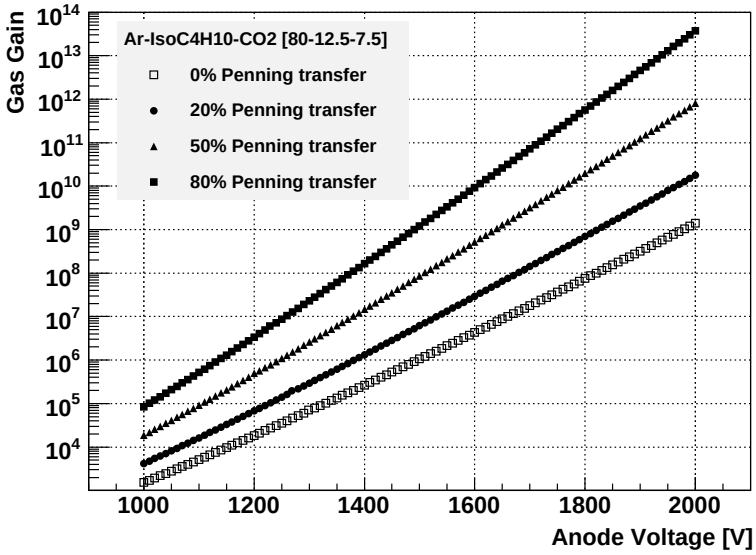

(b)

Figure 6.23: Garfield simulation showing the influence of the Penning effect on the gas gain. The transfer fraction indicates the fraction of exited principle gas states that will liberate additional electrons. Especially for mixtures containing isobutane strong effects are expected. Because of this and the unknown Penning transfer fraction, simulated and measured data can not be easily compared.

and not dependent on the electric field applied. To limit influences of the Penning effect, small concentrations of N_2 can be added to the counting gas [ABBM$^+$04]. Figure 6.23 shows gain variances caused by the Penning effect for different transfer rates in Ar-CO_2 and Ar-isoC$_4$H$_{10}$-CO_2 mixtures simulated with Garfield. As indicated, the gain can be increased by a few orders of magnitude depending on the relative concentration in the gas mixture.

6.4.3 Optimisation of Gas Mixture

As already mentioned above, the choice of a proper gas mixture is essential for the detector performance as it has major influence on ionisation potentials, drift velocity, break down limits, and avalanche formation. In order to optimise the filling gas mixture for the MSPET modules, a gas mixing device has been installed in the laboratory. It allows to produce precise compositions of three different gases.
In detail the device comprises a multi-gas controller unit (MKS *MGC*647*C*) and three mass-flow meters (MKS *mass flo controller* 1179*B*). One of these flow meters is calibrated for argon gas and allows a maximum flow of $10\frac{l}{h}$. The other two are calibrated for nitrogen and allow max. $3\frac{l}{h}$. The minimal flow that can be regulated is 1% of the maximum flow. The accuracy is specified being $< 0.2\%$ of the maximum flow. When using other gases than argon or nitrogen, a gas correction factor has to be used to adapt the specific gas to the calibration. For isobutane ($g_{\text{corr}}^{isoC_4H_{10}} = 0.27$) and carbon dioxide ($g_{\text{corr}}^{CO_2} = 0.7$) this reduces the maximum flow to $0.27 \cdot 3\frac{l}{h}$ and $0.7 \cdot 3\frac{l}{h}$ respectively.
Based on canonical values and Garfield simulations, the detector has been tested with different gas mixtures. Relevant parameters for the validation are most of all the detection efficiency, but also the break down limits and chamber stability. The efficiency has been measured with cosmic radiation using the setup as shown in Figure 6.24(a). The MWPC has been placed in-between two $10 \times 15 \times 150\,\text{mm}^3$ large plastic scintillators that are read out with VALVO XP 2972/PB photomultiplier tubes. The scintillators allow to trigger on cosmic particles (mostly muons with a mean energy of $\approx 4\,\text{GeV}$) that will traverse all three detectors. The efficiency of the MWPC is then

$$\varepsilon_{\text{MWPC}} = \frac{n_{3\text{Co}}}{n_{2\text{Co}}} \tag{6.32}$$

where $n_{2\text{Co}}$ is the number of coincidences between the two scintillators and $n_{3\text{Co}}$ is the number of coincidences measured on all three detectors. The results of the measurements are shown in Figure 6.24(b). Each data point represents three hours of measuring time. One can see that it is possible to reach a detection efficiency for cosmic radiation of above 80% with nearly all of the gas mixtures. Values above 100% and large error bars can be explained with an exceeded break down voltage limit and thus sparking of the wire

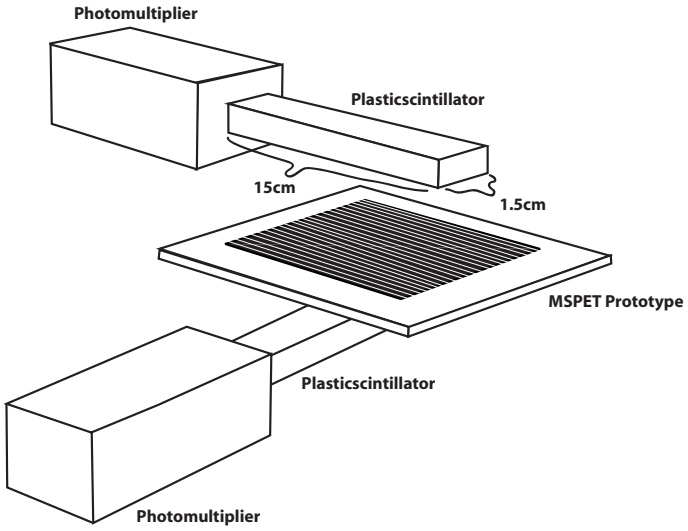

(a)

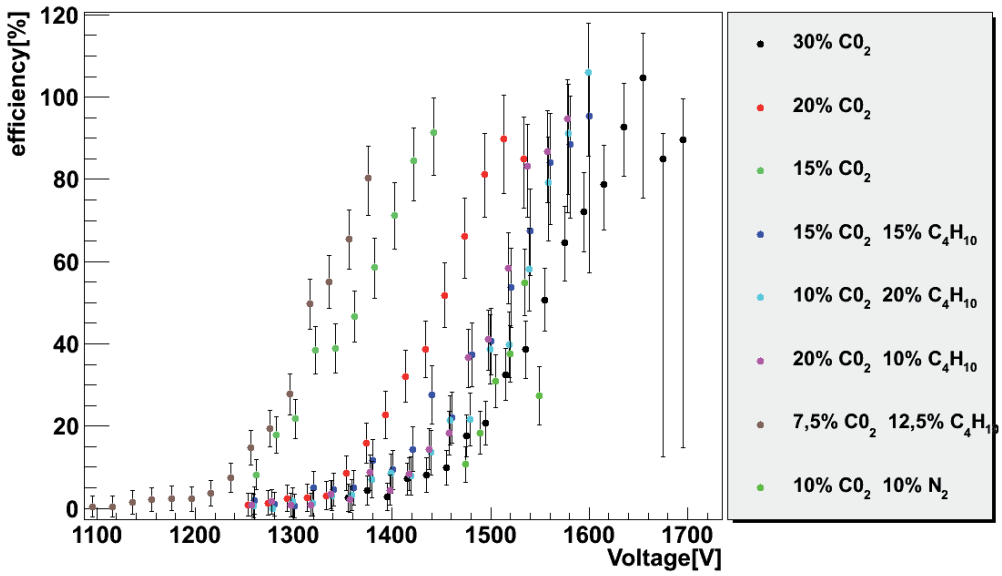

(b)

Figure 6.24: (a) Efficiency measurement setup. The module has been placed between two finger-shaped plastic scintillators which act as a trigger for cosmic radiation. (b) Measured detection efficiency of an MSPET module for different counting gases. Values above 100 % are caused by detector sparking which induces an undefined number of events to the counter electronics [Ver10].

chamber. A spark will influence the sensitive electronics in a way that the counter is increased by a random value between 0 and 20. To correct for that, the number of sparks is counted and considered in the error bars. The most stable operation was observed with a gas mixture containing 70 % Ar and 30 % CO_2.
Considering this to be a good mixture, pulse height distributions with an X-ray device ($E_\gamma = 6-10\,\text{keV}$) described in [Bau05] and a sodium source ($E_\gamma = 511\,\text{keV}$ and $1275\,\text{keV}$) have been measured. The results are shown in Figure 6.25. In case of the X-ray source

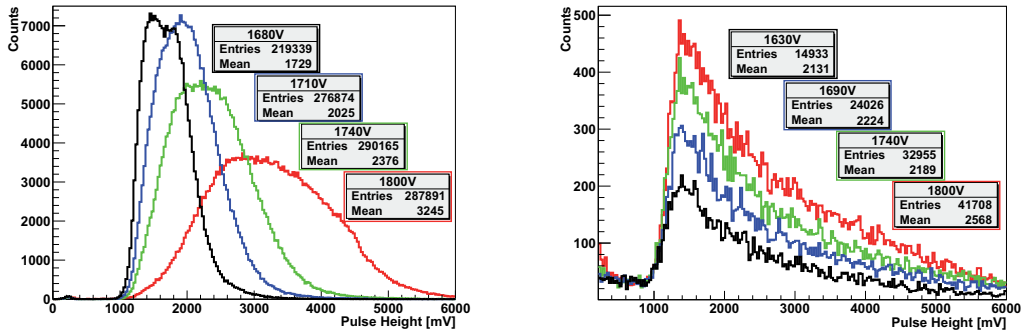

(a) (b)

Figure 6.25: Distribution of pulse-heights summed over ten adjacent pads for X-radiation (a) and for a ^{22}Na source (b) measured with the until then favoured Ar-CO_2 $70-30$ mixture. While the X-ray spectra show a full peak, the spectra for ^{22}Na seem to be incomplete [Ver10]. The edge at approximately 1000 mV is caused by the read-out trigger level applied on the anode pulse heights. Entries below 1000 mV indicate the pads bias.

one can see a full peak indicating the measurement of the whole energy spectrum of the high rate X-ray source. Taking the linear attenuation coefficient for X-rays in argon into account, one can approximate the number of primary encounters following a single photon incident:

$$n_{\text{ion.}} \frac{E_\gamma^{\text{mean}}}{E_{ion.}^{\text{Ar}}} = \frac{8500\ \text{eV}}{15.9\ \text{eV}} = 535. \tag{6.33}$$

The sodium spectrum on the other hand seems to be cut off by the threshold level. A peak cannot be identified since for certain circumstances too few electrons are produced in the detector.
The reason for that can be found in the different detection principles of the sources. While the low energetic X-rays interact directly with the gas molecules, the annihilation photons originating from the ^{22}Na source will be converted to electrons in the detector material,

Gas	Density $\left[\frac{\text{mg}}{\text{cm}^3}\right]$	$\frac{\text{dE}}{\text{dx}}$ $\left[\frac{\text{keV}}{\text{cm}}\right]$	e^--ion pairs $[\frac{1}{\text{cm}}]$
Ar	1.66	2.87	106
Xe	5.50	7.69	312
CO_2	1.84	3.95	100
C_4H_{10}	2.49	6.69	220
$ArCO_2$ 70 – 30	1.714	3.17	104
ArC_4H_{10} 70 – 30	1.909	3.84	140
$XeCO_2$ 70 – 30	4.398	7.13	248
XeC_4H_{10} 70 – 30	4.593	8.20	284

Table 6.1: Stopping power $\langle \text{dE/dx} \rangle$ of $E_{kin} = 280\,\text{keV}$ electrons in gases and gas mixtures as could be used in the MSPET detector. The given values have been taken from [M. 09]. The total number of electron-ion pairs has been taken from [ADA$^+$08] and account for minimum ionising particles (for electrons this equates $E_{kin} \approx 1 \ldots 1.5\,\text{MeV}$). For the gas mixtures, the number of pairs has been appraised neglecting attachment effects.

which will then be detected in the gas volume. The mean energy of these electrons is $E^e_{\text{mean}} = 280\,\text{keV}$ (see Figure 7.12). They possess an angular distribution shown in Figure 6.15. An approximation of the number of produced electrons depending on the exit angle of the primary electron is shown in Fig. 7.13. One has to conclude that only the electrons with large angles will be detected. This will not only reduce the detector efficiency, but also decrease the spatial resolution, that depends mainly on the exit angle of the conversion electrons. To increase the detection efficiency for electrons with smaller exit angles, one has to increase the applied anode voltage or add a gas compound with large stopping power.

As a voltage increase is possible only within certain limits before the chamber breaks down, the second option has been realised. Table 6.1 lists the $\langle dE/dx \rangle$ values for some gas compounds. As a first attempt, the carbon dioxide fraction of the gas was replaced by isobutane, which promisses a larger number of electron-ion pairs in the gas. The pulse height spectrum for this mixture (Ar-isoC_4H_{10}) is shown in Figure 6.26. Since the peaks now show a clear maximum, mixtures with isobutane seem to be preferable over carbon dioxide mixtures.

After all of these tests it can be concluded that a mixture has been found that allows proper testing and operation of the developed wire chambers. Nevertheless, since seemingly not all electrons liberated in the converter are detected, there still is the potential to further improve the mixture. In addition, it has to be concluded that not the converter, but the gas mixture is the dominant factor that limits the detection efficiency unless a proper mixture

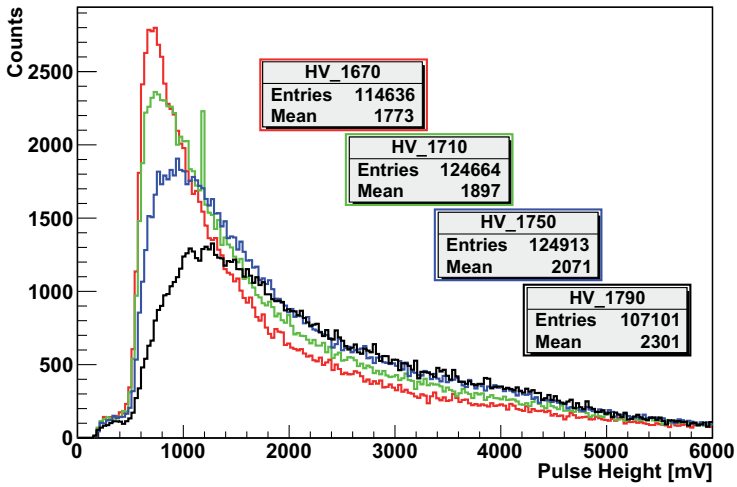

Figure 6.26: Distribution of pulse-heights summed over ten adjacent pads for a ^{22}Na source measured with an Ar-isobutane $70-30$ mixture. Electrons liberated in the converter can be detected with reasonable efficiency using this gas mixture [Ver10]. The distributions follow a superposition of Landau functions accounting for different electron exit angles and energies.

is found. More details on efficiency measurements and performance evaluation of the MSPET detector modules can be found in the diploma thesis of D. Vernekohl [Ver10].

6.5 Readout Electronics

6.5.1 Modular VME-based Read-out

If a particle traverses a MWPC detector, it will ionise the gas volume as already discussed in Section 6.1.2. The electrons produced in the amplification avalanche close to the wire will be instantly extracted, while the larger and slower ions will alter the field of the wire before they start to drift towards the cathode pads. So a fast negative signal can be measured on the anode wires, which can be used as an event trigger, that is used to open a gate that enables the ADC acquisition in order to measure the charges on pad signals.
Forward biased diodes (type 1N4148) mounted directly on the MWPC between pad and ground level will act as a fuse for the subsequent electronics in case of high-voltage sparks. Figure 6.27 shows the schematic signal path from the detector to the PC. The signals are amplified with a charge sensitive pre-amplifier (PNG CATSA) and an appropriate main amplifier (PNG MA8000). For digitisation of the pad charge signals 16

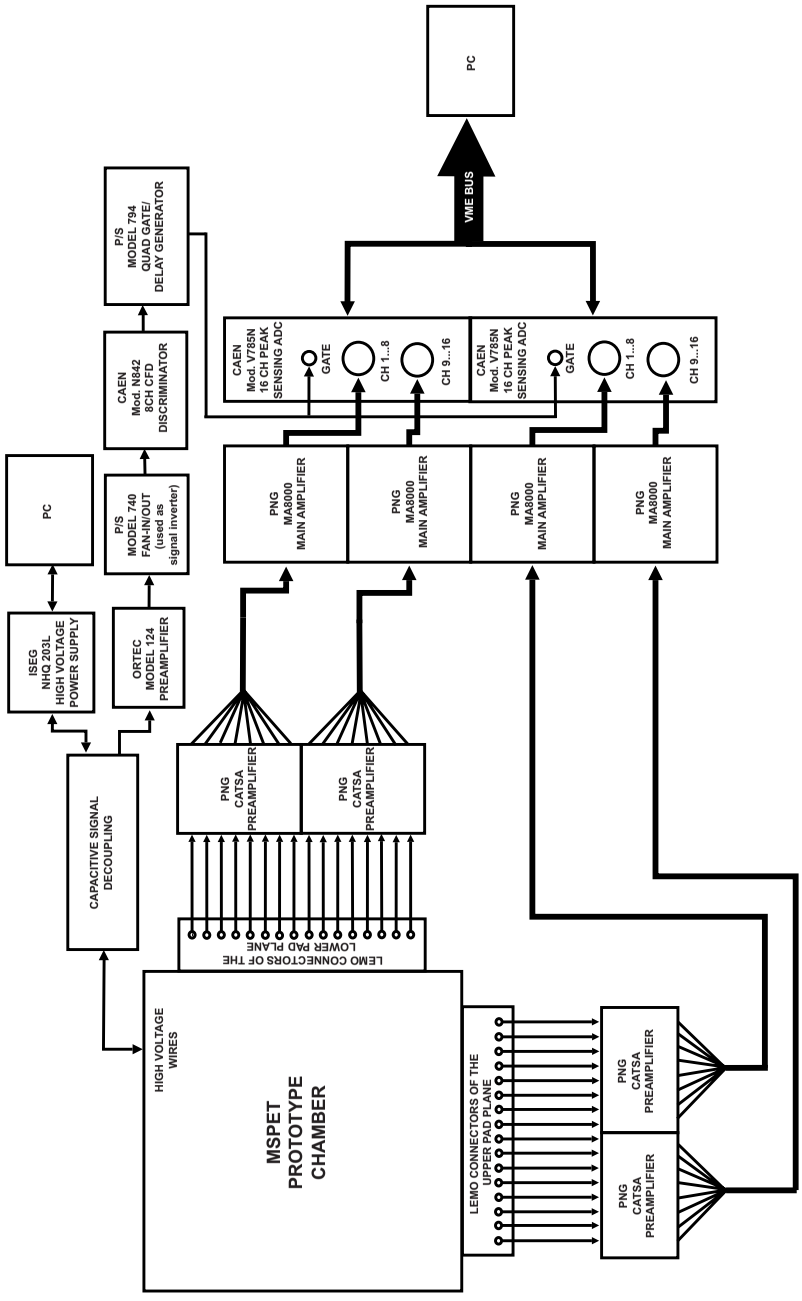

Figure 6.27: Triggered MSPET measurement setup using a VME ADC read-out (drawing by Don Vernekohl).

channel peak sensing ADC modules (CAEN V785N) mounted in a VME[3] crate are used. When a gate signal is applied, the event number counter is incremented by one and the ADC starts to acquire the peak voltage of the input signals using a sample and hold circuit. After the gate is switched off, the data is multiplexed by groups of four channels and subsequently digitized by the 12-bit ADC. Afterwards, the event is written to the multiple event buffer which can hold up to 32 events consisting of up to 34 words, 32-bit each. A word contains a header, the data word and an end-of-block statement. A word stores information on the geographic address, crate number, number of converted channels, the 12-bit converted value and the event counter. After an event is written, a write pointer is set to the next free slot in the buffer.
The PC now constantly polls the event counter, when incremented, the buffered data is read out and the read pointer is moved to the next buffer entry. This indicates that the read buffer can be cleared and refilled with fresh data.
The limiting factor for the data acquisition appears at first sight the optical gigabit link between the PC (SIS1100 PCI) and the VME interface (SIS3100 VME). The nominal transfer rate is here 125 MB/s which leads to a maximum acquisition rate of approximately $\frac{28.7}{\text{Nb.of ADC modules}}$ kHz. For practical reasons this value will be smaller, because the IDE Bus of the used hard drive is limited to a maximum of 100 MB/s if run in UDMA-100 mode which lowers the acquisition rate to not more than $\frac{23}{\text{Nb.of ADC modules}}$ kHz. For a test setup with one or two detector modules these rates are fully sufficient, but for a full PET device alternative approaches have to be found.

6.5.2 Dedicated Low-Cost Amplifier with Commercial ADC

As the used VME ADCs and commercial pre-amplifiers are very expensive when handling large numbers of channels, new low-cost charge sensitive read-out electronics are currently under development. The circuit sketch is shown in Fig. 6.28. A FET[4] (V1) is used to release the input signal by a (theoretically) infinite resistance. R3 specifies the working point of the FET. The input signal is fed into the differentiator (C2) which is unloaded into the amplifier V2 with its gain defining resistors R5/R4. The following integrator (R7,C3) sums up the incoming charges and forwards them to the AD8000 amplifier (V3). The amplifiers are biased via R6 and R9 in order to lower the DC level so that the amplification range can be exploited more completely. C1 as well as C4 and C5 are used to reject possible DC-offsets produced by the amplifiers and the input signal respectively. The second amplifier V3 has a quite small amplification factor and is used to decouple the output of the first amplifier in order to reduce noise. The height of the output pulse is

[3] The **V**ersa **M**odule **E**urocard is a data bus system that provides a bus width of 64-bit.
[4] **F**ield-**E**ffect **T**ransistor

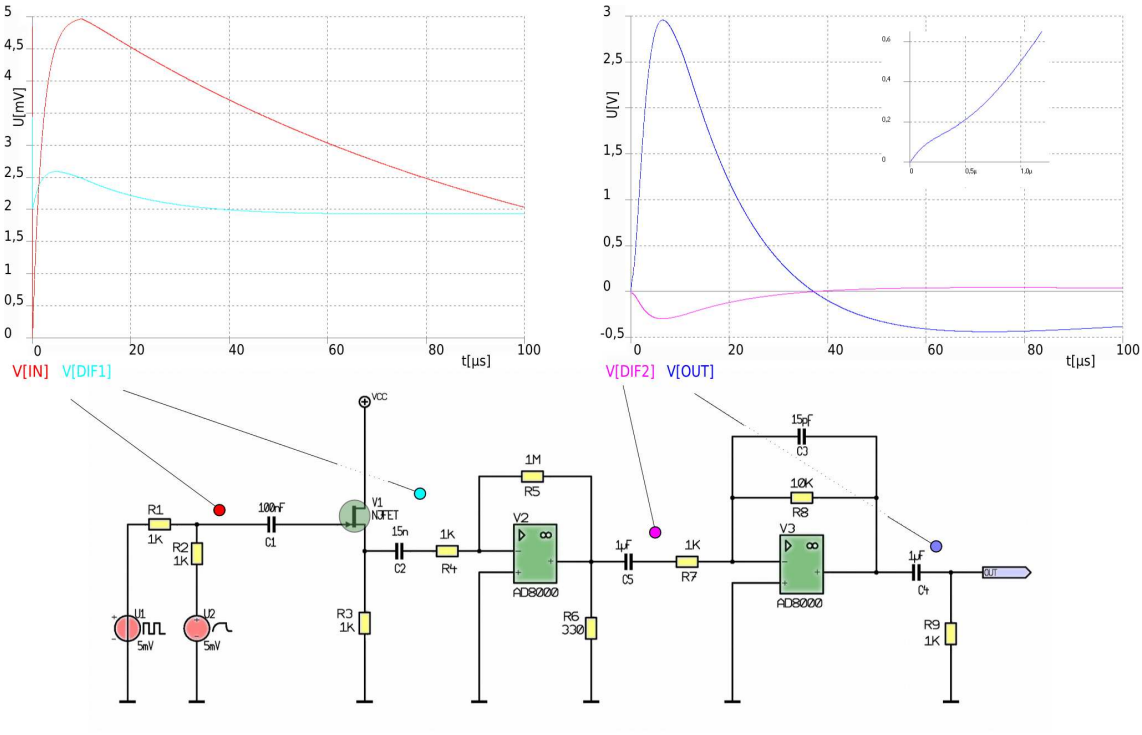

Figure 6.28: Charge sensitive amplifier developed for MSPET prototype operation. The plots above show a simulation of a test signal propagation through the circuit (layout and SPICE simulation by R. Berendes). After the integration, the short 10 ns electrostatic induced fraction vanishes nearly completely.

proportional to the charge deposition.
It is foreseen to pass the output to a commercial ADC (Agilent U2331A) which offers 16-bit resolution on 64 channels that can be sampled with up to 3 MS/s. With a price of ≈1600 € this is about 10 % of the cost of a similar number of VME ADC channels. The pre-amplifiers have material costs of about five Euro/channel and are therefore very cost efficient.
First measurements have shown that this amplifier is less noisy than the commercial PNG amplifiers, so that similar or even better signal-to-noise ratios are expected.

6.5.3 Development of an Integrated Readout Chip

A 50-module quadMSPET device will need approximately 30000 cathode pads. In order to avoid problems that have shown up in the analysis of quadHIDAC data due to missing raw data preservation, it is foreseen to equip each cathode pad with an individual read-out channel. It is obvious that a VME-based read-out scheme as presented in the previous sections is not only too expensive but also just not feasible for that many channels. Furthermore, the cable length and signal attenuation in connectors will limit the detector performance. Highly integrated electronics allow to have a large number of readout channels in a very compact package. Therefore, it can be placed very close to the detector modules without suffering a large signal loss and noise pickup. The development of a prototype read-out system based on a pre-production version of the n-XYTER[5] chip was topic of the diploma thesis of J.-F. Pietschmann [Pie08].

The n-XYTER Chip

The n-XYTER was developed within the European DETNI[6] project for the read-out of silicon-micro-strip detectors, GEMs and, with a alternate design, micro-strip gas chambers used for the detection of thermal neutrons.
The n-XYTER is an highly integrated ASIC[7] chip. It contains 128 independent data driven, self triggered readout channels. Each recorded event is furnished with a time-stamp providing 2 ns resolution [BBD+06]. The channel pitch is just 50 μm.
Figure 6.29 shows the architecture of the chip. It is comprised of an analogue front-end and a digital back-end. The front end contains a charge sensitive pre-amplifier followed by two shapers, a fast one (30 ns peaking time) and a slow one (175 ns peaking time). The signal coming from the pre-amplifier is split up and transferred to both shapers. The fast

[5] n-XYTER = **n**eutron **X**,**Y**,**T**ime and **E**nergy **R**ead-out.
[6] DETNI = **Det**ectors for **N**eutron **I**nstrumentation
[7] ASIC = **A**pplication **S**pecific **I**ntegrated **C**ircuit

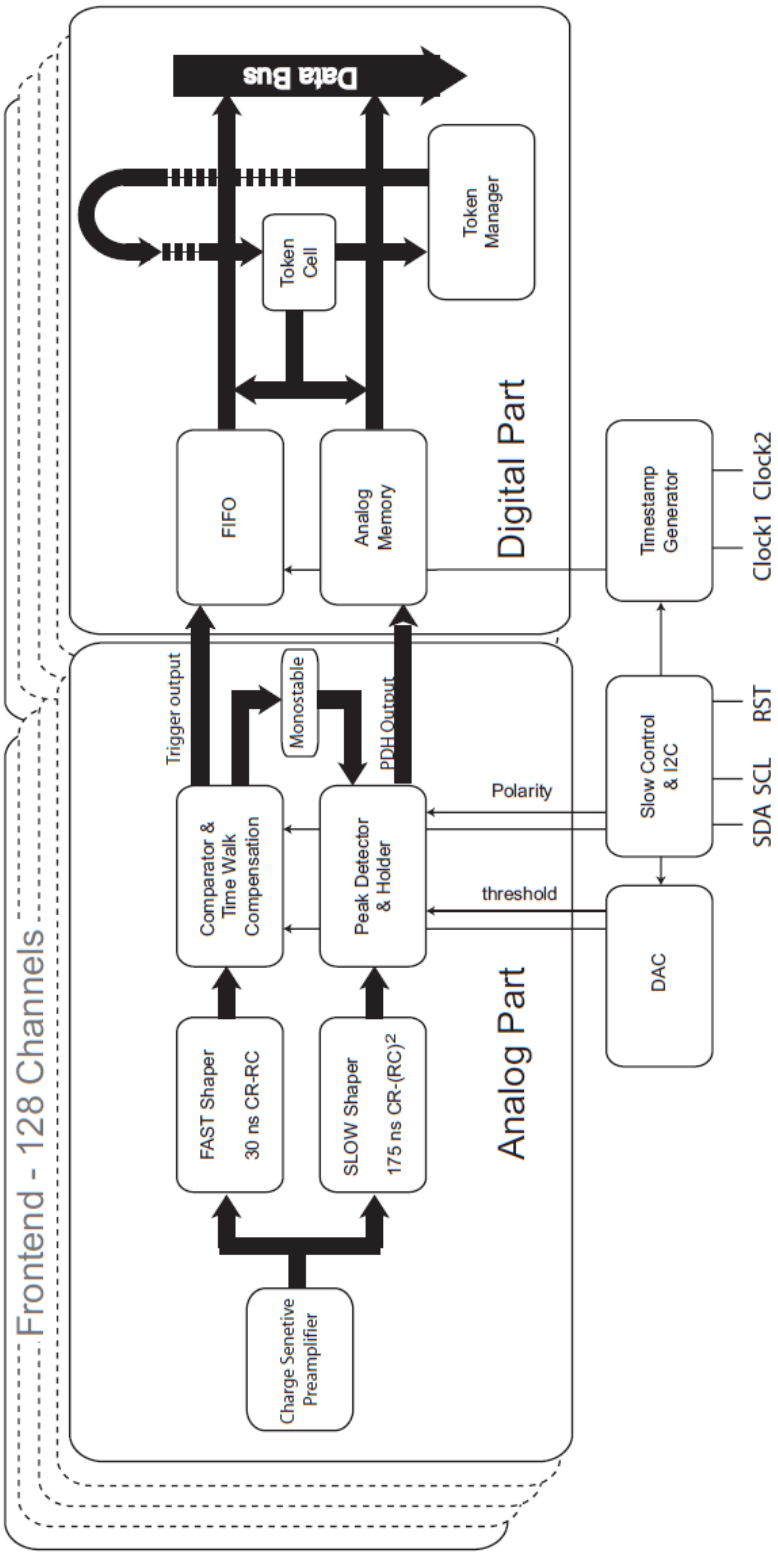

Figure 6.29: The n-XYTER's chip architecture. On the top layer one of the 128 independent . The sketch was taken from [Pie08] which is based on [B+07c].

Nb. of readout channels: 128
Charge sensitive pre-amplifier and peak detector
Timing resolution: 2 ns
10 bit storage for peak information
Self triggered, purely data driven, de-randomising hit detection
Time stamp resolution: 1 ns
Token ring readout frequency: 32 MHz
Dynamic Range: 120.000 e (might differ in later versions)

Table 6.2: Key specifications of the n-XYTER chip.

shaper is followed by a time-walk compensator, providing an amplitude independent time-stamp generation, and a comparator which acts as a trigger. The slow shaper is followed by a sample and hold peak detection circuit which determines the actual pulse height of the signal. The trigger output and the analogue pulse height information is transferred to the digital part. The trigger signal is used to create a time-stamp which is then stored in a FIFO[8] memory. The pulse height information from the slow shaper branch is stored in an analogue memory. Both the time-stamp and the pulse height is further processed by a token ring read out. A token is generated if at least one of the FIFOs contains data. The token is then passed asynchronously from channel to channel and returns to the token manager afterwards. For the channels containing data a readout is initiated at the arrival of the token. The data will be sent to the data bus. The analogue data is converted to a differential standard, the digital data to the LVDS[9] standard. The main characteristics of the chip are summarized in Table 6.2

With its characteristics the n-XYTER not only fulfils the demands of the DETNI detectors but is also predestined for the read-out of MWPCs and thus, the MSPET positron camera.

Since the production version of the n-XYTER as well as a dedicated test readout board is still under development, it was unfortunately not possible to test it with MSPET chambers yet. For a more detailed description of the foreseen MSPET read-out system and a prototype readout board see [Pie08].

Number of Detector Blocks	4
Number of Modules per Block	50
Rotation speed	no rotation foreseen
Size of Modules	as indicated in Table 5.2
Size of Prototype	$100 \times 100\,\mathrm{mm}^2$
Wire material	gold-plated tungsten
Wire diameter	$20\,\mu$m
Wire separation	1.5 mm
Anode-to-Cathode distance	1 mm
Typical anode potential	$1400 - 1600\,$V
Filling gas	Ar-isoC_4H_{10}
Number of Converters per Module	1
Number of Converters per Module	1
Lead Thickness	$40\,\mu$m
or Gold Thickness	$30\,\mu$m
Entrance Window	$500\,\mu$m FR4
Pad Width	3.03 mm
Gap between Pads	0.3 mm

Table 6.3: Key specifications of the MSPET small animal PET scanner.

6.6 Outlook

A summary of the current MSPET design specifications is given in Table 6.3. The most important task for the future of this project will be to provide enough readout channels. On a short time scale, simple and affordable mass production amplifiers combined with an Agilent ADC module can be used to implement a cost efficient and compact readout scheme for an MSPET prototype system consisting of a handful of detectors. A major problem with the VME and also this prototype readout is the timing behaviour. As the dead times should be not larger than some hundred nanoseconds, not the ion drift contribution, but the electrostatic induced signal created by the ion cloud around the wire has to be recorded. This requires a fast ADC or at least a FIFO memory that will retain the charge information until it is read out.

On a medium time scale the solution here will be to use a readout board containing the n-XYTER chip. This would not only be the most elegant solution with sufficient timing resolution, but offers also the opportunity to contribute to the development of a proper readout board by providing the first MWPC signals ever recorded with this multivalent electronics.

As the electroplating of the readout pads has been shown to be problematic, alternative methods have to be investigated. The usage of pre-manufactured lead sheets which are glued on top of the copper pads seems to be promising. The difficulty is here to cut out

[8] FIFO = **F**irst **I**n **F**irst **O**ut

[9] LVDS=**L**ow **V**oltage **D**ifferential **S**ignaling

the pad structure, so that the edges of the pads remain smooth.
The choice of the converter material for a production versions of the MSPET will be mainly affected its machining properties.

7. Results and Outlook

7.1 quadHIDAC Simulations

The development of quantitative methods is in special focus of todays PET research. In order to push current PET techniques into this direction, the development of improved hardware as well as the implementation of new reconstruction algorithms is needed. Modern crystal scanners already offer good energy resolution and low noise that allow the discrimination of trues and scatters up to some extend. However, the quadHIDAC PET small animal PET camera, described in Section 3.5.3 has not been improved during the last ten years. Its count rate and noise behavior has not been studied on a quantitative level. This is also true for its response to scatter due to the absence of energy information.
In order to evaluate the quantification potential of this camera, extensive simulations have been performed. The results of these simulations have then been used to interpret first test measurements quantitatively.

7.1.1 Verification of Suggested Dead Time Models

For the understanding of the count rate behavior of the quadHIDAC, a valid dead time model is needed. Unfortunately, the dead time specifications of the quadHIDAC are not published in detail. The bequeathed values are a coincidence window of 40 ns, a dead time after a single hit of 160 ns and a dead time after coincidences of 400 ns [Jea05]. It is not published whether the dead times apply to single modules, one detector stack, opposite detector stacks or the whole quadHIDAC. To overcome this problem, different dead time assumptions were tested and compared to measured data.

Simple Analytic Ansatz for the Dead Time

In the simplest case a non-paralysable dead time model is suggested. That means that there is no prolongation of dead times in case of an event while the detector is dead. Taken into account is here a coincidence window of 40 ns and a dead time of 160 ns after each single hit for the whole system. For the singles count rate s one gets

$$s = \varepsilon_\gamma(a) \cdot a \cdot \Gamma \tag{7.1}$$

where $\varepsilon_\gamma(a)$ is the detection probability of a single photon, a is the activity and $\Gamma = 1.934$ the number of photons emitted per positronium decay. The probability that the detector is inactive at a certain time is

$$P_{\text{dead}} = s \cdot \tau \quad \text{, valid for } \tau \ll \frac{1}{s} \tag{7.2}$$

with the time interval τ following a hit in which the detector is not active ($\tau = 160\,\text{ns}$). The probability for the detection of a single photon, taking dead time effects into account, is now

$$\begin{aligned} \varepsilon_\gamma &= \varepsilon_\gamma^0 \cdot (1 - P_{\text{dead}}) && (7.3)\\ &= \varepsilon_\gamma^0 \cdot (1 - \varepsilon_\gamma \cdot a \cdot \Gamma \cdot \tau) && (7.4)\\ &= \frac{\varepsilon_\gamma^0}{1 + a \cdot \varepsilon_\gamma^0 \cdot \Gamma \cdot \tau} && (7.5) \end{aligned}$$

with ε_γ^0 being the photon detection efficiency at low count rates where dead time effects can be neglected. The singles rate can now be written as

$$\begin{aligned} s &= a \cdot \Gamma \cdot \varepsilon_\gamma && (7.6)\\ &= \frac{a \cdot \Gamma \cdot \varepsilon_\gamma^0}{1 + a \cdot \varepsilon_\gamma^0 \cdot \Gamma \cdot \tau}. && (7.7) \end{aligned}$$

For the coincidence count rate (trues and scatters, neglecting randoms) it is

$$c_{TS} = a \cdot \varepsilon_C^0 (1 - P_{\text{dead}}) \tag{7.8}$$

with ε_C^0 being the coincidence detection efficiency at low count rates. For the randoms count rate, following Equation (3.19), one can write:

$$c_R = 2 \cdot \Delta t_c \cdot s^2 \cdot \frac{1}{8} \tag{7.9}$$

only counting randoms in opposite detector modules. $2 \cdot \Delta t_c = 40\,\text{ns}$ is the length of the coincidence time window. The total coincidence count rate is now

$$c = c_{TS} + c_R. \tag{7.10}$$

Improved Analytic Ansatz for the Dead Time

In order to get a more precise dead time model, one has to take the different dead times after single hits and measured coincidences into account. Following that idea, the ansatz for an advanced dead time model is

$$P_{\text{dead}} = (s-2c)\cdot\tau_1 + c\cdot\tau_2 \tag{7.11}$$

with a dead time of $\tau_1 = 160\,\text{ns}$ after a single hit and $\tau_2 = 400\,\text{ns}$ after a coincidence. With

$$\begin{aligned}\varepsilon_\gamma &= \varepsilon_\gamma^0\cdot(1-P_{\text{dead}}) &(7.12)\\ &= \frac{\varepsilon_\gamma^0(1+2c\tau_1-c\tau_2)}{1+a\Gamma\varepsilon_\gamma^0\tau_1} &(7.13)\end{aligned}$$

and Equation (7.1) we get a singles rate of

$$s = \frac{a\Gamma\varepsilon_\gamma^0\cdot(1+2c\tau_1-c\tau_2)}{1+a\varepsilon_\gamma^0\Gamma\tau_1}. \tag{7.14}$$

The coincidence count rate of trues and scatters can be expressed as

$$\begin{aligned}c_{TS} &= a\varepsilon_c^0(1-P_{\text{dead}}) &(7.15)\\ &= a\varepsilon_c^0\left(1-c\tau_2-\tau_1\left(-2c+\frac{a\Gamma\varepsilon_\gamma^0(1+2c\tau_1-c\tau_2)}{1+a\Gamma\varepsilon\gamma^0\tau_1}\right)\right) &(7.16)\end{aligned}$$

where ε_c^0 is the efficiency for coincidences without any dead time effects. The count rates for the separated trues and scatters c_T and c_S can be written equivalently by replacing ε_c^0 with the coincidence efficiencies at low activities ε_t^0 and ε_s^0. The randoms count rate, considering randoms in detectors opposite to each other only is calculated as follows:

$$\begin{aligned}c_R &= 2\cdot\Delta t_c\cdot s^2\cdot\frac{1}{8} &(7.17)\\ &= \frac{a^2\Delta t_c\Gamma^2(\varepsilon_\gamma^0+2c\varepsilon_\gamma^0\tau_1-c\varepsilon_\gamma^0\tau_2)^2}{4\cdot(1+a\Gamma\varepsilon_\gamma^0\tau_1)^2}. &(7.18)\end{aligned}$$

The total count rate is derived from Equation (7.10) as

$$c = \frac{a(1+2c\tau_1-c\tau_2\cdot\left(4\varepsilon_c^0\left(1+a\Gamma\varepsilon_\gamma^0\tau_1\right)+a(\varepsilon_\gamma^0)^2\Delta t_c\Gamma^2\left(1+2c\tau_1-c\tau_2\right)\right)}{4(1+a\Gamma\varepsilon_\gamma^0\tau_1)^2}. \tag{7.19}$$

Solving Equation (7.19) finally yields the total count rate.

Detailed Monte Carlo Ansatz for the Dead Time

As shown in the previous section, an analytical model of the quadHIDAC dead time quickly yields to complex expressions, which are difficult to solve. In addition, not even all scenarios are considered in the presented analytical ansatzes. As proclaimed by V. Uhlendorff [Uhl05], the dead time for coincidences influences the whole quadHIDAC, while the singles dead time only affects the detector block that has been hit. Furthermore, events with more than two photons detected will cause a dead time like a valid coincidence, but will be rejected by the coincidence counter.

To describe this complex behavior, a Monte Carlo simulation of the count rate perfor-

Singles efficiency ε_γ^0	14.75%
Coincidence efficiency ε_c^0	2.38%
Trues efficiency	1.49%
Scatters efficiency	0.076%
Coincidence window $2\Delta t_c$	40 ns
Dead time after single τ_1	160 ns
Dead time after coincidence τ_2	400 ns

Table 7.1: Measured efficiencies for a 80 mm line source [S$^+$05] and communicated dead time values [Jea05] for the quadHIDAC. The scatter fraction has been obtained using NEMA[NEM01] methods on the measured data.

mance of the quadHIDAC was implemented. The idea is to use the published values for

dead times and detection efficiencies of singles, coincidences, trues and scatters, summarised in Table 7.1, in order to create a matrix of the following form:

time of decay	hit in detector 1	hit in detector 2	hit in detector 3	hit in detector 4
0.0101872	0	0	0	1
0.0110534	1	0	1	0
0.0143854	0	1	0	0
0.0163364	0	1	0	1
0.0167463	0	1	0	1
0.0188938	0	0	0	1
0.0200904	0	0	1	0
0.0244439	0	0	1	0
0.0258464	0	1	0	1
0.0399541	0	0	0	1
0.0428088	0	0	1	0
...	...	...	...	...

The time until the next decay is drawn from the probability distribution

$$\frac{dP(t)}{dt} = A \cdot e^{-A \cdot t}$$

in the range of $t = 0 \ldots 10/A$, where A is the activity of the source. Using the known detection efficiencies for single hits and coincidences, hits on single or opposite detectors are diced. If a detector hit occurs, a 1 is noted in the matrix and the appropriate time of the decay is added. In a second step the matrix is analysed for coincidences and single hits and the dead times are applied. After a single hit all lines within the single dead time window of 160 ns are identified and the column in which the hit occurred is set to zero here. After a coincidence lines within a time window of 400 ns are set to zero. Then for the randoms, a search is started for two events producing single hits inside the coincidence time window of 40 ns. Since this indicates a time frame of 20 ns before and after a single event and the first occuring event is known due to the algorithm, it is searched for a second single hit occuring within 20 ns after the first identified single hit. To these events the coincidence dead time is applied in addition. Both the coincidence count rate and randoms count rate is increased if there is no third hit inside the current coincidence time window. In case there is, the event is ignored. In the following all hits are summed up for a single count rate. Real coincidences are counted and it is again diced whether it is a true or a scatter.

Figure 7.1 shows the comparison of the three presented dead time models. It can be

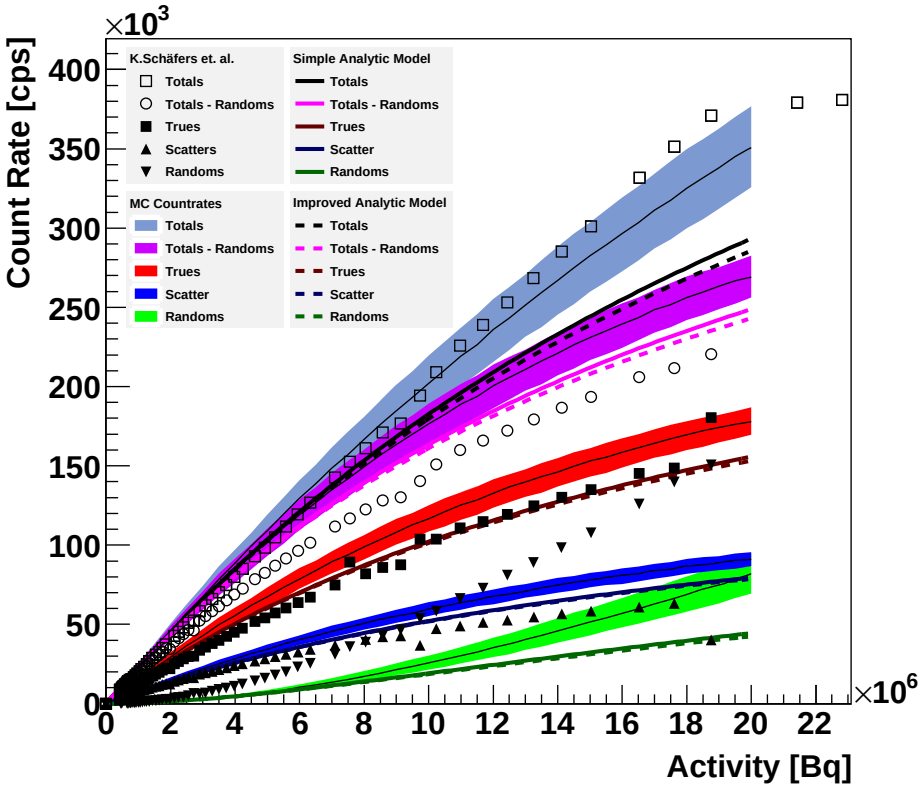

Figure 7.1: Validation of the proposed dead time models: Simple analytical, improved analytical and Monte Carlo count rate simulation in comparison to real data shown in [S$^+$05]. An 80 mm long line source described in Section 5.3.3 was used. The width of the MC-model describes an estimated error of $\pm 10\,\%$ in efficiencies.

seen that most importantly, the measured randoms count rate, also presented in [S$^+$05], does not fit the simulated and calculated ones. The missing factor of two between Monte Carlo and measurement gives a hint towards an possible error in the quadHIDACs random count rate calculation. It seems reasonable, that the formula used by the quadHIDAC misinterprets Δt_c in Formula (7.9) as coincidence time window and thus overestimates the randoms by a factor of two. A first analysis of the decay-corrected total count rate propagation in time of the quadHIDAC output has confirmed the assumption.
Further it can be seen, that the analytical models cannot describe the Monte Carlo count rates for activities above 6 MBq. The denominator in Equation (7.6) induces a linear propagation of the randoms count rates from here on, so that Equation (7.6), and thus the analytic models, holds only for inverse single rates that are small against $\varepsilon_\gamma^0 \tau \Gamma$, and as

already indicated in Equation (7.2) small against τ. As a result of this, also the total count rates does not fit with MC and measurement from 6 MBq on. The MC on the other hand is able to fit the total count rate in good agreement, despite of the difference in randoms count rates. The difference between MC and measured trues- and scatters rates is not worrisome. The imprecise determination following [NEM01] leads to slighty different fractions for each data point, while the simulation uses a constant fraction, obtained in a low activity measurement, for the whole activity range. The width of the Monte Carlo model reflects the inaccuracy resulting from an uncertainty in the published values for single, true and scatter sensitivities, so that a 10 % deviation of the named sensitivities seems to be reasonable.

Misleading Dead Time Information

As shown in Figure 7.1, the measured count rate saturates slightly below 400 kHz. With a dead time of 400 ns one would expect a count rate saturation at above 2 MHz.

In order to find a reason for this behavior raw pulses on the anode grid of a HIDAC module have been recorded and analysed. A typical pulse is shown in Figure 7.2. The pulse measured directly on the wire is indicated in yellow, while the same pulse after the amplifier is shown in blue. The raw pulse has a steady rise followed by a long tail, so that the total length of a pulse is easily some 100 μs long. The differentiating amplifier rejects the long tails so that a pulse of $\approx 2.5\,\mu$s length remains after the amplifier. The threshold for the event trigger was measured 90 mV above the baseline. It can be assumed that the rise time of the differentiated signal is of the order of 400 ns. Since the pulse length and the count rate saturation at $\frac{1}{2.5\,\mu s} = 400\,\text{kHz}$ appear suspiciously connected, it cannot be completely verified that the delivered dead time model analysed in the previous sections is correct.

Nevertheless it is very important to know the exact dead time behaviour for quantitation purposes. Since neither the electronics nor the software of the quadHIDAC is documented, reverse engineering, or more likely, the development of new modern read out electronics and software is essential.

7.1.2 Noise Equivalent Count Rate

The noise equivalent count rate (NECR) is a measure of the image quality. Its definition is given by Formula (3.23). Because of the noiseless randoms determination k was set to 1. Using the count rate simulations presented in Section 7.1.1, the NECR can be easily obtained. One can see in Figure 7.3 that the NECR reaches a maximum at 19 MBq, indicating that the scanner is expected to show the best image quality at an rather large

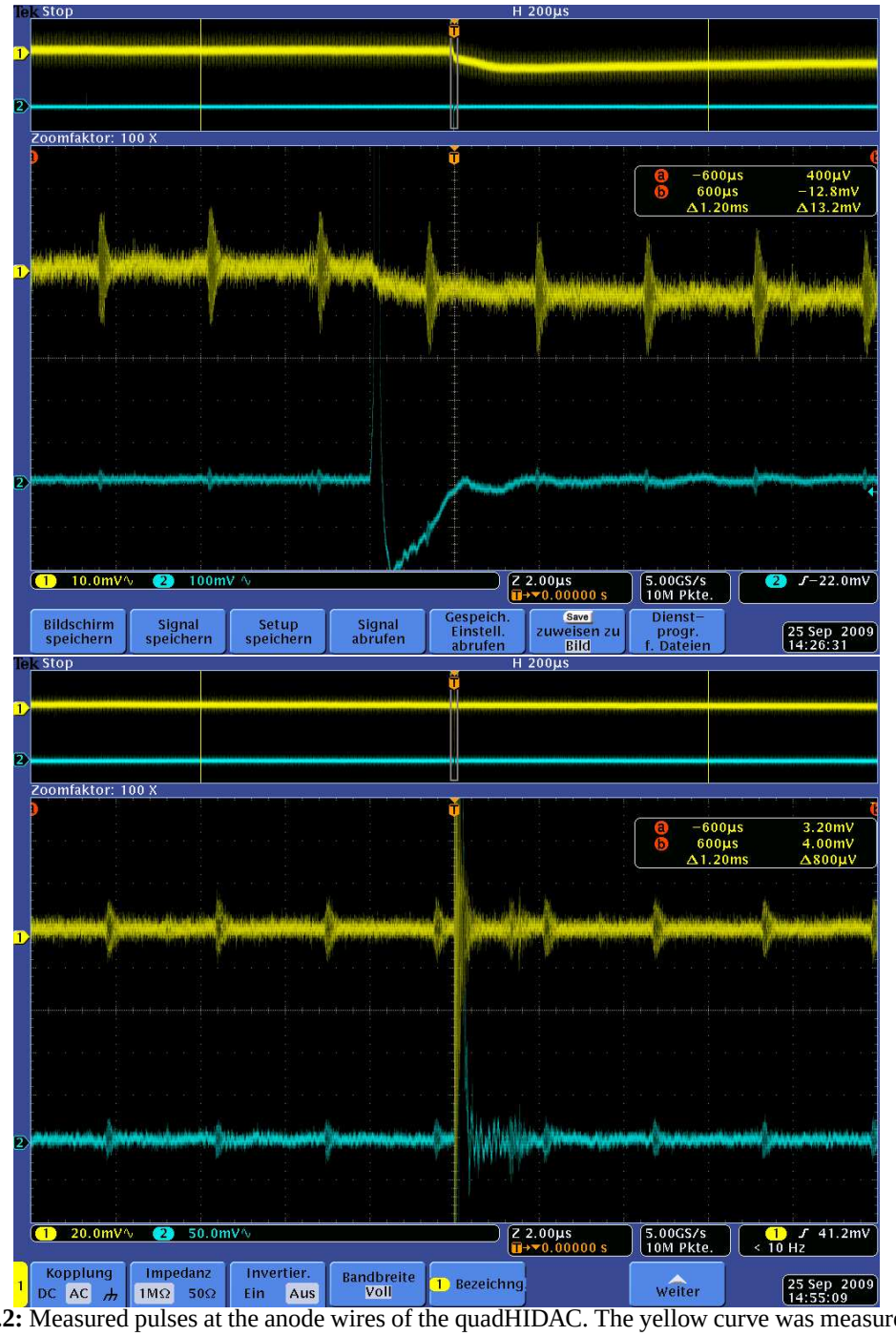

Figure 7.2: Measured pulses at the anode wires of the quadHIDAC. The yellow curve was measured before the amplifier. The blue curve after the differentiating amplifier. The pulse length after the amplifier is approximately 2.5 μs, which most likely causes the count rate to saturate at ≈ 400 kHz. The oscillations might originate from the HIDAC's power supply or disturbances on the power supply line. Panel (a) shows a regular pulse while Panel (b) was triggered on the mentioned noise.

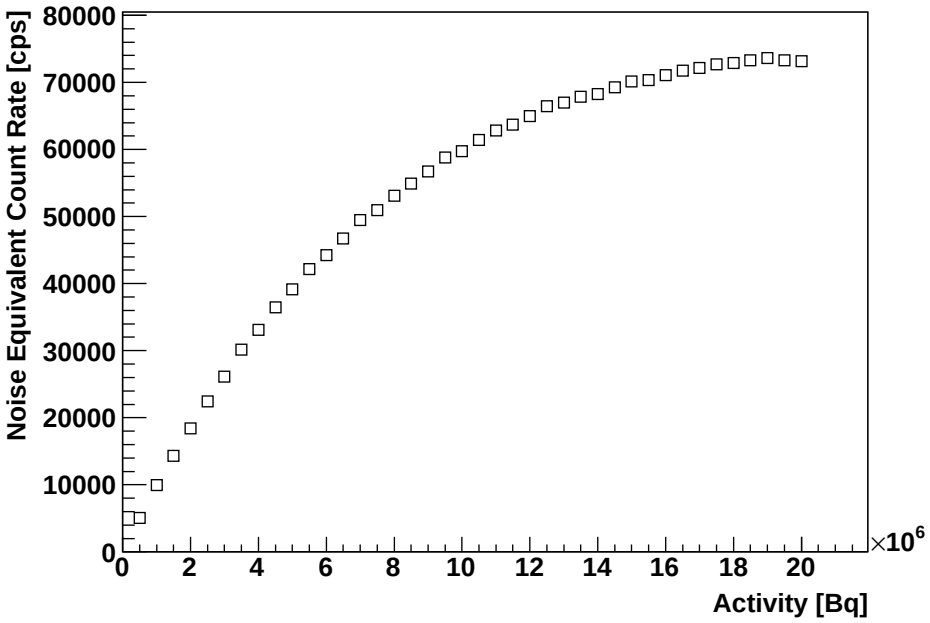

Figure 7.3: Monte Carlo simulation of the noise equivalent count rate of the quadHIDAC.

source activity. The variation of the NECR is less than $\pm 5\,\%$ for activities between 15 and 20 MBq.

7.1.3 Validation of Geant4 Simulations

Positron Range in Water

The positron range of the PET tracer depends on its primary energy. It leads to a reduction of the ideally achievable spatial resolution. The position resolution for ^{18}F has been calculated, measured, and also simulated before. In order to compare the presented simulations with the previous results, the positron range has been determined with Geant4. In order to do that, positrons with energies sampled on the ^{18}F spectrum, shown in Section 5.3.3 are placed in the exact centre of a 100 mm water sphere and emitted in random directions. The distance from the annihilation vertex to the centre of the sphere was calculated. Figure 7.4 shows the results of that simulation. The mean range is 0.47 mm and the maximum range 2.4 mm. The results here differ slightly from the literature, where it has to be noted that the positron ranges vary dramatically between different references. Not only the numbers vary, but also the methods. The comparison of the obtained value with literature turns out to be difficult, as the they vary between 0.102 mm [LH99] derived by a Monte Carlo simulation and measured 1.02 mm [CCE$^+$75] in FWHM, Mean values

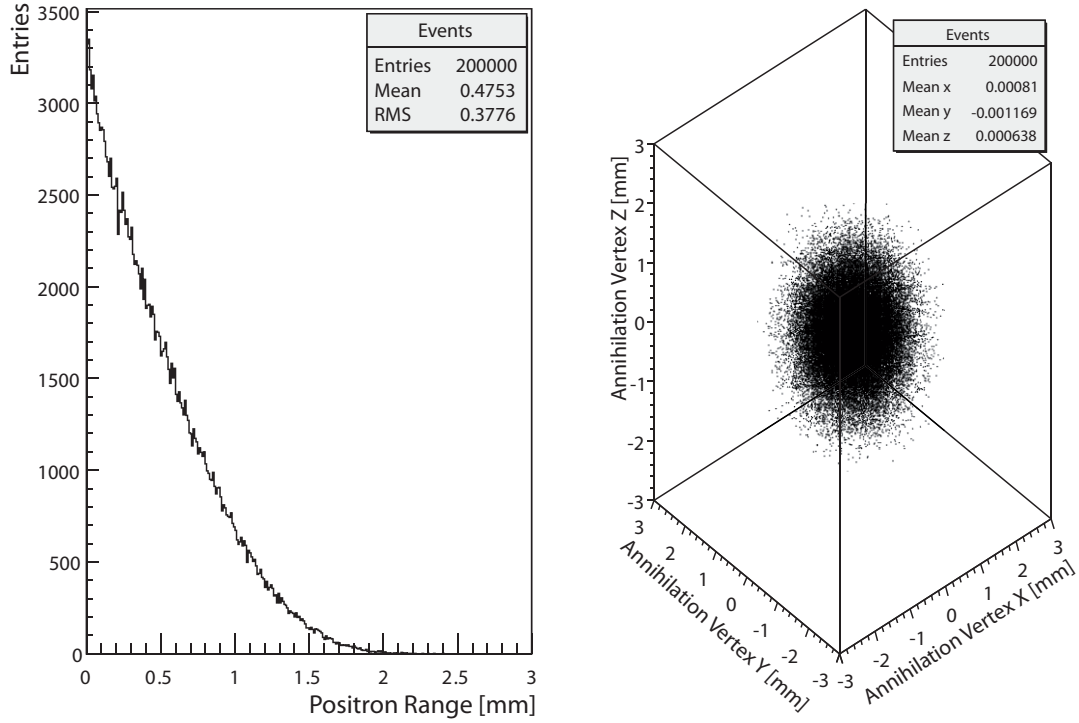

Figure 7.4: Geant4 simulation of the ^{18}F positron range in water. Shown are the annihilation vertices and their distance to the positrons origin.

vary between 0.6 mm [B$^+$05] and 1.4 mm [HRG03]. Nevertheless a value of 0.4 mm in Geant4 simulations seems to be reasonable.

Positron Range and Spatial Resolution Measurements

The positron range is a major factor influencing the resolution of a PET image. Since the achievable resolution is an important performance specification, it is measured for almost every scanner. For the quadHIDAC, K. P. Schäfers et. al. measured values between 1.00 mm and 1.096 mm after the reconstruction of a spongious point-like source in the centre of the FOV. The most recent measurement for the quadHIDAC has been performed by D. L. Hastings et. al. [HRJ$^+$07]. They used a glass pipe, filled with an ^{18}F liquid as positron source. The inner diameter of this glass pipe was just 50 μm. They measured a spatial resolution between 0.86 mm and 1.09 mm depending on the position of the source in the FOV. A source like this with an inner radius of "1 mm or less" is also proposed by NEMA [NEM01]. Figures 7.5 and 7.6 display the simulated positron ranges in the

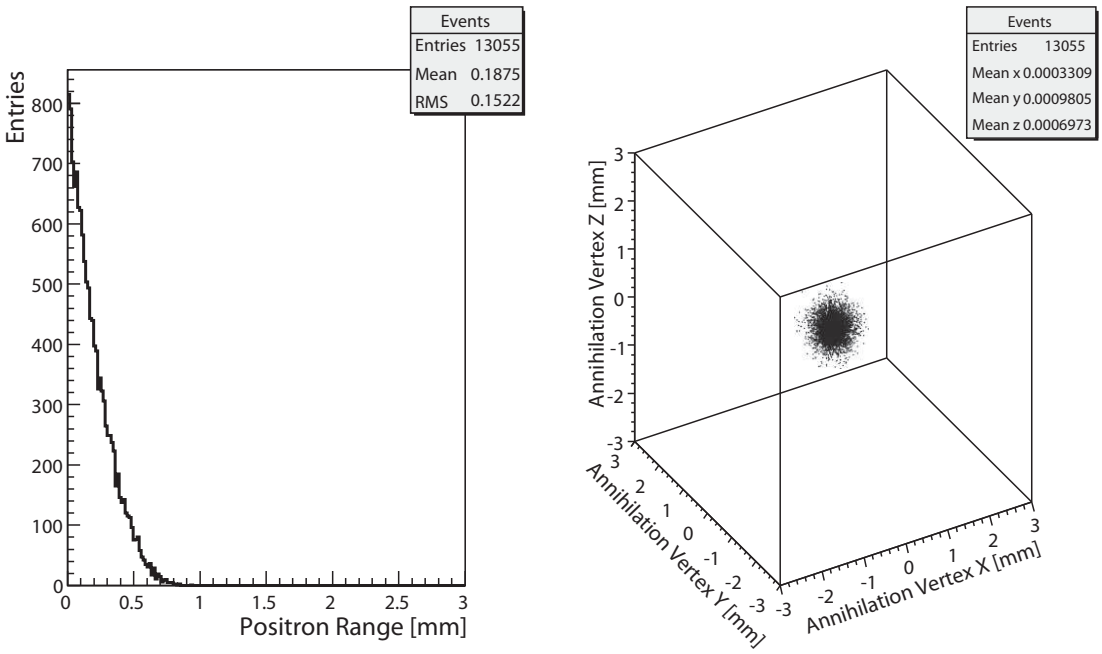

Figure 7.5: Geant4 simulation of the ^{18}F positron range in glass. Shown are the annihilation vertices and their distance to the positrons origin.

common source volume jacket materials glass and polyethylene. One can see, that in glass the range is with a mean value of 0.19 mm less than half of the value in water. Using a glass pipe with a diameter below 400 μm will therefore delude a spatial resolution

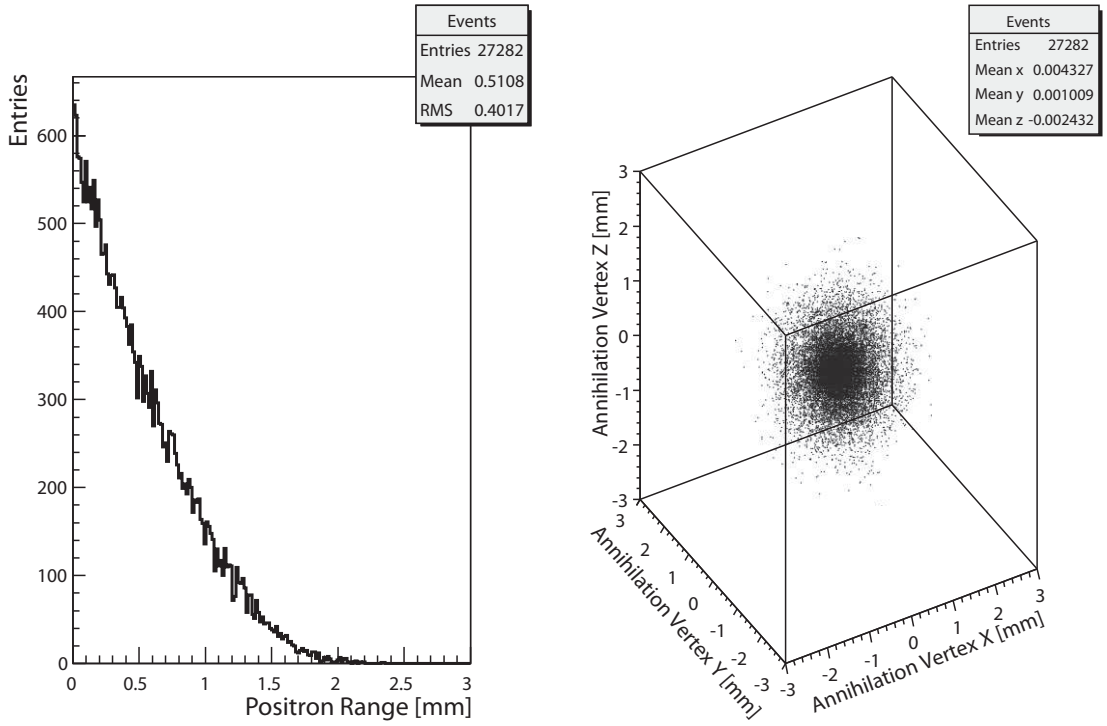

Figure 7.6: Geant4 simulation of the ^{18}F positron range in polyethylene. Shown are the annihilation vertices and their distance to the positrons origin.

that can never be reached in clinical work and is thus only of theoretical interest. The resolution in this case is dominated by the scanner itself. Polyethylene on the other hand seems to be a more adequate replacement for water and thus tissue, offering a comparable positron range of 0.51 mm. As a result of the presented simulations, the use of polyethylene jackets for spatial resolution measurements of the image in small animal PET has to be recommended. In case one wants to measure the effects caused by the scanner only, glass jackets are preferable.

Simulated quadHIDAC Hit-Distributions

The straight forward way to check the quality of a simulation is, to compare simulated raw data with measured raw data. This has been done for a water point source with a diameter of 3.2 mm enclosed by a thin 1 mm thick water hull. The corresponding measured source was a small sponge like sphere drained with 1.35 MBq of a ^{18}F fluid. As the exact dimension of the source was unknown, parallel projections of different sized simulated point sources have been compared with the projection of the measured data. In order to reduce the number of free parameters, only two detector banks and a measurement with no rotation has been taken into account.

For the comparison the hit-positions of half-coincidences, which are single photon incidences belonging to coincidence events, have been recorded. Figure 7.7 shows the results of the comparison. The oscillation of the measured data is caused by the wire gap of 1.5 mm which limits the position resolution in Z-Direction. The simulation here is in very good agreement with the measurement.

Another consistency check was performed by comparing the number of hits per module. Using the same measurement as above, the relative fractions of measured half coincidences are shown in Table 7.2. It has to be noted that the two detector modules on the back of detector bank B and module number 6 of bank A were defective during the measurement. Therefore, we also did not take data from these modules into account in the simulation.

As can be seen, there is a slight trend in the measurement to have more hits in the backward modules than expected from the simulation. This difference has to be explained by variances of detector efficiencies, due to different anode and converter voltages. As a result of this, electronic noise and thus the rate of random coincidences could vary between the modules. In addition, the multiplexed readout scheme could produce hits on apparently wrong detector modules, even if they are turned off.

Figure 7.8 shows the simulated hit distribution of hits the detector modules with all modules turned on. As expected, the back modules have only small influence on the total count rates.

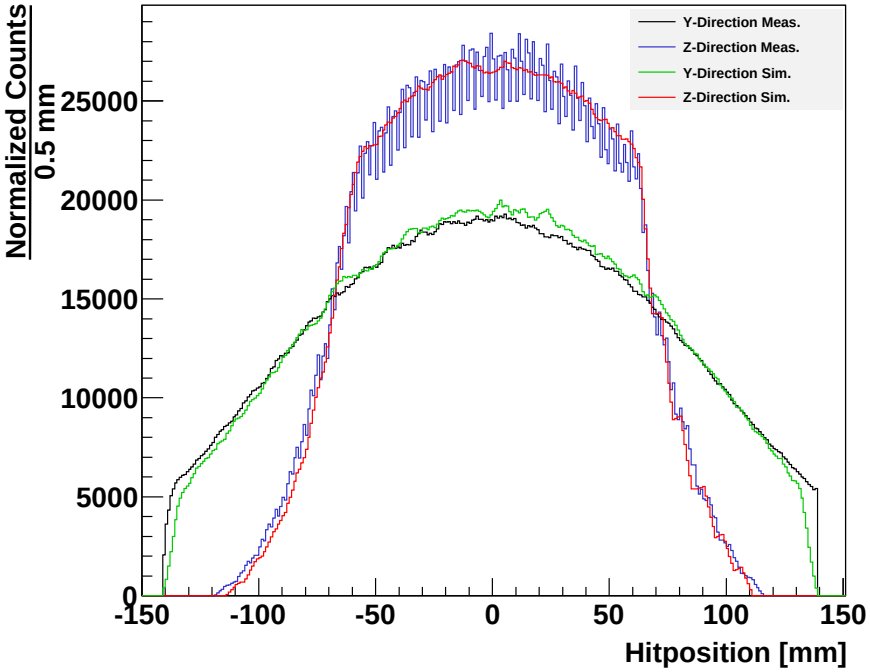

Figure 7.7: Comparison of simulated and measured half-coincidence hit-distributions in Y- and Z- direction. Because of defective modules, only the first six modules are taken into account.

Module Nb.	Measured Half Coincidences [%]	Simulated Half Coincidences [%]
1	24.80 ± 0.02	26.65 ± 0.23
2	20.84 ± 0.02	21.84 ± 0.21
3	17.00 ± 0.01	17.29 ± 0.18
4	14.61 ± 0.01	13.72 ± 0.16
5	11.37 ± 0.01	10.64 ± 0.14
6	4.68 ± 0.01	4.15 ± 0.09
7	3.64 ± 0.01	3.18 ± 0.08
8	3.04 ± 0.01	2.52 ± 0.07

Table 7.2: Comparison of measured and simulated hit-distribution on the modules of 2 detector banks. Modules 6 of bank A and modules 7 and 8 of bank B have been switched off in measurement and simulation because of a hardware failure.

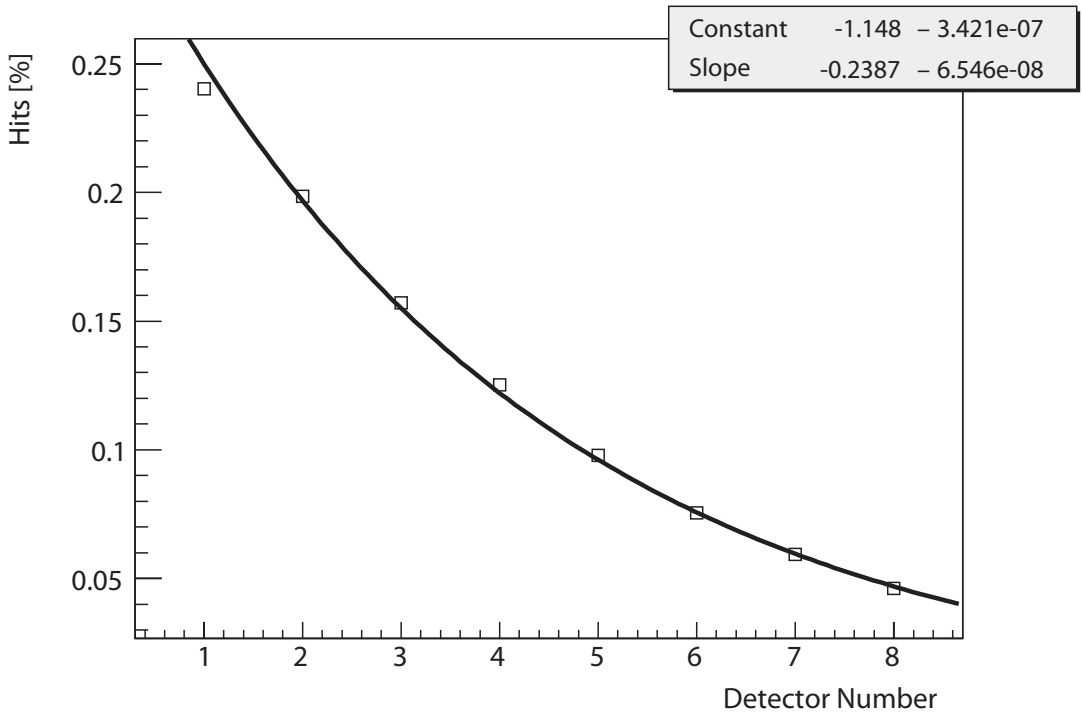

Figure 7.8: Simulated hit-distribution on all quadHIDAC detector modules. Despite different module dimensions the attenuation shows a nearly perfect exponential fall-off.

Absolute Detection Efficiency

Geant4 in its current version 9.0 is not capable of calculating gas gain and avalanche evolution. Hence, the simulation program lists an event at the time an electron enters the gaseous parts of the detector, which are the holes and the MWPC volume itself. The coordinates of the events, which describe the endpoints of the line-of-responses are here the vertex coordinates of the produced electrons. Up to this point it cannot be decided, if the liberated electron interacts with the gas and creates a signal in the detector or not. Therefore, an efficiency factor is proposed, later on called the *f-factor*. It is defined as the ratio of electrons entering the gas over the total number of measured signals and scales the simulated efficiency values to the measured ones:

$$f = \sqrt{\frac{\text{Measured Coincidence Efficiency}}{\text{Simulated Coincidence Efficiency}}} = \sqrt{\frac{0.02}{0.0604}} \approx 0.575. \tag{7.20}$$

The measured value is here taken from data presented in [S$^+$05], which is also shown in Figure 7.1 at low activity values. Here the source was a 80 mm line source with a diameter of 1 mm enclosed by a glass tube. The f-factor was obtained using the coincidence efficiency values and not to the ones for singles because they seem to be more reliable as the quadHIDAC provides no raw data of singles hits but only for coincidences. For singles it returns a total count rate only, which is subject to electronic noise. As a cross-check the simulated singles efficiency $\varepsilon_\gamma^{\text{sim.}} = 19.93\,\%$ was converted using the f-factor to

$$\varepsilon_\gamma = \varepsilon_\gamma^{\text{sim.}} \cdot f = 0.1147. \tag{7.21}$$

A comparable singles measurement can be found in [M$^+$04] with $\varepsilon_\gamma^{\text{meas.}} = 5.79\,\%$ for a 16 module quadHIDAC or extrapolated to 32 modules this would be $\varepsilon_\gamma^{\text{meas.}} = 11.58\,\%$ which is in good agreement with the simulation.
As a first result, looking at the large fraction of undetected electrons, it is proposed to revisit the used argon-di-isopropyl-ether gas composition in order to find a better suited mixture offering a larger ionisation cross section. In the following the f-factor has to be applied to all statements on absolute detection efficiency. It is expected that the f-factor will change with the detector geometry. Especially for simulations in which the geometry is varied this has to be taken into account. As it is not possible to identify the variation without having built adequate prototype detectors, in the following a linear dependence on the detector gas volume is assumed.

Sensitivity for a Line Source

K. Schäfers et. al. have measured the absulute sensitivity of the quadHIDAC for different line source length [S^{+}05]. Since here only the true coincidences are taken into acount, the necessary scatter-correction has been done according to NEMA methods [NEM01]. Assuming a constant scatter fraction and a certain electron detection efficiency described

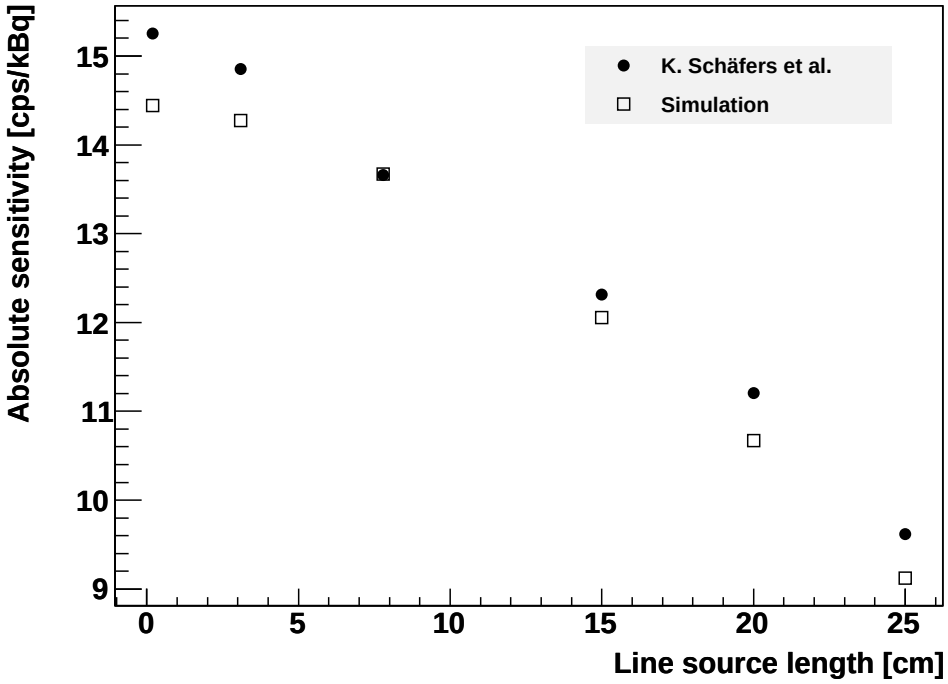

Figure 7.9: Sensitivity measurement and Geant4 simulation using line sources of different length.

by the f-factor, the results of an appropriate Geant4 simulation have been compared with these measurements. Figure 7.9 shows fairly good agreement with the measurements. Nevertheless, a slightly different curvature of the data point progression can be observed. The statistical errors of the simulation data are smaller than the marker size and therefore not visible. The most probable reason for this difference are uncertainties during the realisation of the measurement or their analysis including scatter correction.

7.1.4 Analysis of quadHIDAC System Properties

Intrinsic Energy Cut

Most competing PET scanners provide an energy information which allows scatter rejection by application of energy cuts. The lower cut value is set between 250 keV and

400 keV in most of the commercial scanners. Since MWPC-based scanners do not provide energy information, it is not possible to set such a cut using these devices. Nevertheless it is claimed that the quadHIDAC is not sensitive to gamma radiation below 200 keV [M$^+$04]. The Manchester group has tried to recheck the intrinsic cut of the 16 module quadHIDAC [HRJ$^+$07]. They claim an intrinsic energy cut of 250 keV at which the single efficiency drops to half the value of 511 keV. Unfortunately, because of a lack of adequate sources, they had to extrapolate their result from just two data points below 511 keV. In order to get a more precise understanding of the energy dependence, a simulation of the singles efficiency of both the quadHIDAC and also the MSPET chambers with different converter materials have been performed. Here, an infinitesimal point source of 0.1 μm has been placed in the centre of the field of view. Photons with discrete energies are randomly emitted into all directions. For the MSPET device a detector stack consisting of 50 individual chambers has been used. Figure 7.10 displays the results of the simulations. To be comparable with the quadHIDAC, the efficiencies are normalised to the efficiency obtained at 511 keV. One finds that at 200 keV the efficiency drops below 20% of the value at 511 keV and the 50% value is compatible to the measured value considering the obvious measurement difficulties due to the missing energy information.
For the MSPET device the intrinsic energy cut is shifted about 100 keV towards lower energies. This can be understood by the fact that the effective converter thickness is thinner than in the holes of the HIDAC, where additional insulation material limits the range of low energy electrons. While there is a poorer trend of intrinsic scatter suppression, the MSPET may provide some SPECT (≈ 140 keV) or even X-ray CT ($\approx 50-100$ keV) capabilities, although with poor efficiency.

7.1.5 Energy Information in MWPCs with Converters

Energy information in PET is often used to discriminate between trues and scatters. A major drawback of the quadHIDAC and other MWPC-based PET cameras with electron converters is the missing energy information. This is mostly due to the photon to electron converter itself. An electron that is liberated by a photon incident on the converter will undergo multiple scattering before it will transverse the converter's surface and is measured in the MWPC. Thus the energy of the measured electrons is only weakly correlated with the original photon energy. Figure 7.11 shows the energies of electrons entering the gaseous part of the detector. Trues and scatters spectra are normalised to the count rate of the true spectra. The original singles count rates are noted in the statistics box. Here, the full-energy photo peak caused by photoelectric effect of 511 keV photons is shifted to an energy of 423 keV due to the 88 keV binding energy of K-shell electrons in lead. Entries between 423 keV and 511 keV are caused by photoelectric effects in L- and M-shells

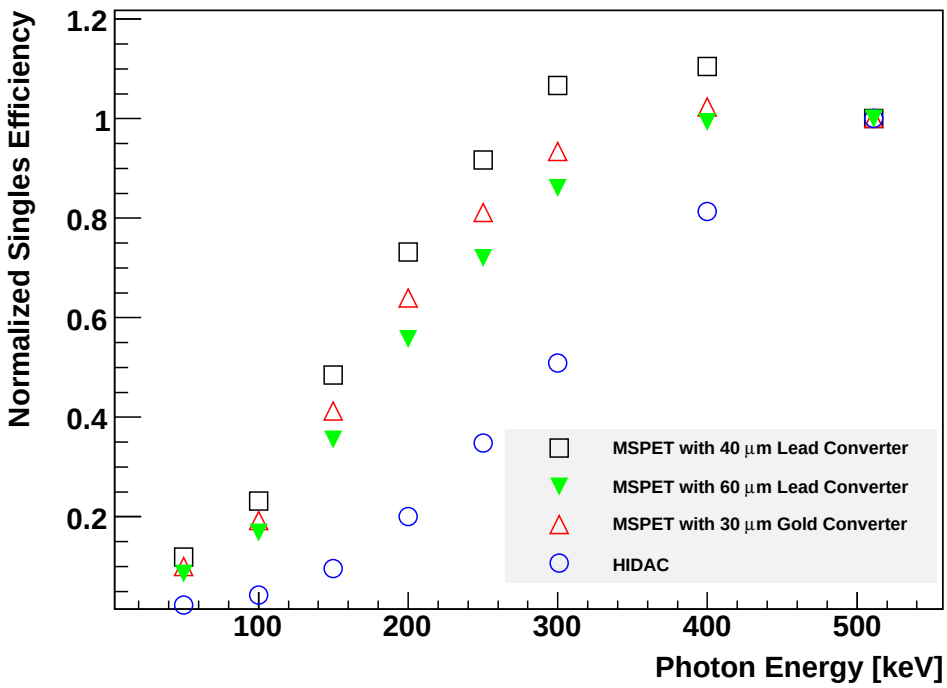

Figure 7.10: The singles efficiency has been simulated for photons emitted at the centre of the FOV with energies up to 511 keV. There is no clear energy cut off visible. At the published intrinsic cut off at 200 keV [M^{+}04] the efficiency drops below 20% of the efficiency at 511 keV. The MSPET detector is more sensitive to lower energies, so that a larger scatter fraction is expected. On the other hand this offers the capability to detect SPECT and also to some extend CT radiation.

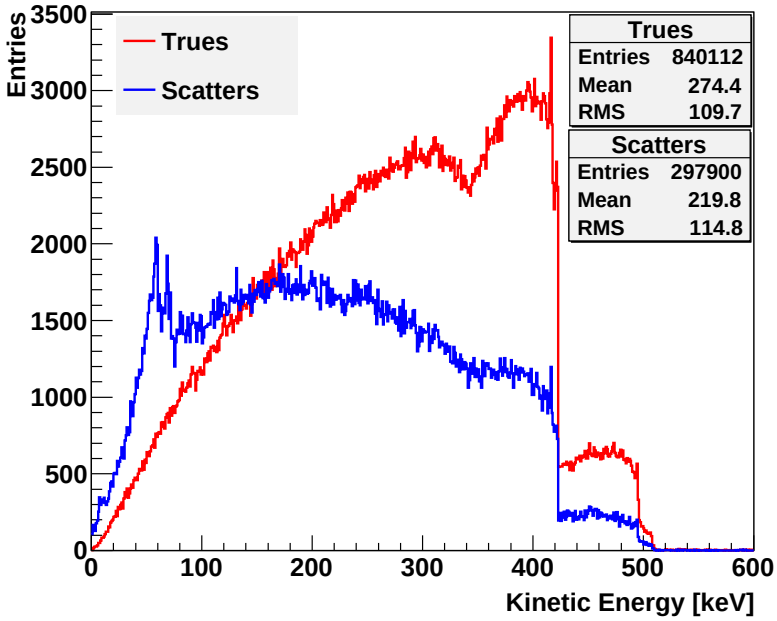

Figure 7.11: Energy spectra of electrons liberated in the HIDAC converters. For better visual comparison, the number of entries in the scatters spectrum has been normalized to the trues count rate.

with lower cross sections. Binding energies are here $13-15.8\,\mathrm{keV}$ for the L-shell and $2.5-3.8\,\mathrm{keV}$ for the M-shell respectively. The compton edge is found at

$$E_e'(180^\circ) = \frac{2E_\gamma^2}{m_e c^2 + 2E_\gamma} = 340.7\,\mathrm{keV}, \tag{7.22}$$

with $E_e'(180^\circ)$ being the energy of a liberated electron caused by Compton scattering with an scattering angle of 180°. $E_\gamma = 511\,\mathrm{keV}$ is the incident photon's energy. Below this energy the Compton continuum begins. Due to multiple scattering of the liberated electrons on their way to the surface, the gap between Compton edge and full energy peaks disapears. It can be seen that both, trues and scatters produce electrons with a broad spectum down to low energies. Therefore, it is hard to apply an energy cut in order to discriminate trues and scatters. Nevertheless one can use these spectra to estimate energy dependent scatter probabilities in reconstruction algorithms. Figure 7.12 shows the corresponding plots for MSPET geometries with a single-sided gold and a double-sided lead converter. The difference of trues and scatters is a little more pronounced than in the HIDAC geometry.

The major problem of scatter suppression in flat-converter-based MWPCs like the

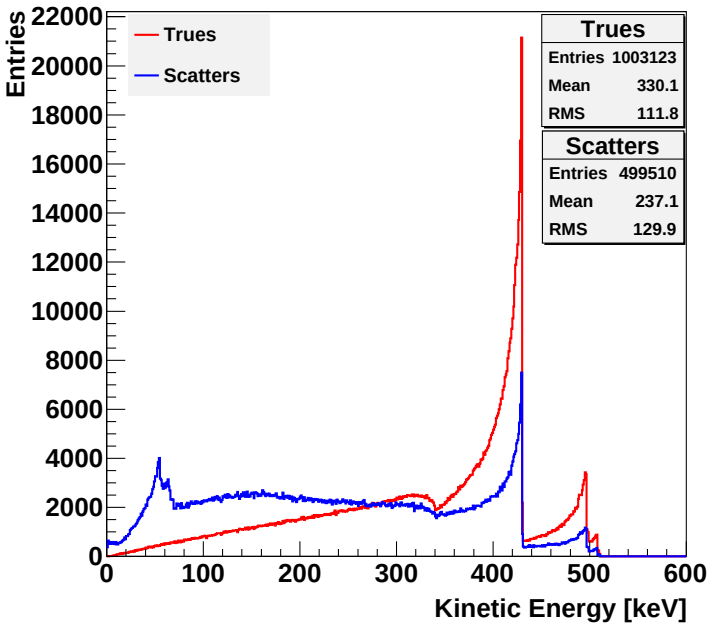

(a)

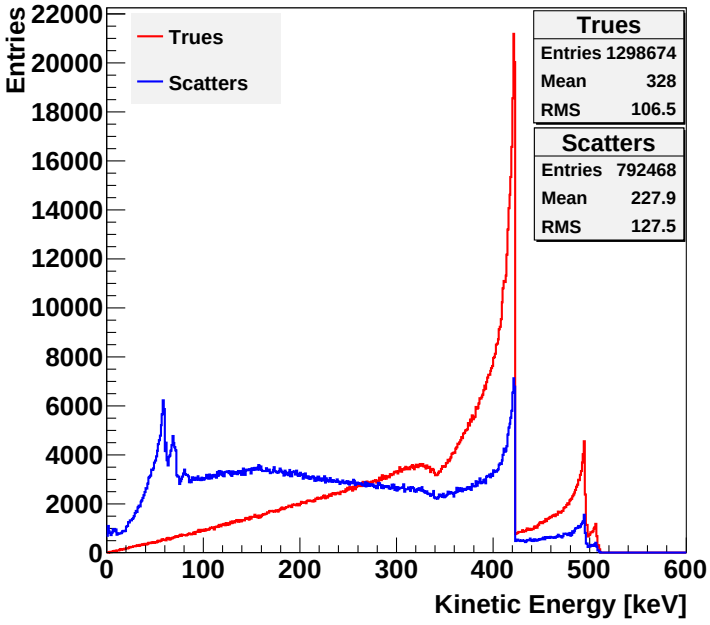

(b)

Figure 7.12: Energy spectra of electrons liberated in the MSPET converters. For a better visual comparison, the number of entries in the scatters spectrum has been normalized to the trues count rate. Panel (a) displays the results for a single-sided 30 μm gold converter, while in (b) a double-sided 40 μm lead converter is used. The differences are caused by different electron binding energies in lead and gold.

MSPET is shown in Figure 7.13. It can be seen that the number of free electrons in the detector shows a stronger dependence on the exit angle of the electron leaving the converter than to the particles energy. Since the angular distribution of these electrons is broad (see Figure 6.15), the measured pulse heights carry little information of the original photon energy.

For the quadHIDAC the converter itself rather than the exit angle will impede any energy information. The pulse height here depends mainly on the electric field in the holes of the converter and the position of the primary ionisation in the hole. As this field is quite irregular and the avalanche size undefined, no information on particle energies can be derived. In conclusion, this kind of detectors cannot be used to discriminate trues and scatters by measuring the deposited energies. Also advanced PET applications like Compton cameras are not realisable using HIDAC or MSPET technologies.

Nevertheless, the converters of both, MSPET and quadHIDAC can be optimised in order to reach the best efficiency at 511 keV by variation of the material thickness and hole design. Lower photon energies, and thus scatters are suppressed then.

7.1.6 Quantitative PET with the quadHIDAC

For a quantitative description of PET images it is necessary to identify the contributions of trues, scatters, randoms and detector noise (see Section 3.2). The quantity as well as the spatial distribution of these constituents has to be known in great detail.

The goal is the separation of the true, unscattered events within the blurring background. First approaches usually aim towards a scatter discrimination by the measurement of the particle energy. However in case of MWPC-based detectors with solid converters this is not an option, as already discussed in the previous subsection. The approach to solve this problem is now to make use of proper detector simulations. In the simulations it is comparably easy to identify the needed components in the data since the particle energies as well as possible scatter processes can be retained and analysed. Figure 7.14 shows the dependence of the module number on the fraction of scattered events simulated for the quadHIDAC. Simulations show that the mean scattering probability is 45.4% for all modules. As shown in Figure 7.14, hits detected in the outer modules show a higher scattering propability, as expected. A correction for scattering can now include the quantitative knowledge of the spatial distribution of scattered events. Therefore, the obtained simulation output has been visualised using an adequate graphic rendition: parallel projections. The results of such a Geant4 quadHIDAC detector simulation are shown in Figures 7.15 and 7.17. One can see the parallel projections of a line source, a mouse phantom and a rat phantom which have been placed in the centre of the FOV of the simulated quadHIDAC scanner. The total hit distribution, marked in black, can be split up

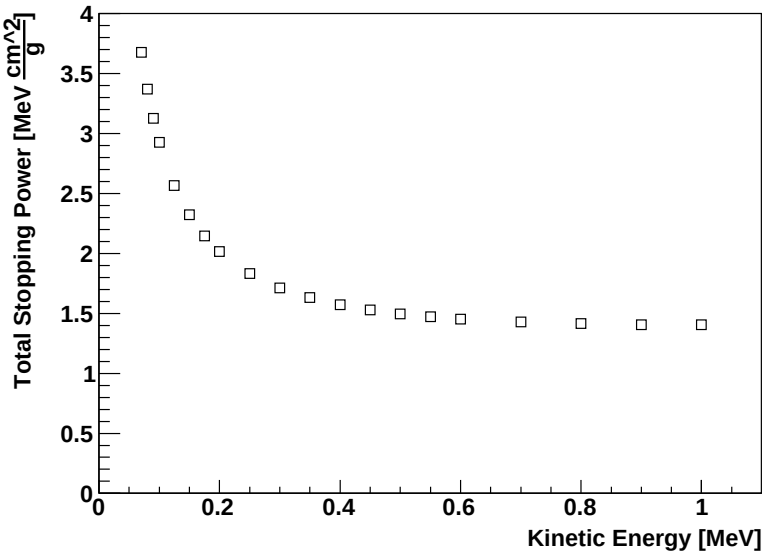

(a)

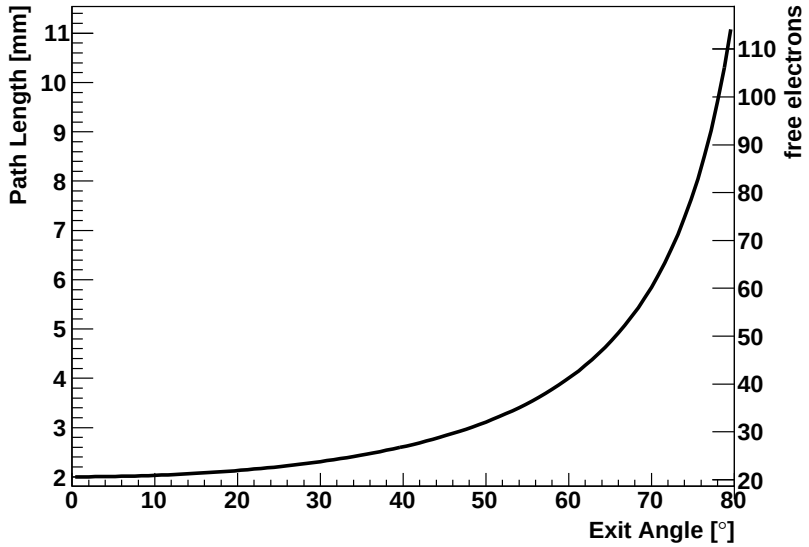

(b)

Figure 7.13: Panel (a) shows the energy dependence of the $\frac{dE}{dx}$ variation for electrons in argon gas [M. 09]. Since the energy loss is directly connected to the number of gas interaction encounters, it influences the number of primary electrons in the gas. For relevant energies between 100 keV and 500 keV changes of $\sim 60\%$ are observable. Panel (b) shows the variation in free electrons depending on the exit angle of the primary electron out of the converter with the approximation of the electron being a minimum ionising particle. The value of 10.3 free electrons/mm counts for m.i.p.'s ($\beta\gamma \approx 3$) and was published by the Particle Data Group [Par98].

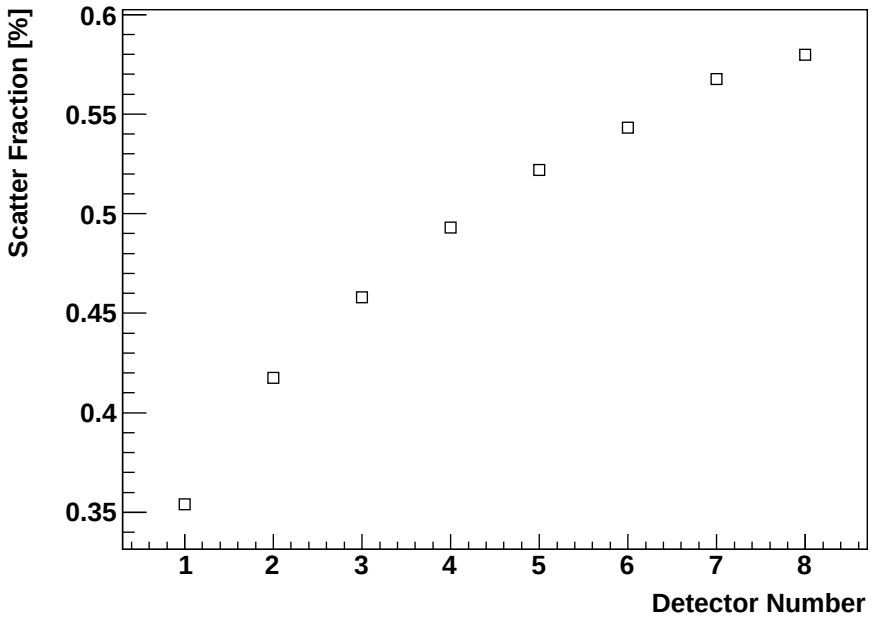

Figure 7.14: Simulated fraction of scattered events measured by the quadHIDAC depending on the module number.

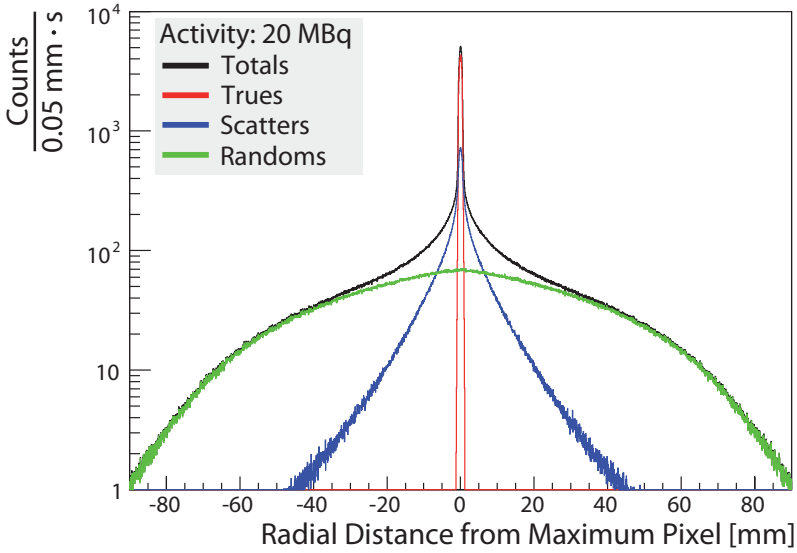

(a)

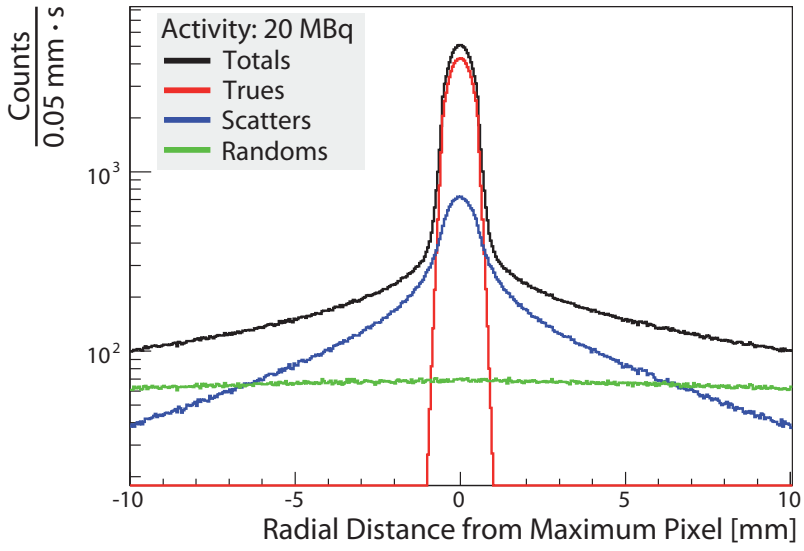

(b)

Figure 7.15: Parallel projection of the results of a Geant4 simulation of a line source with an activity of 20 MBq in the quadHIDAC. As can be seen in Panel (b), the broad distribution of the randoms can be approximated with a constant in the relevant areas.

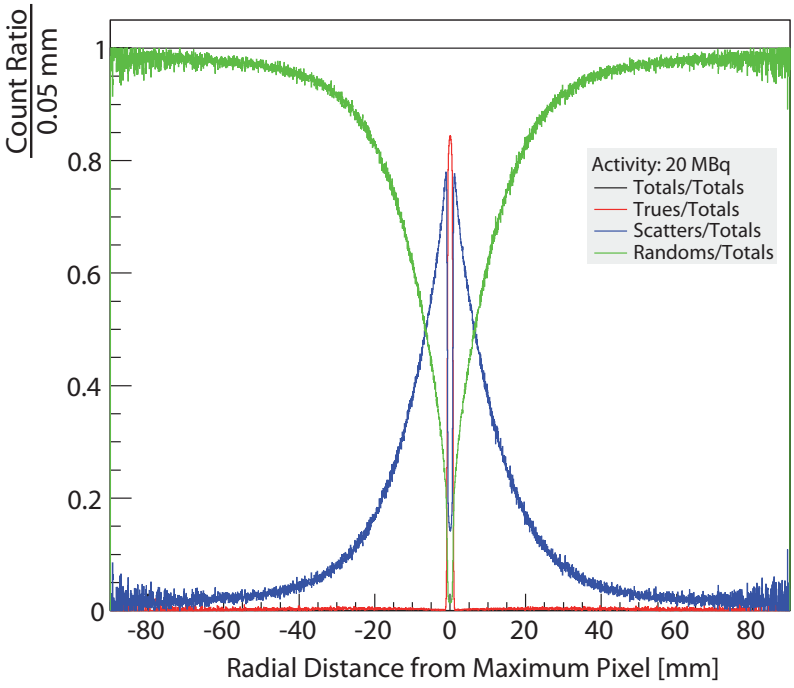

(a)

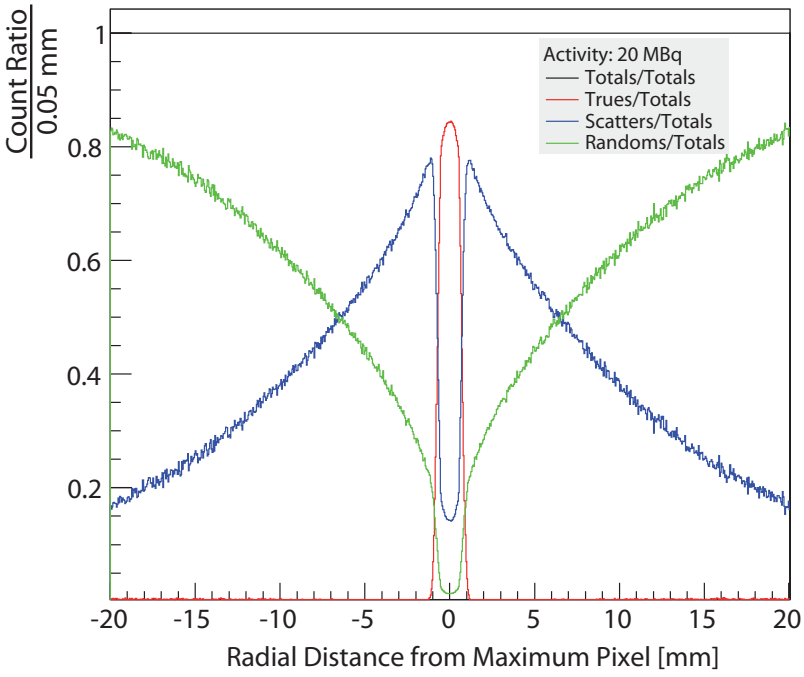

(b)

Figure 7.16: A different representation of Figure 7.15. Shown are the ratios of trues, scatters and randoms to the overall distribution of a line source. For a more detailed view panel (b) shows a zoomed view.

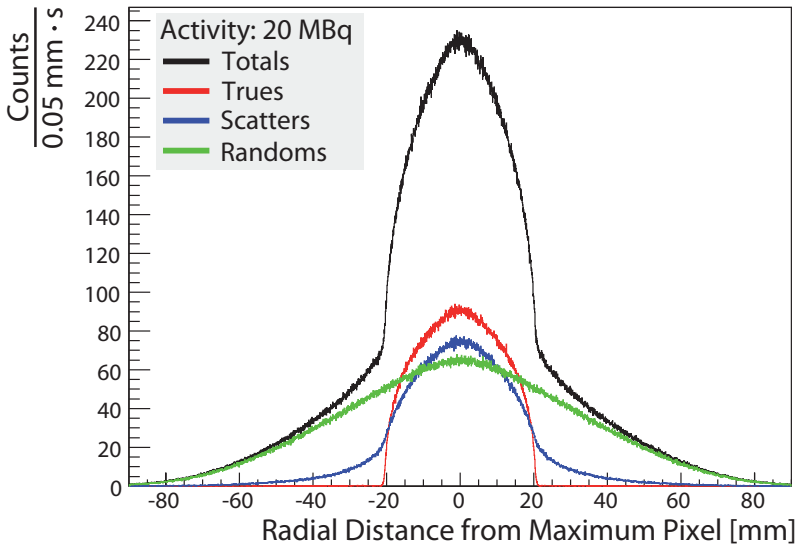

(a)

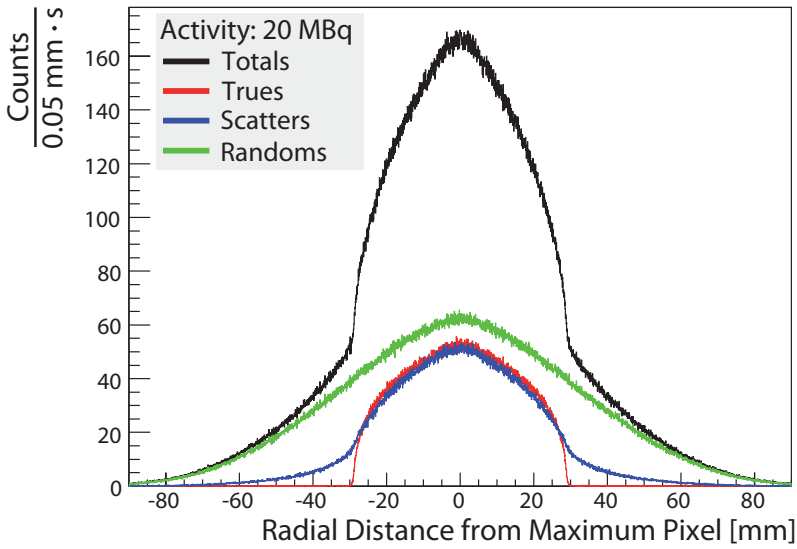

(b)

Figure 7.17: Parallel projection of the results of a Geant4 simulation of a mouse phantom (a) and a rat phantom (b) source. The number of randoms was again adapted to a source activity of 20 MBq. Note the linear scale used here.

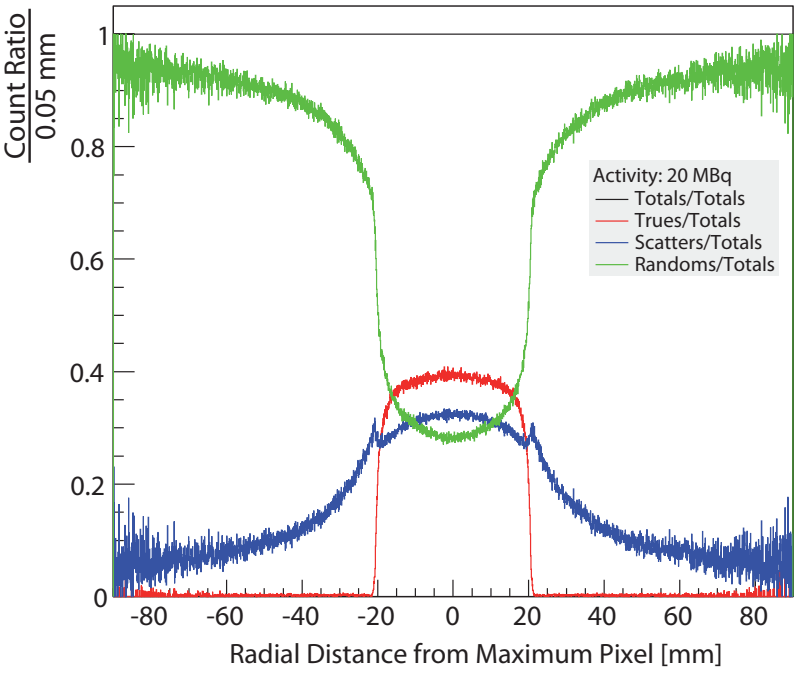

(a)

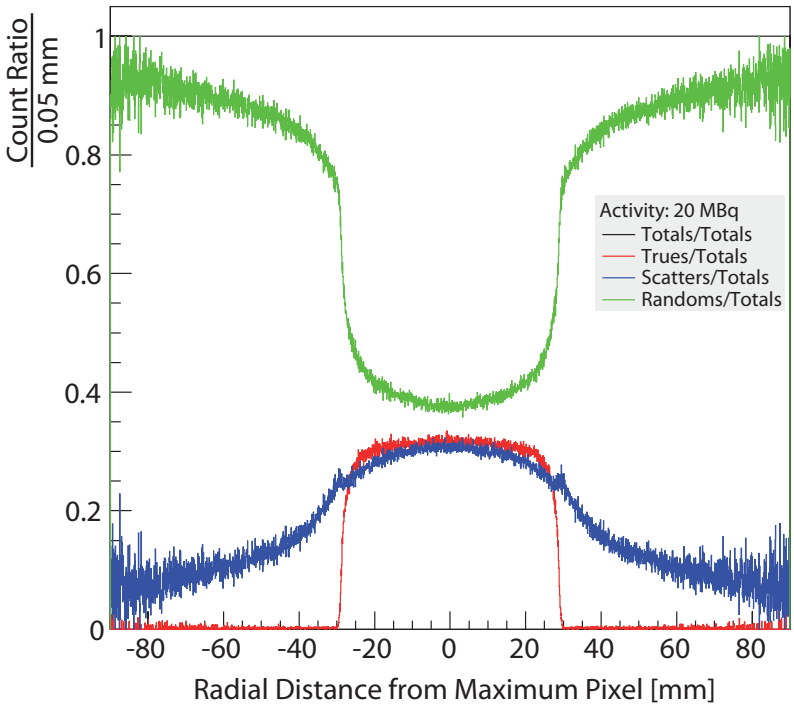

(b)

Figure 7.18: A different representation of Figure 7.17. Shown are the ratios of trues, scatters and randoms to the overall distribution of a mouse phantom (a) and a rat phantom (b).

into its components. One can identify the trues within the source volume, while scatters are peaked, but broader in their distribution. Random coincidences have been scaled to an activity of 20 MBq, which is typical for a real measurement. Here a coincidence window of 40 ns and the measured efficiencies displayed in Table 7.1 have been considered. Figures 7.16 and 7.18 show the fractions of trues, scatters and randoms to the overall distributions. It can be seen, that randoms dominate the outer areas of the distributions. In case of a mouse- or rat phantom source, randoms dominate even the whole distribution. An slight increase of scatters can be observed in the glass hull of the line source and the polyethylene hull sourounding the other two sources respectively.
For the scattered events, it is conspicuous that most of the counts are still found inside the source volume. That means that a large fraction of the scatters occurs at small scattering angles. This is interesting, because the common methods of scatter discrimination published by NEMA [NEM01] assume a linear extrapolation of the shoulders of the totals distribution.
Therefore one has to conclude that the NEMA method underestimates the scatter fraction in the central peak region. On the other hand one can discuss the meaning of a *true* event in the context of PET, meaning perhaps not necessarily a non-scattered-, but an event whose LOR is still close to the original one, allowing small scattering angles. Nevertheless such a question does not arise for practical applications due to the limited energy resolution of common detectors.
In this thesis a scattered event is called *scattered*, if one or both of the participant particles have undergone a physical scattering process before being detected, no matter whether the scattering angle was small or large.

7.1.7 Different Methods for the Estimation of Randoms

Depending on the activity of the used tracer and the coincidence time window of the device, the fraction of random events can become very large. For the case of the quadHIDAC this fraction can reach 35 % of all counts for an activity of 20 MBq, as indicated in Figure 7.1.
Therefore a quantitative analysis of PET images requires not only the information on the total number of random events, but also their spatial distribution depending on the shape and position of the source volume.
A good method to describe this distribution is to measure independent single photon incidences and then combine them to coincidences. Some PET devices provide intrinsic random subtraction based on the so-called delay line method. Here a positron emitter is measured while a time delay of more than the nominal coincidence time window is applied to one of the two opposite detectors. The problem with this method is the quite poor

count rate and the additional statistical noise in the time frame. The quadHIDAC neither provides raw data of single events, as it stores only coincidence events, nor is a delay line foreseen to determine random distributions.
A method proposed by A. Divoli et. al. [DED+04] uses a distribution of shuffled half-coincidences to generate pseudo-random events. Information on the singles is not needed. The method was developed for a large area PET detector called PETRRA, which is comprised of BaF_2 crystal detectors and MWPCs [DFE+05]. In order to validate the applicability of this method for the quadHIDAC scanner, simulations of point-like sources with 1 mm diameter in different positions of the FOV of the quadHIDAC have been performed. For a later comparison of these simulations with measurements, a full four block quadHIDAC has been emulated by switching the coordinate system in one of two simulation runs and merging the two simulated data sets as described in Section 5.3.1. The raw single data of these simulations have been used to produce an authentic random coincidence distribution. In addition, the filtered coincidences of these data sets have been shuffled and combined to random coincidences following the method of A. Divoli et. al..
To get a full picture of the situation, adequate random coincidence measurements have been done using a single photon emitting ^{137}Cs source, placed in corresponding positions in the FOV. Figure 7.19 now shows the results of the analysis. One can clearly see that the simulated randoms distribution produced from the singles data fit well at all positions with the measured ^{137}Cs source. The method of Divoli et. al. on the other hand fails, when the source is not placed in the centre of the FOV. While for crystal scanners with a quite small FOV this is not really a problem, the method seems to be inapplicable for quantitative statements in off-centre positions in the large FOV of the quadHIDAC.
In clinical practice often up to four mice are imaged at the same time with the quadHIDAC, where none of them is placed in the centre of the scanner. For a quantitative randoms correction using the shuffled half-coincidence method, these mice placed off-centre are not convenient because of the inconsistent estimate of the randoms fraction.

7.1.8 Discrepancy of Measured and Simulated Randoms

The number of random coincidence background is provided by the quadHIDAC. Based on the number of measured single events, the quadHIDAC provides a calculated number of randoms based on the system dead time and the coincidence window. Since this number relies on the correct determination of the singles quantity, the results from these calculations can be questioned when looking at the pulse shapes. Single pulses measured on the anodes of a quadHIDAC module are shown in Figure 7.2. Especially panel (b) indicates that the trigger level for single event registration does not discriminate efficiently between noise and real events. Even oscillations, seemingly caused by the quadHIDAC's

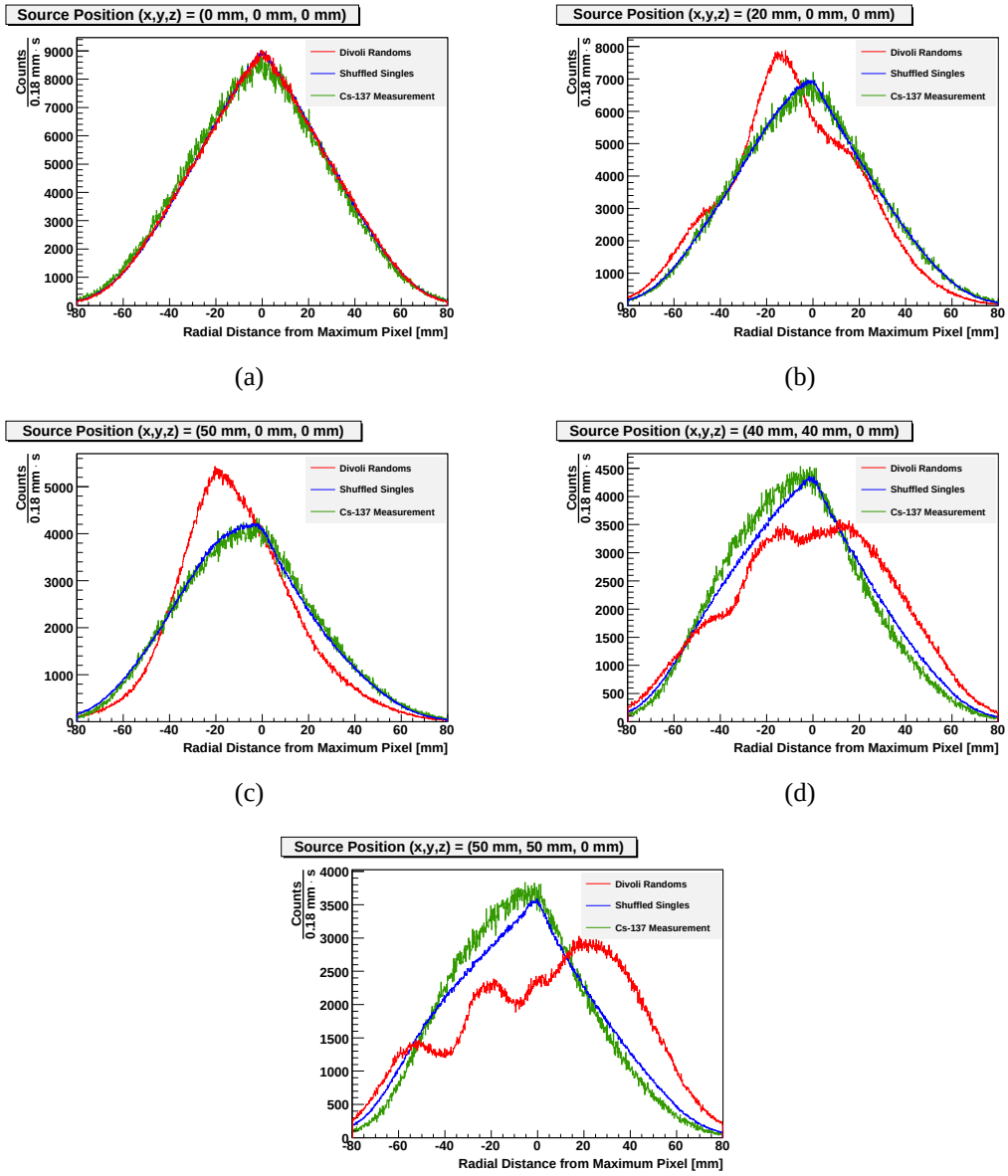

Figure 7.19: Comparison of different randoms distribution estimation methods for point-like sources placed in different positions of the FOV. While the ^{137}Cs measurements and the simulations produce comparable results, the method proposed by A. Divoli et. al. fails for sources off-centre shifted.

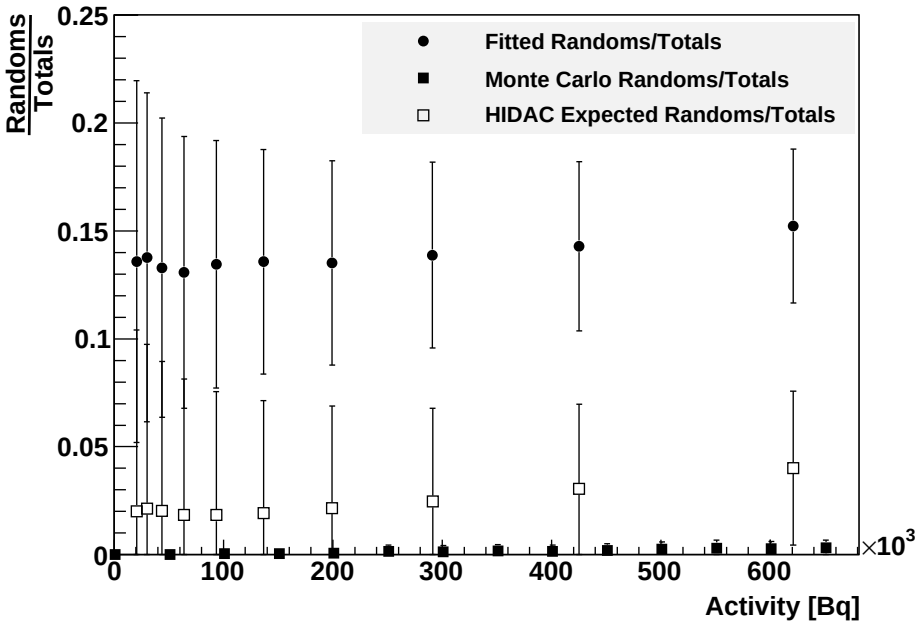

Figure 7.20: Differences between observed, calculated and system-expected randoms fractions in the quadHIDAC. For the fitted values, randoms have been added to a simulation, until the tails of the parallel projections fitted to the corresponding measurement. Monte Carlo randoms have been obtained following Section 7.1.1. HIDAC expected is the number of randoms that is output by the quadHIDACs DAQ itself.

power supply or other devices sharing the same electricity circuit lead to frequent triggers. In addition, detector aging is a problem in the quadHIDAC. Heavy deposits caused by polymerisation in the gas has been observed on the wires and in the holes of defective modules (see Figure 7.21). As this influences the electric field of the MWPC, error prone measurements and increased sparking will lead to increased single rates.

An alternative ansatz for randoms quantification can be made using simulations as they

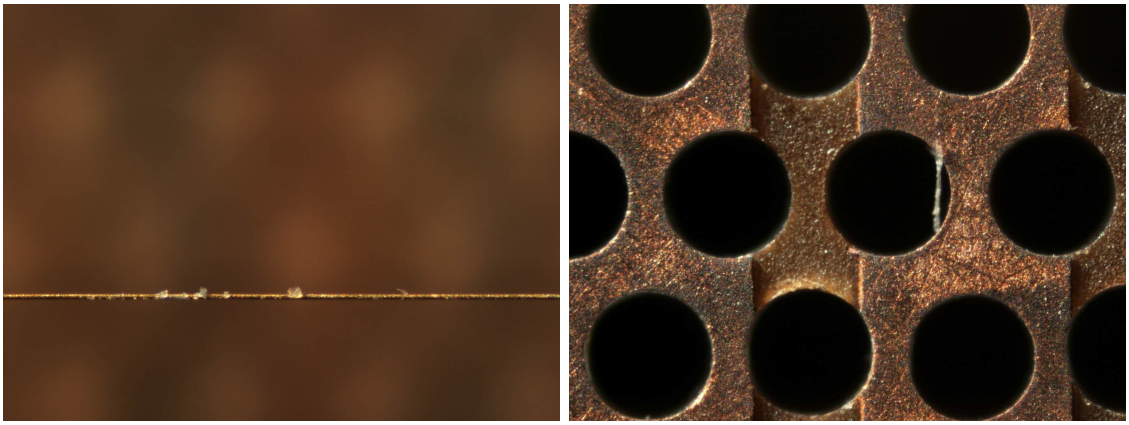

Figure 7.21: Polymerisation crystals grow on wires (a) and in converter holes (b) and lead to detector defects.

are shown for example in Figure 7.15. In areas far away from the centre of the FOV, the parallel projections are dominated by randoms. Hence, the quantity of randoms can be obtained by fitting a known randoms distribution to these parts of the measured totals distribution. The randoms distribution can be taken from a ^{137}Cs measurement, an adequate simulation or a shuffled half coincidence distribution of a centred point-source measurement.

The randoms count rate is given by the data aquisision system of the quadHIDAC, which calculates its quantity on the basis of singles count rates. Independently, and under the assumption that the dead time model is known, the number of randoms can also be simulated using the Monte Carlo code described in Section 7.1.1. As a third method, one can use parallel projections of a measurement and a comparable simulation containing no randoms at all. A randoms distribution is then added to the simulation until the projections fit each other.

Using a point source with a very low initial activity of $a = 1.3\,\mathrm{MBq}$ these three methods have been applied for different subsets of the measured data indicating different activities. The results are shown in Figure 7.20.

One can see that the quadHIDAC overestimates the number of randoms expected by the simulation (as already mentioned in Section 7.1.1), but underestimates the number that

is based on the parallel projection fit method. As a result of this observation, it is concluded on the one hand, that the number of singles is too high, which leads to an increased number calculated by the HIDAC. This is reasonable, looking at the anode signals shown in Figure 7.2. On the other hand, the parallel projections are influenced by a distribution shaped like a randoms distribution. The origin of this distribution is most likely not caused by classical randoms but by detector noise.

7.1.9 quadHIDAC Detector Noise

As a possible reason for the randoms discrepancy in the first place detector noise is considered. In order to verify this suggestion, a quadHIDAC measurement without any radiation source has been performed. The result should be a good approximation of a randoms distribution. During 48 hours of data taking, 745.000 coincidences have been recorded. The parallel projections of this measurement data is shown in Figure 7.22. One can see that the

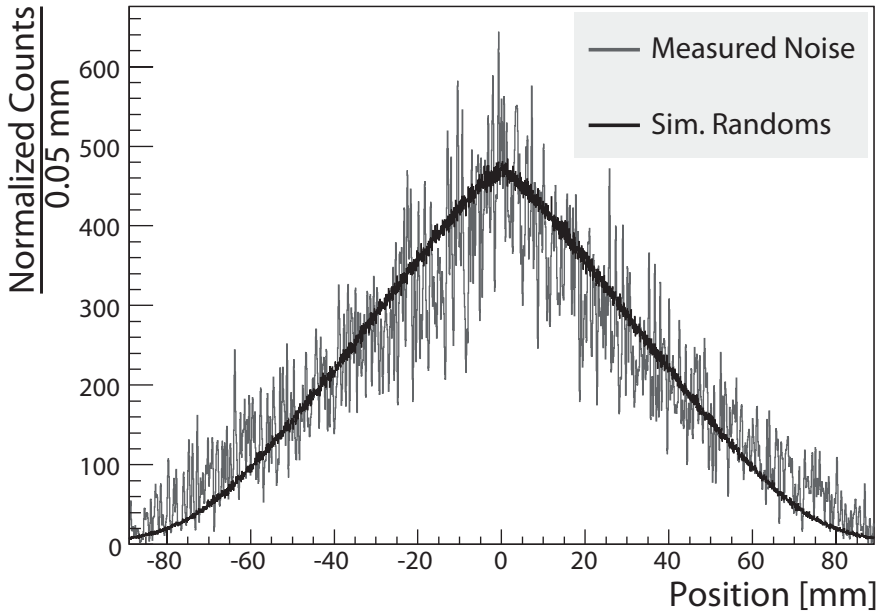

Figure 7.22: Noise measurement of 48 hours compared with the shape of a normalised randoms distribution. It can be concluded that detector noise can be described by a randoms distribution.

measured distribution is in good agreement with a simulated randoms distribution. This indicates that electronic noise cannot be separated from randoms and therefore might be a possible explanation for the quadHIDACs hit distributions. However, the total quantity

of the recorded events corresponds to a 15 minute measurement, and is therefore orders of magnitude too small to explain the observed difference.
A possible reason might be that the noise itself depends on the applied radiation activity in the scanner. Another possibility for the random like distribution are misinterpreted real coincidence events. Due to the channel-grouping read out scheme of the quadHIDAC, explained by Figure 3.14, it is possible that small disturbances in the clock cycle of the multiplexed read out can shift the measured positions nearly randomly across the FOV. As an indication for a problem here, it has already been observed, that depending on the clock timing, counts are measured by the DAQ-PC even on modules that are switched off. Unfortunally it is not possible to test this theory without detailed knowledge on the quadHIDACs read out electronics. Since this information is not available, massive reverse engineering efforts or, more likely, new detector read out electronics for the quadHIDAC modules are needed at this point.

7.1.10 Quantification of a Point Source Measurement

As a demonstration of the capabilities offered by the Geant4 simulations, a point source measurement with the quadHIDAC has been quantified using an adequate simulation. The measurement was done with a small point source with initially unknown diameter that was placed in the centre of the FOV. The sponge source was drained with FDG. The exact position of the source was determined by comparison with reconstructed images as $(x,y,z) = (-0.65\,\text{mm}, 3.25\,\text{mm}, 0.65\,\text{mm})$. The diameter has been determined by comparing parallel projections of simulations to the measurement as $d = 3.2\,\text{mm}$. For the best agreement, the active source volume has been encapsuled in a 1 mm thick water jacket in the simulation. Figure 7.23 shows the parallel projection of both the simulation and the measurement. The double peak structure can be explained by the slight off-centre position of the point source. It would be possible to correct for that in the projection algorithm, but since this would lead to an asymmetrical distribution on both sides of the central peak, this operation has been omitted. The simulation has been scaled to the integral of the measurements count rate. One can see that the green curve, consisting of simulated true and scattered events does not fit to the measurement exactly. Mostly in the areas far away from the centre of the FOV a lack of count rate is observed. As a result of this, the double peak of the simulation appears nearly 20 % too high. In the previous section it has been shown that noise or noise-like true coincidences blur the measured distribution. Hence, a noise distribution shown in Figure 7.22 has been added to the simulated data, so that the resulting distribution now contains 16.9 % of noise. With nearly perfect agreement, the violet curve now fits to the measured distribution. Hence, it can be concluded that a mea-

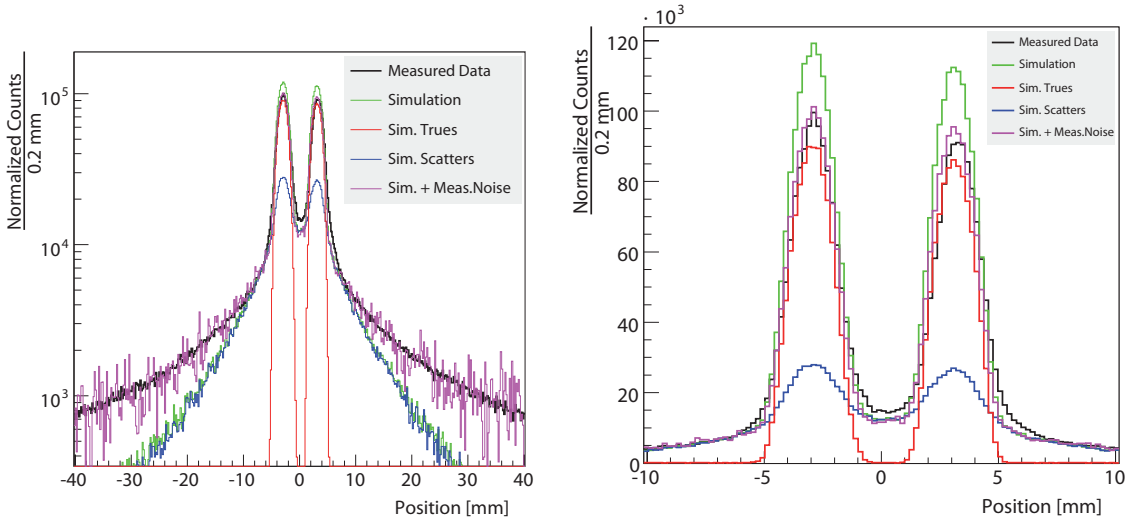

(a) (b)

Figure 7.23: Comparison of a point-source measurement with an appropriate simulation. The double peak is a result of a slightly off-centre positioned source. As the initial activity of the source was very low ($a = 1.3\,\mathrm{MBq}$), the random events are negligible.

sured distribution of a known source can be split up by the use of adequate simulations into its constituents trues, scatters, randoms and noise.

7.1.11 Advanced quadHIDAC Converter Design

As already described above, the quadHIDAC converter has a very sophisticated design and provides good photon conversion efficiency. It was shown that this efficiency cannot be matched by a reasonable number of conventional MWPCs with simple metal foil converters. But even though its specifications are already prominent in the field of MWPC-based PET devices, the design of the quadHIDAC has still potential for improvements. It would be important to replace all hard-to-machine materials by materials which are easier to handle and less toxic in order to simplify machining and assembly. First of all, the lead converters should be replaced by converters consisting of a more stable lead alloy, a not too hard tungsten alloy or even gold. Nevertheless, the material choice should not decrease the performance of the device. Presumably geometry variations are needed to optimise the design for the changed materials. In order to propose an improved converter design, simulations for different materials and converter designs have been performed. Figure 7.24 and Table 7.3 shows the influence of certain parameters of the quadHIDAC design on the efficiency of the detector. Listed are the simulated efficiencies, which may

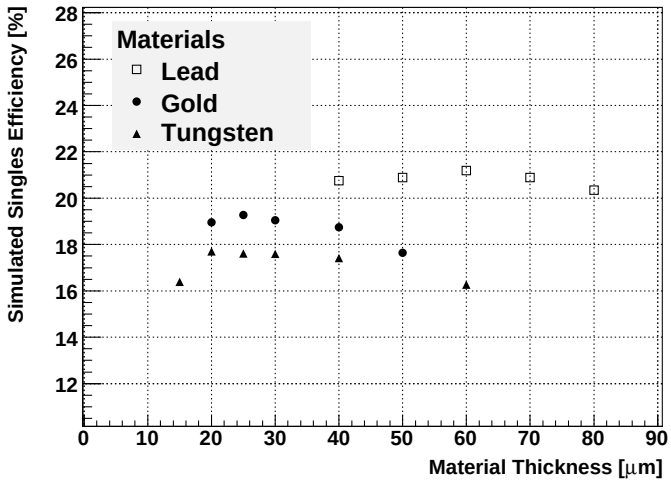

(a)

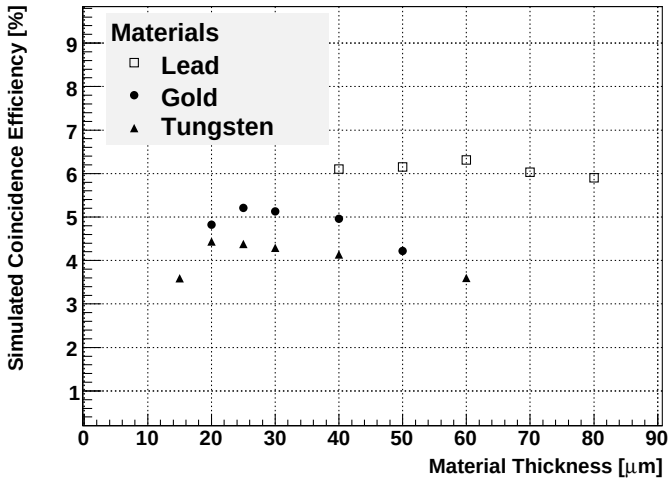

(b)

Figure 7.24: Simulation of the detection efficiencies for (a) single hits and (b) coincidences as a function of the converter material and thickness. The hole diameters and separations has been kept at $0.4\,\mathrm{mm}/0.5\,\mathrm{mm}$. A line source was used as source volume.

vary from the real efficiency because the electron detection probability, already described in Section 7.1.3 and not considered within these results.

Table 7.3: Simulated efficiencies with different material configurations in a quadHIDAC design.

ConverterDesign	Simulated Singles Efficiency [%]	Simulated Coinc. Efficiency [%]
16 Layers 60 μm Lead 140 μm Insulation Hole Diameter: 0.4 mm Hole Separation: 0.5 mm Entrance Foil: 50 μm (Standard quadHIDAC design)	21.19 ± 0.15	6.31 ± 0.11
24 Layers 25 μm Gold 140 μm Insulation Hole Diameter: 0.4 mm Hole Separation: 0.5 mm Entrance Foil: 30 μm	22.17 ± 0.15	7.18 ± 0.12
32 Layers 25 μm Gold 140 μm Insulation Hole Diameter: 0.4 mm Hole Separation: 0.5 mm Entrance Foil: 30 μm	23.41 ± 0.16	8.11 ± 0.13
32 Layers 25 μm Gold 25 μm Insulation (Kapton Foil) Hole Diameter: 0.4 mm Hole Separation: 0.5 mm Entrance Foil: 30 μm	15.51 ± 0.13	3.23 ± 0.08
32 Layers 25 μm Gold 25 μm Insulation (Kapton Foil) Hole Diameter: 0.1 mm Hole Separation: 0.125 mm Entrance Foil: 30 μm	38.37 ± 0.20	19.15 ± 0.20
32 Layers 25 μm Gold 140 μm Insulation Hole Diameter: 0.1 mm Hole Separation: 0.125 mm Entrance Foil: 30 μm	39.51 ± 0.20	22.92 ± 0.21
32 Layers 25 μm Tungsten 140 μm Insulation Hole Diameter: 0.1 mm Hole Separation: 0.125 mm Entrance Foil: 40 μm	37.95 ± 0.20	21.21 ± 0.21

Table 7.3: Simulated efficiencies with different material configurations in a quadHIDAC design.

ConverterDesign	Simulated Singles Efficiency [%]	Simulated Coinc. Efficiency [%]
32 Layers 60 μm Lead 140 μm Insulation Hole Diameter: 0.1 mm Hole Separation: 0.125 mm Entrance Foil: 50 μm	43.56 ± 0.21	27.88 ± 0.24

An interesting aspect of these results is that not only the thickness of the high-Z converter material, but also the thickness of the interspersed insulation sheets plays an important role when optimising for efficiency. It seems as if the liberated electrons escape more easily through the low-Z insulation as through the converter material itself.
In conclusion, an optimised HIDAC converter would have an increased number of alternating insulation/converter material layers. Lead is still the first choice material, but due to its difficult machining properties, gold is also a good alternative. The hole diameter and separation should be smaller, where the ratio of diameter and separation needs to also consider the spatial resolution, as will be shown in the next section.
In reality some of these suggestions will be challenging to realise. Most of all, the production of small equidistant holes in a multilayer construction is not easy, especially when using lead as converter material. Lead in the holes has the tendency to smear during drilling and therefore to produce shortcuts between the different layers which would immediately destroy a converter. In addition, sharp edges or disturbances in the drilling channels will disturb the electric field in the holes and therefore reduce the electron efficiency. Since these disturbances will get worse with increasing hole depth, an increase of conversion/insulation layers may be challenging.

7.1.12 Spatial Resolution

The determination of the spatial resolution using simulated data is non trivial since the exact signal generation process in the quadHIDAC has not been investigated yet. In an classical MWPC the signal is usually created on a single wire, which means that the wire separation is the limiting factor for the position resolution perpendicular to the wire direction. Since in the quadHIDAC avalanches of electrons are created already in the converter, it seems feasible that multiple wires participate so that the centre of charges might be detected even in between the wires.
The simulation itself does not allow to determine the intrinsic spatial resolution of the detector, as it outputs the creation point of the electron entering the gaseous parts of the detector without any signal generation processes included. In order to obtain a value, one

has to make certain assumptions in order to modify the output of the simulation.
The real quadHIDAC returns not only the number of the module in which a hit has occurred, but also the converter. This information is gained by comparing the pulse heights on the pad planes on both sides of the wires. A proper cut value is implemented in the HIDAC electronics or software [J+99]. Following this knowledge, all simulated hit positions have been shifted to the centre of the converter in which they have been generated.
As non-collinearity of annihilation photons, described by Equation (3.12), is not implemented in the Geant4 version used, all hit positions have been smeared to account for this effect.

Separation [mm]	Diameter [mm]	Expected Sensitivity [%]	True Coinc. Fraction [%]	Spatial Resolution Smeared to Holes [mm]	Spatial Resolution Smeared to Wires [mm]
0.5	0.4	2.06	54.9	1.27 ± 0.003	1.506 ± 0.003
1.0	0.8	0.81	57.6	1.396 ± 0.004	1.648 ± 0.002
0.5	0.45	2.70	54.5	-	-
0.5	0.2	0.24	52.5	-	-
0.25	0.2	4.23	51.1	1.277 ± 0.002	1.565 ± 0.002
0.25	0.1	0.80	51.4	-	-
0.125	0.1	6.75	44.7	1.345 ± 0.002	1.648 ± 0.002
0.125	0.08	4.87	46.1	-	-
0.14[1]	0.07[1]	2.65	47.7	1.295 ± 0.002	1.597 ± 0.003

[1] GEM-like dimensions

Table 7.4: Simulation results of a quadHIDAC with changed hole diameters and separations. Needed efficiency factors are estimated by comparing the gas volumes.

Now there are two different possible limits of the position resolution. In the case of single wire events, the wire separation is the limiting factor, because only on the wires signals can be generated. Hence, the simulated hit positions have to be shifted onto the next wire position in order to account for this effect. In the case of multi-wire events, the limiting factor is most likely the separation of the holes in the converter. In this case, the simulated hit positions have to be shifted onto the coordinates of the next hole.
Table 7.4 lists the determined spatial resolution for different hole-distance combinations of a HIDAC converter referring to simulation results. The values indicate the FWHM of a Gaussian fit to the parallel projection of the smeared simulation data. Simulated was a infinitesimal point source covered by a 4 mm diameter water sphere, which accounts for the positron range. As a result, the minimal obtainable resolution is 1.27 mm for the current quadHIDAC dimensions. Because of an increased scatter fraction, smaller holes cannot improve the spatial resolution.

The difference to the published values of $\approx 1\,\text{mm}$ [J$^+$99, S$^+$05, HRJ$^+$07] arise from

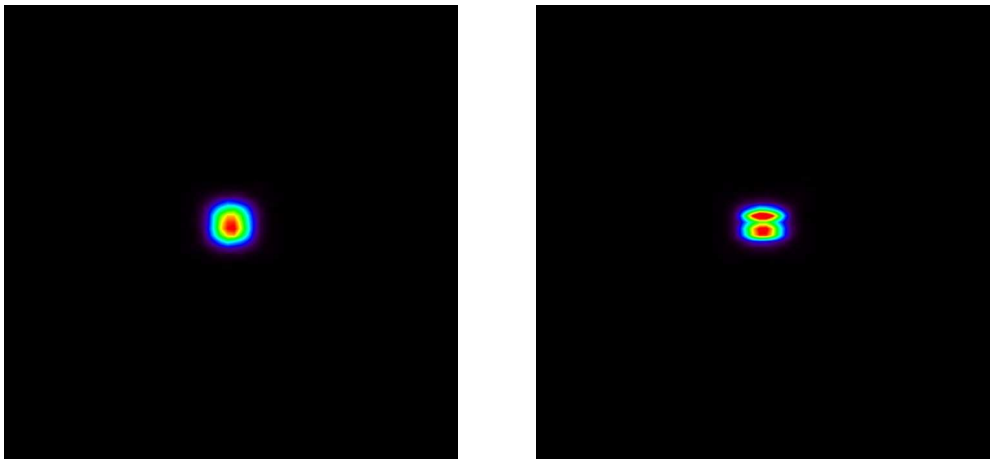

(a) (b)

Figure 7.25: OSEM reconstruction of a simulation of two infinitesimal point sources that are placed 1 mm apart from each other. A HIDAC detector with a hole diameter of 0.4 mm and a separation of 0.5 mm has been used. In Panel (a) the hit positions are shifted onto the nearest wire position, in Panel (b) into the coordinates of the closest hole, indicating multi-wire events. The reconstruction algorithm was written by T. Kösters.

the different determination schemes. The use of glass pipes with very small inner diameters decrease the positron range, and the use of filtered reconstructions will improve the resolution to smaller, but more subjective values. Under these considerations the simulation results are compatible with the measured values. Figure 7.25 shows the results of an OSEM reconstruction of two infinitesimal point sources placed 1 mm apart from each other. The detector geometry was set to the current HIDAC values. One can see that even though the FWHM of the parallel projection is wider than the point source separation, it is possible to distinguish both point sources. When shifting the hit positions onto the next wires coordinates, the two sources appear as one. This also intensifies the hints for a multi-wire interaction of the converter avalanches. Thus the hole separation seems to be a reasonable limit for the theoretical resolution capabilities of the quadHIDAC. So as a further result, the spatial resolution is strongly dependent on the reconstruction strategy. This again underlines the difficulties when comparing different devices or even the results of different working groups with each other.

7.1.13 Outlook

The presented simulations have shown that it is not feasible to improve all performance parameters of the quadHIDAC at the same time. One has to make a tradeoff between resolution, detection efficiency, and not least realisation potential. The use of smaller holes will, for example, increase the detection efficiency. Nevertheless, due to the thinner wall thicknesses in the converter, the position resolution might decrease at the same time. Also the optimisation of the thickness of the insulation sheets should not be neglected. The improvements easiest to realise would concern the choice of the gas. Since detector aging is an issue within the HIDAC modules, the polymerisation prone di-isomethyl-ether quencher should be replaced by the non-organic CO_2 or at least a smaller organic molecule. A next step then concerns the material choice in order to simplify the machining and manageability of the detector modules. Not only the lead in the converters should be replaced, but also the insulation materials and the glue- and sealing technique could be reassessed. Since the rotation of the device has shown to produce wear, especially for the cables, a cylindrical design might solve this problem and imply an increase in detection efficiency by increasing the acceptance angle.
In terms of quantification, the results of the presented point-like source simulations will be used as an input for an advanced reconstruction algorithm. The fractions of randoms and scatter can then be subtracted according to their simulated point-spread function at the desired position in the FOV.

7.2 MSPET Simulations

A detailed, simulation-based evaluation of the detection efficiency with different converters has already been shown in Chapter 6. In addition to these results, the MSPET concept has been evaluated for its quantification potential, especially in the face of the established quadHIDAC scanner. For this, the two most promising converter configurations, a single sided 30 μm gold converter and a double sided 40 μm lead converter, have been investigated.

7.2.1 Distribution of Detector Hits

Due to attenuation and module sizes, detector modules placed in the front of the stack will see more hits than the rear modules. The absolute fraction of the hits depending on the module number has been simulated with Geant4. Figure 7.26 shows the hit distribution depending on the module number. The module sizes have been initialised according to Table 5.2. The source volume was a 1 mm diameter water filled point-like volume. The

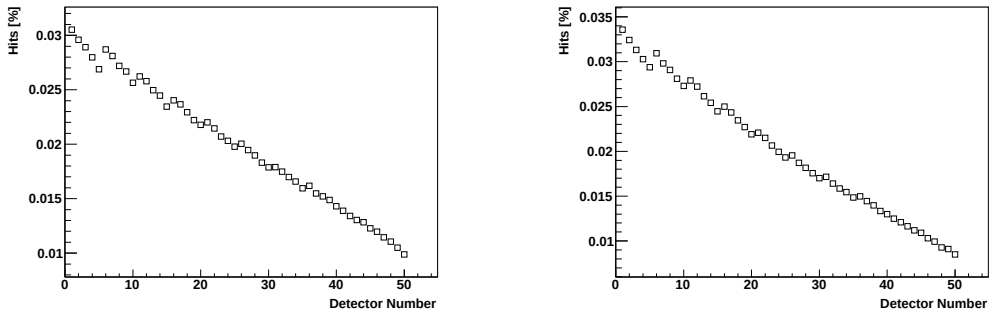

(a) (b)

Figure 7.26: Fractional hit-distribution on all MSPET detector modules implemented with a single-sided 30 μm gold converter (a) and a double-sided 40 μm lead converter (b). The size of the modules has been adapted to the opening angle of the quadHIDAC. The 50 module stack is arranged into eight subdetector blocks consisting of equal sized detector modules. These blocks are responsible for the discontinuities in the distributions.

energy distribution of the created positrons was sampled according to the ^{18}F spectrum. One can see that the increasing module sizes, especially for the first 15 modules, can compensate the efficiency decrease to some extent. The larger attenuation for the double sided lead converters in comparison to the single sided gold converter leads to a sharper decline of the hits quantity in rear modules. In conclusion, the gradient of detection efficiency increase gets smaller with increasing number of modules. At some point a trade off between module costs and efficiency gain has to be made.

7.2.2 Distribution of Detector Scatter

With increasing material thickness the probability to detect a hit that has undergone scattering before being detected increases. Figure 7.27 shows a simulation of the scatter fraction of all detected hits with respect to the position of the detector module in the stack. The mean fraction of scattered events within all detected events is 55.7 % for a single sided gold converter and 61.6 % for a double sided lead converter. Hence, the scatter fraction for a 50 module MSPET device is expected to be approximately 10 % larger than for the quadHIDAC (see Section 7.1.6). For the modules in the back it can exceed 70 % but seems to reach a saturation level here in case of a double sided lead converter. For a scattering fraction of below 57 %, as reached by the quadHIDAC, the MSPET scanner should not consist of more than 25 detector modules in case of a single sided gold converter and not more than 15 modules in case of a double sided lead converter.

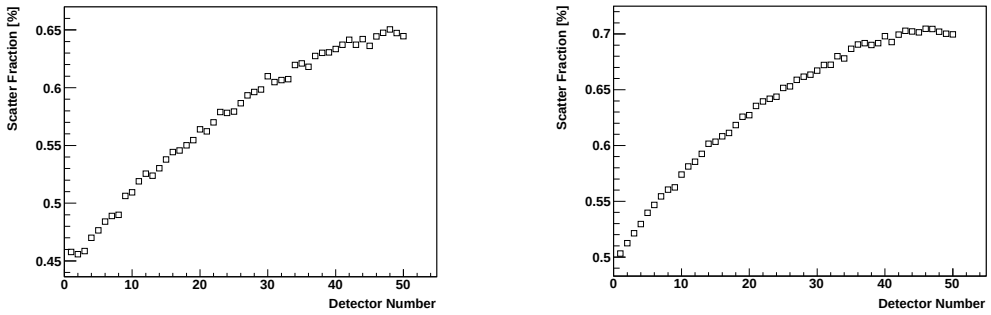

(a) (b)

Figure 7.27: Scatter fraction on all 50 MSPET detector modules implemented with a single-sided 30 μm gold converter (a) and a double-sided 40 μm lead converter (b) respectivly. The size of the modules has been adapted to the space angle of the quadHIDAC. The 50 module stack is arranged into eight subdetector blocks consisting of equal sized detector modules.

7.2.3 Count Rate Performance and NEC Rates

Equivalent to the Monte Carlo count rate simulations for the quadHIDAC, presented in Section 7.1.3, MSPET count rate simulations have been performed. Since no real measured data is available, the corresponding values for single and coincidence efficiencies as well as the trues- and scatters fractions have been taken from the simulations. The dead times after single and coincidence events as well as the coincidence time window is chosen identically to the quadHIDACs values. An electron detection efficiency, equivalent to the f-factor for the quadHIDAC has not been applied. Since the structure of the MSPET converter is simpler and less structured, it is assumed that this factor is closer to 1. The limiting factor is here, as already discussed in Section 6.4.3 the choice of a gas mixture that needs to provide a large interaction cross section for the liberated electrons. The anticipated count rate performance of a 50 module MSPET small animal PET scanner is shown in Figure 7.28. It is striking that the count rate in case of a two sided lead converter is large in comparison to a single sided gold converter. Nevertheless, the additional count rate consists mostly of scattered events.

Using the obtained count rates the noise-equivalent count rates can be easily calculated. They are shown in Figure 7.29 for both, the single sided gold converter and the double sided lead converter. The NECR reaches for none of the designs a maximum below 20 MBq. The different converter thicknesses have only minor effects on the slope of the curve, indicating that the image quality is comparable. Due to the larger scatter fraction, the count rate gain of the lead converter will not lead to an improved image quality.

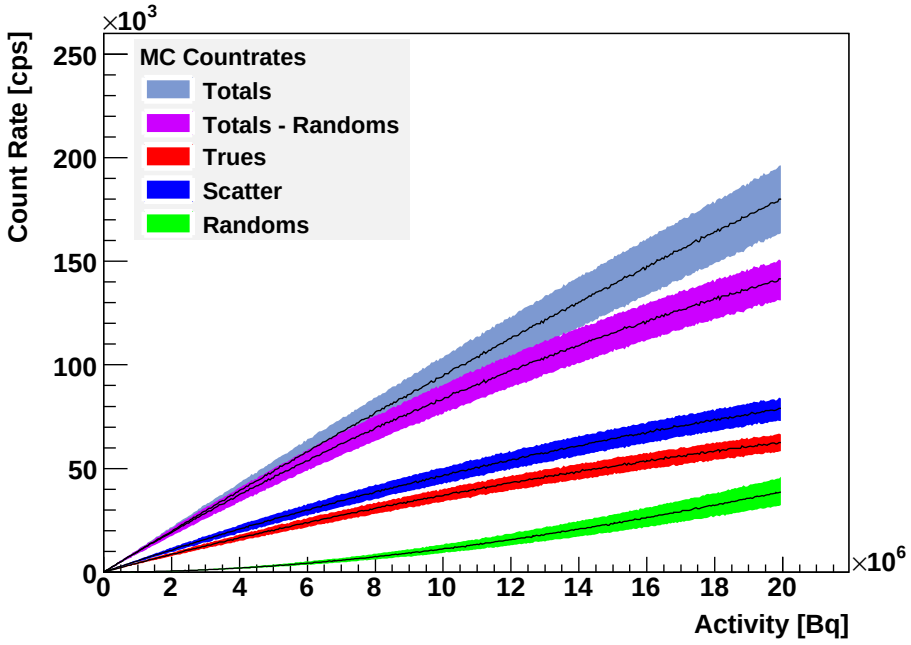

(a)

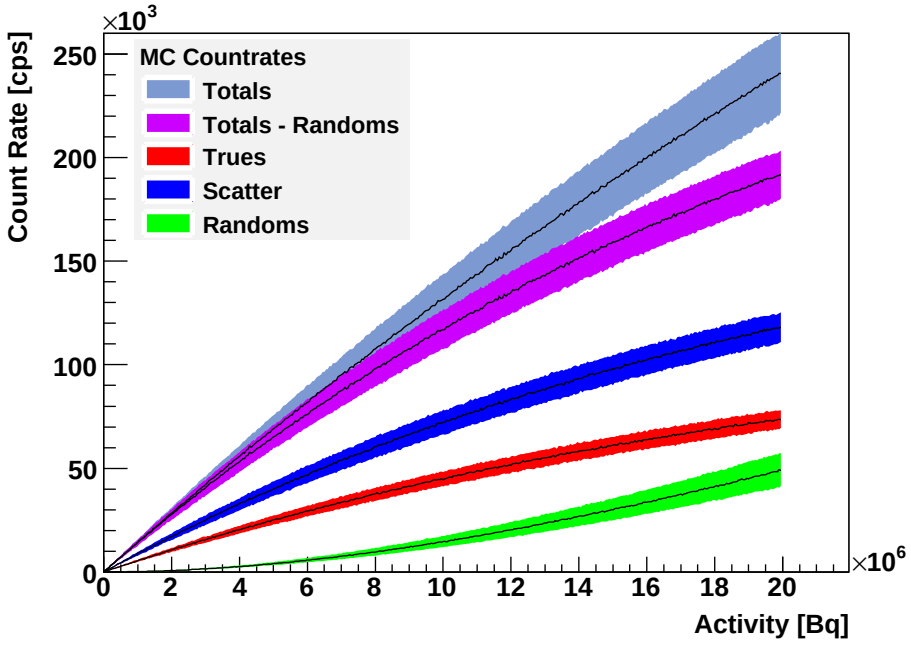

(b)

Figure 7.28: Simulated count rate performance for a fully equipped MSPET detector. Panel (a) shows the results for a single sided 30 μm gold converter. Panel (b) has a double sided 40 μm lead converter. The efficiencies for singles, trues and scatters have been taken from Geant4 simulations presented in Figure 6.17 and Section 7.2.2. The dead times have been chosen identically to the ones for the quadHIDAC.

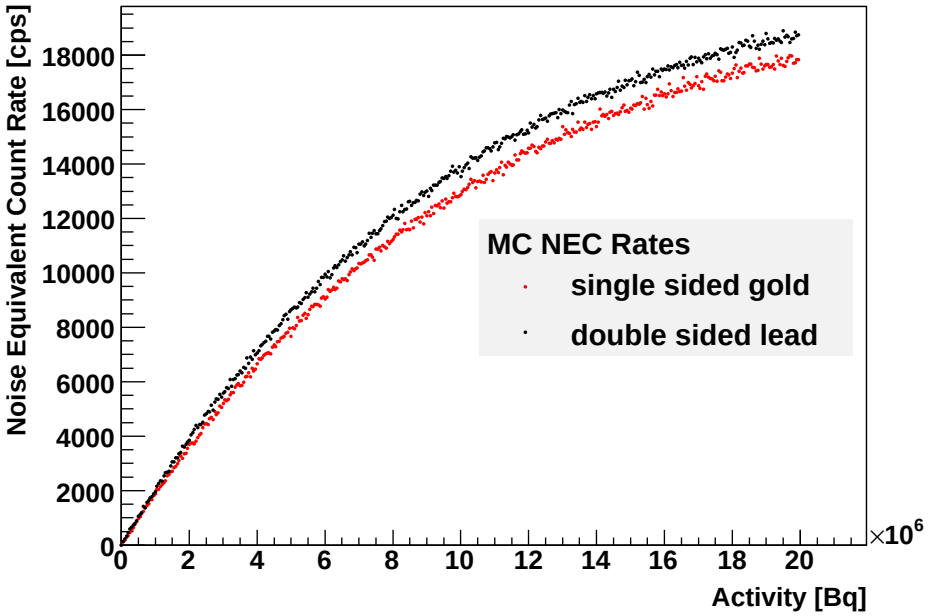

Figure 7.29: NEC rates for the MSPET scanner determined with the values shown in Figure 7.28.

In comparison to the quadHIDAC (see Figure 7.3) the NECR turns out to be rather poor, reaching only one fourth of its level.

7.2.4 Comparison of MSPET and quadHIDAC

It has been shown that the presented Geant4 simulations allow a detailed description of the detector properties of the quadHIDAC and the MSPET device under arbitrary design variations. The imaging capabilities of the quadHIDAC and the MSPET device can therefore be compared with each other using simulations. For this a point-like source with a diameter of 1 mm has been placed in the simulated quadHIDAC and also the 50 module MSPET device. The source volume is made of water. The energy distribution of the emitted positrons follows the ^{18}F spectra.
To be on the one hand independent from reconstruction effects or filters, and on the other hand have a quantitative analysis, the obtained simulated data has been visualised using parallel projections. Figure 7.30 shows the results over the whole FOV. The main difference is found in the tails of the distribution. The larger scattering fraction of the MSPET lead to a broader distribution in comparison to the quadHIDAC. Also in the gas volume of the MSPET comparably large pathways transverse to the original beam direction can occur. The hole structure of the quadHIDAC leads to smaller aberrations from the origi-

nal photons direction in case of scattering. It was shown that electronic noise leads to an increased count rate in these tails of the distribution. As this fraction was not considered in this illustration, the comparison here holds for the assumption of a similar large noise emergence in the MSPET device. Since the use of modern read out electronics promises a low noise level, the MSPET and the quadHIDACs distribution might even end up on a similar level in the tails. Panel (b) of Figure 7.30 shows a close-up view of the same simulation, allowing a better investigation of the distributions peak. The MSPET produces here sharper edges that let the image appear less blurred. An explanation of this behavior goes one on one with the tail enhancement. Due to the low-Z gas volume in forward direction, scattered events tend to depart further away from the true peak in the MSPET. So the trues peak remains sharp. This can be verified when looking at the distribution of the double sided lead converter MSPET in comparison to the gold converter. The single sided converter produces sharper edges, because scattered photons appearing in the backward plane can be converted in the next lead layer, separated just by the 0.5 mm thin FR4 plate, without passing through the gas layer, where larger deviations are possible. Figure 7.31 shows another representation of Figure 7.30 indicating the ratio of the MSPET distributions in comparison to the quadHIDAC distribution. It can be clearly seen, that the tails of the MSPET distribution is enhanced, while the central area suffers from lower count rate.
What is not considered at this point, is the restriction in spatial resolution caused by the exit angle of the liberated electrons in the MSPET and the converter design in general and the hole separation in special for the quadHIDAC.

7.3 Measurements with the MSPET Wire Chambers

The basic performance parameters have been measured using prototype chambers, in order to determine the capabilities of the MSPET concept. Most of these measurements were done with detectors without converters.

7.3.1 Pad Response Functions

A theoretical description of the pad response function for different detector geometries has already been presented in Section 6.1.2.
To verify the expected pad response function shown in Figure 6.7, a corresponding measurement has been performed. Here, one of the MSPET detectors has been irradiated with the X-ray source introduced in Section 6.4.3. The measured charge ratio of the pad with the maximum charge deposition and the sum of this pad and its two neighbors is calculated and plotted in Figure 7.32. The theoretical curve is drawn in black. It can be seen,

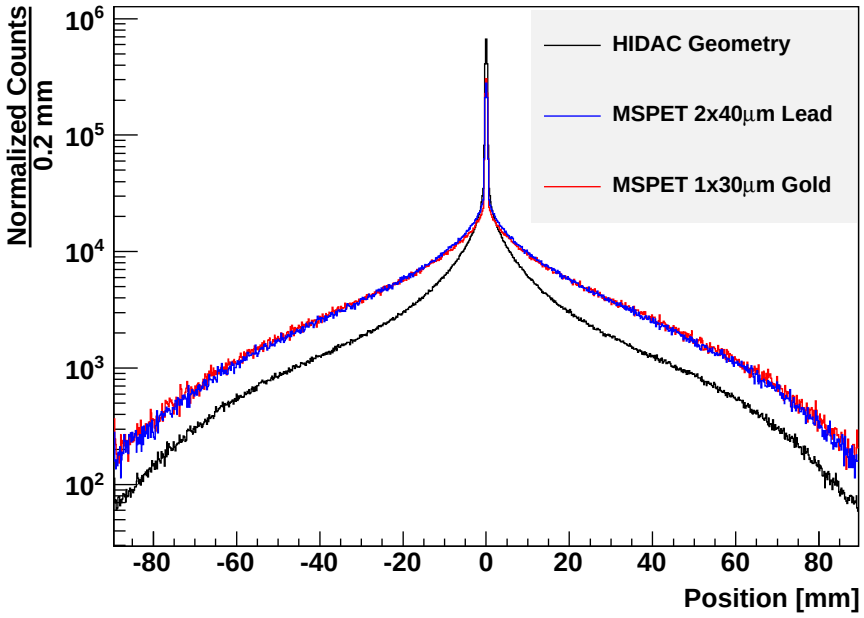

(a)

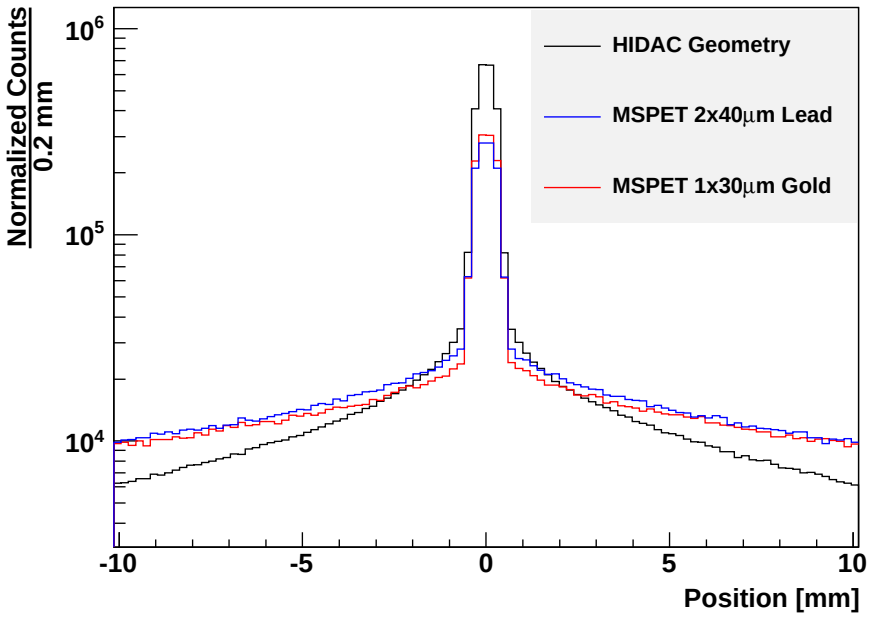

(b)

Figure 7.30: Comparison of the simulated detector responses of the quadHIDAC and the MSPET concepts to a point-like source volume with a diameter of 1 mm. Random events and detector noise are neglected. Panel (b) shows a zoomed view. The count rates have been normalised to the same value.

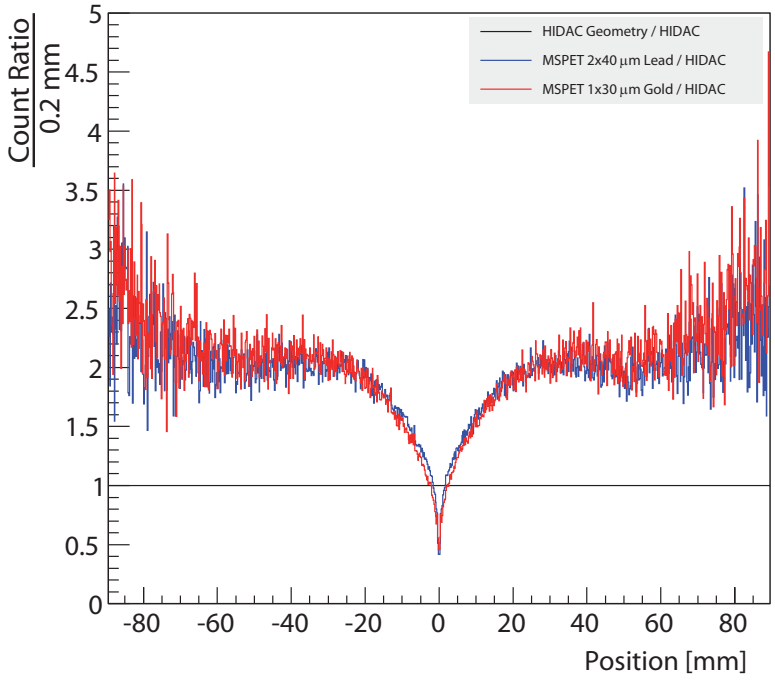

(a)

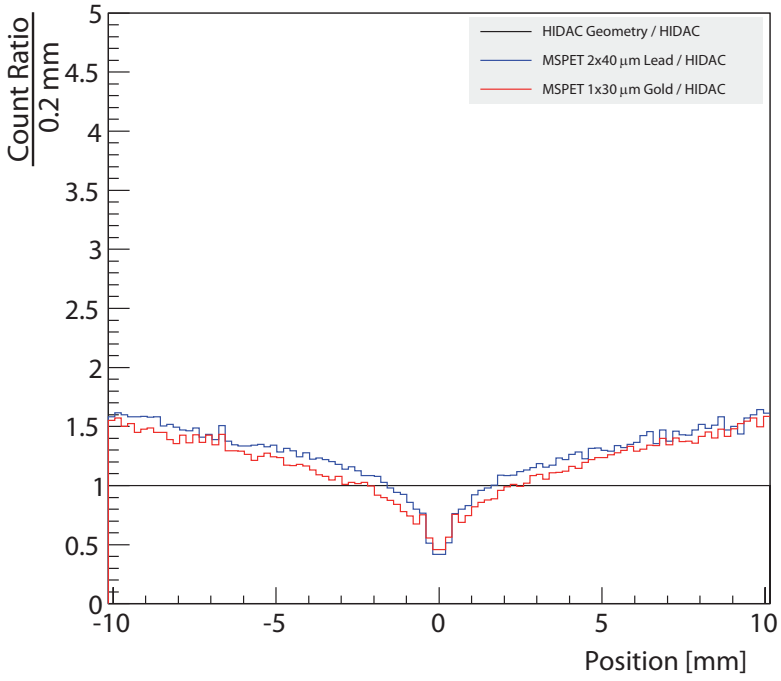

(b)

Figure 7.31: Different representation of Figure 7.30. Shown is the ratio of the MSPET distributions in comparison to the quadHIDACs distribution.

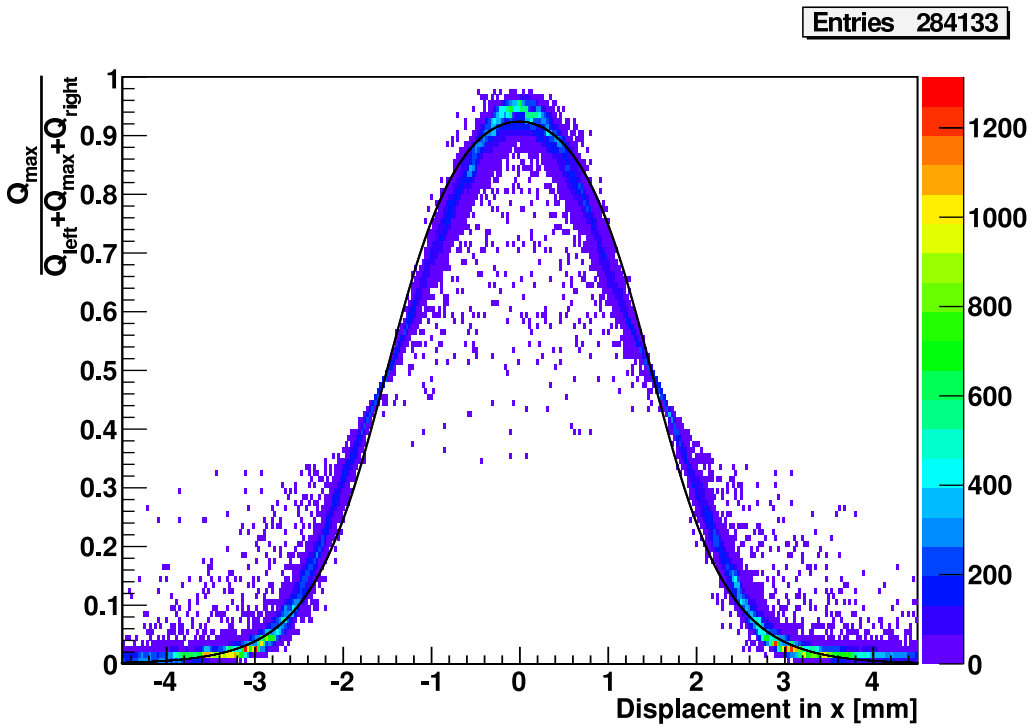

Figure 7.32: Pad response function for an MSPET chamber irradiated with X-rays. The black curve indicates the theoretical expected curve [Ver10].

that the theory curve is in good agreement with the measurement.
In a second test, the chamber was irradiated by a sodium source. Again, the pad response function was measured. The results can be seen in Figure 7.33. In contrast to the X-ray measurements this one appears heavily washed out. The behavior can be explained with

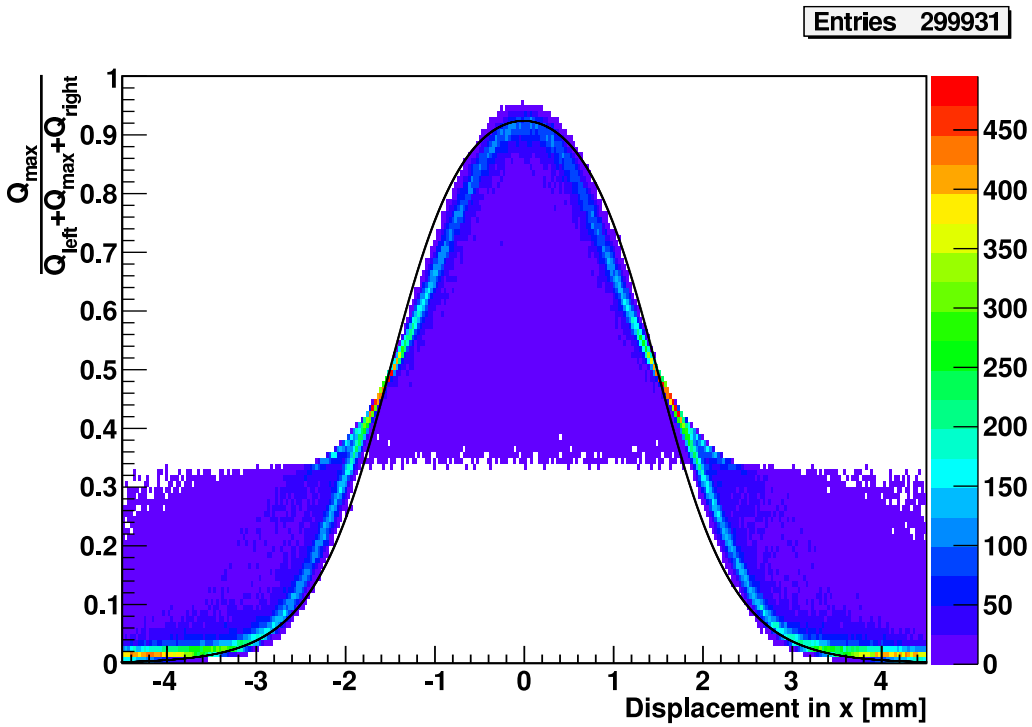

Figure 7.33: Pad response function for an MSPET chamber irradiated with a ^{22}Na positron emitter. The black curve indicates the same theoretical expected curve as shown in Figure 7.32 [Ver10].

the different detection principles of X-rays and conversion electrons. Since the low energetic X-rays directly interact with the gas, the ionisation encounters are straight forward peaked. In case of a positron emitter, the annihilation photons are converted into electrons via Compton- and photoelectric effect in the solid parts of the detector. The angular distribution of these electrons is shown in Figures 4.1 (measurement) and 6.15 (simulation). The mean exit angle of the electrons leaving the converter was determined as 45°. For these angles the pad response function is not well defined and has limited validity here. The large angles cause a broader signal in the detector, so that the charge-ratio gets widely smeared. As a result, this means that the theoretical PRF is not an unique measure of the position of the avalanche, but nevertheless the most probable. To account for this blurring in the position reconstruction of positron incidence, one has to use the measured PRF as

probability distribution rather than using the formalism described in Section 6.1.2 that is based on the theoretical function.

7.3.2 Count Rate Performance

In order to test the effectiveness of the gold plated converter, the count rate performance has been quantified by measurements.
These have been done with a detector containing a gold plated converter and also with a

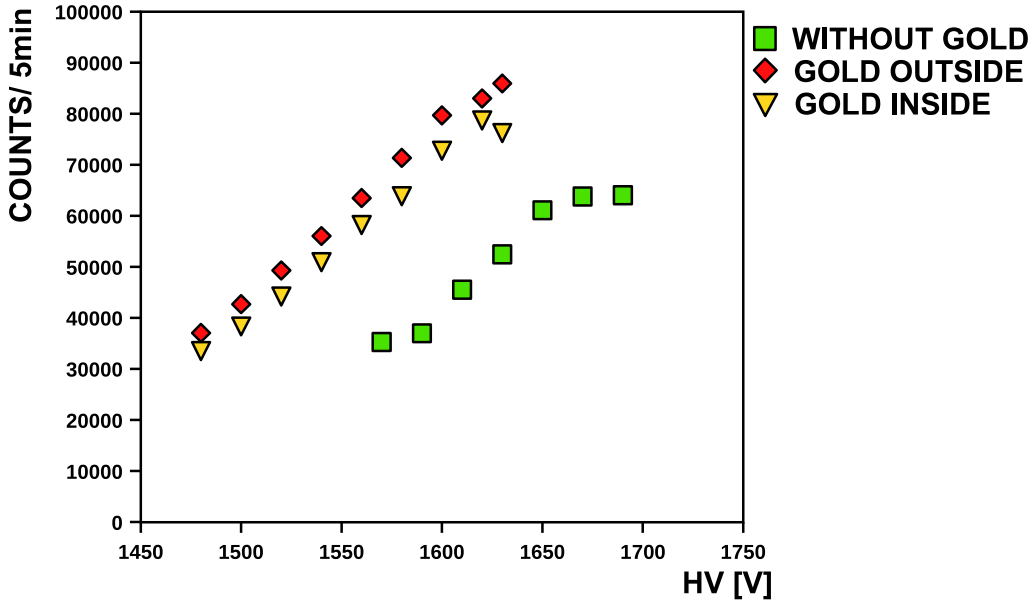

Figure 7.34: Count rate performance of an MSPET detector with and without a gold converter (mean thickness $\approx 60\,\mu$m) as a function of the anode voltage. *Inside* indicates the entry side of the X-radiation [Ver10].

detector with a pure copper pad plane without any coating in it. The gold thickness was measured depending on the location as $30\,\mu\text{m} - 120\,\mu\text{m}$ with a mean of roughly $60\,\mu$m (see Section 6.3.2). The filling gas was Ar-CO_2 (70-30). The chambers have been irradiated with a 47 kBq ^{22}Na-source. During a measuring time of 5 minute the wire signals have been counted. The results of these measurements are displayed in Figure 7.34. Referring to simulations shown in Figure 6.17 one would expect a count rate increase of approximately 80 % in case of the usage of a regular $60\,\mu$m gold converter. The measurements now show an increase of approximately $35 - 55$ % depending on the anode voltage. The difference can be explained by the already mentioned, very uneven gold converter and also by the use of two different chambers, since both chambers are unique prototypes with slightly different characteristics.

7.3.3 Spatial Resolution

Beside the detection efficiency, the limit of the detection processes spatial resolution is the most important performance parameter of a small animal PET scanner. In the case of the MSPET concept, this resolution is subject to limitations originating from the photon converter and the wire chamber. Electrons liberated in the converter have a broad angular distribution with a mean value of $\alpha = 45^\circ$, as has been shown in Figure 6.15. The mean position deviation from the photon-to-electron conversion point in such an MWPC with anode to cathode gap of 1 mm is therefore $\Delta x_{\text{mean}} = \tan(45^\circ)\,\text{mm}$. With a standard deviation of $\sigma = 28^\circ$ the position is measured on a circle with an inner diameter of $\tan(45^\circ - 28^\circ)\,\text{mm} = 0.31\,\text{mm}$ and an outer diameter of $\tan(45^\circ + 28^\circ)\,\text{mm} = 3.27\,\text{mm}$ around the conversion point. The probability distribution of a measured particle hitting the converter at position $(x,y) = 0,0$ can be described analytically as a Gaussian shaped circle:

$$f(x,y) = \frac{1}{\tan(28^\circ)\sqrt{2\pi}} \cdot \exp\left(-\frac{1}{2}\left(\frac{((x^2+y^2) - \tan(45^\circ))}{\tan(28^\circ)}\right)^2\right). \tag{7.23}$$

Figure 7.35 shows a plot of this distribution. It can be seen that the distribution has a minimum at the original conversion point. An area corresponding to an Gaussian σ-environment and thus covering 68.2% of all entries is reached at integration limits of $\Delta x \approx \pm 1.0454\,\text{mm}$. Nevertheless, the knowledge of the exact distribution can be used as input for the implementation of proper reconstruction algorithms which might replace the common lines-of-response by *cylinders-of-response* and therefore account for this special detector characteristic.

In addition to the uncertainty coming from the converter, the influence of the wire chamber itself has been investigated. Since X-radiation produces measurable charges prominently within the gaseous volume and not in the converter, a measurement setup shown in Figure 7.36 has been installed. The X-ray source is equipped with different sized, exchangeable collimators. In a first attempt to test the separation capabilities of the wire chamber, a collimator containing four holes each with a diameter of 750 μm and a centre-of-hole distance of 1 mm have been drilled into an solder plugged brass pipe. The collimator is also shown in Figure 7.36. A detector module filled with Ar-CO_2 $(70-30)$ has been irradiated with this collimated beam. The detector response has been measured for multiple source positions, 500 μm apart from each other. The results of these measurements are shown in Figure 7.37. For each measurement approximately 10000 events have been recorded, which took about 10 min per position. The position has been reconstructed using weighted charge distribution methods explained in Section 6.1.2. The holes can be easily separated most notably in wire direction. Perpendicular to the wire direction the

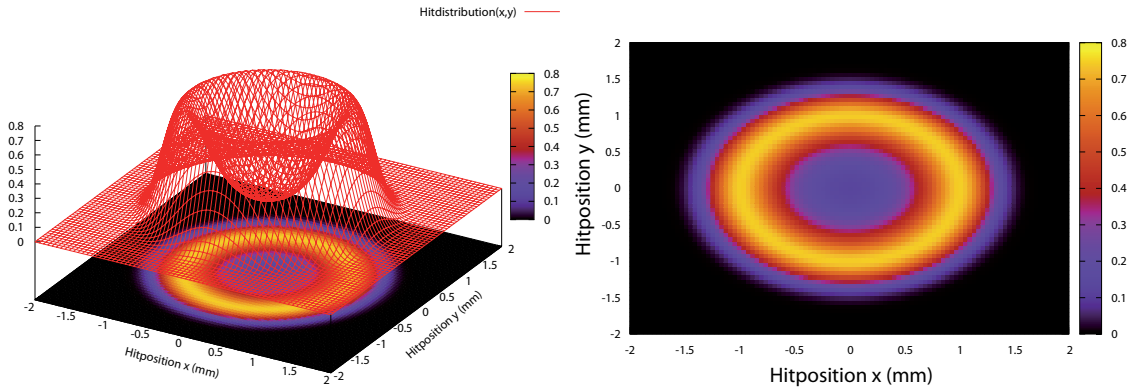

(a) (b)

Figure 7.35: Propability distribution of the measured position of an electron that is produced at position $(0,0)$ in the converter, caused by the conversion process and multiple scattering in the converter.

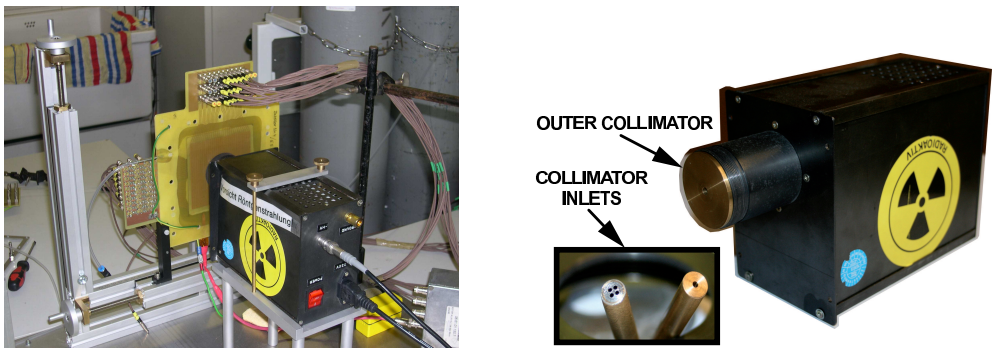

(a) (b)

Figure 7.36: Setup of the spatial resolution measurements (a). The X-ray source is placed directly in front of an MSPET detector. Collimators with different shapes (b) have been manufactured.

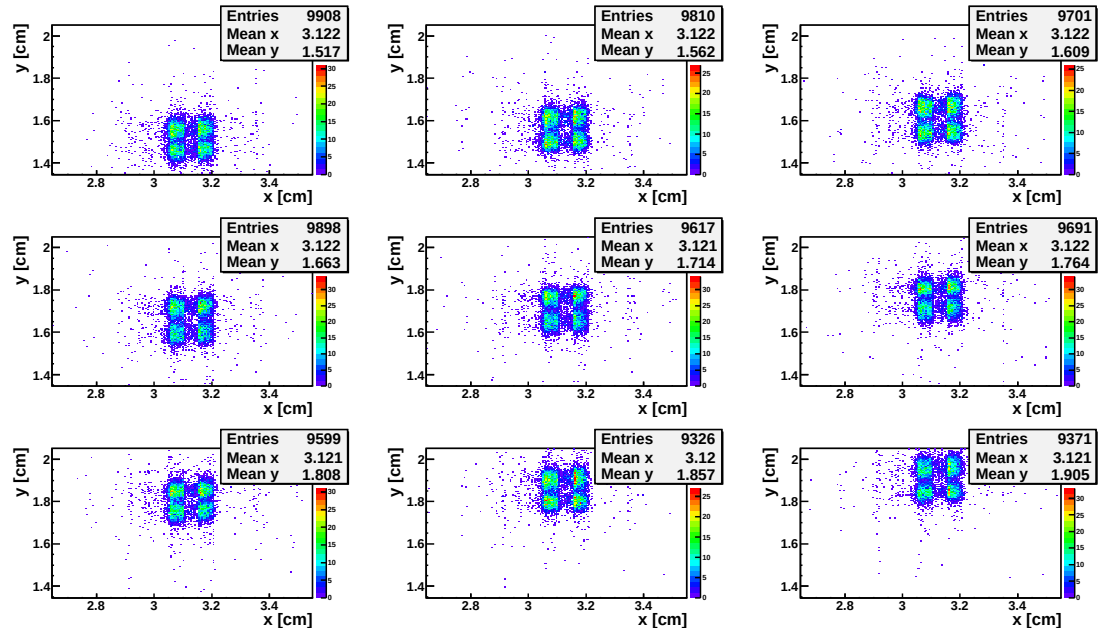

(a)

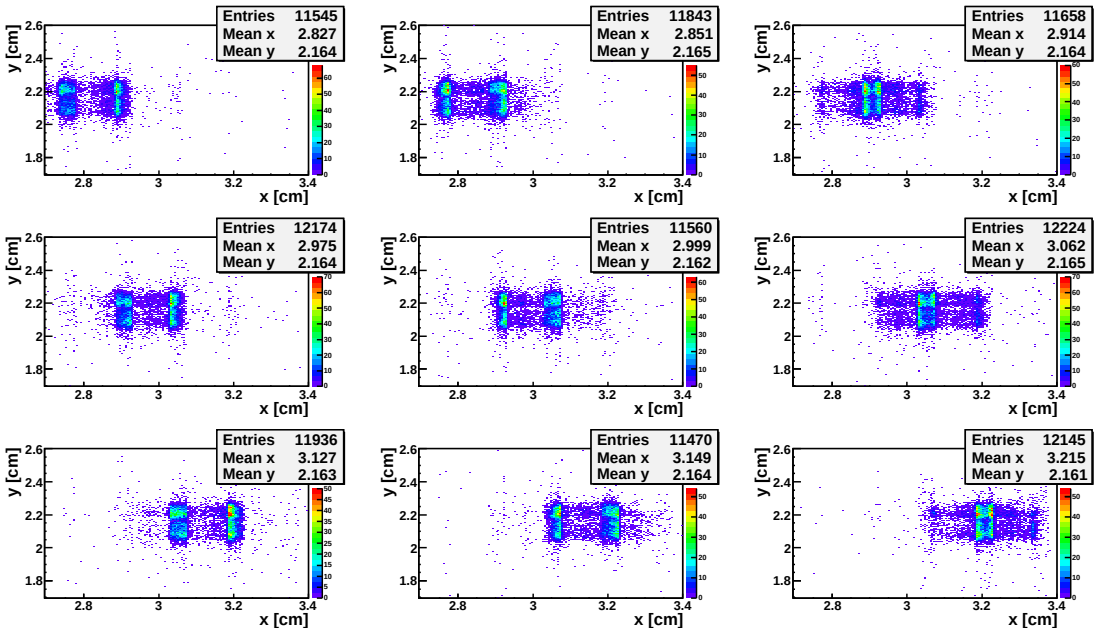

(b)

Figure 7.37: Detector response to collimated X-radiation. The collimator has four openings with a diameter of 750 μm and a centre-of-hole separation of 1 mm. The subfigures indicate a source shift of 500 μm in (a) wire direction and (b) perpendicular to the wire direction [Ver10].

wire-gap limits the separation capabilities, as the measured electron avalanches always occur close to the wires. The expected resolution in this direction is therefore just $\frac{1}{\sqrt{12}} \cdot s$ where $s = 1.5\,\text{mm}$.
As a result of these measurements, it has been shown that the separation capability of the MSPET modules is below 1 mm in both directions with respect to the wires.
In order to further quantify the spatial resolution of the MWPC, measurements with very small collimators have been done. Figure 7.38 shows the reconstruction of the detector answer to a 200 μm diameter collimator. Figure 7.39 indicates an equivalent measurement with a 100 μm collimator. Since the hit distribution does not get sharper for the thinner collimator, the 200 μm collimator can be interpreted as a delta shaped beam. Using this collimator the distributions of six measurements performed at different positions have been projected to the axis representing the wire direction and fitted with a Gaussian function. The mean value of the standard deviations of these Gaussian fits was determined as

$$\sigma_{\text{mean}}^{par-to-wire} = 161\,\mu\text{m}. \tag{7.24}$$

The resolution perpendicular to the wire direction is given by the wire separation $s = 1.5\,\text{mm}$ as

$$\sigma_{\text{mean}}^{orth-to-wire} = \frac{1.5\,\text{mm}}{\sqrt{12}} = 433\,\mu\text{m}. \tag{7.25}$$

More details on the accomplishment of these and all other measurements can be found in the diploma thesis of D. Vernekohl [Ver10].
For the total resolution one has to fold the uncertainty-distribution caused by the converter with the MWPC resolution:

$$\begin{aligned} \sigma_{\text{tot}}^{\parallel} &= \sqrt{\sigma_{\text{Conv.}} + \sigma_{\text{mean}}^{par-to-wire}} = \sqrt{\tan(28^\circ)^2 + 0.161^2}\,\text{mm} && (7.26)\\ &= 0.556\,\text{mm} && (7.27)\\ \sigma_{\text{tot}}^{\perp} &= \sqrt{\sigma_{\text{Conv.}} + \sigma_{\text{mean}}^{orth-to-wire}} = \sqrt{\tan(28^\circ)^2 + 0.433^2}\,\text{mm} && (7.28)\\ &= 0.686\,\text{mm} && (7.29) \end{aligned}$$

By inserting these values into (7.23) one gains different functions for both directions shown in Figure 7.40. As a conclusion, the total spatial resolution is mainly dependent on the interaction processes in the converter. If one again wants to quantify the area in which 68.3 % of all hits are measured, one gets $\Delta x_{\parallel} \approx \pm 1.045\,\text{mm}$ and $\Delta x_{\perp} \approx \pm 1.049\,\text{mm}$.
In terms of spatial resolution it can be concluded, that the MSPET in its presented design is fully capable for small animal PET applications. Using proper reconstruction algo-

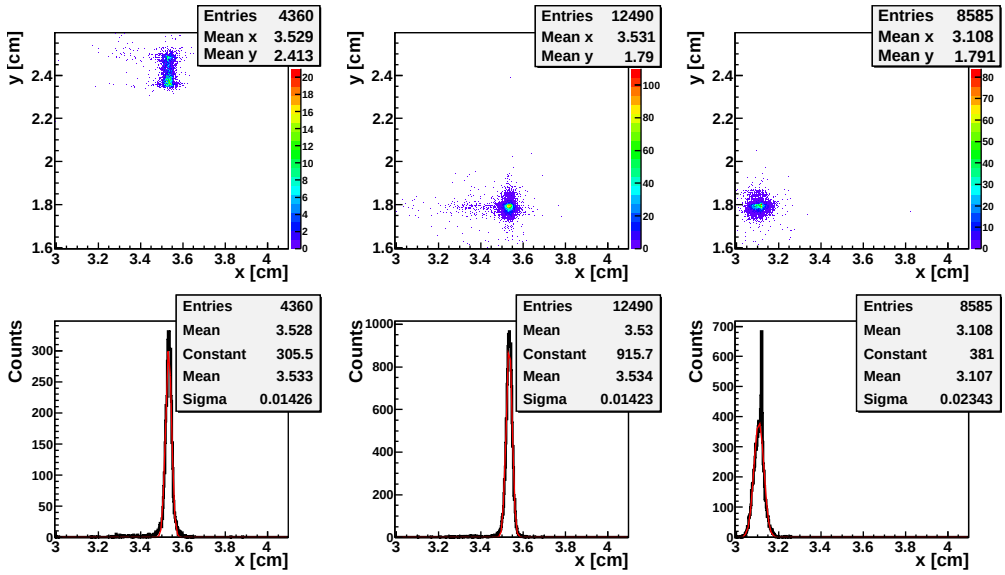

(a)

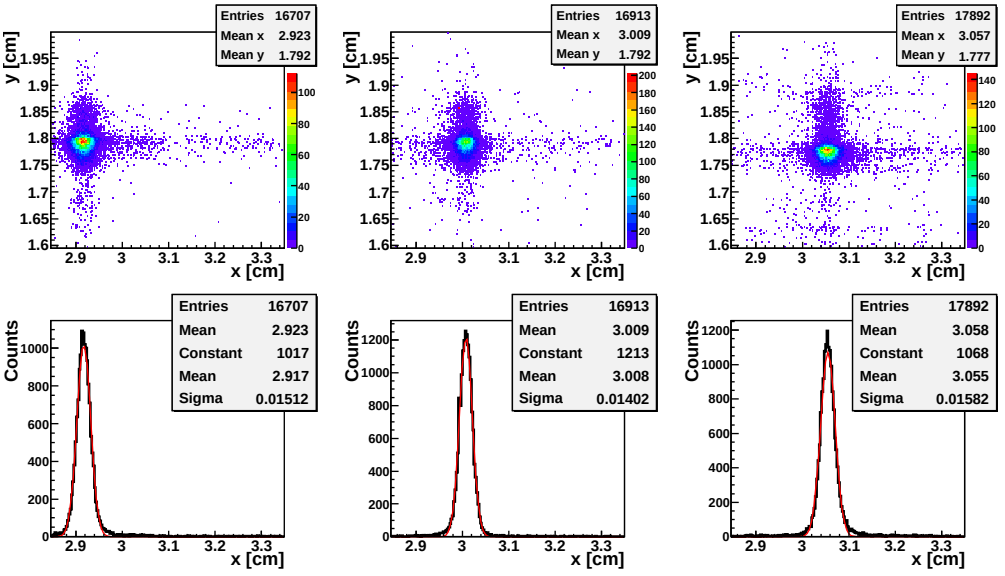

(b)

Figure 7.38: Detector response to collimated X-radiation on different positions of the pad plane. The diameter of the collimator is 200 μm. Note the different scaling of the axes [Ver10].

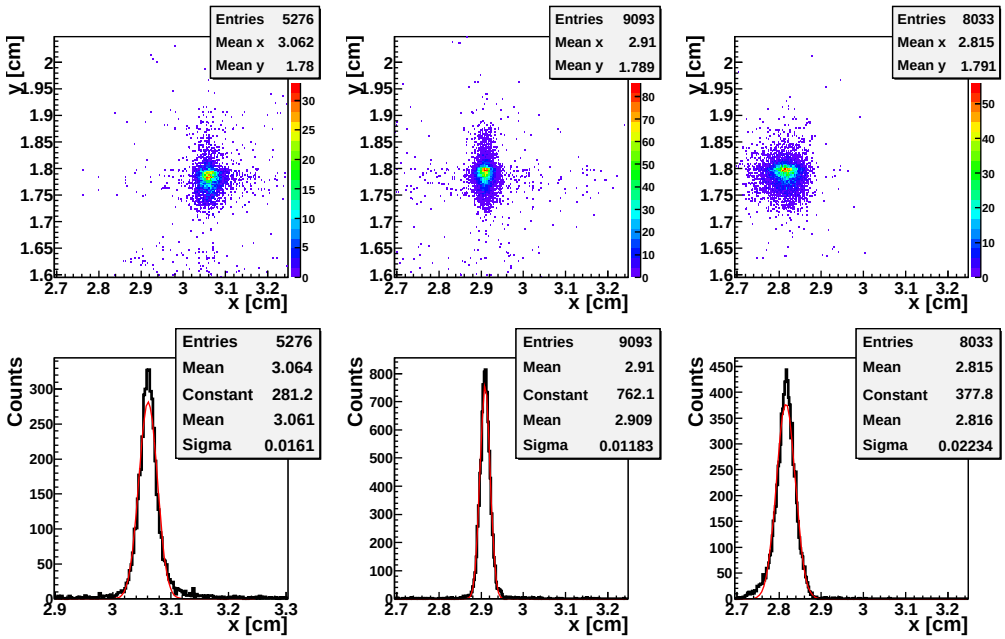

Figure 7.39: Detector response to collimated X-radiation different positions of the pad plane. The diameter of the collimator is 100 μm [Ver10].

rithms that account for the special shaped hit distribution, is should even be possible to reach sub-millimetre resolution for PET images.

7.3.4 PET Measurements

Finally, first PET measurements have been performed using two MSPET detector modules. The setup is shown in Figure 7.41. A 47 kBq ^{22}Na source has been placed in the middle of the two detectors, which are placed 90 mm apart from each other. Due to the lack of ADCs, only 20 pads were read out in each of the two chambers. This results in an active detection area of 29.7 mm^2 per chamber.
To demonstrate the principle, the sodium-22 source has been measured at three different positions in the FOV of the readout area. Figure 7.42 shows the superposition of the OSEM reconstructions of these three measurements (indicated as $1-3$). The wire signals of one of the two chambers has been used to open an acquisition gate of 10 μs on all channels. The valid coincidences have been reconstructed offline. The measuring time was 111 h and 137 h for source positions 1 and 2. During this time 523 coincidences for Pos. 1 and 8257 coincidences for Pos. 2 were recorded. For the more central position 3 10108 coincidences were measured with 68 h. The rates are limited by the activity of

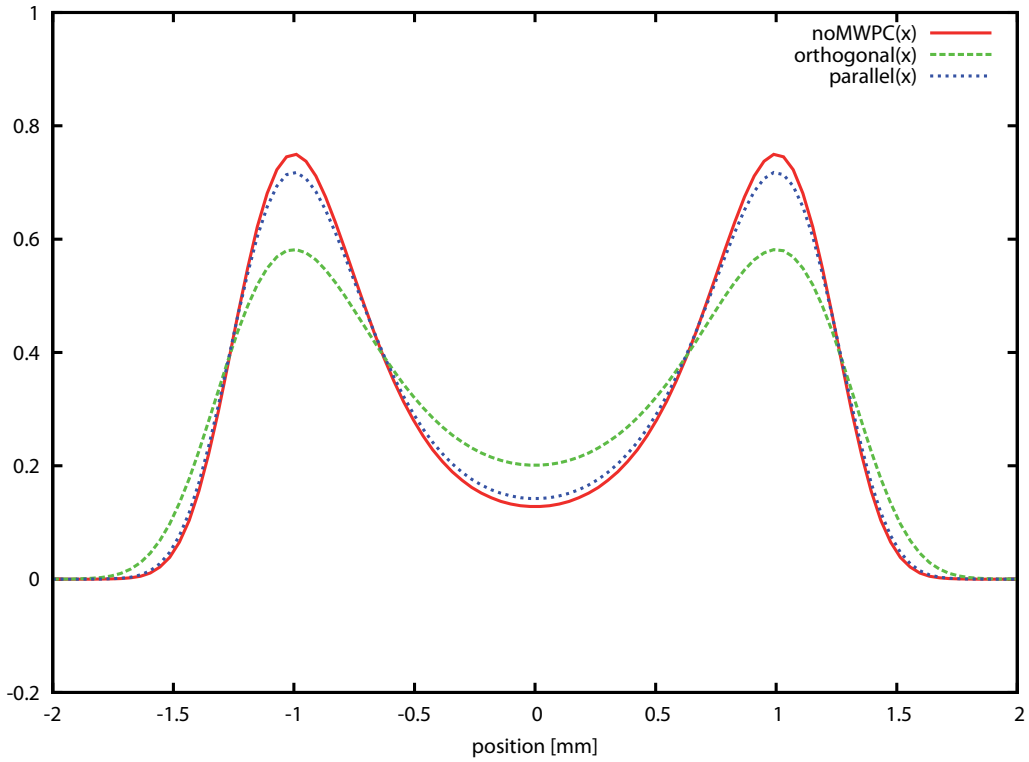

Figure 7.40: Hit-distribution functions with respect to both the converter- and MWPC-caused deviations. Plotted is the distribution parallel and orthogonal with respect to the wire direction. The red curve just accounts for errors resulting from the converter (cf. Fig. 7.35).

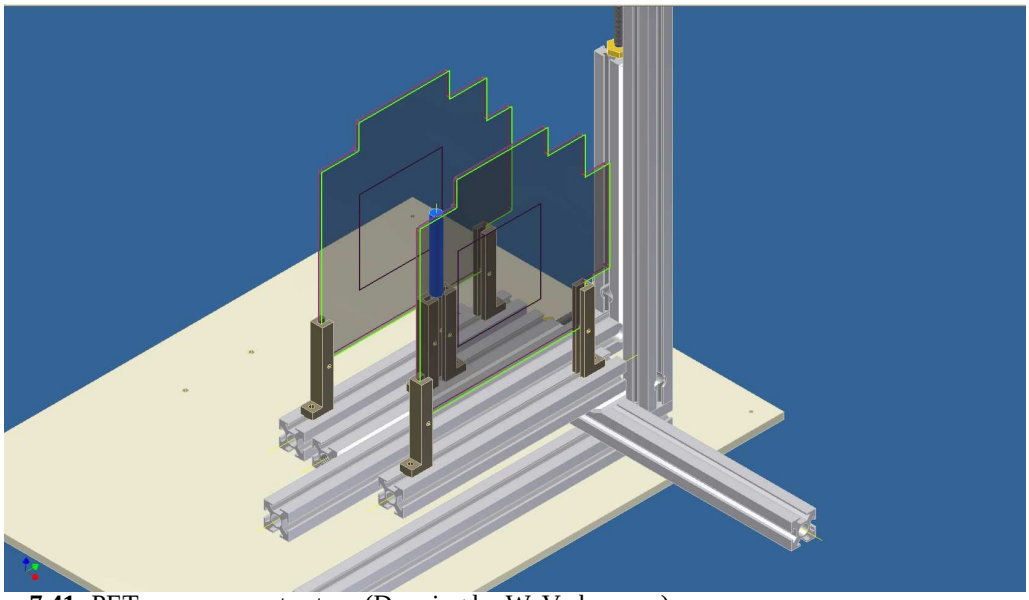

Figure 7.41: PET measurement setup. (Drawing by W. Verhoeven.)

the source, the efficiency of the detectors and, most of all, the very small active detection area. They are even more reduced at the edges of the FOV, where it is less likely to find valid coincidences, as the solid angle in which valid coincidences could appear, disappears. One can clearly separate three spots in the sagital plane, representing the three

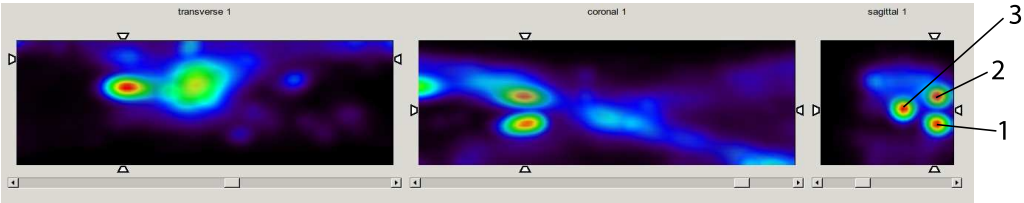

Figure 7.42: PET reconstruction of a Na^{22} positron source. Three measurements at different positions have been superimposed [Ver10].

source positions. A shift of 6 mm in Y-direction between position 1 and 2 and a shift of 6 mm in Z- and an accidentally tilt resulting in a Y-direction shift is visible in the image. Further interpretations about the shape and size of the active elements inside the source cannot be made. The reason for that can most probably found in the low statistics and, again, the very small detection area. Nevertheless it could be shown that it is possible to produce PET images with the new detectors that offer position discrimination, though only on a basic level so far.

7.3.5 Outlook

The biggest benefit of the new MSPET small animal PET scanner in comparison to the quadHIDAC is its easy and fast to build design. Further on, the singles raw data is fully accessible in the MSPET. Using proper read out electronics and mass storage it will be ensured that this data is retained and accessible for later analysis and interpretation. The quantification potential and the detector characterisation using test measurements would be eased having these raw data.
While the expected position resolution is on a comparable level with the quadHIDAC, the detection efficiency is legging behind. An improvement could be realised using spherical MWPCs that reduce the dead angles. First simulations resulted in a singles efficiency of 12.26 % and a coincidence efficiency of 1.29 % using a single sided gold converter and 50 detector layers. This equals a count rate increase of approximately 30 % in comparison to a flat detector design. For the realisation of such a detector design most of all a solution for the the problematic wire winding procedure has to be found.
Another, technically more complex approach for an advanced design, would be the use of liquid xenon instead of a filling gas mixture. Without an electron-to-photon converter in

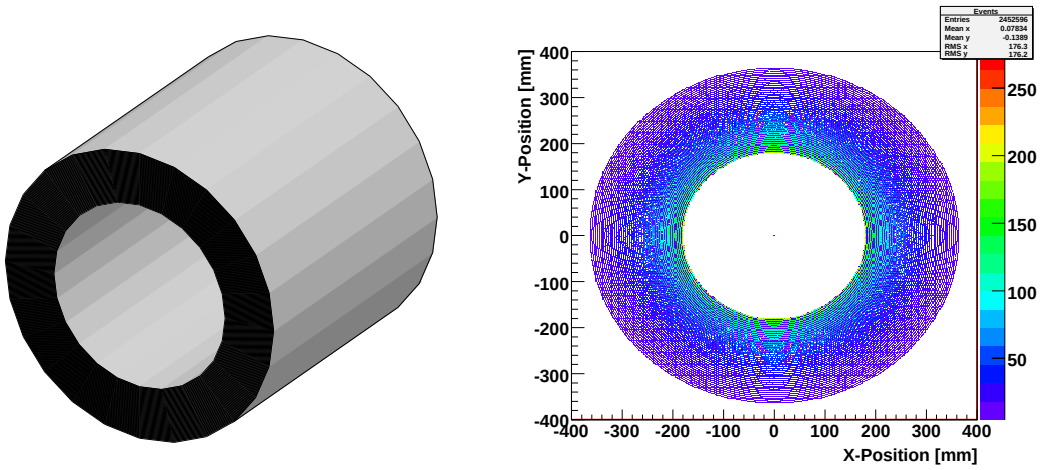

(a) (b)

Figure 7.43: Design and simulated hit-map using an advanced, cylindrical MSPET design.

such a detector also energy information would be possible allowing scatter discrimination and Compton camera capabilities. On the other hand the cooling and thermal insulation as well as the read out are amitious. Low-noise amplifiers, mounted closely to the detector modules are needed. Currently, also the ease of use for medical staff in clinical practice seems questionable, since such a device would need frequent service. The relevance of the argument of cost advantage in comparison to scintillator-based scanners may vanish. Nevertheless from the technological standpoint, a liquid xenon MWPC for small animal PET remains interesting.

Summary

This thesis treated the simulation, design, construction, testing and performance evaluation of multi-wire proportional counter (MWPC) based small animal PET scanners.
The design of a PET scanner for small animals is driven by the demand for high spatial resolution and good detection efficiency for 511 keV photons. As an adequate detector modality for this application, multi-wire proportional counters offer large detection areas and sub-millimetre position resolution at reasonable costs. Since the interaction cross section of the annihilation photons with the gaseous media inside such a detector is rather low, the multi-wire chamber has to be combined with a dense photon-to-electron converter.
A sophisticated converter design has been developed in the quadHIDAC small animal PET scanner by Oxford Positron Systems. It uses a converter consisting of alternating layers of lead and insulation that is drilled with a dense matrix of small holes. Liberated electrons that escape into these holes are transported to the MWPC where they can be detected. With this scanner a spatial resolution in the order of 1 mm and reasonable efficiency can be achieved, limited by hole spacing and material thickness.
Due to the difficult production, handling and error-proneness arrising from the complex HIDAC design, a detector with a simpler converter geometry using flat sheets of gold or lead has been suggested within this thesis. In the case of such an alternative approach, the spatial resolution is limited by the angular spread of the liberated electrons entering the multi-wire chamber. In order to find an optimal geometry for this detector extensive simulations, mostly based on Geant4, have been performed. In order to gain a better understanding of its characteristics, also the quadHIDAC has been simulated in great detail.
As a result of these efforts, the MSPET small animal PET scanner has been introduced. It consists of 200 wire chambers with an anode-to-cathode spacing of 1 mm and a flat, combined pad-plane-converter electroplated with 30 μm of gold or 40 μm of lead respectively. The modules are arranged in four blocks surrounding the field-of-view, containing 50 modules each.
Prototype MSPET modules with and without converters, as well as appropriate read-out electronics, have been designed, built and tested. It was shown that the intended spatial

resolution of 1 mm for annihilation photons can be reached. As a drawback, the count rate performance currently suffers from the small gaseous volume of the MWPC. More sophisticated gas mixtures or even other media like liquid xenon may be used in the future to improve the detection efficiency.
It has been shown that the results obtained with the developed quadHIDAC simulation programm are in good agreement with real measurements. This accounts for hit distributions, efficiencies and spatial resolution. For the adaptation of efficiency values, a proportionality factor depending on the system's properties has been introduced in order to account for effects that cannot be considered in the simulations.
The simulations also allowed to investigate influences of the positron range on the spatial resolution of a PET scanner in order to gain a better understanding of dedicated spatial resolution measurements and their interpretation.
As a drawback of all MWPC detectors with converters, no energy information is provided, as it is lost during the detection process. Nevertheless, it has been shown that a quantitative analysis of trues-, scatters- and random-coincidence contributions to the PET image is possible using the simulation program. A mean scatter fraction of 45.4 % for the quadHIDAC and 55.7 % for an 200 module MSPET device with flat gold converters was obtained. The spatial distributions of these constituents have been evaluated and used for the quantification of a test measurement, in case of the quadHIDAC. Thereby, it was shown that an additional count rate contribution, most likely caused by source activity dependent detector noise cannot be neglected in a quadHIDAC measurement. For small activities below 1 MBq, the noise contribution is three times larger than the measured random-coincidence contribution and more than 15 times larger than the theoretical random-coincidence rate. Therefore noise provides a major factor to the blurring of the count distribution. The source of this noise could not be exactly identified, but some prominent candidates have been isolated. These are a noisy power supply, affecting the single hit quantity and hence the random-coincidence rate, and an undocumented multiplexed read out. In interaction with a grouped pad read out scheme, the read out can shift real coincidences to random positions. In addition, detector sparking caused by soiled wires and holes leads to increased singles- and thereby randoms rates.
In a next step, the design of the quadHIDAC was evaluated and optimised in terms of spatial resolution and detection efficiency. Different parameters for hole diameters, hole separation and material thickness have been investigated. While the efficiency increases with smaller hole size and separation, the spatial resolution reaches its best value at the current geometry with 0.4 mm holes and 0.5 mm separation. At smaller values, liberated electrons can traverse the thin walls.

The results of the presented simulations will now be used as input parameters for advanced, quantitative reconstruction algorithms.

The work initiated by this thesis, especially the detector development efforts, have lead to the regular project B6 being part of the Sonderforschungsbereich 656 ”Molecular Cardiovascular Imaging”, where it will be continued.

Zusammenfassung

Diese Dissertation behandelte Simulation, Entwicklung, Konstruktion, Test und Charakterisierung von Vieldrahtproportionalzähler basierten Klein-Tier PET Kameras.
Das Designziel bei der Entwicklung solcher Geräte ist es, eine hohe räumlichen Auflösung und Detektionseffizienz für 511 keV Photonen zu ermöglichen. Eine Detektormodalität mit großem Potential sind hier Vieldrahtproportionalzähler, die bei geringem Kostenaufwand eine Auflösung unter einem Millimeter ermöglichen und eine große Detektorfläche bieten. Da die Nachweiswahrscheinlichkeit für Annihilationsphotonen im Gasvolumen eines solchen Detektors recht gering ist, muss ein effizienter Photonen-zu-Elektronen Konverter aus einem dichten Material hoher Ordnungszahl mit dem eigentlichen Detektor kombiniert werden.
Ein ausgereiftes Konverterprinzip wurde in der quadHIDAC Kleintier PET Kamera von Oxford Positron Systems realisiert. Der Konverter besteht hier aus abwechselnden dünnen Lagen aus Blei und Isolationsmaterial, welche mit einer feinen Lochmatrix versehen wurden. Im Konverter ausgelöste Elektronen können in diese Löcher entkommen. Ein angelegtes elektrisches Feld transportiert die Elektronen zum angeschlossenen Vieldrahtproportionalzähler, wo sie detektiert werden können. Mit diesem Detektor ist, beschränkt durch Loch- und Materialgeometrie, eine Auflösung von etwa 1 mm bei zufriedenstellender Nachweiswahrscheinlichkeit erreichbar.
Aufgrund der komplexen Struktur des quadHIDAC-Konverters, der problematischen Herstellungsverfahren und auch seiner Fehleranfälligkeit wurde im Rahmen dieser Arbeit ein vereinfachtes Konverterprinzip ohne Löcher, bestehend aus Gold- oder Bleifolien, vorgeschlagen. Bei einem solchen Ansatz wird die räumliche Auflösung des Systems hauptsächlich durch die Winkelverteilung der aus dem Konverter austretenden Elektronen beschränkt. Um eine optimale Geometrie für einen solchen Detektor zu finden, wurden umfangreiche, meist auf Geant4 basierende Simulationen durchgeführt. Um ein besseres Verständnis der Funktionsweise und der Eigenschaften des quadHIDACs zu erhalten, wurde auch dieser detailgetreu simuliert.
Als ein Ergebnis dieser Simulationen wurde die MSPET Kleintier Kamera vorgeschlagen. Sie besteht aus 200 einzelnen Drahtkammermodulen mit einem Anoden-zu-Kathoden

Abstand von 1 mm und einem flachen Konverter, der galvanisch auf die Auslesepads der Kathode aufgebracht werden kann. Als optimale Konverterdicke wurden 30 μm im Falle eines Gold- und 40 μm im Falle eines Bleikonverters ermittelt. Die Module sind in vier Blöcken zu je 50 um das Sichtfeld der Kamera angebracht.
Prototypen dieser Detektoren, sowohl mit als auch ohne Konverter, und entsprechender Ausleseelektronik wurden entwickelt, gebaut und getestet. Es ist gezeigt worden, dass die angestrebte Auflösung von 1 mm für Annihilationsphotonen erreicht werden kann. Als ein Nachteil dieses Konzeptes hat sich das kleine Gasvolumen der dünnen Module herausgestellt, welches die Nachweiswahrscheinlichkeit beschränkt. Besser geeignete Gasmischungen oder andere Füllstoffe wie flüssiges Xenon könnten in Zukunft genutzt werden, um die Effizienz der neuen Detektoren zu verbessern.
Es wurde gezeigt, dass die Ergebnisse der quadHIDAC Simulationen gut mit den Ergebnissen aus Messungen übereinstimmen. Dies gilt sowohl für Trefferverteilung als auch für Effizienz und Ortsauflösung. Um die simulierten Effizienzen an die realen anzupassen wurde ein Proportionalitätsfaktor eingeführt, welcher von den Detektoreigenschaften abhängt. Dieser berücksichtigt Effekte, die nicht von der Simulation erfasst werden können.
Desweiteren ermöglichten die gezeigten Simulationen die Untersuchung des Einflusses der Positronenreichweite auf die Ortsauflösung einer PET Kamera. Hierdurch konnten Erkenntnisse für das Verständnis und die Interpretation von Ortsauflösungsmessungen mit PET Detektoren gewonnen werden.
Ein Nachteil aller Vieldrahtproportionalkammer basierten Detektoren mit Konverter ist der Verlust der Energieinformation während des Detektionsprozesses. Trotzdem konnte gezeigt werden, dass eine quantitative Analyse von wahren, gestreuten und zufälligen Koinzidenzbeiträgen durch den Einsatz von Simulationen möglich ist. So wurde ein mittlerer Streuanteil von 45.4% für den quadHIDAC und 55.7% für ein 200 Modul MSPET Gerät mit flachem Goldkonverter bestimmt. Die räumliche Verteilung der Koinzidenzbeiträge wurde genutzt um eine quadHIDAC Testmessung zu quantifizieren. Hierbei wurde ein zusätzlicher, nicht vernachlässigbar grosser Koinzidenzbeitrag gefunden, der wahrscheinlich auf aktivitätsabhängiges Detektorrauschen zurückzuführen ist. Bei kleinen Aktivitäten unter 1 MBq ist der Rauschanteil dreimal größer als der vom quadHIDAC bestimmte Anteil der Zufallskoinzidenzen und 15-mal größer als der theoretisch bestimmte Wert der zufälligen Ereignisse. Der Rauschanteil trägt daher entscheidend zur Verschmierung der räumlichen Trefferverteilung bei. Die exakte Ursache des Rauschens konnte nicht exakt bestimmt werden. Ein mögliche Erklärung hierfür liegt in der verrauschten Stromversorgung, welche die Einzeltrefferrate und somit die Rate der zufälligen Koinzidenzen erhöht. Außerdem könnte die Multiplex-Auslese im Zusammenspiel mit in Gruppen angeordneten Auslesepads dazu führen, dass gültige

Koinzidenzen auf zufällige Positionen verschoben und somit falsch gemessen werden. Hinzu kommt ein häufiger Funkenüberschlag in den Detektoren, welcher durch gealterte und verschmutzte Drähte und Konverterlöcher hervorgerufen wird. Auch hierdurch entsteht eine höhere Einzeltreffer- und Zufallskoinzidenzrate.
In einem nächsten Schritt wurde die Konstruktion des quadHIDAC im Hinblick auf Detektionseffizienz und Auflösungsvermögen untersucht und optimiert. Verschiedene Lochabstände und Materialstärken wurden hierzu simuliert. Während die Detektionseffizienz mit kleiner werdendem Lochabstand und -durchmesser ansteigt, erreicht die Ortsauflösung ihren optimalen Wert bei der aktuell realisierten Geometrie mit Lochdurchmessern von $0,4\,\mathrm{mm}$ und Lochabständen von $0,5\,\mathrm{mm}$. Bei kleineren Werten können die freigesetzten Elektronen durch die dünnen Wände wandern.

Die Ergebnisse der gezeigten Simulationen werden als Eingabeparameter für verbesserte, quantitative Rekonstruktionsalgorithmen Verwendung finden.
Die Arbeiten die im Rahmen dieser Dissertation begonnen worden sind, im Speziellen die Detektorentwicklungen, führten zum eigenständigen Teilprojekt B6 des Sonderforschungsbereichs 656 ”Molekulare Kardiovaskuläre Bildgebung”, wo sie fortgesetzt werden.

A. Technical Drawings

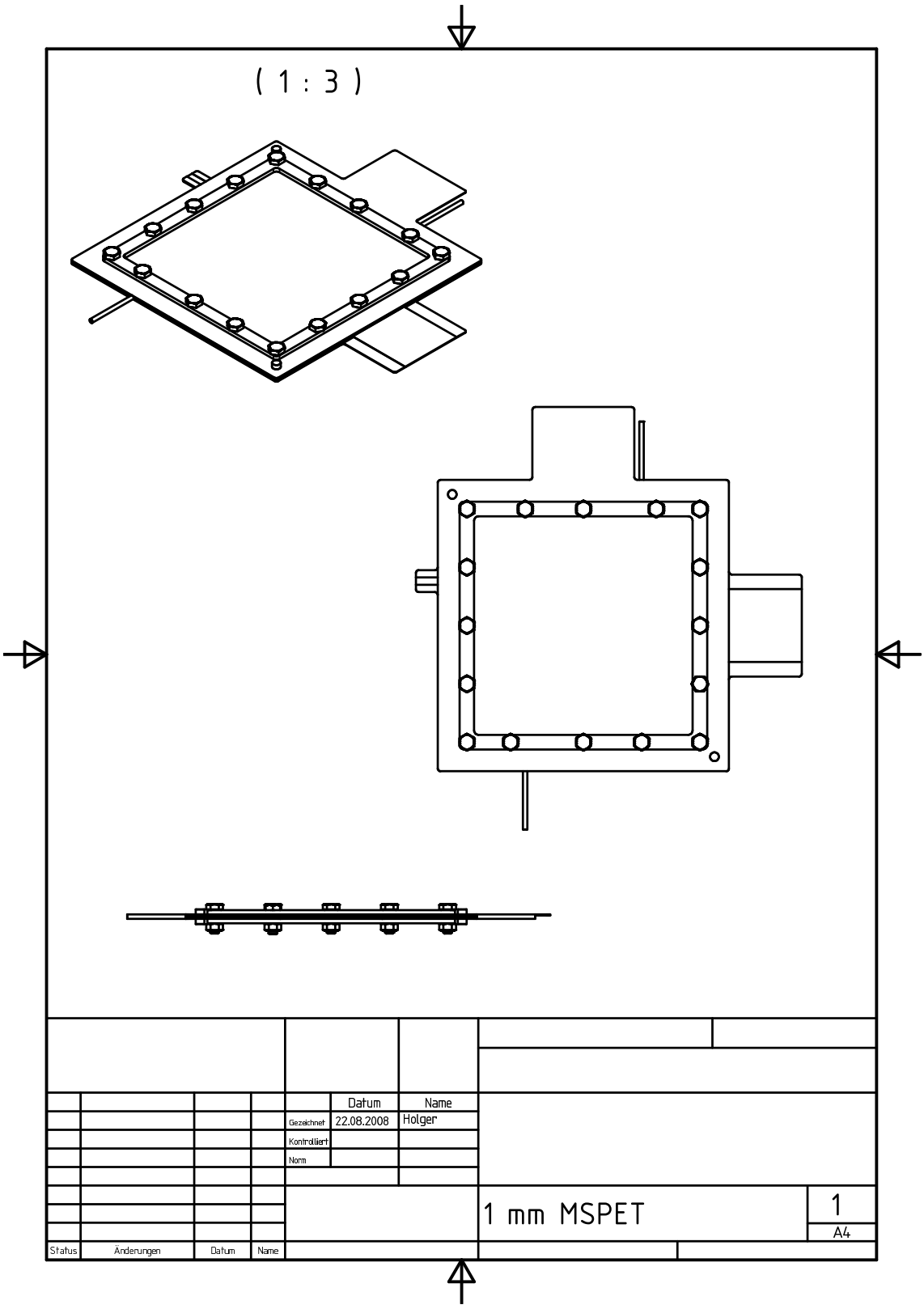

Figure A.1: Overview drawing of an MSPET detector module.

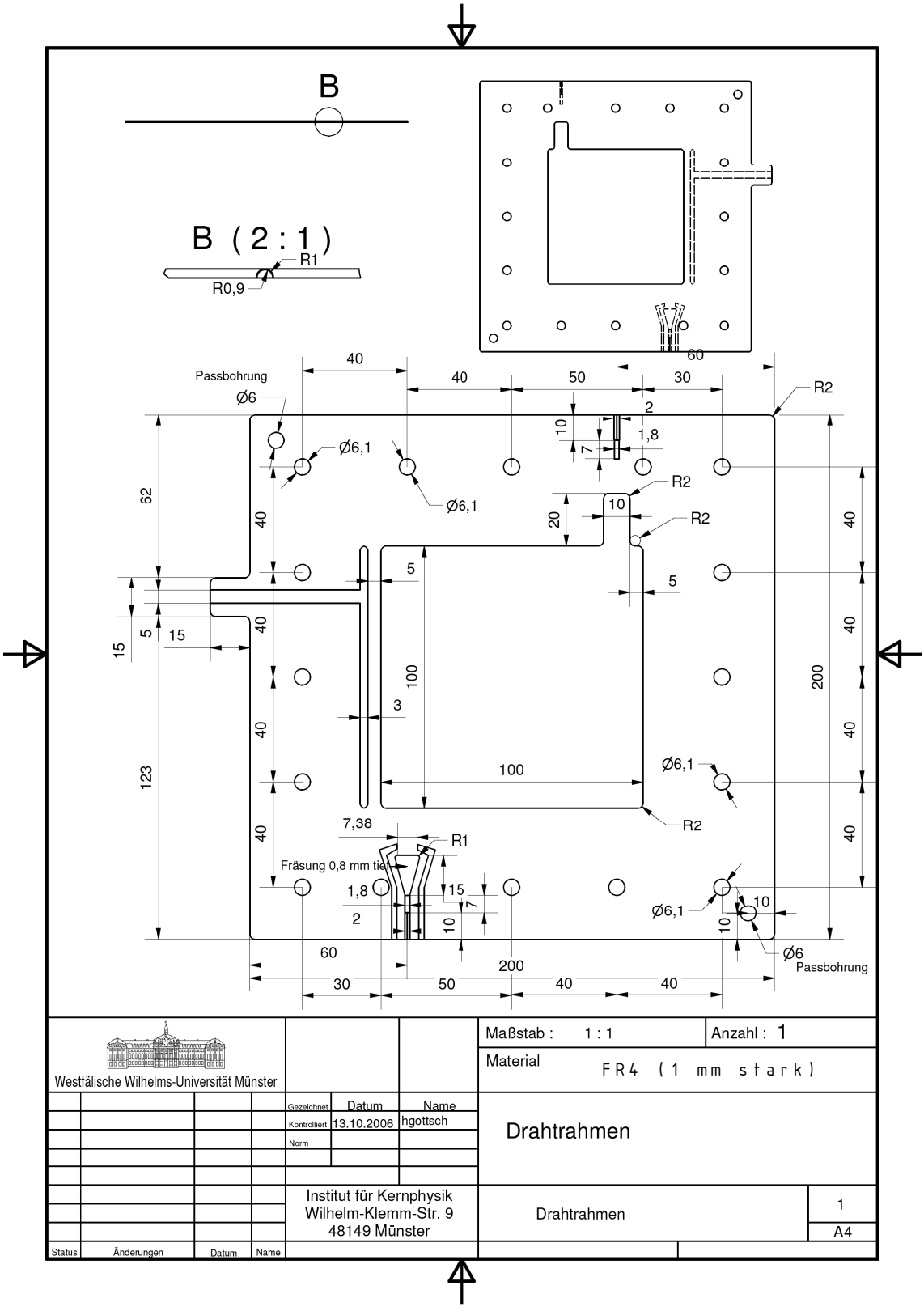

Figure A.2: Wire frame drawing.

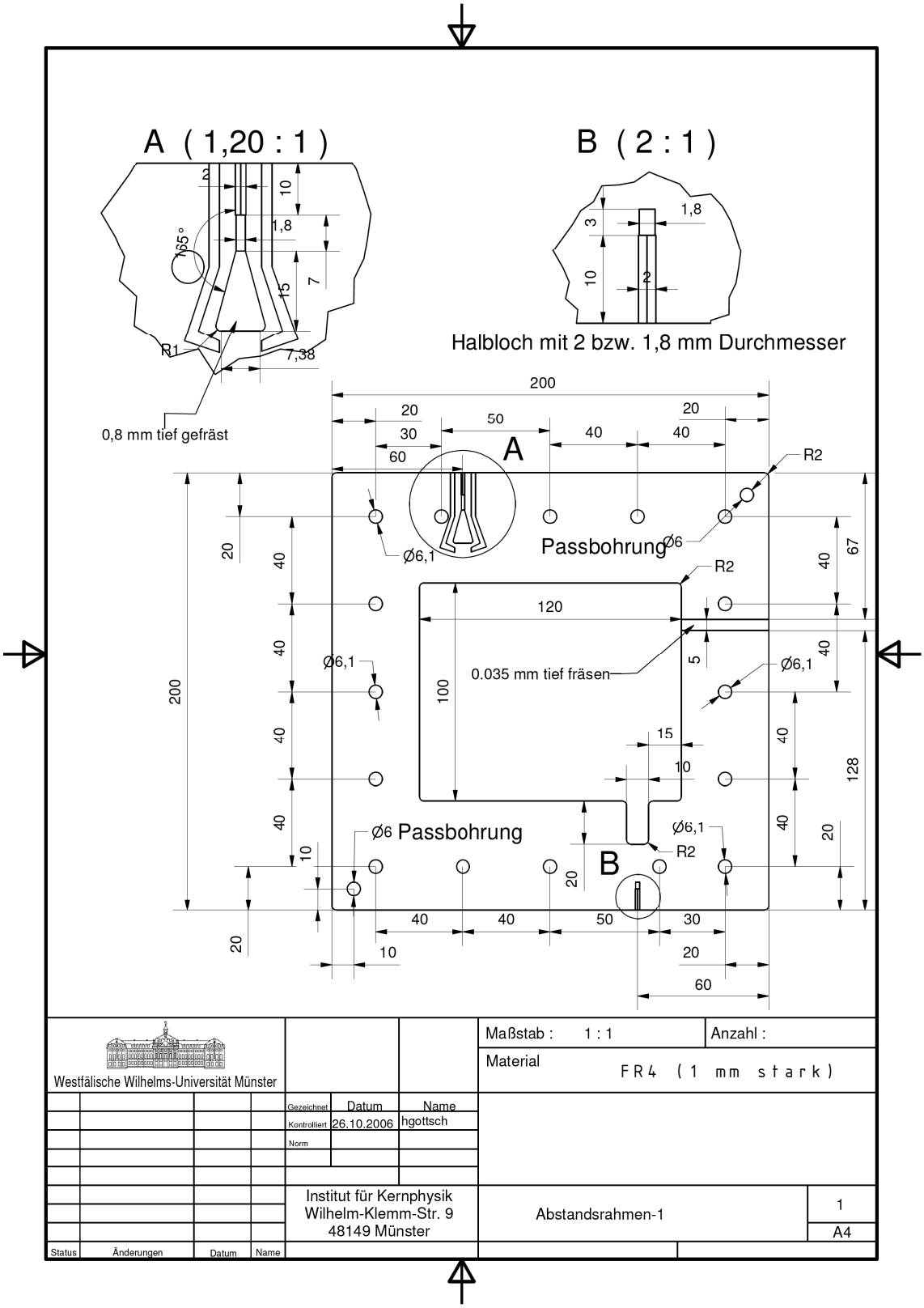

Figure A.3: Distance frame drawing.

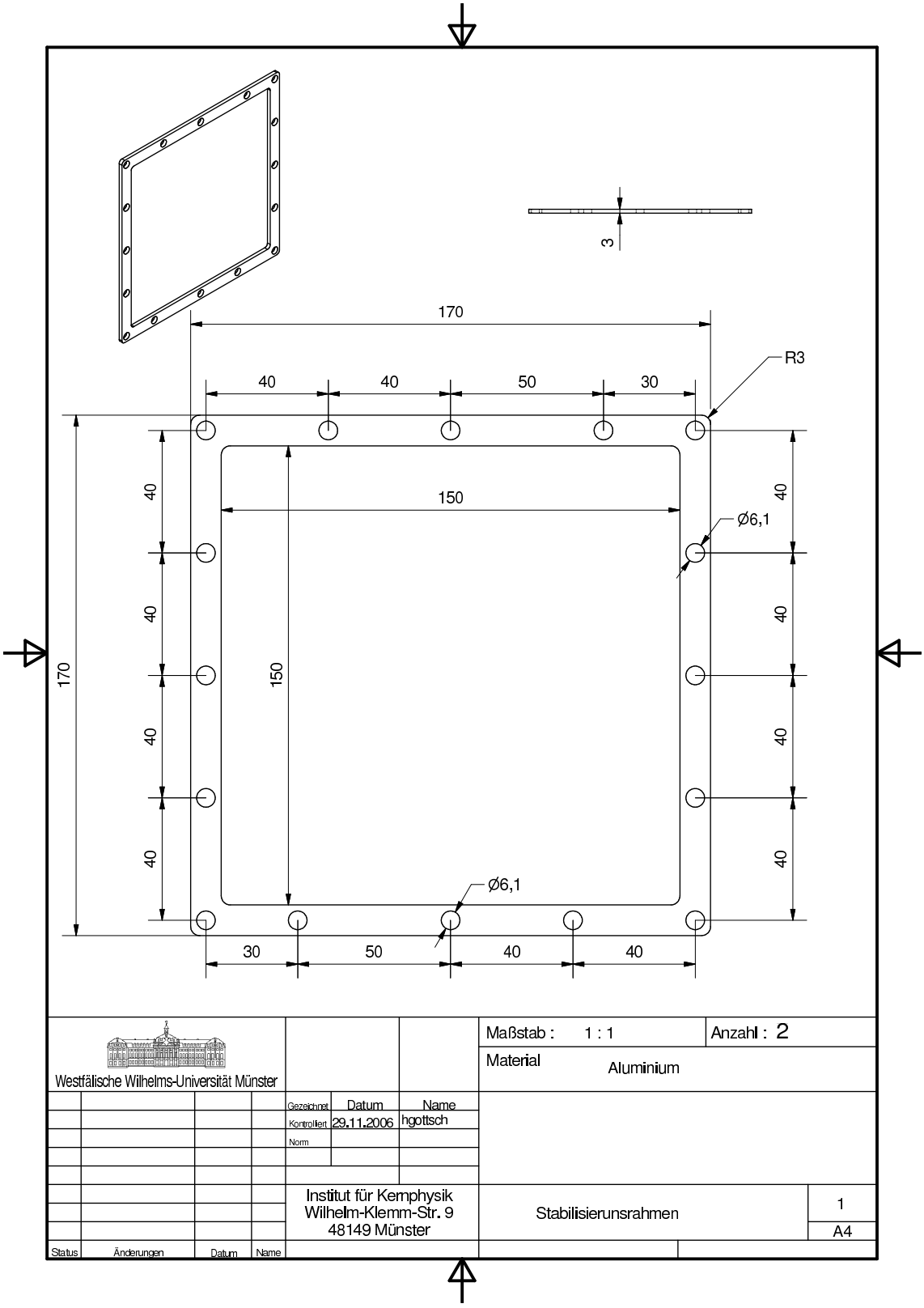

Figure A.4: Stabilising frame.

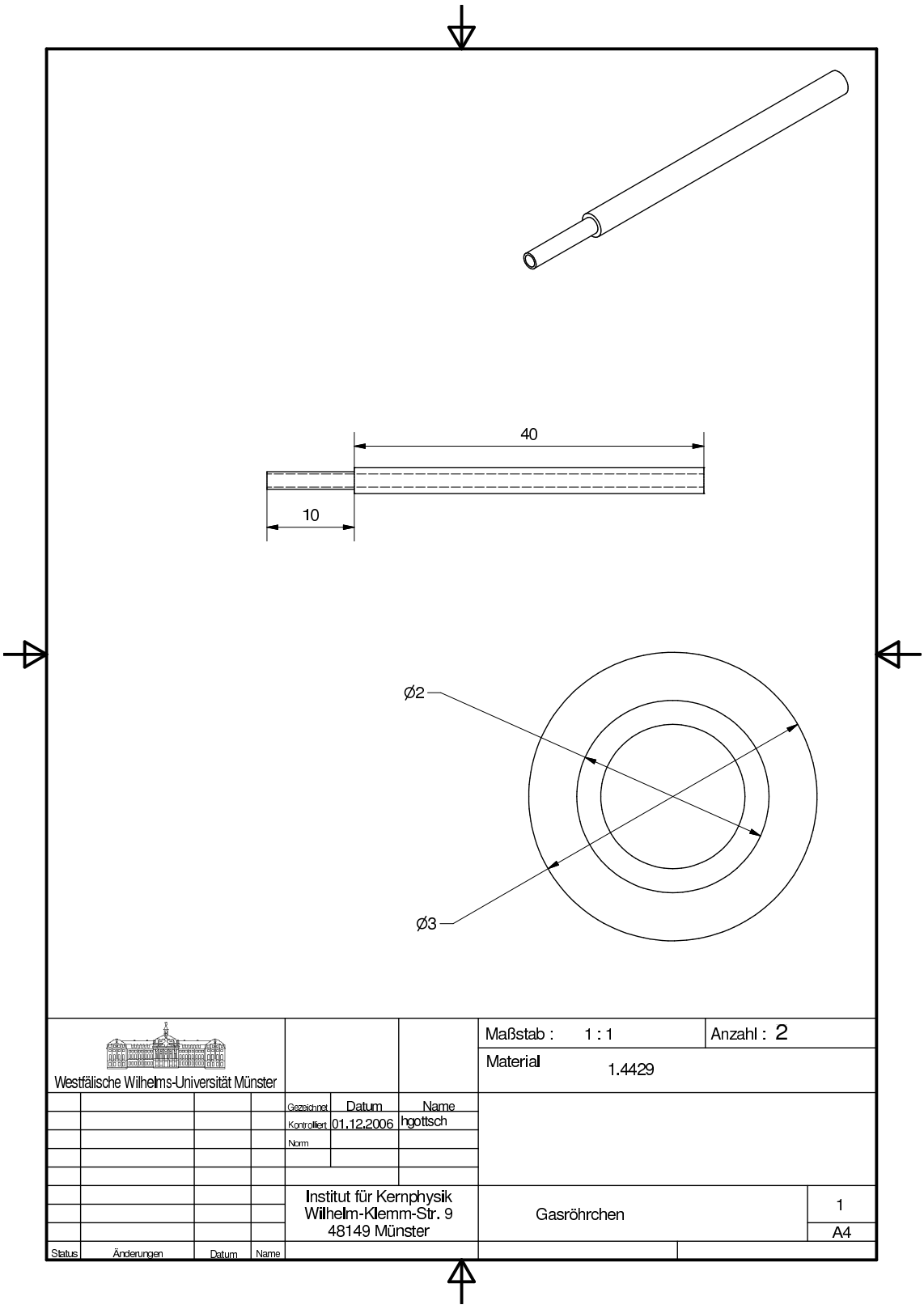

Figure A.5: Gas inlet/outlet pipe.

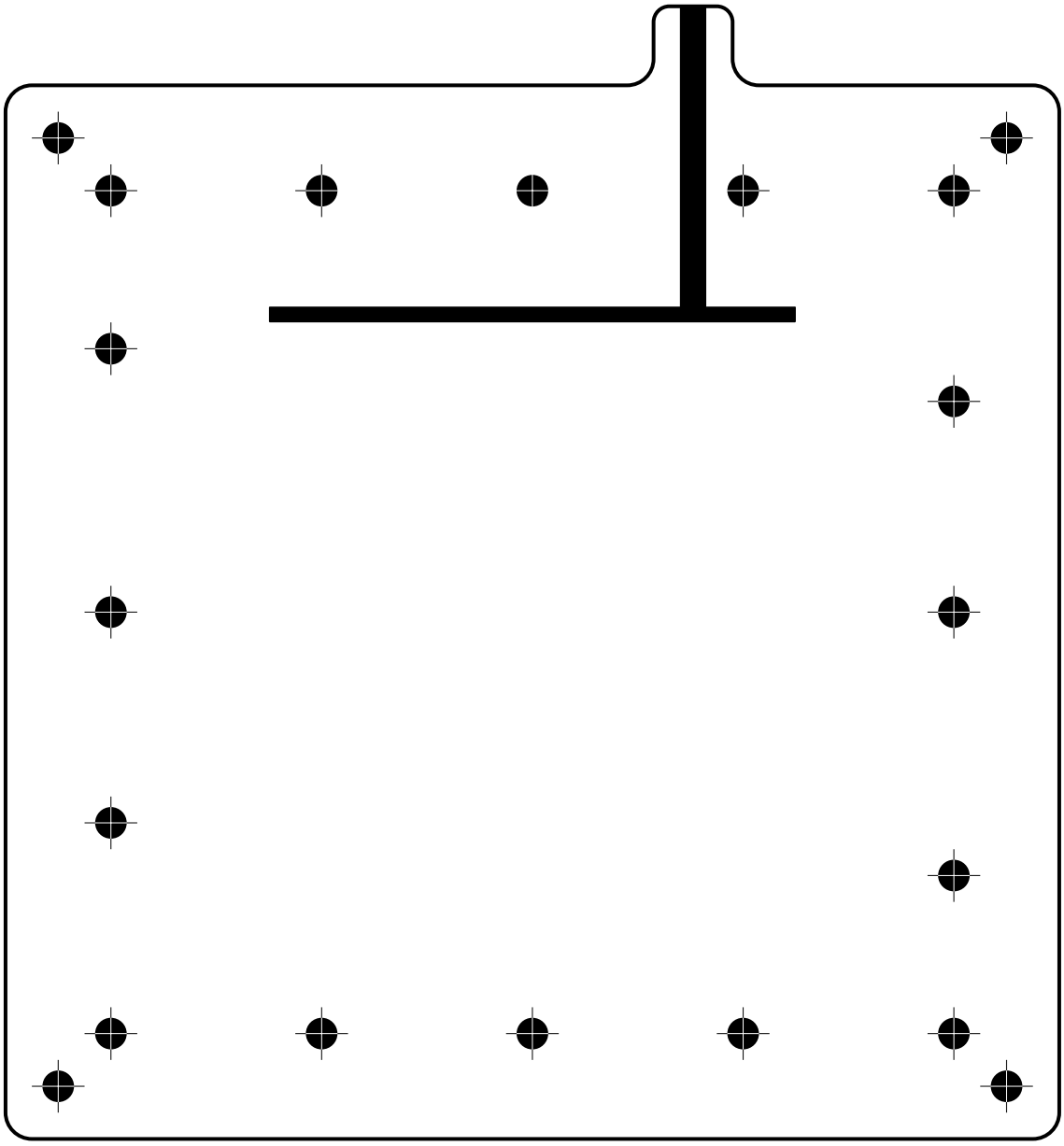

Figure A.6: Etching film for the high voltage supply of the wire grid. Drawing by N. Heine.

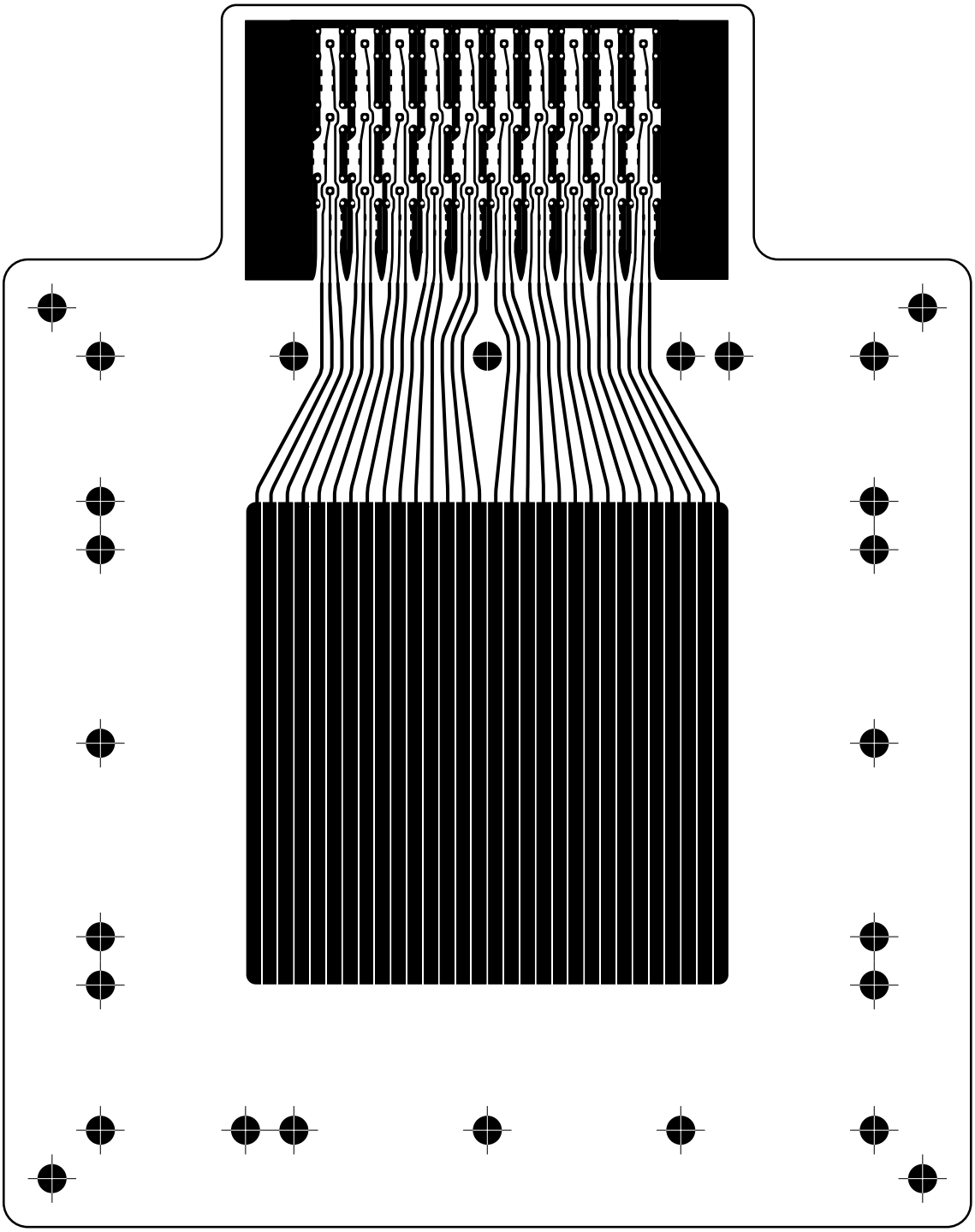

Figure A.7: Etching film for the pad plane. Drawing by N. Heine.

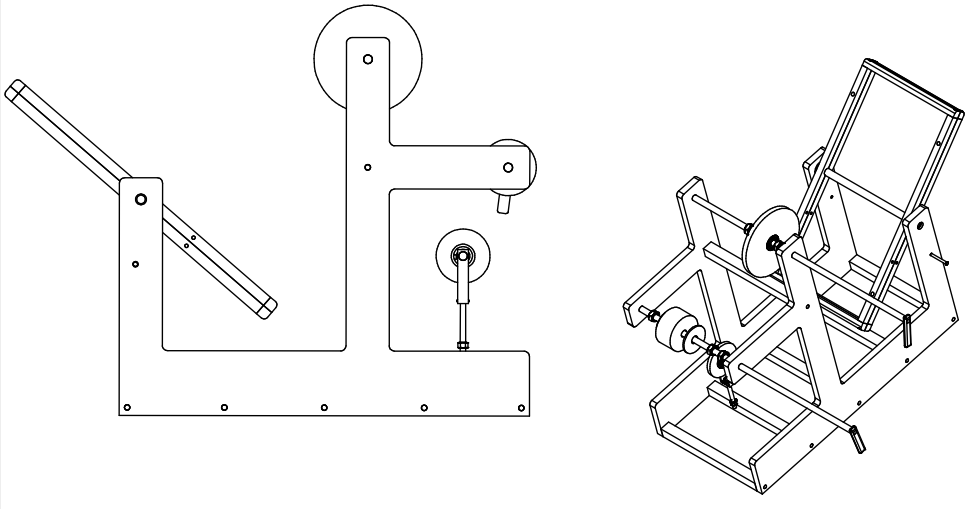

Stückliste

OBJEKT	ANZAH	BAUTEILNUMMER	BEZEICHNUNG
1	1	Seitenplatte2	
2	6	Quergrundrahmen	
3	1	Seitenplatte	
4	4	RK 608	
5	1	Rahmenachse	
6	4	Drahtrahmen1	
7	4	Drahtrahmen2	
8	2	M8x0.75x420 Gewindestange	
9	1	Drahtrolle	
10	2	Pressscheibe	
11	1	Führungsscheibe	
12	8	ISO 4032 - M8	Sechskantmutter
13	1	Gewichtshalter2	
14	1	Gewichtshalter3	
15	1	ISO 4034 - M5	Sechskantmutter
16	1	DIN 6921 - M5 x 50	Sechskantschraube mit Flansch
17	1	Gewichtsrolle	
18	2	Drehhebel	
19	2	ISO 2341 - A - 3 x 30	Bolzen

Westfälische Wilhelms-Universität Münster

Maßstab : 1 : 1 | Anzahl : 1

Material

Gezeichnet | Datum | Name

Kontrolliert 18.01.2007 hgottsch

Norm

Drahtspannmaschine

Institut für Kemphysik
Wilhelm-Klemm-Str. 9
48149 Münster

Apparat | 1 | A4

Status | Änderungen | Datum | Name

Figure A.8: Wire grid winding machine.

Bibliography

[A+99] J. Apostolakis et al. *Geant4 Low Energy Electromagnetic Models for Electrons and Photons*. *CERN preprint* **OPEN-99-034**.

[A+03] S. Agostinelli et al. *Geant4 - A Simulation Toolkit*. *Nucl. Instrum. Methods* **A506** (2003) 250.

[ABBM+04] A. Andronic, S. Biagi, P. Braun-Munzinger et al. *Drift velocity and gain in argon and xenon based mixtures. Nucl. Instrum. Methods* **A523** (2004) 302. arXiv:physics/0402044.

[ADA+08] C. Amsler, M. Doser, M. Antonelli et al. *Review of particle physics. Phys. Lett. B* **667 1-5** (2008) 1.

[AGI+05] K. Amako, S. Guatelli, V. N. Ivanchenko et al. *Comparison of Geant4 Electromagnetic Physics Models Against the NIST Reference Data*. *IEEE Trans. Nucl. Sci.* **52** (2005) 910.

[ALI01] ALICE TRD Collaboration. Technical Design Report, CERN/LHCC, 2001.

[Ang58] H. O. Anger. *Scintillation Camera*. *Rev. Sci. Instrum.* **29** (1958) 27.

[Ang64] H. O. Anger. *Scintillation Camera with Multichannel Collimators. J. Nucl. Med.* **5** (1964) 515.

[Aoy84] T. Aoyama. *Generalized Gas Gain Formula for Proportional Counters*. *Nucl. Instrum. Methods* **A234** (1984) 125.

[ASM+08] A. Athanasiades, L. Sun, C. Martin et al. *A new PET scanner for functional brain imaging based on 2-mm straw detectors*. In *IEEE Nucl. Sci. Symp. Conf. Rec., 2008*. 2008 5445–5451, 5445–5451.

[B+03] V. Bettinardi et al. *Integrated CT/PET systems*. *Proc. Suppl. Nuc. Phys. B* **125** (2003) 139.

[B+05] D. Bailey et al. *Positron emission tomography: basic sciences*. Springer, 2005.

[B+07a] E. Bombardieri et al. *Advances in Nuclear Oncology*. Informa Healthcare, 2007.

[B+07b] D. J. Brenner et al. *Computed Tomography - An Increasing Source of Radiation Exposure*. *N. Engl. J. Med.* **357** (2007) 2277.

[B+07c] A. Brogna et al. *The n-XYTER Reference Manual*. 2007.

[Bat80] J. Bateman. *The development of the Rutherford Laboratory MWPC positron camera*. *Nucl. Instrum. Methods* **176** (1980) 83.

[Bau05] C. Baumann. *X-ray Transmission of Radiators for the ALICE-TRD*. Diplomarbeit, Institut für Kernphysik, Münster, 2005.

[BBB+99] R. Bellazzini, M. Bozzo, A. Brez et al. *The micro-groove detector*. *Nucl. Instrum. Methods Phys. Res., Sect. A* **424 2** (1999) 444.

[BBD+06] A. Brogna, S. Buzzetti, W. Dabrowski et al. *N-XYTER, a CMOS read-out ASIC for high resolution time and amplitude measurements on high rate multi-channel counting mode neutron detectors*. *Nucl. Instrum. Methods Phys. Res., Sect. A* **568 1** (2006) 301.

[BCC+06] A. Blanco, N. Carolino, C. Correia et al. *RPC-PET: a new very high resolution PET technology*. *IEEE Trans. Nucl. Sci.* **53 5** (2006) 2489.

[BCH+07] R. Ballabriga, M. Campbell, E. Heijne et al. *The Medipix3 prototype, a pixel readout chip working in single photon counting mode with improved spectrometric performance*. *IEEE Trans. Nucl. Sci.* **54 5** (2007) 1824.

[BCS+84] J. Bateman, J. Connolly, R. Stephenson et al. *Rutherford Appleton Laboratory's Mark I multiwire proportional counter positron camera*. *Nucl. Instrum. Methods Phys. Res., Sect. A* .

[BDR+07] A. Bamberger, K. Desch, U. Renz et al. *Readout of GEM detectors using the Medipix2 CMOS pixel chip*. *Nucl. Instrum. Methods Phys. Res., Sect. A* **573 3** (2007) 361.

[BDS+09] F. Büther, M. Dawood, L. Stegger et al. *List Mode-Driven Cardiac and Respiratory Gating in PET*. *J. Nucl. Med.* **50 5** (2009) 674.

[Bia99] S. F. Biagi. *Monte Carlo simulation of electron drift and diffusion in counting gases under the influence of electric and magnetic fields*. *Nucl. Instrum. Methods* **A421** (1999) 234.

[BR+97] R. Brun, F. Rademakers et al. *ROOT-an object oriented data analysis framework*. *Nucl. Instrum. Methods Phys. Res., Sect. A* **389 1** (1997) 81.

[Bro99] G. L. Brownell. *A History of Positron Imaging*. 50th year of service presentation by the author to the Massachusetts General Hospital, 1999.

[Bud83] T. F. Budinger. *Time-of-flight positron emission tomography: status relative to conventional PET*. *J. Nucl. Med* **24** (1983) 73.

[Buz08] T. M. Buzug. *Computed Tomography: From Photon Statistics to Modern Cone-Beam CT*. Springer, 2008.

[C+68] G. Charpak et al. *The use of multiwire proportional counters to select and localize charged particles*. *Nucl.Instrum. Methods* **62** (1968) 262.

[C+83] W. G. Cross et al. *A short atlas of beta-ray spectra*. *Phys. Med. Biol.* **28 11** (1983) 1251.

[C+99] I. Castiglioni et al. *Scatter Correction Techniques in 3D PET: A Monte Carlo Evaluation*. *IEEE Trans. Nucl. Sci.* **46 6** (1999) 2053.

[CBM05] CBM Collaboration. Technical Status Report, GSI, Darmstadt, 2005.

[CCE+75] Z. Cho, J. Chan, L. Ericksson et al. *Positron ranges obtained from biomedically important positron-emitting radionuclides*. *J. Nucl. Med.* **16 12** (1975) 1174.

[CDGR02] G. Charpak, J. Derre, Y. Giomataris et al. *Micromegas, a multipurpose gaseous detector*. *Nucl. Instrum. Methods Phys. Res., Sect. A* **478 1-2** (2002) 26.

[CHK97] D. Cullen, J. Hubbell and L. Kissel. *EPDL97: The evaluated photon data library, 97 version*. *UCRL-50400* **6**.

[CJSS73] G. Charpak, A. Jeavons, F. Sauli et al. *High-accuracy measurements of the centre of gravity of avalanches in proportional chambers*. technical report, CERN–73-11, European Organization for Nuclear Research, Geneva (Switzerland), 1973.

[CLS+02] V. Chepel, M. Lopes, V. Solovov et al. *Development of liquid xenon detectors for medical imaging* arXiv:physics/0211117.

[Cul95] D. Cullen. *A simple model of photon transport*. *Nucl. Instrum. Methods Phys. Res., Sect. B* **101 4** (1995) 499.

[DBL+07] M. Dawood, F. Büther, N. Lang et al. *Respiratory gating in positron emission tomography: a quantitative comparison of different gating schemes*. *Med. Phys.* **34** (2007) 3067.

[DED+04] A. Divoli, K. Erlandsson, J. Dickson et al. *Estimation of random coincidences from the prompt PET data*. In *IEEE Nucl. Sci. Symp. Conf. Rec.*. Vol. 6, 2004 .

[Der79] S. E. Derenzo. *Precision measurement of annihilation point spread distributions for medically important positron emitters*. Positron Annihilation, R. R. Hasiguti and K. Fujiwara, Eds. Sendai, Japan:The Japan Institute of Metals, 1979.

[DFE+05] A. Divoli, M. Flower, K. Erlandsson et al. *The PETRRA positron camera*. *Phys. Med. Biol.* **50** (2005) 3971.

[DGB07] A. Del Guerra and N. Belcari. *State-of-the-art of PET, SPECT and CT for small animal imaging*. *Nucl. Instrum. Methods Phys. Res., Sect. A* **583 1** (2007) 119.

[DGLL+82] A. Del Guerra, C. Lim, G. Lum et al. *Medical positron imaging with a dense drift space multiwire proportional chamber*. *IEEE Trans. Med. Imaging* **1 1** (1982) 4.

[dJ+07] H. de Jong et al. *Performance Evaluation of the ECAT HRRT: An LSO/LYSO double layer high resolution scanner*. *Phys. Med. Biol.* **52** (2007) 1505.

[DMHB93] S. Derenzo, W. Moses, R. Huesman et al. *Critical instrumentation issues for< 2 mm resolution, high sensitivity brain PET*. *Ann. Nucl. Med.* **7** (1993) 3.

[E+08] S. Eberl et al. *Comparison of 3 ring and 4 ring Biograph TruePoint PET/CT Systems*. *J. Nucl. Med. Meeting Abstracts* **48** (2008) 409.

[Ers72] G. Erskine. *Electrostatic problems in multiwire proportional chambers*. *Nucl. Instrum. and Methods* **105** (1972) 565.

[Eva55] R. D. Evans. *The Atomic Nucleus*. TATA McGraw-Hill, 1955.

[Gat79] E. Gatti. *Optimum geometry for strip cathodes or grids in MWPC for avalanche localization along the anode wires*. *Nucl. Instrum. Methods* **163** (1979) 83.

[Got05] H. Gottschlag. *Entwicklung einer Apparatur zur automatisierten Positions- und Spannungsbestimmung von Drähten in Vieldrahtproportionalkammern*. diploma thesis, Institut für Kernphysik, WWU Münster, 2005.

[H+04] H. Herzog et al. *NEMA NU2-2001 Guided Performance Evaluation of four Siemens ECAT PET Scanners*. *IEEE Trans. Nucl. Sci.* **51 5** (2004) 2662.

[HÖ7] H. Hünteler. *Development and Evaluation of a Multiwire Proportional Chamber for a High Resolution Small Animal PET scanner*. diploma thesis, Institut für Kernphysik, WWU Münster, 2007.

[Hev23] G. Hevesy. *Absorption and translocation of lead by plants: a contribution to the application of the method of radioactive indicators in the investigation of the change of substance*. *Biochem. J.* **17** (1923) 439.

[HL94] H. Hudson and R. Larkin. *Accelerated image reconstruction using ordered subsets of projection data*. *IEEE Trans. Med. Imaging* **13 4** (1994) 601.

[HØ79] J. Hubbell and I. Øverbø. *Relativistic atomic form factors and photon coherent scattering cross sections*. *J. Phys. Chem. Ref. Data* **8** (1979) 69.

[Hol92] E. Holzschuh. *Measurement of the neutrino mass from tritium beta-decay*. *Rep. Prog. Phys.* **55** (1992) 1035.

[HRG03] J. Humm, A. Rosenfeld and A. Guerra. *From PET detectors to PET scanners*. *Eur. J. Nucl. Med. Mol. Imaging* **30 11** (2003) 1574.

[HRJ+07] D. Hastings, A. Reader, P. Julyan et al. *Performance characteristics of a small animal PET camera for molecular imaging*. *Nucl. Instrum. Methods Phys. Res., Sect. A* **573 1-2** (2007) 80.

[IAE09] IAEA Nuclear Data Services. *Charged-particle cross section database for medical radioisotope production*, 2009. `http://www-nds.ipen.br/medical/`.

[J+94] R. J. Jaszczak et al. *Pinhole collimation for ultra high resolution, small-vield-of-view SPECT*. *Phys. Med. Biol.* **39** (1994) 425.

[J+99] A. P. Jeavons et al. *A 3D HIDAC-PET Camera with Sub-millimetre Resolution for Imaging Small Animals. IEEE Trans. Nucl. Sci.* **46 3**.

[JAN01] D. M. J. Als-Nielsen. *Elements of Modern X Ray Physics*. Wiley & Sons, 2001.

[JC76] A. Jeavons and C. Cate. *The proportional chamber gamma camera. IEEE Trans. Nucl. Sci.* **23 1** (1976) 640.

[JCS75] A. Jeavons, G. Charpak and R. Stubbs. *The high-density multiwire drift chamber*. *Nucl. Instr. Methods* **124** (1975) 491.

[Jea79] A. Jeavons. *The CERN proportional chamber positron camera*. In *Proc. 5th Int. Conf. Positron Annihilation, Lake Yamanaka, Japan*. 1979 355–370, 355–370.

[Jea95] A. Jeavons. *Radiographic detector with perforated cathode*, 1995. US Patent 5,434,468.

[Jea02] A. Jeavons. *Imaging system using a high-density avalanche chamber converter*, 2002. US Patent 6,404,114.

[Jea05] A. Jeavons. private communication, 2005.

[JFL+76] A. Jeavons, N. Ford, B. Lindberg et al. *Two-Dimensional Proportional Chamber Readout Using Digital Techniques*. *IEEE Trans. Nucl. Sci.* **23 1** (1976) 259.

[JHH+83] A. Jeavons, K. Hood, G. Herlin et al. *The high-density avalanche chamber for positron emission tomography*. *IEEE Trans. Nucl. Sci.* **30 1** (1983) 640.

[JKL+80] A. Jeavons, K. Kull, B. Lindberg et al. *A proportional chamber positron camera for medical imaging*. *Nucl. Instrum. Methods Phys. Res., Sect. A* **176** (1980) 89.

[Jon96] T. Jones. *The role of positron emission tomography within the spectrum of medical imaging*. *Eur. J. Nucl. Med. Mol.Imaging* **23 2** (1996) 207.

[JTF+78] A. Jeavons, D. Townsend, N. Ford et al. *A high-resolution proportional chamber positron camera and its applications*. *IEEE Trans. Nucl. Sci.* **25 1** (1978) 164.

[K+98] P. Kinahan et al. *Attenuation correction for a combined 3D PET/CT scanner*. *Med. Phys.* **25 10** (1998) 2046.

[K+04] A. Kuhn et al. *Design of a lanthanum bromide detector for time-of-flight PET*. *IEEE Trans. Nucl. Sci.* **51 5** (2004) 2550.

[K+08] J. S. Karp et al. *Benefit of time-of-flight in PET: experimental and clinical results*. *J. Nucl. Med.* **49 3** (2008) 462.

[Kan02] S. A. Kana. *Introduction to Physics in Modern Medicine*. Taylor & Francis Ltd, 2002.

[KE63] D. E. Kuhl and R. Q. Edwards. *Image Separation Radioisotope Scanning*. *Radiology* **80** (1963) 653.

[Kno89] G. F. Knoll. *Radiation Detection and Measurement*. John Wiley and Sons, 1989.

[Kol07] H. Kolem. *Medizintechnik*, Springer. 2007 271–283, 271–283.

[Kow85] T. Z. Kowalski. *Generalized Parametrization of Gas Gain in Proportional Counters*. *Nucl. Inst. Methods* **A243** (1985) 501.

[LCK+75] C. Lim, D. Chu, L. Kaufman et al. *Initial characterization of a multi-wire proportional chamber positron camera*. *IEEE Trans. Nucl. Sci.* **22 1** (1975) 388.

[Lec09] R. Lecomte. *Novel detector technology for clinical PET*. *Eur. J. Nucl. Med. Mol. Imaging* **36 Suppl 1** (2009) 69.

[LH99] C. Levin and E. Hoffmann. *Calculation of positron range and its effect on the fundamental limit of positron emission tomography system spatial resolution*. *Phys. Med. Biol.* **44** (1999) 781.

[LMA01] J. Lacy, C. Martin and L. Armendarez. *High sensitivity, low cost PET using lead-walled straw detectors*. *Nucl. Instrum. Methods Phys. Res., Sect. A* **471 1-2** (2001) 88.

[Loh86] E. Lohrmann. *Hochenergiephysik*. Teubner, 1986.

[M. 09] M. J. Berger, J. S. Coursey, M. A. Zucker and J. Chang. *NIST estar: Stopping-Power and Range Tables for Electrons*, 2009. `http://physics.nist.gov/PhysRefData/Star/Text/contents.html`.

[M+88] G. Musiol et al. *Kern- und Elementarteilchenphysik*. VCH, 1988.

[M+04] J. Missimer et al. *Performance evaluation of the 16-module quad-HIDAC small animal PET camera*. *Phys. Med. Biol.* **49** (2004) 2069.

[M+06] W. W. Moses et al. *Factors influencing timing resolution in a commercial LSO PET camera*. *IEEE Trans. Nucl. Sci.* **53 1** (2006) 78.

[Man78] A. Manuel. *An application of proportional chambers to the measurement of the electronic properties of solids by positron annihilation*. *Nucl. Instrum. Methods* **156** (1978) 67.

[Mat88] E. Mathieson. *Cathode charge distributions in multiwire chambers: 4. Empirical formula for small anode-cathode separation*. *Nucl. Instrum. Methods Phys. Res., Sect. A* **270 2-3** (1988) 602.

[MDH+88] B. McKee, H. Dinsdale, M. Hogan et al. *Description and performance of a prototype PET system for small volume imaging*. *Nucl. Instrum. Methods Phys. Res., Sect. A* **269** (1988) 392.

[MDH94] B. McKee, A. Dickson and D. Howse. *Performance of QPET, a high-resolution 3D PET imaging system forsmall volumes*. *IEEE Trans. Med. Imaging* **13 1** (1994) 176.

[MEF+88] P. Manfrass, W. Enghardt, W. Fromm et al. *High-density avalanche chambers for positron emission tomography*. *Nucl. Instrum. Methods Phys. Res., Sect. A* **273** (1988) 904.

[MK94] T. Mayer-Kuckuk. *Kernphysik*. B. G. Teubner, 1994.

[MOB+89] P. Marsden, R. Ott, J. Bateman et al. *The performance of a multiwire proportional chamber positron camera for clinical use*. *Phys. Med. Biol.* **34 8** (1989) 1043.

[Mog74] O. E. Mogensen. *Spur reaction model of positronium formation*. *J. Chem. Phys.* **60 3** (1974) 998.

[MU49] N. Metropolis and S. Ulam. *The Monte Carlo Method*. *J. Amer. Stat. Assoc.* **44 247** (1949) 335.

[N+85] W. R. Nelson et al. *EGS4 code system*, 1985.

[Nat09a] National Institute of Standards and Technology. *NIST XCOM: Photon Cross Sections Database*, 2009. `http://physics.nist.gov/PhysRefData/Xcom/Text/XCOM.html`.

[Nat09b] National Nuclear Data Center. *Chart of Nuclides*, 2009. http://www.nndc.bnl.gov/chart/.

[NEM01] NEMA. *Performance Measurement of Positron Emission Tomographs. NEMA Standards Publication* **NU 2-2001**.

[NW01] F. Natterer and F. Wübbeling. *Mathematical methods in image reconstruction*. Soc. Ind. Math., 2001.

[OWEJ06] R. Ott, L. White, N. Evans et al. *A Study of the Application of MWPC-Based Positron Cameras for Breast Imaging*. In *IEEE Nucl. Sci. Symp. Conf. Rec.*. Vol. 5, 2006 .

[Par98] Particle Data Group. *Review of particle physics. Eur. Phys. J. C* **3** (1998) 1.

[PCC+91] S. Perkins, D. Cullen, M. Chen et al. *Tables and graphs of atomic subshell and relaxation data derived from the LLNL Evaluated Atomic Data Library (EADL), Z= 1–100*. technical report, UCRL-50400-Vol. 30, Lawrence Livermore National Lab., CA (United States), 1991.

[PCS97] S. Perkins, D. Cullen and S. Seltzer. *Tables and graphs of electron-interaction cross sections from 10 eV to 100 GeV derived from the LLNL evaluated electron data library (EEDL)*. technical report, UCRL-50400-Vol. 31, Lawrence Livermore National Lab., CA (United States), 1997.

[Phe06] M. E. Phelps (Ed.) *PET: Physics, Instrumentation, and Scanners*. Springer, 2006.

[Phi09] Philips Healthcare. *PET/CT Product Information Webpage*, 2009. http://www.medical.philips.com/main/products/.

[PHJ+75] C. Parkman, Z. Hajduk, A. Jeavons et al. *Two-dimensional MWPC readout at 10 MHz*. In *Conference: ISPRA Symp. Stresa, Italy*. 1975 .

[Pie08] J.-F. Pietschmann. *Development and Evaluation of a Multiwire Proportional Chamber for a High Resolution Small Animal PET scanner*. diploma thesis, Institut für Kernphysik, WWU Münster, 2008.

[PKMC06] V. Panin, F. Kehren, C. Michel et al. *Fully 3-D PET reconstruction with system matrix derived from point source measurements. IEEE Trans. Med. Imaging* **25 7** (2006) 907.

[Rad17] J. Radon. *Über die Bestimmung von Funktionen durch ihre Integralwerte längs gewisser Mannigfaltigkeiten. Berichte Sächsische Akademie der Wissenschaften, Leipzig, Mathematisch-Physikalische Klasse* **69** (1917) 262.

[RD06] C. Rodgers and E. Defects. *Questions about prenatal ultrasound and the alarming increase in autism. Midwifery Today* **80** (2006) 16.

[RLV03] W. Riegler, C. Lippmann and R. Veenhof. *Detector physics and simulation of resistive plate chambers. Nucl. Instrum. Methods Phys. Res., Sect. A* **500 1-3** (2003) 144.

[RSO75] R. Reynolds, R. Snyder and T. Overton. *A multiwire proportional chamber positron camera: Initial results (for radioisotope imaging). Phys. Med. Biol.* **20** (1975) 136.

[S+99] J. Seidel et al. *Depth identification accuracy of a three layer phoswich PET detector module. IEEE Trans. Nucl. Sci.* **46 3** (1999) 485.

[S+03] D. Strulab et al. *GATE (geant4 application for tomographic emission): a PET/SPECT general-purpose simulation platform. Nucl. Phys. B Proc. Suppl.* **125** (2003) 75.

[S+05] K. P. Schäfers et al. *Performance Evaluation of the 32-module quadHIDAC Small-Animal PET Scanner. J. Nucl. Med.* **46 6** (2005) 996.

[S+06] K. Shibuya et al. *A Healthy Volunteer FDG-PET Study on Annihilation Radiation Non-collinearity. IEEE Nucl. Sci. Symp. Conf. Rec.* **M06-107**.

[S+07] S. Surti et al. *Performance of Philips Gemini TF PET/CT Scanner with Special Consideration for Its Time-of-Flight Imaging Capabilities. J. Nucl. Med.* **48 3** (2007) 471.

[Sau77] Sauli, F. and CERN. Geneva. *Principles of operation of multiwire proportional and drift chambers. Imprint* **3** (1977) 92.

[Sau97] F. Sauli. *GEM: A new concept for electron amplification in gas detectors. Nucl. Instrum. Methods Phys. Res., Sect. A* **386 2** (1997) 531.

[SBJ+98] A. Sarvestani, H. Besch, M. Junk et al. *Gas amplifying hole structures with resistive position encoding: a new concept for a high rate imaging pixel detector. Nucl. Instrum. Methods Phys. Res., Sect. A* **419 2** (1998) 444.

[Sch66] H. Schopper. *Weak Interactions and Nuclear Beta Decay*. North-Holland Publishing Co., 1966.

[Sch08] K. Schäfers. private communication, 2008.

[SFVS01] F. Salvat, J. Fernández-Varea and J. Sempau. *PENELOPE, a code system for Monte Carlo simulation of electron and photon transport*. In *Proceedings of a Workshop/Training Course, OECD/NEA*. Citeseer, Vol. 5, 2001 .

[Sie07] Siemens Medical Solutions USA. *Are you HD-ready?*. Product brochure, 2007.

[SIM09] SIMSET collaboration. *SIMSET Overview*, 2009. `http://depts.washington.edu/simset/html/simset_main.html`.

[Smi05] I. Smirnov. *Heed Users Manual*, 2005. `http://consult.cern.ch/writeup/heed/`.

[SML+02] N. Shehad, C. Martin, J. Lacy et al. *Ultra-high resolution PET detector using lead walled straws*. In *IEEE Nucl. Sci. Symp. Conf. Rec.*. Vol. 3, 2002 .

[SSD73] P. A. Souder, J. Sandweiss and A. A. Disco. *A "scaled" MWPC with 0.5 mm wire spacing*. *Nucl. Instrum. Methods* **109 2** (1973) 237 .

[Swe51] W. H. Sweet. *The use of nuclear disintegration in the diagnosis and treatment of brain tumor*. *N. Engl. J. Med.* **245** (1951) 875.

[T+92] C. J. Thompson et al. *PETSIM: Monte Carlo program simulation of all sensitivity and resolution parameters of cylindrical positron imaging systems*. *Phys. Med. Biol.* **37** (1992) 731.

[T+07] M. Teräs et al. *Performance of the new generation of whole-body PET/CT scanners: Discovery STE and Discovery VCT.*. *Eur. J. Nucl. Med. Mol. Imaging* **34 10** (2007) 1683.

[Tao76] S. J. Tao. *The Formation of Positronium in Moleular Substances*. *Appl. Phys.* **10** (1976) 67.

[TBA+02] E. Tsyganov, A. Buzulutskov, P. Antich et al. *Triple GEM structure for medical imaging*. In *IEEE Nucl. Sci. Symp. Conf. Rec.*. Vol. 2, 2002 .

[TCM+83] D. Townsend, R. Clack, R. Magnanini et al. *Image reconstruction for a rotating positron tomograph*. *IEEE Trans. Nucl. Sci.* **30 1** (1983) 594.

[TFJ+87] D. Townsend, P. Frey, A. Jeavons et al. *High density avalanche chamber (HIDAC) positron camera*. *J. Nucl. Med.* **28 10** (1987) 1554.

[TK97] S. Tanaka and M. Kawaguti. *DAWN for GEANT4 Visualization*, 1997.

[Tow88] D. Townsend. *PET with the HIDAC camera?*. *Nucl. Instrum. Methods Phys. Res., Sect. A* **269** (1988) 443.

[TP04] J. M. Tsutsui and R. T. Porter. *The use of microbubbles to target drug delivery*. *Cardiovasc. Ultrasound* **2(1):23**.

[Tsa74] Y. Tsai. *Pair production and bremsstrahlung of charged leptons*. *Rev. Mod. Phys.* **46 4** (1974) 815.

[Uhl05] V. Uhlendorff. private communication, 2005.

[V+00] P. Vetter et al. *Studies of Positronium Decay Modes Using GAMMASPHERE*. Annual Report LBNL-47549, Nuclear Science Division, Lawrence Berkley National Laboratory, 2000.

[Va'92] J. Va'Vra. *Wire chamber gases*. *Nucl. Instrum. Methods Phys. Res., Sect. A* **323 1-2** (1992) 34.

[Vee08] R. Veenhof. *A drift chamber simulation program*, 2008. `http://garfield.web.cern.ch/garfield/`.

[Ver10] D. Vernekohl. *Measurements with a Multi-Wire Proportional Chamber for Small Animal Positron Emission Tomography*. diploma thesis, Institut für Kernphysik, WWU Münster, 2010.

[VSK85] Y. Vardi, L. Shepp and L. Kaufman. *A statistical model for positron emission tomography*. *J. Amer. Stat. Assoc.* (1985) 8.

[vV+08] F. van Velden et al. *Comparison of 3D-OP-OSEM and 3D-FBP on HRRT studies: effects of randoms estimation methods*. *Phys. Med. Biol.* **53** (2008) 3217.

[VWS+04] P. Vaska, C. Woody, D. Schlyer et al. *RatCAP: miniaturized head-mounted PET for conscious rodent brain imaging*. *IEEE Trans. Nucl. Sci.* **51 5** (2004) 2718.

[W+51] J. Wrenn et al. *The use of positron emitting radioisotopes for localisation of brain tumors*. *Science* **113** (1951) 525.

[W+06] D. Weishaupt et al. *How does MRI work?*. Springer, 2006.

[WA04] M. N. Wernick and J. N. Aarsvold (Ed.) *Emission Tomography: The Fundamentals of PET and SPECT*. Elsevier Academic Press, 2004.

[WB93] L. R. W. Blum. *Particle Detection with Drift Chambers*. Springer, 1993.

[WB04] S. Weber and A. Bauer. *Small animal PET: aspects of performance assessment*. *Eur. J. Nucl. Med. Mol. Imaging* **31 11** (2004) 1545.

[WB08] L. R. W. Blum, W. Riegler. *Particle Detection with Drift Chambers*. Springer, 2008.

[WMU04] H. Wellisch, M. Maire and L. Urban. *Geant4 Physics Reference Manual*, 2004. `http://cern.ch/geant4/support/index.shtml`.

[Z+05] K. Ziemons et al. *The ClearPET project: development of a 2nd generation high-performance small animal PET scanner*. *Nucl. Instrum. Methods Phys. Res., Sect. A* **537 1-2** (2005) 307.

[Zar89] A. Zarubin. *Properties of wire chamber gases*. *Nucl. Instrum. Methods Phys. Res., Sect. A* **283** (1989) 409.

Danksagung

Ich möchte mich abschliessend bei allen bedanken, die zum Gelingen dieser Arbeit beigetragen haben.
Herrn Prof. Dr. Johannes P. Wessels danke ich für die Möglichkeit diese Arbeit in seiner Arbeitsgruppe anzufertigen, die hervorragenden Arbeitsbedigungen und die Ermöglichung der zahlreichen Teilnahmen an Konferenzen und Fachveranstaltungen im In- und Ausland.
Herrn PD Dr. Klaus Reygers danke ich für die Betreuung meiner Arbeit. Seine Ratschläge, Hinweise und Hilfen sowie viele interessante Diskussionen zu physikalischen und technischen Themen haben entscheidend zu dieser Arbeit beigetragen.
Den ehemaligen Diplomanden Henning Hünteler, Jan-Frederik Pietschmann und Don Vernekohl danke ich für die gute und erfolgreiche Zusammenarbeit an der gemeinsamen Sache.
Thomas Kösters danke ich für die gute Zusammenarbeit, die Diskussionen und die vielen, geduldigen Rekonstruktionen.
Dem Sonderforschungsbereich 656 und dem EIMI, hier besonders PD Dr. Klaus Schäfers, Dr. Frank Wübbeling, Thomas Kösters und Torsten Budumlu danke ich für die vielen Diskussionen und Anregungen. Für die technische Unterstützung und die hsvervorragende Zusammenarbeit danke ich Norbert Heine, Roland Berendes, Wolfgang Verhoeven und den Teams der Elektronik- sowie der Feinmechanischen Werkstatt.
Für die kritische Durchsicht der Arbeit möchte ich mich vor allem bei Dr. Christoph Baumann, Dr. Christian Klein-Bösing und Daniel Gottschlag bedanken, sowie bei Dr. Thomas Dietel, Alexander Wilk, Dr. David Emschermann, Dr, Matus Kalisky, Jan-Frederik Pietschmann und Thomas Kösters.
Bei Christoph Baumann möchte ich mich darüber hinaus für die hervorragende Zusammenarbeit während der letzten 10 Jahre, sowie für die aussergewöhnlich gute Büroatmosphäre zu der auch Bastian Bathen, Henning Hünteler, Jan-Frederik Pietschmann, Don Vernekohl und Markus Rammler beigetragen haben bedanken. Ausserdem danke ich allen aktuellen und ehemaligen Mitgliedern der Arbeitsgruppe für die gute Zusammenarbeit und tolle Arbeitsklima: Björn Albrecht, Jonas Anielski, Jan Auffenberg, Dr. Christoph

Baumann, Cyrano Bergmann, Jennifer Bersch, Katharina Büscher, Dr. Thomas Dietel, Dr. David Emschermann, Henriette Gatz, Dr. Richard Glasow, Helge Grimm, Jan Fiete Grosse-Oetringhaus, Markus Heide, Norbert Heine, Dr. Matus Kalisky, Sebastian Klamor, Dr. Christian Klein-Bösing, Dr. Melanie Klein-Bösing, Stefan Korsten, Michael Kowalik, Ansgar Kumpmann, Robert Lüchtenborg, Manuel Moreno Garcia, Friederike Poppenborg, Markus Rammler, Priv.-Doz. Dr. Klaus Reygers, Baldo Sahlmüller, Prof. em. Dr. Rainer Santo, Eva Sicking, Anton Sperling, Wolfgang Verhoeven, Matthias Walter, Uwe Westerhoff, Martin Wilde, Alexander Wilk, Svenja Wulff, Dr. Oliver Zaudtke.
Nicht zuletzt bedanke ich mich bei meinen Eltern, meiner Familie und meiner Freundin Anita, die mich immer unterstützt und motiviert haben.